UNIVERSITY OF ICELAND

Thesis for the degree of Philosophiae Doctor

in Geophysics

Improving modelling of crustal deformation in relation to magmatic and geothermal processes

Chiara Lanzi

September 2025

FACULTY OF EARTH SCIENCES

UNIVERSITY OF ICELAND

FACULTY OF EARTH SCIENCES

Improving modelling of crustal deformation in relation to magmatic and geothermal processes

Chiara Lanzi

Dissertation submitted in partial fulfillment of a
Philosophiae Doctor degree in Geophysics

Supervisor
Freysteinn Sigmundsson

Doctoral Committee
Freysteinn Sigmundsson
Halldór Geirsson
Michelle Maree Parks
Vincent Drouin

Opponents
Alessandro Bonforte
Emily Montgomery-Brown

Faculty of Earth Sciences
School of Engineering and Natural Sciences
University of Iceland
Reykjavik, September 2025

Improving modelling of crustal deformation in relation to magmatic and geothermal processes

Dissertation submitted in partial fulfillment of a *Philosophia Doctor degree in Geophysics*

Faculty of Earth Sciences
School of Engineering and Natural Sciences
University of Iceland
Askja, Sturlugata, 7
102, Reykjavik
Iceland

Telephone: 525 4000

Bibliographic information:

Chiara Lanzi, 2025, Improving modelling of crustal deformation in relation to magmatic and geothermal processes, PhD dissertation, Faculty of Earth Sciences, University of Iceland, 216 pp.

Author ORCID: 0000-0002-1322-9563
ISBN: 978-9935-9772-6-7

Abstract

Understanding small crustal deformation signals is important for improving volcano monitoring and hazard mitigation. Spatial and temporal ground displacement patterns were mapped with Global Navigation Satellite System (GNSS) geodesy and Interferometric analysis of Synthetic Aperture Radar (InSAR) images, allowing detection of millimeter- to centimeter-scale deformation. Geodetic modelling, through inversion or forward modelling, was used to infer deformation source parameters and increase understanding of volcanic, geothermal and tectonic processes. In summer 2018, a change in the pattern of ground deformation at the Krafla caldera coincided with increased pressure in a monitoring well. This occurred at a similar time as re-injection of water, in relation to geothermal utilization, was modified. The difference between GNSS and InSAR velocity fields from 2015–2018 and 2018–2020 reveals an inflation pattern with horizontal motion up to 8–10 mm/yr. Geodetic inversion shows that the difference velocity field can be fit with a 2.1–2.5 km deep point-source, near the magma-hydrothermal interface. The observations are broadly explained by local variations in intra-caldera crustal elasticity and pressure increase at ~2.2 km depth, consistent with the well data. The study also examined how local elastic and viscoelastic crustal and mantle properties at volcanoes located at divergent plate boundaries influence deformation by regional processes like plate spreading, using a Finite Element Method model to simulate local rheological anomalies beneath calderas and rifts. This approach helps explaining the observed decades-long subsidence at Krafla (1989–2018) and Askja (1985–2021). The results show that extensional forces and rheological anomalies can drive volcanic subsidence. At Krafla, this account for much of observed 2015-2018 subsidence, but only 20–30% at Askja. Finally, the ~40-60 mm subsidence during the 2021 Fagradalsfjall eruption was analyzed and evaluated how changes in deformation relate to changes in eruption rate, geochemistry of eruptive products, and eruptive style. Surface lava loading within 1-2 km significantly contributed to the subsidence. After removing this effect, geodetic inversion locates a 12–14 km deep sill source with volume contraction of 21–27 Mm^3. This research highlights the need to consider complex geological settings when interpreting small ground deformation signals, as multiple interacting processes may produce observed deformation.

Útdráttur

Aukinn skilningur á minniháttar jarðskorpuhreyfingum er mikilvægur til að bæta vöktun eldfjalla og draga úr áhrifum af náttúruvá af þeirra völdum. Munstur jarðskorpuhreyfinga í tíma og rúmi var mælt með GNSS-landmælingum (e. Global Navigation Satellite System geodesy) og bylgjuvíxmælingum úr ratsjárgervitunglum (e. InSAR, Interferometric analysis of Synthetic Aperture Radar), sem gerir kleift að mæla smáar hreyfingar jarðskorpunnar (af stærðargráðunni millimetrar og sentimetrar). Líkangerð var notuð til að finna uppsprettur jarðskorpuhreyfinganna og eiginleika þeirra með því að beita andhverfum vörpunum, eða með beinum samanburði mældra jarðskorpuhreyfinga við niðurstöður reiknilíkana, með það að markmiði að auka skilning á ferlum sem eiga sér stað á eldfjöllum og jarðhitasvæðum sem og tektónískum ferlum.

Sumarið 2018 mældist breyting á munstri jarðskorpuhreyfinga í Kröfluöskjunni, á sama tíma og þrýstingsbreytingar mældust í borholu sem notuð er til að vakta jarðhitakerfið í Kröflu. Þetta gerðist á svipuðum tíma og breytingar voru gerðar á niðurdælingu vatns í jarðhitakerfið í tengslum við jarðhitanýtingu. Mismunur á GNSS og InSAR hraðasviðum á Kröflusvæðinu fyrir tímabilin 2015-2018 og 2018-2020 sýnir þenslu með láréttar færslur jarðskorpunnar allt að 8–10 mm/ári. Skýra má jarðskorpuhreyfingarnar sem afleiðingu af þrýstiaukningu í litlu kúlulaga rúmmáli (e. point-source) á 2.1–2.5 km dýpi undir Kröfluöskjunni, nálægt mörkum jarðhitakerfis og kviku. Ef tekið er tillit til fjaðureiginleika jarðskorpunnar innan öskjunnar og hvernig þeir eru breytilegir frá því sem gerist í nágrenni öskjunnar þá getur þrýstiaukning af svipaðri stærðargráðu og mældist í vöktunarborholunni útskýrt að mestu jarðskorpuhreyfingarnar.

Einnig var rannsakað hvernig fjaðrandi og seigfjaðrandi eiginleikar jarðskorpu og möttuls í eldstöðvakerfum á flekaskilum hafa áhrif á jarðskorpuhreyfingar vegna svæðisbunda ferla í jarðskorpunni eins og flekareks. Unnið var reiknilíkan með bútaaðferð (e. FEM; Finite Element Method) og seigfjaðrandi efnishegðun til að líkja eftir efnishegðun undir öskjum og gliðnunarbeltum. Líkanið sýnir að samspil á milli staðbundinna efniseiginleika í rótum eldstöðva og krafta vegna flekahreyfinga getur leitt til landsigs á eldvirkum svæðum. Slíkt samspil getur skýrt stóran hluta landsigs sem mældist í eldstöðvakerfi Kröflu 2015-2018, en aðeins 20-30% af landsigi sem mældist í Öskju á sama tímabili.

Loks var rannsökuð þróun landsigs (~40-60 mm) í 2021 eldgosinu í Fagradalsfjalli og metið hvernig breytingar á jarðskorpuhreyfingum tengjast breytingum á kvikustreymi, efnasamsetningu gosefna og gosvirkni. Metin voru áhrif fergingar vegna hraunsins sem myndaðist og niðurstöður sýna að fergingin hefur áhrif á landsig innan við 1-2 km frá hrauninu. Líkangerð með andhverfri vörpun þar sem tekið var tillit til fergingarinnar sýnir að jarðskorpuhreyfingarnar má skýra með sillulaga líkani í fjaðrandi hálfrúmi á 12-14 dýpi sem dregst saman um 21-27 milljón rúmmetra.

Rannsóknarvinnan sýnir að þörf er á að taka tillit til flókinna jarðfræðilegrar aðstæðna á eldfjöllum þegar minniháttar jarðskorpuhreyfingar eru túlkaðar og að samspil margra mismunandi ferla getur skýrt mælt munstur jarðskorpuhreyfinga.

Table of Contents

List of Figures

List of Tables

List of Publications

Paper I: Lanzi, C., Drouin, V., Sigmundsson, F., Geirsson, H., Hersir, G. P., Ágústsson, K., Parks M. M, Hreinsdóttir S., Guðmundsson Á. (2023). Pressure increase at the magma-hydrothermal interface at Krafla caldera, North-Iceland, 2018–2020: Magmatic processes or hydrothermal changes? *Journal of Volcanology and Geothermal Research*, *440*, 107849. https://doi.org/10.1016/j.jvolgeores.2023.107849

Paper II: Lanzi, C., Sigmundsson, F., Parks, M.M., Geirsson, H., Drouin, V., 2024. Strain Localization at Volcanoes Undergoing Extension: Investigation of Long-Term Deformation at Krafla and Askja Volcanic Systems in North Iceland. Geophysical Research Letters 51, e2024GL110299. https://doi.org/10.1029/2024GL110299

Paper III: Lanzi, C., Geirsson, H., Parks M. M, Drouin, V., Sigmundsson, Transient ground deformation observed by GNSS and InSAR during and following the 2021 Fagradalsfjall eruption, Iceland submitted to *Bulletin of Volcanology*.

Abbreviations

GNSS	Global Navigation Satellite System
SAR	Synthetic Aperture Radar
InSAR	Interferometric Synthetic Aperture Radar
FEM	Finite Element Method
RP	Reykjanes Peninsula
WVZ	Western Volcanic Zone
EVZ	Eastern Volcanic Zone
NVZ	Northern Volcanic Zone
SISZ	South Iceland Seismic Zone
TFZ	Tjörnes Fracture Zone
RR	Reykjanes Ridge
LOS	Line-of-Sight
PRN	Pseudorandom noise
PPP	Precise Point Positioning
ITRF	International Terrestrial Reference Frame
DEM	Digital Elevation Model
SBAS	Small Baseline Subset
PS	Persistent Scatterer
E	Young modulus
C-model	Caldera model
CFS-model	Caldera and Fissure Swarm model

Acknowledgements

First and foremost, I would like to express my deepest gratitude to my supervisor, Freysteinn Sigmundsson, for accepting me as his PhD for this project. His calm but steady mentorship, unwavering support and valuable feedbacks have encouraged me at every stage of my academic journey.
I am also grateful to the members of my committee, Halldór Geirsson and Vincent Drouin, for their support on the GNSS and InSAR, their comments and promoting critical thinking. Thanks to Michelle Parks, who has offered invaluable advice on modelling strategies and was always ready to make me feel confident in my abilities.
I would like to thank Sigrún Hreinsdóttir, who was always willing to share her experience with the GNSS processing from the other side of the world. I am grateful for the chance to meet wonderful scientists at Askja at the University of Iceland that shared their knowledge and expertise during stimulating conversations: Páll Einarsson, Magnús Tumi Guðmundsson, Bryndís Brandsdóttir, Guðfinna Aðalgeirsdóttir, Finnur Pálsson and many more that contributed to the Wednesday meetings. You help me "navigating" volcanic processes in Iceland and always provided interesting point of views. Special thank is for Sveinbjörn Steinþórsson for all the field work together, the assistance provided made successful GNSS campaigns and always ensure that I did not get lost somewhere in Iceland.
A few months after I moved to Iceland to begin my PhD, COVID-19 started. It was quite overwhelming being in that situation in a new country. I would not have made it through if not for two special people, Cécile and Siqi, always providing a good chat, fun and support.
To Yilin and Sonja, who shared most of my PhD journey: thanks for the continuous support, discussions, field work times, the more challenging and funny moments together in our never-boring-office and outside the workspace (PS: by the way, hope we can go to check the status of the tree at some point!!). Also, I would like to thank my other office mates: Didas, TingTing, Patricia, Araksan, Cat, Ylse, Greta, Alberto, Nico, Daniel and Jonas for the time together.
Thanks to my long-time friends, which I consider my "chosen" family: Cecca, Marco, Gianmarco, Martina and Manuela, who had to deal more than once with my "no-stop talking moments" about volcanoes. And will keep hearing them!
I am also deeply thankful to my parents and my sisters for their understanding when I decided to start a chapter of my life abroad. Also, to my nephews and niece, who always make me laugh and ask whether we can go through the Volcanoes book once more, every time I am visiting. No, worries little ones, I'll never say no to that.
This PhD project was mainly founded by research projects of Freysteinn Sigmundsson. The project continued through funding from the EPOS-Iceland project, the MaDRe Project (RANNIS grant number 228933-051) and the Teaching Assistant Grand from the University of Iceland.

1 Introduction

Volcano geodesy, the study of ground deformation on volcanoes, can help to evaluate processes that take place in volcano roots, e.g. by comparing observed deformation with predicted displacement patterns that depend on size, shape and volume change of subsurface sources (e.g., Dzurisin, 2006). Many regional and local processes contribute to ground deformation, including mass movement, magma intrusion, magma flux variability at depth, tectonics and faulting, and geothermal processes. These processes can produce detectable surface deformation at the meter (m), centimeter (cm) or millimeter (mm) scale. In order to build up a long-term understanding of a volcanic area and to assess the relation between magmatic activity and observed crustal deformation measured with geodetic techniques e.g., Global Navigation Satellite System (GNSS) geodesy and Interferometric analysis of Synthetic Aperture Radar (InSAR) satellite images, it is important to discern between the contributions from different magmatic and amagmatic on-going processes. In addition to improving scientific understanding, such information is useful for civil protection and in decision-making processes by relevant institutions managing or utilizing volcanic/geothermal areas, for mitigating the impact of volcanic hazards on society.

Ground deformation changes occurring at variable depth are transmitted to the surface through the mechanical properties of the crust (e.g., Biggs et al., 2014). Deeper sources of deformation (>20 km deep) in the fully ductile part of the crust may not cause any detectable surface deformation (e.g., in interferograms or GNSS time series), unless large volume mass transport is involved. For such a case, if an eruption occurs, information on the origin of the deep source may be retrieved from petrological and geochemical investigations of eruptive products, including studies of evolution of crystal and xenoliths in erupted lava, or if deep earthquake seismic swarms are observed (Dayton et al., 2023). Magma movements may also be detected by repeated geodetic measurements revealing surface deformation, such as due to magma accumulation (leading to inflation) or magma withdrawal from a crustal volume where magma resides (leading to deflation). In the former case, magma may reach the surface or intrude in the surrounding rocks. Inflation has been documented prior to many eruptions: e.g., the 2011 Grímsvötn eruption (Hreinsdóttir et al., 2014) or the Sundhnúkur eruptions in 2023-2024 in Iceland (Sigmundsson et al., 2024a; Parks et al., 2025), the 2011 Hudson volcano eruption in Southern Andes, Chile (Delgado et al., 2014), and the 2015 Mt. Hakone eruption in Japan (Kobayashi et al., 2018). However, volcanic eruptions may begin without detectable pre-inflation of the ground, like at Dalafilla and Borale in Africa (Pagli et al., 2012). Years-to-decades-long uplift can also be observed without any eruption taking place, with the amount of uplift without eruptive activity influenced by tectonic setting and length of previous repose interval at a volcano, that is different for each volcano. This has e.g., been observed at Colli Albani in Italy (Salvi et al., 2004), near the Three Sisters volcanic center, Oregon (Riddick and Schmidt, 2011), and at Campi Flegrei (Amoroso and Crescentini, 2022). Eruptions may though occur in these areas in the future. Movement of magma in the subsurface is not the only process causing ground deformation. Hydrothermal activity may play a role (Battaglia et., 2006;

Fournier and Chardot, 2012), sometimes in relation to migration of fluids of magmatic origin (e.g., Currenti et al., 2017) or interplay between the regional tectonics and the volcanic system crustal structure (e.g., Ellis et al., 2007).

Geodetic modelling of ground deformation data helps to discriminate between processes occurring in volcanic areas. Advanced numerical modelling techniques (e.g., based on the Finite Element Method, FEM, or the Boundary Element Method) are becoming important to understand volcano behaviour, in addition to analytical models. The analytical models are based on first-order approximations, and are widely used to interpret observed volcano deformation (Taylor et al., 2021). Advanced numerical approaches can provide models with increased complexities. More realistic Earth's crust models have been developed to include topography and heterogeneous and elastic medium (Trasatti et al., 2003; Currenti et al., 2008), variable rheology (e.g., elastic and viscoelastic material, Hickey et al., 2014; Currenti, 2017) or to investigate the thermal properties of the crust (Henk, 2006; Gottsmann et al., 2014; Head et al., 2021). Consideration of thermal effects on ground deformation is relevant in volcanic settings where the presence of hot liquid magma or magma mush (Sparks and Cashman, 2017; Liao et al., 2018) alters significantly the physical properties of the crust. In a relatively high-temperature environment, inelastic effects may be dominant, and time-dependency behavior of the crustal material becomes an important component of the deformation (e.g., Ranalli, 1995). Pressurization/depressurization of sources in an elastic medium lead to instantaneous volume changes (either expansion or contraction). In a viscoelastic regime, the imposed condition of a deformation source affects stress and strain patterns differently in both space and time (Head et al., 2019).

Modelling of the same processes may lead to different results and interpretation according to imposed boundary conditions. For example, the kinematics of a divergent plate boundary or in general any local extensional regime has been widely reproduced by considering a uniform spreading velocity (Peltier et al., 2009; Cabaniss et al., 2018) or, alternatively, a constant rate of external stress (Costa et al., 2011; Karaoğlu et al., 2020) applied on the sides of a numerical model domain. In Iceland, several plate spreading models have attempted to reproduce deformation across different plate boundary segments (Árnadóttir et al., 2009), including the use of horizontal crustal layers in the Western Volcanic Zone (WVZ) and Eastern Volcanic Zone (EVZ) (e.g., Jónsson et al., 1997; LaFemina et al., 2005) or FEM models linking the observed inter-rifting deformation field to rheological variations within the en-echelon arrangement of the fissure swarms in the Northern Volcanic Zone (NVZ) of Iceland (Pedersen et al., 2009; Islam et al., 2015) by applying uniform velocity.

In this thesis, emphasis is first put on investigating how ground deformation patterns at Krafla and Askja volcanic systems in North Iceland are affected by the interplay between crustal heterogeneity and deformation fields due to localized sources of deformation or plate spreading. FEM numerical models, implemented in the COMSOL Multiphysics® software (Pryor, 2011), are used to investigate short-term ground deformation and pressure changes at the Krafla caldera in 2018-2020. FEM models are then used to evaluate the expected deformation patterns at Krafla and Askja volcanic systems, located at the plate spreading boundary, during inter-rifting periods, considering rheological anomalies in volcano roots. The aim is to contribute to better understanding long-term rift evolution. In the last part of the thesis, observed transient deformation during and after the 2021 Fagradalsfjall eruption on the Reykjanes Peninsula in south-west Iceland is investigated in terms of its relationship to the evolution of conditions in

magmatic plumbing system and the effects of the loading of newly emplaced lava on the surface of the Earth.

1.1 Deformation processes in Iceland and geological context

Iceland is a portion of the Mid-Atlantic oceanic ridge above the sea level at the divergent boundary between the Eurasian and North American plates. According to plate motion models, the two plates separate at ~18–19 mm/yr in direction N104.5°E in Iceland (DeMets et al., 2010), in agreement with GNSS measurements (e.g., Geirsson et al., 2006; Árnadóttir et al., 2009). As a result, it is possible to observe continuous deformation due to several regional and local processes in Iceland (e.g., Sigmundsson, 2006).

Regional ground deformation in Iceland is mostly driven by both plate spreading processes and ongoing glacial isostatic adjustment. The plate boundary is divided into zones (Figure 1): the Reykjanes Peninsula oblique rift (RP), the Western Volcanic Zone (WVZ), the Eastern Volcanic Zone (EVZ), the Northern Volcanic Zone (NVZ), and two transform zones, one left-lateral transform zone in south Iceland, the South Iceland Seismic Zone (SISZ), and a right-lateral transform zone, the Tjörnes Fracture Zone (TFZ) in North Iceland (Einarsson, 1991). The rift zones can be divided into volcanic systems, based on their structural and petrological characteristics (Sæmundsson, 1978; Jakobsson, 1979). They usually include a central volcano and a transecting fissure swarm. The fissure swarms are narrow (5–20 km wide), elongated (up to more than 100 km long) structures that are normally aligned sub-parallel to the rift axis (e.g., volcanic systems in the NVZ; Sæmundsson, 1978; Hjartardóttir et al., 2013) or oblique to the rift axis (e.g., the RP volcanic systems; Einarsson, 1991; Einarsson, 2008). They often have the structure of a graben bounded by normal faults (Einarsson, 2008). Episodic high rates of deformation in volcanic systems may relate to rifting events (e.g., Wright et al., 2012). Rifting episodes are characterized by dike intrusion/s within the brittle part of the crust, which potentially may, but not necessarily, reach the surface. Geodetically monitored rifting episodes in Iceland include the 1975-1984 Krafla Fires, the 2014–2015 Bárðarbunga-Holuhraun eruption (Sigmundsson et al., 2015) and the on-going period of activity on the RP that started in December 2019 (Sigmundsson et al., 2022; Parks et al., 2023; Sigmundsson et al., 2024a).

In addition to plate movements, another source of broad-scale regional deformation in Iceland relates to variation in glacier mass. About 10% of the surface of Iceland is at present covered by glaciers (Sigurðsson, 2006; Björnsson and Pálsson, 2008), with Vatnajökull (Figure 1) being the largest ice cap. Due to thinning and retreat of ice since about 1890, ongoing Glacial Isostatic Adjustment (GIA) produces uplift and horizontal motion away from the ice caps (e.g., Árnadóttir et al., 2009; Auriac et. al., 2014; Drouin and Sigmundsson, 2019). InSAR analysis shows a maximum GIA uplift rate of 31±4 mm/yr at the northern edge of Vatnajökull, during 2004–2009 (Auriac et al., 2014). The rate decays with distance from the ice cap (e.g., 2015-2018 InSAR observations; Drouin and Sigmundsson, 2019), and there have been periods when the rates accelerate with time (1995-2014 GNSS observations, Compton et al., 2015). Extension of the InSAR analysis until 2021 appear to show continuation of this acceleration in central Iceland (Cao et al., 2023). However, the deformation pattern observed by GNSS measurements

near Vatnajökull are not characterized by steady acceleration between 2010 and 2023; rather the rate varies considerably in relation to irregular variations in ice loss of the nearby Vatnajökull ice cap (Geirsson et al., 2020; Sigmundsson et al., 2024b).

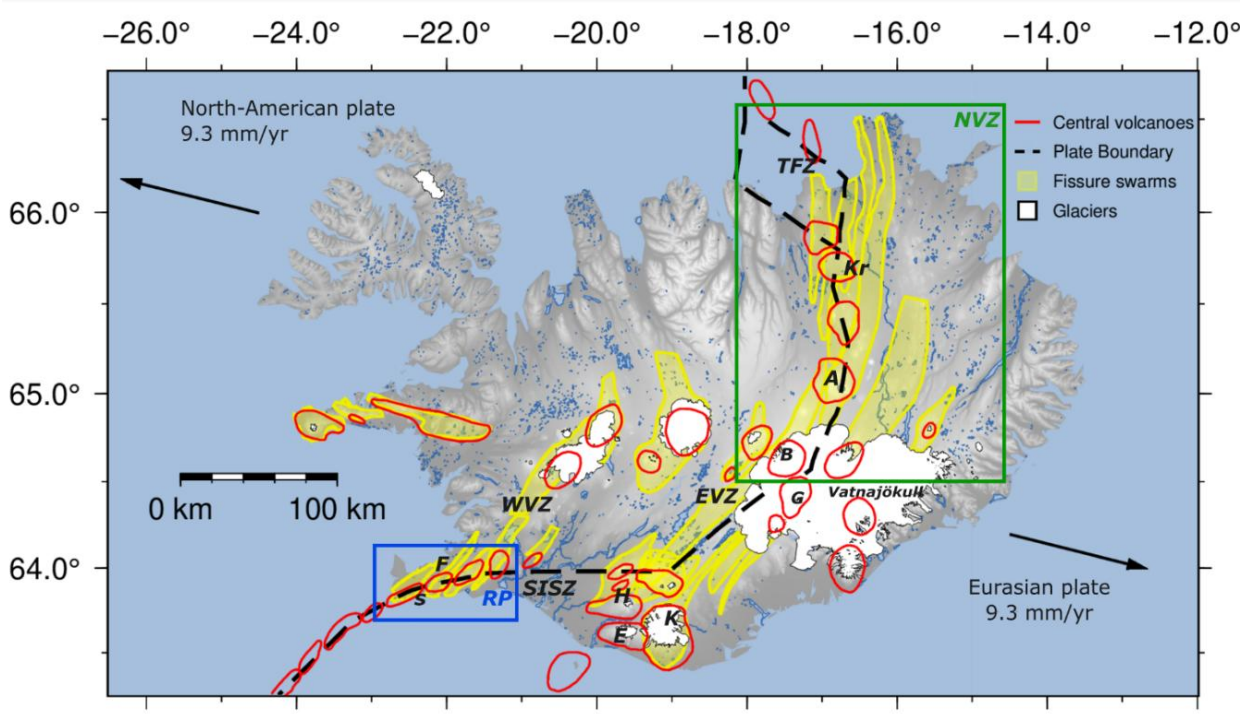

Figure 1. Grey-to-white shaded topography map showing fissure swarms, glaciers and central volcanoes of Iceland (Jóhannesson and Sæmundsson, 2009). Names of the seismic and volcanic zones in Iceland (from west to east/north-east): RP = Reykjanes Peninsula oblique rift, WVZ = Western Volcanic Zone; SISZ = South Iceland Seismic Zone; EVZ= Eastern Volcanic Zone; NVZ = Northern Volcanic Zone; TFZ= Tjörnes Fracture Zone. Selected names of volcanic systems: S = Svartsengi, F= Fagradalsfjall; H = Hekla; E= Eyjafjallajökull; K = Katla; G= Grímsvötn; B= Bárðarbunga; A = Askja, Kr= Krafla. Rectangles mark the areas studied in this thesis, the RP in blue and the NVZ in green. Thick black hatched lines show a simplified version of the central axis of plate boundary across Iceland (Drouin et al., 2017; Sigmundsson et al., 2022). Ocean, rivers and lakes shown in light blue.

Unloading and loading events due to large ice mass variations may alter stress conditions around magmatic systems. Such perturbations may induce a variation in the stress state of the crust and reduce or increase the pressure threshold for dike propagation and trigger the onset of an eruption (Albino et al., 2010; Sigmundsson et al., 2010). Currently, about half of the 33 active volcanic systems in Iceland (https://icelandicvolcanos.is/) lie beneath ice caps (e.g., Katla, Eyjafjallajökull, Grímsvötn, Bárðarbunga; Figure 1). The presence of thick ice cover plays a critical role in modulating both the mechanical loading on the crust and the interaction between magma and meltwater during eruptions. Thus, explosive eruptions are common due to water-magma interaction at such ice-covered volcanoes, which amplify the explosivity,

generating fine-grained tephra like the 2010 Eyjafjallajökull eruption (Dellino et al., 2011) and the 2011 Grímsvötn eruption (Petersen et al., 2012; Hreinsdóttir et al., 2014), both accompanied by extensive ash fallout.

In addition to GIA, other surface loading on the crust may induce detectable surface displacement. There are different kinds of loads locally acting on the surface like emplacement of new lava (Odbert et al., 2015) or ocean tidal effects (You et al., 2021), especially in coastal areas. Lava emplaced on the surface of the Earth during eruptions can cause progressive subsidence of the surrounding substrate (Briole et al., 1997; Lu et al., 2005; Dietterich et al., 2012; Chaussard, 2016). In Iceland, this has been observed, e.g. at Hekla volcano (Grapenthin et al., 2010; Wittmann et al., 2017). Additionally, GNSS observations in Iceland reveal a seasonal (sinusoid-like) signal well explained as the Earth response to loads considering a combination of the annual mass balance of glaciers, snow load on non-glaciated areas, response to on-land seasonal variation in pressure and oceanic loading (Drouin et al., 2016a).

Local deformation can occur in geothermal areas due to geothermal processes. The geothermal activity in Iceland is linked with the country's volcanism. According to their temperature, geothermal areas can be divided into high-temperature geothermal reservoirs (in active rift zones), where the temperature at 1000 m reaches over 230°C; or low-temperature geothermal reservoir (on the flanks of the active zones and in seismic zones), where the temperature does not exceed 150°C at 1000 m depth (Arnórsson, 1995). Some of the geothermal fields are exploited for energy production (e. g., Hengill, Krafla, and the Reykjanes geothermal fields). This can cause local deformation due to the extraction of geothermal fluids as well as due to re-injection of fluids into the geothermal fields to counteract the effects of extraction (e.g., Drouin et al., 2017; Juncu et al., 2020; Parks et al., 2020; Ducrocq et al., 2021).

Earthquakes produce deformation fields due to fault slip but can also cause further transient local deformation on two spatiotemporal scales. For examples, a M_w 6.5 earthquake in 2000 in the South Iceland Seismic Zone (SISZ) caused post-seismic deformation lasting around 2 months after the event and extending about 5 km away from the two main shock ruptures, related to poroelastic rebound due to post-earthquake pore pressure changes (Árnadóttir et al., 2005). Additionally, a year-long deformation viscoelastic relaxation of the lower crust and upper mantle in response to the co-seismic stress changes was observed (Árnadóttir et al., 2005; Decriem and Árnadóttir, 2012).

Eruptions are frequent in Iceland and about 90% of the Icelandic rock is of direct volcanic origin, with about 10% of consolidated sediments, mainly in the form of interbedded tuffaceous layers and moraines (Jakobsson, 1979). Volcanism in Iceland is diverse, spanning a range of common terrestrial magma types and eruption styles (Thordarson and Larsen, 2007). Eruptions can be purely explosive or effusive or a mixture of them (Thordarson and Höskuldsson, 2008). The volcanic rocks are made up of 85-90% basalt, with about 4% being basaltic andesite, 1% andesite and 3-5% are dacite-rhyolites (Jakobsson et al., 2008). In hydrothermal areas, usually located at central volcanoes or calderas, the geothermal heat often causes high alteration of rocks. Partial melt of hydrothermally altered rocks has been suggested to be the origin of the rhyolites at Krafla (Jónasson, 1994). Because of the alteration, geothermal areas may display local variability and lower elastic properties of the crust (Pereira et al., 2024).

1.2 Areas of study

1.2.1 The Northern Volcanic Zone and the Krafla and Askja volcanic systems

The NVZ of Iceland (Figure 2) hosts several volcanic systems. From north to south, they are: Theistareykir, Krafla, Fremrinámar, Askja, and Kverkfjöll. In this thesis, the focus is on the Krafla and Askja volcanic systems.

The Krafla volcanic system consists of a central volcano with a 9×7 km caldera formed ~100,000 years ago (Sæmundsson, 1991), and ~5-8 km-wide transecting fissure swarm, extending 40 km to the south and 50 km to the north from the caldera (e.g., Hjartardóttir et al., 2012). The volcanic system hosts two geothermal areas, the Krafla geothermal field in the caldera and the Bjarnarflag geothermal area, ~10 km south of the caldera, both exploited for energy production. A rifting episode occurred there from 1975 to 1984 (Einarsson, 1991; Einarsson and Brandsdóttir, 1980; Buck et al., 2006; Wright et al., 2012) with a total cumulative horizontal extension up to a maximum of about 9 m (Tryggvason, 1985). The total volume of the erupted material is about 0.25-0.3 km^3, covering an area of 36 km^2 (Einarsson, 1991). An inflating/deflating shallow magma reservoir was inferred from geodetic measurements at a depth of about 2.5 km in the caldera during the rifting episode and continued to inflate five years after the last eruption, until 1989 (Tryggvason, 1985). Between 1989-1992, deflation was measured in the caldera with a subsidence rate of ~5 cm/yr (Tryggvason, 1994), exponentially decaying to ~3-5 mm/yr in 1995-2015 (Sturkell et al., 2008; Drouin et al., 2017). The deformation pattern changed in summer 2018. Difference velocity fields (between 2015–2018 and 2018–2020) reveal minor inflation inside the caldera with an inferred point-source of pressure at 2.1–2.5 km depth (Lanzi et al., 2023). Zones of seismic attenuation identified by seismic tomography – specifically, the analysis of S-wave shadow – suggest the presence of a shallow magma storage at 3–7 km depth inside the caldera, as first proposed by Einarsson (1978). More recent seismic tomography results show low V_p/V_s zones ($\leq$1.65) underneath the geothermal system at 2–3 km depth below sea level (bsl) (Schuler et al., 2015), close to a borehole (IDDP-1) that intersected rhyolitic magma at 2.1 km depth in 2009 (Elders et al., 2011). The low V_p/V_s zone has been suggested to be associated with a superheated steam layer, at the boundary between host rock and felsic melt. Vertical seismic profiling mapped a reflector at the same depth as the bottom of IDDP-1 drillhole, as well as at depths ranging from 4 to 6 km, interpreted as evidence for a distributed system of magmatic sills (Kim et al., 2020). The volcanic activity at Krafla has a bimodal behavior with basalts being dominant during rifting episodes, but also rhyolites can be found as testified by studies of eruptive products in the region (Sæmundsson, 1991; Nicholson et al., 1991; Jónasson, 1994). In 2009, a rhyolitic body at 2.1 km depth was encountered during drilling of the IDDP-1 well of the Iceland Deep Drilling Project (Elders et al., 2011).

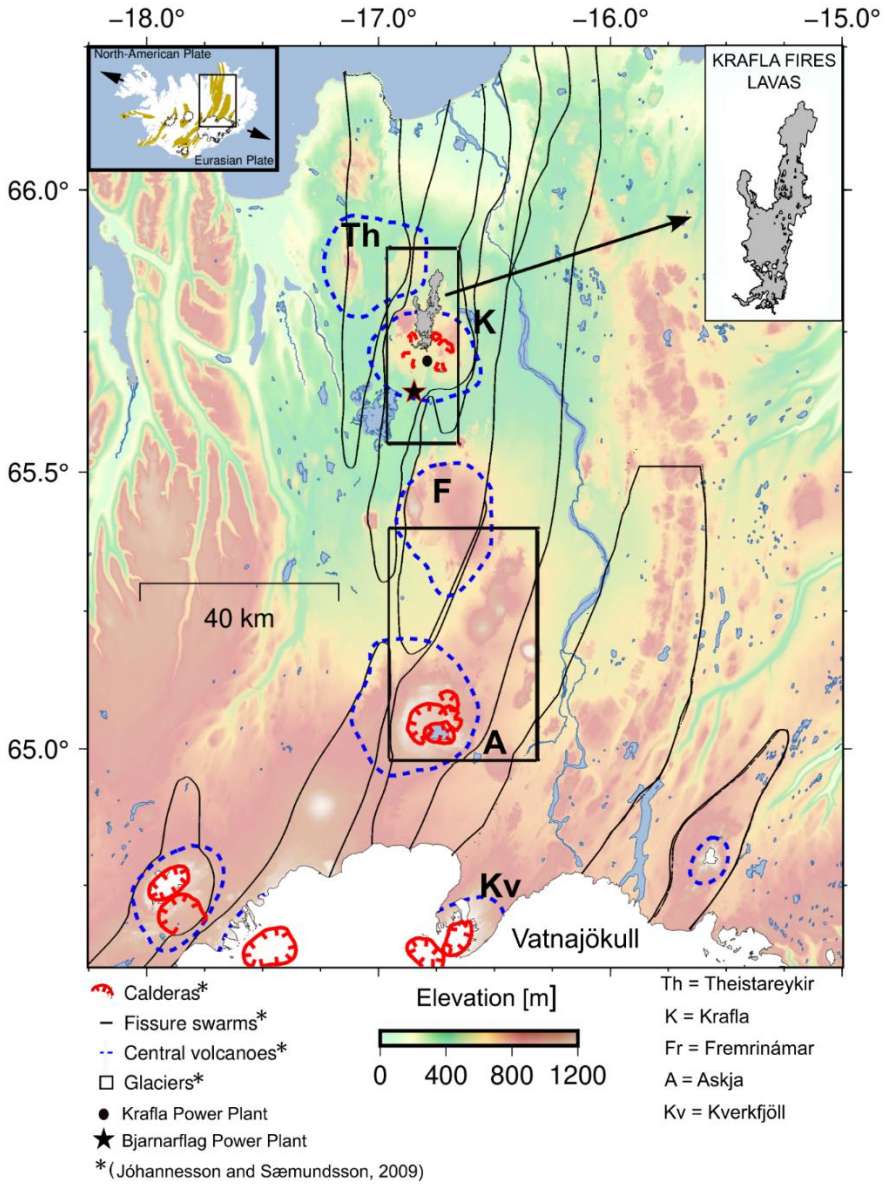

Figure 2. Map of the NVZ of Iceland. Volcanic systems from north to south: Th = Theistereykir, K= Krafla, F= Fremrinámar, A =Askja, and Kv= Kverkfjöll. Central volcanoes shown with blue dashed lines, calderas shown with red hatched lines and outline of fissure swarms with black lines (Jóhannesson and Sæmundsson, 2009). Inset map on the left shows the fissure swarms in Iceland (yellow), and the location of the NVZ in Iceland together with the spreading direction of the North American and Eurasian plates. Inset map on the right shows the Krafla Fires (1975-1984) lavas.

The Askja volcanic system (Figure 2) hosts a central volcano with several calderas where geothermal activity occurs, and a transecting 20 km-wide and 190 km-long fissure swarm (Hjartardóttir et al., 2009). The main Askja caldera has a diameter of ~8 km, and the most recent

eruption occurred in 1961 when a fissure opened at its north-eastern boundary, producing a lava field of ~0.1 km^3 (Thorarinsson and Sigvaldason, 1962). Previously, a major rifting episode occurred in 1874-1875 with basaltic and rhyolitic erupted material (Sigurdsson and Sparks, 1978a, b). In an early stage of this rifting episode, a fissure eruption occurred 50-70 km north of Askja, with a series of pulses of activity lasting for several months, most likely following a lateral dike intrusion into the rift zone fed from a reservoir located beneath Askja (Sigurdsson and Spark, 1978a). It is inferred that lateral magma withdrawal and later readjustment of the crust largely contributed to the formation of the Öskjuvatn caldera, which now hosts a lake, with dimensions of 3×4 km and a depth of 267 m, within the main Askja caldera (Sigurdsson and Spark, 1978a and b). Most of the volcanic products within the Askja volcanic system are basaltic, but silicic deposits are also evident (Sigurdsson and Sparks, 1981; Sigvaldason, 2002; Jónasson, 2007). Levelling (since 1966), GNSS (since 1993), and InSAR (since the early 1990s) showed deflation in the caldera in the 1983-2021 period. Maximum deflation occurred in the middle of the caldera at an initial rate of ~5 cm/yr (Sturkell et al., 2006), exponentially decaying to 2.5-3 cm/yr in 2000-2009 (de Zeeuw-van Dalfsen et al., 2012). In summer 2021, deformation changes and inflation centered in the caldera complex began. In the following two years, the uplift amounted to ~70 cm due to inferred pressure increase at ~2.8 km depth (Parks et al., 2024). The inferred source of inflation compares well to a ~3 km depth of the deflation source inferred by Sturkell et al. (2006) for the 1983-2003 period, from GNSS and levelling observations. Low seismic velocity zone imaged at 6–11 km bsl beneath Askja caldera has been interpreted as a magma storage region containing high-temperature solid rock with two main magma storage regions at ~5 and ~9 km bsl (Mitchell et al., 2013; Greenfield et al., 2016). In the lower crust, the seismic ray coverage is not as good as in the upper crust, but low V_s and high V_p/V_s areas can be identified, suggesting areas of melt storage as well as regions where melt is transported from a deeper source (Soosalu et al., 2010; Greenfield et al., 2016).

1.2.2 The Reykjanes Peninsula oblique spreading plate boundary and volcanic systems

Volcanism occurs at several volcanic systems on the Reykjanes Peninsula (Figure 3). From west to east, they are: Reykjanes, Svartsengi, Fagradalsfjall Krýsuvík, Brennisteinsfjöll and Hengill (Sæmundsson et al., 2020). They are spaced about 5 km apart, with an average strike of N40°E (Clifton et al., 2006; Hjartardóttir et al., 2023), characterized by eruptive fissures with crater rows and extensive normal faulting (Einarsson, 2008). Strike-slip faults (trending N-S, left-stepping) cut through the plate boundary, typically spaced between 0.4 -1 km (Einarsson, 2008). Most of the strike-slip faults are associated with mainshock-aftershock earthquakes sequences mainly in the Krýsuvik and Hengill areas (Tryggvason, 1973; Árnadóttir et al., 2005; Keiding et al., 2008; Hreinsdóttir et al., 2009). Earthquake swarms are more typical in the western part, e.g., at Fagradalsfjall. Pronounced swarm activity occurred there, at 2-6 km depth, in 1997-2006 (Keiding et al., 2008) and 2017 (Hrubcová and Vavryčuk, 2023). The Reykjanes, Svartsengi, Krýsuvík and Hengill volcanic systems host geothermal areas, all of them exploited except Krýsuvík. Ground deformation related to geothermal utilization has been observed e.g., by Parks et al. (2020) and Juncu et al. (2020). Non-eruptive periods, up to 800-1000 years, interrupted by eruptive activity lasting a few hundred years, characterize the latest

stages of the Holocene where the geological records allow the derivation of the eruptive history (Sæmundsson et al., 2020). In each activity episode, activity may occur in several volcanic systems (Sæmundsson et al., 2020) with effusive fissure eruptions affecting one volcanic system at time, with a minor ash component being produced (Gudmundsson et al., 2008). The peninsula is at present undergoing major volcano-tectonic unrest and volcanic activity, involving highly increased earthquake activity, inflation-deflation episodes, diking and eruptions (Çubuk-Sabuncu et al., 2021; Flóvenz et al., 2022; Sigmundsson et al., 2022; Parks et al., 2023; Sigmundsson et al., 2024a).

Initial precise distance measurements in 1968–1972 showed that a combination of left-lateral and extensional movement occurred on the Reykjanes Peninsula in SW-Iceland (Brander et al., 1976). The nature of the oblique spreading in the area has been well established by both GNSS and InSAR observations (Sturkell et al., 1994; Hreinsdóttir et al., 2001; Keiding et al., 2008; Sigmundsson et al., 2020).

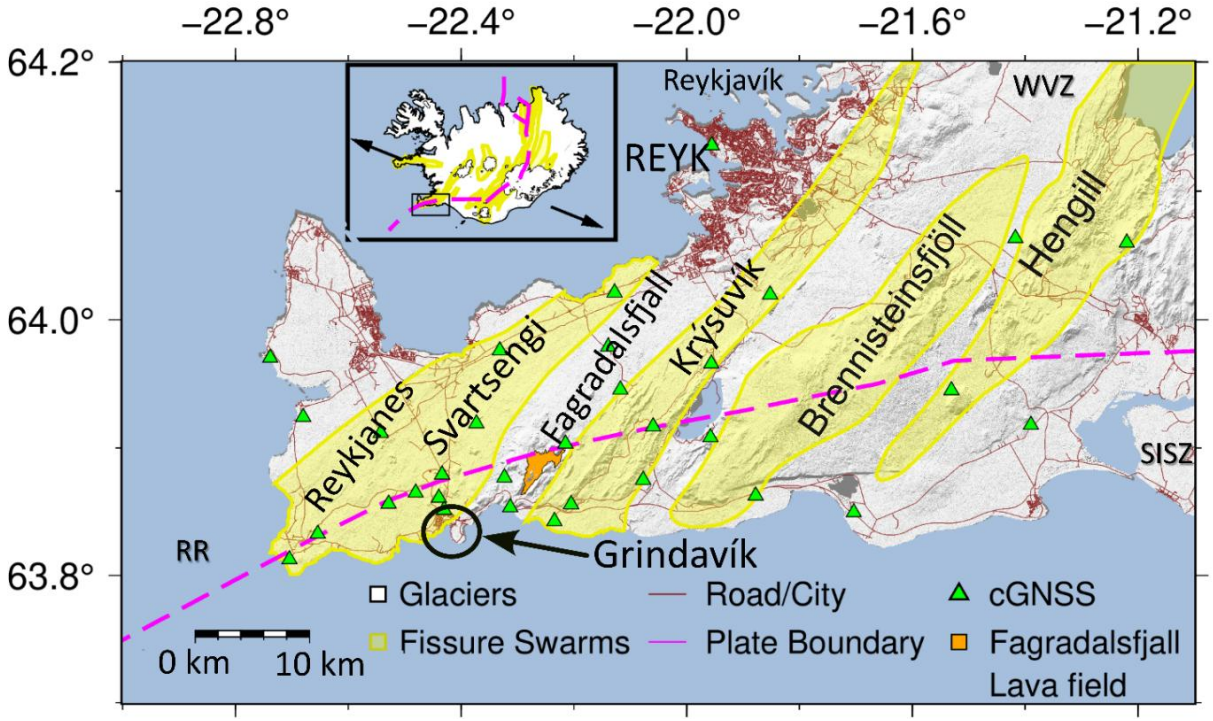

Figure 3. Map of the Reykjanes Peninsula showing volcanic systems with their fissure swarms (in yellow, Jóhannesson and Sæmundsson, 2009), the 2021 Fagradalsfjall lava field in orange (Pedersen et al., 2022), the continuous GNSS (cGNSS) network and the approximate location of the central axis of the plate boundary (Sigmundsson et al., 2022). Name (REYK) of the first continuous GNSS station in Iceland indicated. SISZ = South Iceland Seismic Zone, RR= Reykjanes Ridge and WVZ = Western Volcanic Zone. Inset: Iceland with fissure swarms, glaciers, and the plate boundary axis (magenta, Árnadóttir et al., 009; Drouin et al., 2017; Sigmundsson et al., 2022). The arrows indicate the spreading direction. The Reykjanes Peninsula is marked by a black rectangle.

In December 2019, seismicity rose above background level in the Fagradalsjall area. In 2020, three inflation-deflation cycles occurred at the Svartsengi volcanic system where each inflation was followed by continuous deflation and diminishing seismicity (Çubuk-Sabuncu et al., 2021; Flóvenz et al., 2022). The inflation events were likely related to the intrusion of magma into sill-type bodies at 3.2-4.3 km depth (Çubuk-Sabuncu et al., 2021; Geirsson et al., 2021) or magma accumulation in a magma domain, consisting of liquid magma, partial melt, magma mush, and hot solid rock (Sigmundsson et al., 2024a). Two more periods of inflation were observed there between April to May 2022 and 27 October - 10 November, 2023. Around 8 July 2020, inflation began at the Krýsuvík volcanic system (15-20 km east of the Svartsengi area), continuing until about 10 January 2021. A M_w 5.6 earthquake occurred there on 20 October 2020. On 24 February 2021, a M_w 5.64 earthquake occurred at the Fagradalsfjall volcanic system following an intense seismic swarm that began several hours earlier in the area. Intense seismicity was ongoing in the following weeks as well as high rate of deformation observed by continuous GNSS and InSAR Sentinel-1 data, in accordance with gradual intrusion a 9-km long dike intrusion in the crust, divided into a northern and a southern segment differing somewhat in strike and depth range (Sigmundsson et al., 2022). The volume intruded was estimated around 26–34 Mm^3 between the surface and 7.5 km depth (the northern segment) and 6 km depth (the southern segment) (Sigmundsson et al., 2022). Rates of seismicity and deformation gradually decreased to minor levels before the eruption onset, on 19 March 2021. The eruption lasted six months until 18 September 2021, with an initial time-averaged effusion rate up to 4.9 m^3/s, which increased to 11 m^3/s in May (Pedersen et al., 2022). At this stage, the eruptive style changed from continuous effusion of lava to episodic activity (Eibl et al., 2023; Eibl et al., 2024). At the end of the eruption the total bulk lava volume was estimated around 150 ± 3 Mm^3 (Pedersen et al., 2022).

A period of inflation began at the end of the eruption and continued until 21 December 2021 when a new diking event occurred beneath Fagradalsfjall, lasting for about one week. Bayesian geodetic modelling for this event estimated a dike median volume equal to 19 Mm^3 and median top of the dike at ~2 km (Parks et al., 2023). Two more dike-eruption sequences occurred in the area in July-August 2022 (dike intruded volume in the range of 8–14 Mm^3, Parks et al., 2023; bulk volume of the material erupted = 11 ± 0.4 Mm^3, Pedersen et al., 2024) and July-August 2023 (bulk volume of the material erupted = ~15 Mm^3). The 2022 eruption lasted around 18 days, while the 2023 eruption lasted 26 days. Following this, deformation as well as seismic and volcanic activity concentrated mostly at the Svartsengi volcanic system.

On 25 October 2023, seismicity increased drastically beneath Svartsengi and inflation was detected starting on 27 October. On the morning of 10 November 2023, around 7:00 UTC, low-magnitude seismicity began at 4 to 6 km depth near the center of the Svartsengi volcanic system, which gradually migrated 3.5 km in the NNE-SSW direction in the next 8.5 hours (Sigmundsson et al., 2024a). After a M_W4.1 event at 15:23, seismicity, with larger events, started to propagate southwards towards the town of Grindavík (Sigmundsson et al., 2024a). By 18:30 the events had reached the town of Grindavík and by 19:30, earthquakes were detected south of the town. No surface deformation signal was detected until around 16:40, when GNSS began to show high displacement rates both in the vertical and horizontal components, up to a total displacement of ~1 m by 20:00. Afterwards, the deformation rates and seismicity decreased. Associated with the seismic swarms and deformation, the formation of two grabens separated by a horst (~4.5 km width in total) was documented in the town of Grindavík (Figure 3 for location) (De Pascale et al., 2024). The modelling of GNSS and InSAR displacements (10

to 12 November) indicated a ~15-km long dike formed with a volume of 130-139 Mm^3. Between December 2023 and November 2024, seven eruptions occurred at the Svartsengi volcanic system (Parks et al., 2025). These eruptions were preceded by an inflation period for several weeks or longer, and short-lived (usually several hours) diking events associated with intense seismicity (Parks et al., 2025).

1.3 Geodetic monitoring techniques

At present, two space geodetic techniques are widely used for precise measurement of crustal deformation: GNSS (Global Navigation Satellite System), that measures three-dimensional displacements at single points; and InSAR (Interferometric Synthetic Aperture Radar), which measures the displacement in so-called Line-Of-Sight (LOS) direction, oblique from ground to satellite. Other non space-based techniques include levelling, which measures the difference in elevation between benchmarks, and Electronic Distance Measurements (EDM), which use laser phase changes to measure the length between two points (Dzurisin, 2006). The following paragraphs give an introduction of GNSS and InSAR, which were extensively used in this project.

1.3.1 Global Navigation Satellite System (GNSS) geodesy

GNSS is a general term that refers to any constellation of satellites orbiting over the Earth's surface that can provide continuous three-dimensional high precision positioning (longitude, latitude and elevation), navigation and time services (Hofmann- Wellenhof et al., 2008). GNSS is widely used for many applications in addition to precise ground surveying, including telecommunication, aviation, urban environment, mining, emergency response, plate boundary and volcano deformation, and seismology (Freymueller, 2017; Jin et al., 2013). There are currently several operational GNSS satellite constellations: i) the Global Positioning System (GPS) developed by the US Department of Defense. ii) the GLObal NAvigation Satellite System (GLONASS), operated by Russia. This was the second navigation system to achieve global coverage after the GPS. iii) The GALILEO system (www.galileognss.eu), owned by the European Commission and operated by the European Union Agency for the Space Programme (EUSPA), and specifically designed for civilian use worldwide. iv) The Beidou system (www.beidou.gov.cn), owned and operated by the China National Space Administration. Additional, regional satellite systems have also been developed for geodesy, e.g., the Indian Regional Navigation Satellite System (IRNSS, https://www.isro.gov.in/IRNSS_Programme.html), owned by the Indian government, and the Japanese Quasi-Zenith Satellite System (QZSS, www.qzss.go.jp), which provide precise and stable positioning services in the Asia-Oceania region.

The GNSS architecture and broadcast signals may differ between the different satellite systems but generally each system has space, ground control and user segments. The space segment includes a constellation of satellites orbiting above the Earth and usually arranged in several or more orbital planes. For example, the space segment of the GPS counts 32 satellites orbiting in six orbital planes (referred also to as satellite paths) inclined at 55° with respect to

the equator, equally spaced, at an altitude of approximately 20,000 km (www.gps.gov). Receiver location (X, Y, Z) and time are obtained using a configuration of at least four transmitting satellites (Hofmann-Wellenhof et al., 2008). The ground control segment of each GNSS consists of master and control stations on Earth, with primary responsibility being the maintenance of the whole system by tracking satellite paths for the prediction and correction of on-board and orbital parameters. Revised orbits, clocks and earth orientation parameters are provided by online services like the International GNSS Service for Geodynamics (IGS, by the Jet Propulsion Laboratory, JPL, http://igscb.jpl.nasa.gov). The user segment consists of antennas and receivers that can detect the signals transmitted by the satellite or services of the GNSS.

In simple terms, GNSS positioning is based on using known locations of satellites (or estimating them), and measurements of the time that it takes for a signal broadcasted by a satellite to reach a user antenna on the Earth to infer the distance to the satellites. With multiple such observations, the antenna location can be determined (Figure 4). Ideally, if the receiver station and satellite clocks are perfectly synchronized, the measurements of distances to three satellites would be sufficient to derive a receiver location on Earth. Three spheres with origin at each of the satellites, and radius equal to the distance to a receiver, intersect at one point on Earth. However, a fourth satellite is needed to provide information on precise timing and estimate receiver clock/timing bias (Bock and Melgar, 2016). The satellite-to-receiver distance, referred to as range, is obtained by the signal propagation time multiplied by the speed of light. The time is controlled by high-precision on-board satellite atomic clocks, commonly reaching fractional frequency performance at the 10^{-13} - 10^{-15} level (Giorgi et al., 2019) and by the presence of crystal quartz clocks in the receiver, sufficient for synchronization with the satellite clocks.

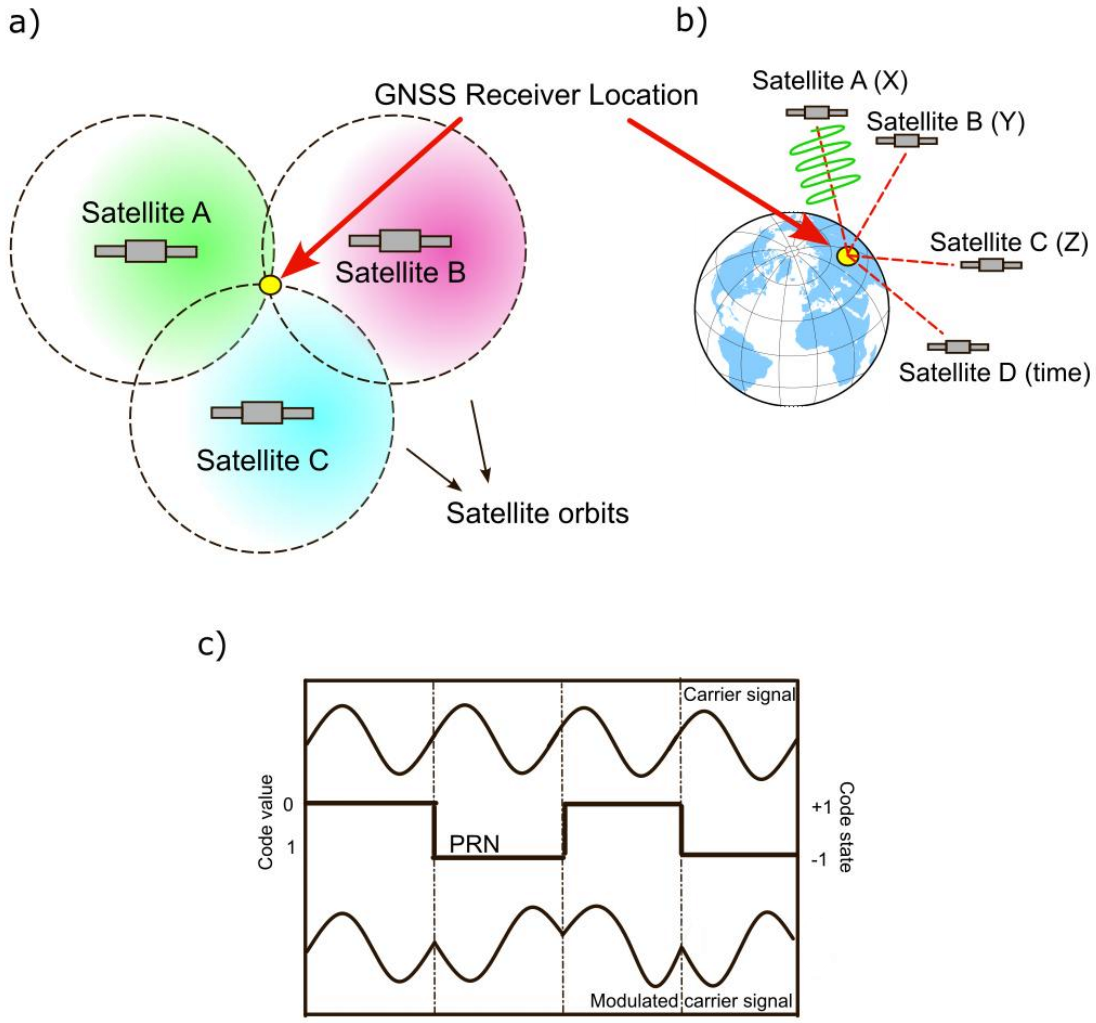

Figure 4. a) Graphical illustration of localization by measuring distances to three satellites of known locations; the three 'spheres' intersect on one point on the surface of the Earth, at the receiver location. b) In reality, distance measurements to a minimum of four satellites are needed, corresponding to the four unknows of the system: longitude (X), latitude (Y), altitude (Z) and the receiver clock error (time). The range from satellite to receiver is shown with dashed red lines, while sinusoidal curve present schematically the phase. The location on Earth of the receiver is shown with a yellow circle. The panel c) shows an example of binary modulation of a carrier signal by a PRN code. Whenever the state of the PRN code is -1, corresponding to the binary value 1, the phase of the carrier signals shifts by 180 degrees. When the code state is +1 (binary value 0), the signal is unchanged. Reproduced after Dzurisin (2006).

The encoded signal is transmitted by each satellite with two or more frequencies characterized by three components: carrier, a ranging code, and navigation message (containing e.g., orbit parameters) (Bock and Melgar, 2016). The carrier is a sinusoidal signal, onto which the ranging code and navigation message are encoded (Figure 4c). Carrier wave measurements

can obtain the mm-level accuracy whereas the ranging code approach only results in meter to cm-level accuracy. However, they provide valuable constraint on the so-called ambiguity resolution (Bock and Melgar, 2016). The ambiguity resolution relates to the knowledge of the integer number of cycles (i.e., the number of waves) of the signal between satellite and receiver, which is not directly measurable. The satellite carrier signals are modulated by binary pulse code, the PseudoRandom Noise (PRN), a periodic code with a sequence of zeros, corresponding to +1 value or normal state and a sequence of ones, corresponding to -1 value, or mirror state (Figure 4). The code sequence, unique to each satellite, is sent by the satellite and recorded by the receiver which will generate its own replica of the PRN code and determine the transmission delay between the satellite and the receiver (Bock and Melgar, 2016). When the transmitted carrier signal is in normal state, its phase remains the same; on the contrary, when the carrier signal is in mirror state, the phase of the carrier signal is shifted by 180° (Figure 4) (Dzurisin, 2006). Carrier phase measurements are more complicated in terms of recording methods, but the measurement uncertainty is much lower (the pulses are much closer together and therefore more accurate) than the code-based measurement (Teunissen, 1998; Hofmann- Wellenhof et al., 2008). The integer ambiguity resolution, needed when using carried phase measurements, can be performed with the help of algorithms or statistical methods that compare the resulting inferred ranges to multiple satellites.

When propagating from satellite to receiver, the signal is delayed due to the interaction with the different layers of the atmosphere, causing ionospheric and tropospheric delays, and errors in positioning if not corrected for (Gent, 2024). The use of multifrequency signal approach is routinely used in GNSS analyses to reduce the part of signal propagation-related error due to the dispersive Earth's ionosphere (Geng, 2024). Most of the global GNSS broadcast L-bands of dual-frequency in L1 and L2 configuration with wavelength of ~19 and 24 cm, respectively (Jin et al., 2014a). However, continuous advancements have enabled the introduction of the L5 frequency (wavelength ~25 cm), which, when combined with the L1 frequency, offers improved error correction compared to the L1 and L2 frequency combination. On the contrary, the troposphere is not dispersive (Kaplan and Hegarty, 2006). The tropospheric delay can be removed to some degree by modelling, but it never fully as it relates to local conditions (temperature, pressure and relative humidity) which varies by season, day and night and geographical area (Davis et al., 1985; Kačmařík et al., 2019; Li et al., 2023). Multipath is another phenomenon that can degrade the GNSS signal in both code and phase measurements before reaching the receiver. Multipath occurs when an antenna records not only the signal along the direct satellite-receiver path, but rather by multiple paths, due to electromagnetic effects such as signal reflation from structures near GNSS antennas (Jin et al., 2014b). It can be minimized by using high-quality antenna and placing the equipment in an environment without or limiting instrument installation in areas with high-reflective surface e.g., rocks or buildings. Alternatively, a multipath ray-tracing method considering the reflection process, the antenna characteristic and the way the signal is reflected, can be applied (Lau and Cross, 2007), although the phenomenon cannot be fully corrected for. Additional measurement uncertainties may come from satellite-related errors such as orbital errors, satellite clock offsets and relativistic effects or receiver-related errors which include receiver clock errors, uncertain radiation pattern of an antenna and its interaction with the surrounding structures and receiver noise (Grewal et al., 2020). Orbital errors can be mostly reduced by using precise orbits published by several analysis centers that provide high-precision orbits.

Systematic errors in GNSS observations can be minimized by a process called differencing. There are several types of differencing: the single difference, double difference, and triple difference (Bock and Melgar, 2016). The single difference configuration is either with two receivers and one satellite or two satellites and one receiver. The main idea is that if two receivers are located relatively near each other and both are receiving signal broadcasted from a single satellite at the same epoch, then by subtracting each receiver's observation the satellite clock error can be removed. Furthermore, atmospheric errors may be nearly identical at both receivers if they are located close to each other, and thus atmospheric errors are reduced. If the transmitted signals (either carrier phase or pseudorange) from two satellites are received by two receivers a double differencing can be performed. Triple difference is formed by considering two double differences over two different times.

There are two main approaches to post-processing GNSS analysis for crustal deformation studies: one involves a network positioning method (differential relative positioning) where the receiver position is determined with respect to one or more fixed reference stations, in a local or regional network (Blewitt, 1989). An alternative to this method is the Precise Point Positioning (PPP, Zumberge et al., 1997). The PPP uses only one GNSS receiver to estimate station positions directly with respect to a global reference network (Zumberge et al., 1997; Kouba and Heroux, 2001). The PPP can provide accurate positioning solutions with observation times typically about 20-40 minutes. The convergence time is primarily influenced by carrier-phase ambiguities, which can be reduced by combining signals from multiple GNSS constellations (Guo et al., 2017; Li et al., 2015).

Ground GNSS equipment (receiver and antenna) can be installed at fixed stations for continuous recording (continuous cGNSS) or for shorter periods, days or weeks (campaign measurements). Longer acquisition time leads to more accurate results. There are several GNSS equipment and types. One of the most used campaign measurement approaches in Iceland is to place GNSS antennas on tripods above benchmarks, as shown in Figure 5. In Iceland, the first GNSS survey was carried out in 1986 (Foulger et al., 1987) and the first permanent station was installed in Reykjavik in 1995 (see Figure 3 for location and Figure 5 for the time series). Since then, the GNSS network has steadily increased with permanent stations installed all over the country (Geirsson et al., 2010), supported by campaign sites which are measured on an annual basis at the most active volcanic areas.

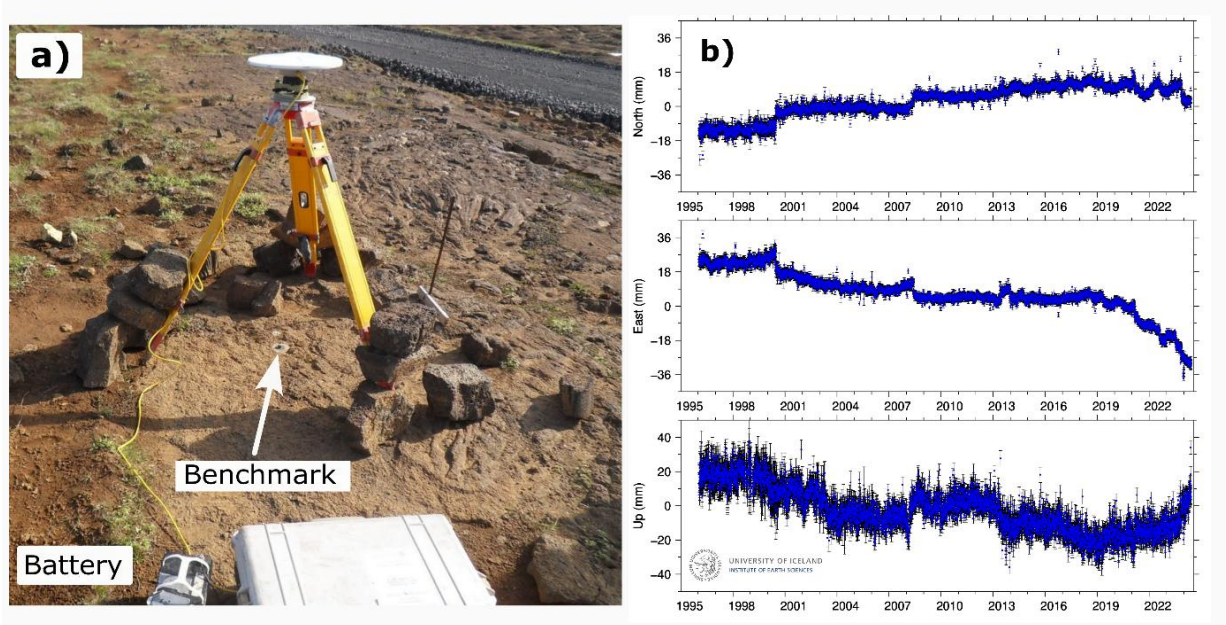

Figure 5. (a) Campaign GNSS sites with antenna placed on a tripod installed for several days, aligned with the benchmark (circular metal) on the ground. The antenna is connected through the yellow cable to a receiver (inside the grey box), which is connected to a battery. Photo source: https://strokkur.raunvis.hi.is/gpsweb/pictures/THER/sdc14431.jpg.
(b) GNSS time series (ITRF14 reference frame) at station REYK processed with GAMIT/GLOBK by Sigrún Hreinsdóttir. Displacement in the north (mm), east (mm) and up (mm) components. Linear trends as well as annual and semi-annual terms have been estimated and removed. The time series have abrupt jumps most to two large earthquakes in June 2000 (Ms = 6.6 occurred in the central part of the SISZ, Árnadóttir et al., 2005) and in May 2008 (Ms= 6.3, Decriem et al., 2010). A significant change is visible in the east component of the time series starting between 2019-2020, in response to events on the Reykjanes Peninsula. The change is more subdued in the north component, while it is quite clear in the east component since 2020 and in vertical components since 2023.

Most common GNSS processing software include GAMIT/GLOBK (Herring and McClusky 2010); GIPSY-OASIS II (current version GipsyX/RTGx) (Zumberge et al., 1997); Bernese (Dach et al., 2015); EPOS P8 (Uhlemann et al., 2015), NAPEOS (Springer et al., 2011) and PRIDE (Geng et al., 2019). In this PhD project, GNSS data were processed with the GAMIT/GLOBK (Herring et al., 2010) and GipsyX/RTGx (Bertiger et al., 2020) softwares. The GAMIT/GLOBK ("GNSS at MIT" and "Global Kalman filter") software operates through a series of distinct programs and modules, that can be run separately but are tied together through data flow to estimate relative coordinates of GNSS stations. The software has been developed by MIT, Scripps Institution of Oceanography and Harvard University. GAMIT includes a weighted least squared algorithm to estimate relative positions of a set of stations, orbital Earth-rotation parameters and phase ambiguities by using double differenced phase observations. The workflow includes: a coordinate file with a *a priori* coordinate values (solution provided in the raw data can be used) which will be later updated with a higher precision coordinates estimation; a *a priori* orbits estimates (IGS orbits can be used as input).

a file containing all the information related to the measurements, like antenna and receiver types, site names and time of recording. Additionally, tides correction can be made (Lyard et al., 2004); The daily position solutions estimated can be used to generate velocities or time series in GLOBK. The GipsyX/RTGx is the Jet Propulsion Laboratory's (JPL) software after GIPSY-OASIS and Real Time GIPSY. The software combines estimates of geodetic/geophysical parameters using a Kalman filter approach on real or simulated data in both post-processing and in real-time (Bertiger et al., 2020). Similarly to GAMIT/GLOBK, also GipsyX/RTGx implements several categories accounting for orbit integrations force models and Earth models.

Once daily solutions have been obtained, they can be combined to form time series and thus, displacement time series can be visualized. For each site, three files are usually created: one for the east, one for the north and one for the vertical components, containing time of the observation, the estimated difference in north, east and height (NEU) coordinate components relative to a reference position and the last column is the standard deviation. There are several approaches to GNSS time series analysis. Once a trend is observed, it may prove useful to model it with a mathematical function that best represents it, and remove a best-fitting function from the time series. Such an approach is called "detrending". The detrending can be applied to the whole times series or alternatively, by selecting a specific time between two periods, where a change in the times series occurs, e.g., due to earthquakes, diking events. GNSS time series at volcanoes may show a variety of different patterns: exponential, linear or seasonal, for relatively short or long periods, indicating e.g., inflation/deflation episodes at volcanic or geothermal areas, steady processes occurring on regional scale, or repetitive events. Time series may also show sudden events like earthquakes, diking episodes or change of the equipment in use at a particular site.

The Earth 'crust deforms and moves due to various geological processes. Thus, it is important to ensure clear convention (i.e., a reference frame) that allows the interpretation of the GNSS results without any confusion. A reference frame includes the definition of an origin with a coordinate system that describes the position and motion of any points on Earth. Depending on the use, there are different reference frames, but one of the widely used for GNSS is the International Terrestrial Reference Frame (ITRF, Altamimi et al., 2023). The ITRF has origin at the center of mass of the Earth including the atmosphere and the oceans. The system is updated every few years, using the most recent mathematical and surveying techniques to ensure optimal precision. The latest version was released in 2020.

1.3.2 InSAR - Interferometric analysis of Synthetic Aperture Radar satellite images

The InSAR technique provides images of the Earth's surface using Synthetic Aperture Radar, SAR (Massonnett et al., 1993; Bürgmann et al., 2000; Dzurisin, 2006; Osmanoğlu et al., 2016). The innovation of the radar sensors lies in their capacity to provide images during both daytime and night, and irrespective of cloud coverage. For crustal deformation studies, the use of InSAR greatly improved the possibility to investigate cm- to mm-scale ground deformation changes in large regions not easily detectable with previous monitoring tools. In the past few

decades, InSAR became a commonly used tool by volcano monitoring agencies/observatories to detect surface deformation. The increasing number of InSAR observations provide timely monitoring of ground deformation creating a long-term history at volcanoes with the establishment of databases helping monitoring and volcanic hazards assessment (Phillipson et al., 2013; Wauthier et al., 2013; Biggs et al., 2014; Dzurisin et al., 2019; Biggs and Wright, 2020). As with the GNSS technique, InSAR can also be used for several applications other than volcano geodesy e.g., co-seismic (Xu et al., 2020) and post-seismic deformation (Zhao et al., 2024), aquifer depletion (Castellazzi et al., 2018); landslides (Ye et al., 2004); underground storage of CO_2 (Vasco et al., 2010; Fibbi et al., 2022); cryospheric processes (Tarricone et al., 2022; Björnsson et al., 2010) and deformation due to anthropogenic sources (Parsons et al., 2023).

SAR is a type of radar that transmits side-looking microwave signals, from an antenna mounted on a moving vessel (travelling along an orbital path), towards the Earth's surface (Curlander and McDonough, 2001). The electromagnetic signal, after reaching the ground surface, is reflected (creating an echo signal) to the moving satellite along what is called the Line-of-Sight direction (LOS). Thus, the InSAR LOS displacement is not a vertical but rather in an inclined direction, and it does not distinguish purely horizontal and vertical displacement components. In such a side-looking configuration, the electromagnetic signal defines an angle, called incidence angle, θ, with the vertical direction at the point on the ground (Figure 6). The satellite moves in the azimuth (or along-track) direction, and the ground range is defined as the direction perpendicular to the radar's flight path (Figure 6). The ground range extent reached by the signal is called swath width. The satellite path or orbit is termed ascending when the satellite moves south-to-north direction or descending, when the satellite moves north-to-south direction. When both ascending and descending orbits are available (thus, known are the satellite viewing, orbiting geometry, the incidence angle and the heading of the satellite, the angle of the moving satellite with relative to the north) it is possible to decompose the LOS displacements from ascending and descending orbits together into approximate estimates of vertical (Near-Up) and east (Near-East) displacement components (e.g., Drouin and Sigmundsson, 2019). The LOS displacement has poor sensitivity in the North-South movement because of the satellite near-polar orbit geometry.

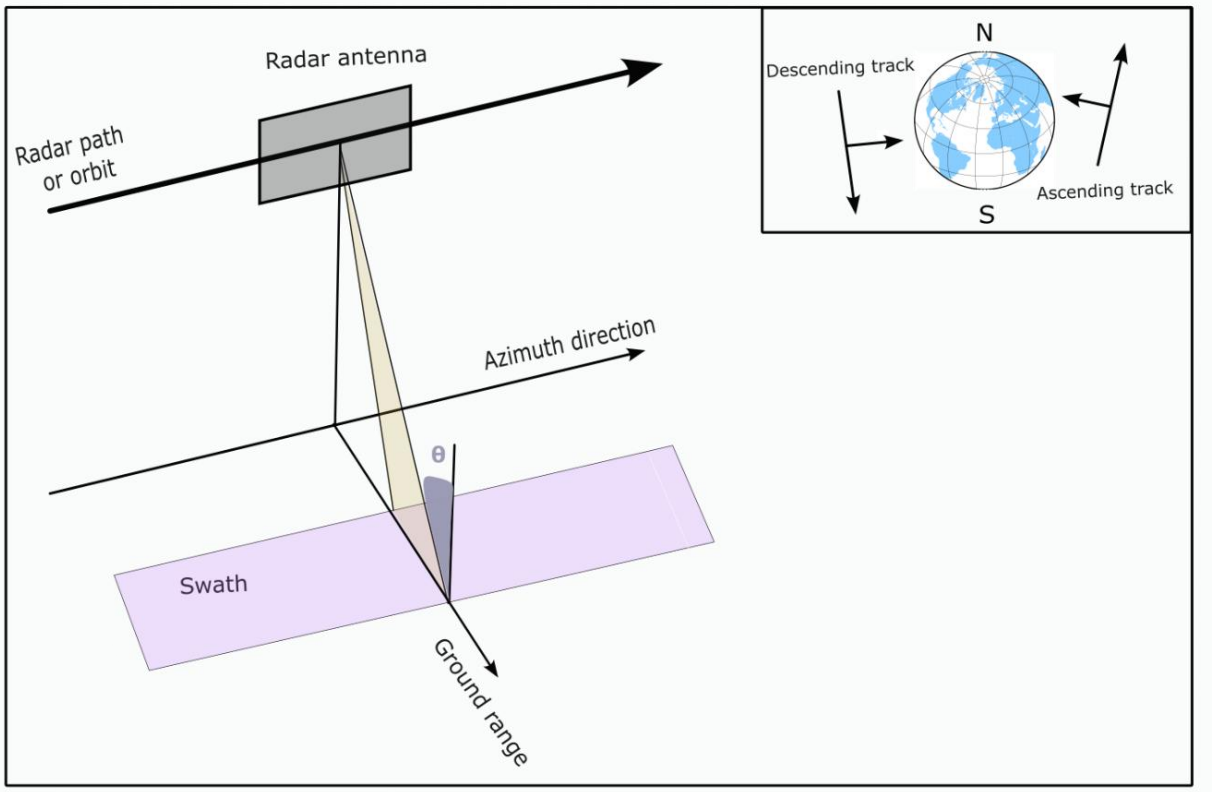

Figure 6. SAR satellite geometry. The satellite pulses (in yellow) cover a swath on the ground (in pink compared to the surrounding ground). θ = incidence angle. Ascending (satellite heading towards the north) and descending (satellite heading towards the south) configuration.

The dimensions of the antenna mounted on the satellite determine the spread of the radar beam or signal and consequently, the size of its footprint (area) on the ground (Bamler and Hartl, 1998). Most SAR systems designed for Earth orbit use an antenna 1–4 m wide and 10–15 m long, with a look angle in the range 10–60° (Lu and Dzurisin, 2014). In general, the backscattered signal decreases with the incidence angle (Bamler and Hartl, 1998). The synthetic aperture technique consists of collecting an array of successive radar signals transmitted, and reflected from a single location on the surface of the Earth, and received back by a physical antenna as it moves along the orbital path (Bamler and Hartl, 1998; Massonnet and Feigl, 1998). The synthetic aperture term refers to the moving antenna used to simulate a larger (synthetic) aperture than the physical size of the antenna, while collecting reflected signal energy to form an image. This is the key to achieving high azimuth resolution.

There are several SAR acquisition modes defined either by geometric configuration of the SAR antenna or by their temporal properties, which play a key role in defining the resolution. The most common modes used are: stripmap, scanSAR, spotlight, and interferometric wide (IW) swath. In the Stripmap mode, there is one fixed scanning strip (or swath) of terrain parallel to the flight direction. The spatial resolution varies from 3 to 10 meters,

dependenting on the swath width (30 to 70 km) and to the used signal wavelength, e.g., X-band, L-band or X-band (see Table 1) (Cumming and Wong, 2005a). Wider swath can be obtained in the ScanSAR mode, where the antenna beam is successively directed to different look angles (Guarnieri and Prati, 1996; Cumming and Wong, 2005b; Table 1). In the spotlight mode the angle of the radar signal varies constantly along the azimuth direction, focusing continuously on a specific area, allowing for an improved spatial resolution of SAR image. The varying angle and thus extension of the synthetic aperture allows ~2 m of resolution (Table 1). In the IW mode the antenna switches sequentially backward and forward to create progressive scans of the ground. The IW mode is used by Sentinel-1, which provides a coverage around ~250 km ground swath (with three ~80 km-long sub-swath).

Table 1. *Different SAR acquisition modes with examples of spatial resolution and swath.*

SAR acquisition Mode	**Spatial Resolution**	**Swath width**	**Examples of satellite**
Stripmap	~3 m	30 km	X- band
	~5 m	80 km	C-band
	3-10 m	50-70 km	L-band
ScanSAR	60-100 m	300-500 km	
Spotlight	~1-2 m	10 × 5 km (range x azimuth)	Terra-SAR-X
IW	5 m × 20 m	250 km ground swath (80 km sub-swaths)	Sentinel-1

The SAR electromagnetic wave contains two different types of information: amplitude and phase that can be resolved for each pixel on the ground (Hanssen, 2001). The amplitude is the strength of the back-scattered electromagnetic wave and is related to the targets shape (roughness), orientation, and electrical reflectivity (Massonnet and Feigl, 1998). The phase is mainly controlled by two factors: the radar signal's round-trip travel distance between the SAR satellite and the ground, and interactions between the signal and surface materials (Lu and Dzurisin, 2014). The phase cannot be interpreted directly from a SAR acquisition. However, by comparing the phase of two SAR images acquired over the same area at different times – commonly referred to as the primary and the secondary images – it is possible to compute the difference in phase between them. This process, called interferometry, forms the basis of InSAR, which relies on the coherent combination of two SAR signals to generate an interferogram showing the differential phase. If the surface remains unchanged between

acquisitions, the radar waves reflected from the same point will maintain similar phase relationships, resulting in minimal phase difference. Conversely, changes in surface elevation, deformation, or atmospheric conditions can cause a measurable phase shift, which appears as a pattern of fringes (alternating bands of color) in the interferogram. These interferograms are typically referred to as "wrapped", meaning the phase differences are expressed within a range of $-\pi$ to $+\pi$ radians (Figure 7a).

Each full cycle of 2π change (each fringe) corresponds to a specific amount of LOS displacement of $\lambda/2$, with λ being the radar wavelength. Since phase measurements are inherently ambiguous modulo 2π, the full LOS displacement must be recovered through phase "unwrapping". This process resolves the integer (2π) ambiguity and converts the wrapped phase into continuous values representing actual ground movement, producing the unwrapped interferogram (Figure 7b). A variety of approaches and algorithms address this problem; for example the SNAPHU algorithm (Chen and Zebker, 2002), that considers phase unwrapping as a maximum *a posteriori* probability estimation problem computing the most likely unwrapped solution given the observable input data.

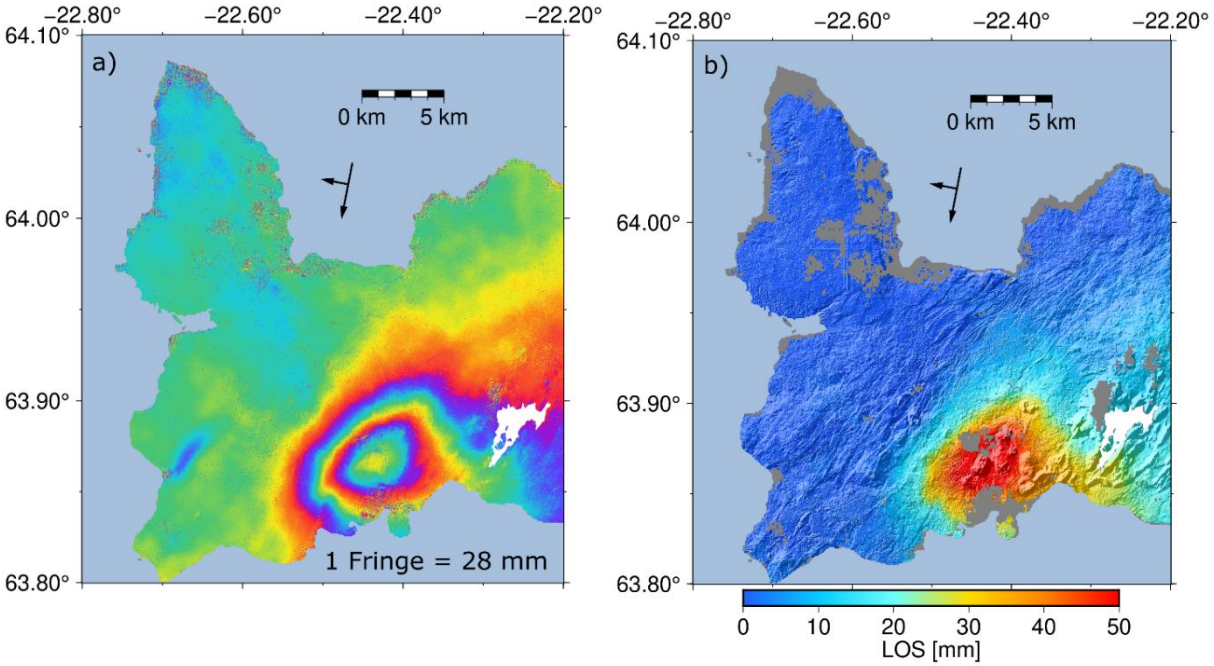

Figure 7. InSAR interferogram produced from Sentinel-1 SAR images (acquired between 13 April to 12 June 2022, 2022, T155 orbit) showing the deformation of one inflation episode at Svartsengi volcanic system. LOS displacements shown in a) wrapped interferogram and b) unwrapped interferogram. In b), the LOS displacements are shown with topography in the background. Incoherent areas are grey. Light blue area is the ocean. The 2021 Fagradalsfjall lava field is in white. The black arrows indicate the heading and side-looking of the satellite.

The final phase shown in an interferogram represents the change in topography and scattering properties of the ground, and is affected by several artifacts deriving from satellite's

orbital position and geometric configuration (Zebker and Villasenor, 1992), atmospheric delay (Massonnet and Feigl, 1998; Hassen, 1998).A key quality indicator of the interferometric phase is the coherence (i.e. the correlation between two images), ranging from 0 (no correlation) to 1 (perfect correlation). Coherence can be estimated by cross-correlation of two SAR images over a small ground area in range and azimuth (Lu and Freymueller, 1998), requiring that the ground scattering surface is relatively undisturbed at the scale of the radar wavelength between the two-time measurements (Li and Goldstein, 1990; Zebker and Villasenor, 1992).

While a single interferogram captures relative displacement between two SAR images over a specific time interval, time-series InSAR techniques such as Permanent Scatterer Interferometry (PSInSAR) and Small Baseline Subset (SBAS) analyze multiple interferograms to estimate mean deformation velocities and identify long-term trends. These methods help reduce errors due to temporal atmospheric fluctuations, and decorrelation by combining data from many acquisitions. The PSInSAR approach proposed by Ferretti et al. (2000) was the first complete solution to mitigate temporal and geometrical decorrelation by identifying stable reflectors – typically man-made structures – that return consistent radar signals over time. However, this method relies on high-coherence reflectors, which are commonly found in urban areas. To address this, Hooper et al. (2004) developed an alternative approach that identifies natural targets with stable phase behavior over time, even when their reflectivity is relatively low. Over the years, the PSInSAR has grown significantly, with several algorithms proposed to improve detection and reliability (Crosetto et al., 2016). Another widely used technique is the Small Baseline Subset (SBAS) method, which helps minimize spatial and temporal decorrelation effects and enhance the reliability of the deformation data (Berardino et al., 2002). In this context, the perpendicular baseline refers to the orthogonal distance between the satellite's orbital paths during two different acquisitions. Smaller perpendicular baseline generally leads to reduced geometric decorrelation, making the method more efficient when detecting ground deformation. The SBAS estimates the mean deformation rate by using a network of interferograms with small temporal and spatial baselines by applying temporal high-pass and spatial low-pass filtering to isolate deformation signals while suppressing noise. However, the classic SBAS method has several limitations e.g., due to sparse stable points within a certain area. Several studies have focused on improving the SBAS technique to increase the number of high-coherence points and enhance the accuracy of deformation monitoring. A review of these advancements is provided by Li et al. (2022).

The first spaceborne scientific SAR mission dedicated to Earth observation were the Shuttle Imaging Radar (SIR) missions carried aboard NASA's Space Shuttle in the 1980s, including SIR-A (1981), SIR-B (1984), and SIR-C/X-SAR (1994). These missions demonstrated the potential of SAR for geological and environmental studies. However, the first dedicated scientific SAR mission with long-term Earth observation capabilities was the European Remote-Sensing satellite (ERS), launched in 1991 and operational until 2000 (Attema et al., 1998). Additional missions have been or are currently running on different frequency bands and wavelengths by several public and/or private companies. The wavelength and the frequency bands are important characteristics of the SAR satellites in consideration of the phenomena and area of investigation. The most used frequency bands are the X-band (~3.1 cm of wavelength), C-band (wavelength ~5.6 cm) and L-band (wavelength ~23.5 cm) (Figure 8). For example, L-band can penetrate vegetation as well as upper soil to some extent in dry conditions, making it more suitable for use in forested areas. Interferograms produced from L-band sensor may even maintain coherence during winter months with snow cover on the

ground. However, due to the wavelength, small ground movements will only show up as a small fraction of one fringe. An X-band sensor can well detect small deformation signal, though is not suitable for use in vegetated or snow-covered areas. Thus, integration of satellite data with different but complementary characteristics may increase our ability to detect land motion. This study uses data from both ascending and descending orbits from the Sentinel-1 satellite. The Sentinel-1 satellite operates on C-band frequency (wavelength = 5.6 cm) with a right-side looking configuration and IW mode. The Sentinel-1 satellite orbits used in the project are shown in Figure 9.

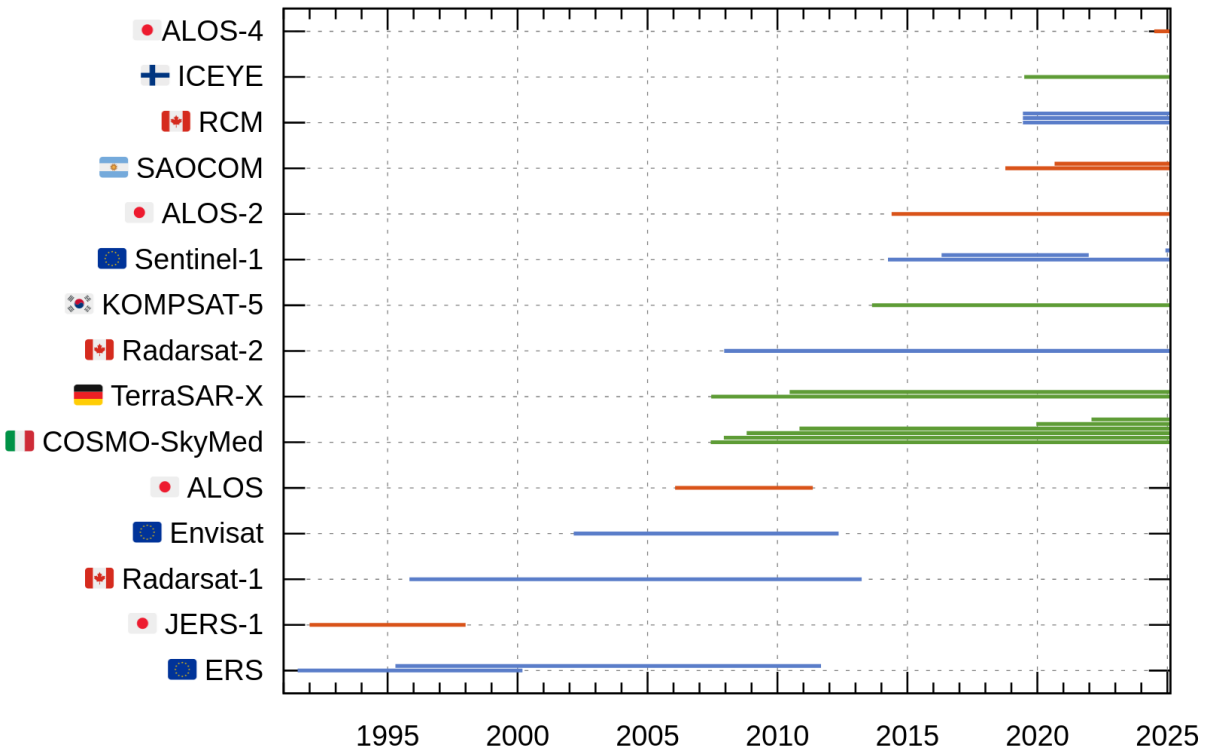

Figure 8. Timeline of the main SAR missions operated by different companies or institutions: X-band (green); L-band (blue) and C-band (red). Courtesy of Vincent Drouin; modified from Drouin (2016b).

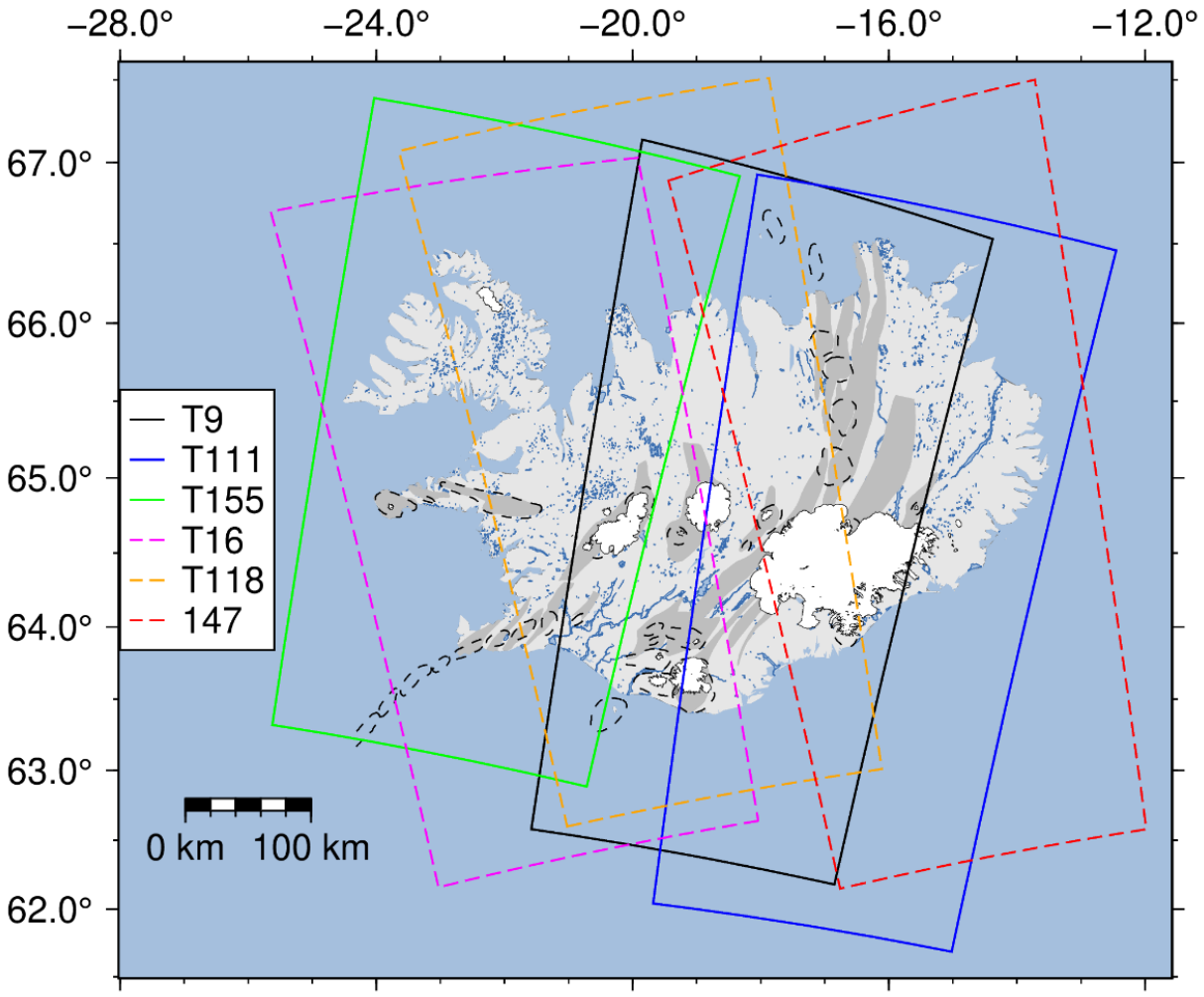

Figure 9. Outlines of the Sentine-1 images used in this study. (dashed: ascending; continuous: descending) used in this project. The outline of the main glaciers (white), fissure swarms (dark grey) and central volcanoes (black dashed lines) are shown.

1.4 Modelling approaches

The variety of processes causing deformation at volcanic areas can be investigated with theoretical mathematical models of crustal deformation to distinguish among the possible sources of deformation (Segall, 2010; Crozier et al., 2023). There are two main groups in terms of how the models are applied: forward modelling and inverse methods. A forward model is used to calculate an expected deformation pattern given fixed source parameters. On the contrary, the inversion method uses a known deformation pattern to infer best-fit parameters of a deformation source, often through an iterative optimization process. Generally, it is possible

to distinguish between analytical and numerical modelling approaches. An overview of both modelling approaches is provided in the following paragraphs.

1.4.1 Analytical models

Analytical models are mathematical approaches describing a problem in the form of closed mathematical expressions based on specific assumptions. Due to their relatively simple formulation, they are widely used in volcano deformation studies to characterize deformation-driven processes and to constrain source location, size and orientations (Gottsmann and Battaglia, 2008; Amoruso and Crescentini, 2013). The main assumptions of commonly used analytical solutions to interpret geodetic data at volcanoes are the assumptions of a deformation source embedded within a uniform, elastic and homogeneous half-space, flat topography and regular source geometry. The limitation of such models lies in their inability to account for the complexity of an actively deforming volcano: crustal heterogeneity, topography, visco- or poroelastic response, and irregular source geometry, all of which affects the deformation at surface (Trasatti et al., 2003; Manconi et al., 2007; Hickey et al., 2014). Nonetheless, the analytical solutions are quite useful as they provide a good approximation of source parameters in a relatively short time. Such models are typically used to derive first-order constraints on magmatic processes that take place inside volcanoes, and they can provide critical information for an operative real-time monitoring situation for decision-making responses in case of imminent eruption or diking near populated zones.

There are several analytical models used when interpreting volcano deformation, considering different types of sources within an elastic halfspace: point-source, approximating a small spherical source, also known as a Mogi source (Mogi, 1958); a rectangular dislocation with opening and slip (Okada, 1985); a horizontal penny-shaped sill, where pressure is uniformly applied to the boundary of the sill (Fialko et al., 2001); or a change in pressure within a prolate spheroid source representing a pressure change within a finite ellipsoidal body (Yang et al., 1988) , which is a special case of an ellipsoid where the horizontal axes are equal and larger than the vertical axis ($a = b > c$); and a general triaxial ellipsoid (Davis, 1986), where all three semi-axes (a, b, c) differ ($a \neq b \neq c$), offering the greatest flexibility for modeling complex, asymmetric magmatic sources. Many analytical models of ground deformation used in volcano geodesy, although useful, do not account directly for physical properties or composition of magma. However, several studies show how the compressibility of magma remaining within a deflating magma chamber, affected by exsolving volatiles, and stiffness of the host rock, influences the difference in volume of deflation and amount of magma extracted from a deflating magma chamber, that can be considerably different (e.g., Rivalta and Segall, 2008). In this work, we mostly focus on the use of Mogi and Okada sources. The Mogi model is a widely used approach for representing inflation or deflation from a spherical pressure source at depth and provides a useful baseline for interpreting volume changes. The Okada model was selected to explore more complex, planar source geometries, such as sills. While it is known that the Okada model can introduce edge effects, its analytical formulation and flexibility in geometry make it a practical tool for inversion and comparative analysis. Despite these

limitations, both models provide valuable insights into the source characteristics, and serve as a starting point for more complex or physically realistic models in future work.

The Mogi model (Mogi, 1958) estimates the displacement field due to a contracting/expanding point-source, approximating a spherical source with a small radius compared to its depth, embedded in elastic, homogeneous and isotropic half-space (Figure 10). The model parameters can be represented as: location of the source (X, Y and depth) and a parameter quantifying the strength of the source (equations 1-4). The displacements at the surface are axisymmetric with the maximum vertical displacement above the center of the source (Figure 10), while the horizontal displacement obtains its maximum value at a distance of $0.7d$ (Lisowski, 2006), where d is the depth to the center of the source. Horizontal and vertical surface displacements are given by equations 1 and 2:

$$U_z = C\ \frac{d}{(r^2+d^2)^{3/2}} \tag{1}$$

$$U_r = C\ \frac{r}{(r^2+d^2)^{3/2}} \tag{2}$$

where r is the horizontal distance along the surface from the source center, d is the source depth, and C is the source strength parameter. The source strength parameter is a term that connects either the pressure change, ΔP, or a volume change, ΔV, to the elastic properties of the crust (shear, μ, and Young's modulus, E) with the following relationships (e.g., Sigmundsson, 2006):

$$C = \frac{1-\nu}{\pi}\ \Delta V \tag{3}$$

$$C = \frac{1-\nu}{\mu} a^3\ \Delta P \quad \text{or} \quad C = \frac{2(1-\nu^2)}{E} a^3\ \Delta P \tag{4}$$

where ν is the Poisson's ratio of the elastic half-space.

An approximation that Mogi solution is based on is that the point-source is located at a depth more than five times its radius and thus, is not valid when the source approaches the surface (Lisowski, 2007). A numerical model using the Finite Element Method is used to evaluate this effect and to study as well the influence of heterogeneities in the elastic moduli of the crust in Chapter 2. The Mogi model does not allow the separate determination of the radius of the source (which ideally one would like to know to infer size of the deforming source), as it is coupled with the pressure change. McTigue (1987) provides a more complete solution to approximate the deformation for a pressurized spherical cavity in an elastic half-space, considering its finite dimensions:

$$U_z = \frac{a^3\ \Delta P\ (1-\nu)\ x}{GR}\ \left(1 + \left(\frac{a}{d}\right)^3 \left(\frac{1+\nu}{2(-7+5\nu)} + \frac{15d^2(-2+\nu)}{4R^2(-7+5\nu)}\right)\right) \tag{5}$$

$$U_r = \frac{a^3\ \Delta P\ (1-\nu)\ d}{GR}\ \left(1 + \left(\frac{a}{d}\right)^3 \left(\frac{1+\nu}{2(-7+5\nu)} + \frac{15d^2(-2+\nu)}{4R^2(-7+5\nu)}\right)\right) \tag{6}$$

where $R = (x^2 + d^2)^{0.5}$, x is the coordinate of the point at surface, where the displacement is estimated, and all the symbols are the same as for the point-pressure source.

Okada (1985) and (1992) present analytical expressions for the surface deformation and internal deformation, respectively, due to inclined finite rectangular sources in a half-space with

uniform opening and slip. These analytical formulations provide an approach to model tectonic faults (earthquakes) or magma sheet intrusions (dipping sill-like magma bodies or dikes) (Figure 10c and 10d). The surface displacement pattern for a horizontal rectangular dislocation with uniform opening may appear quite similar to the Mogi source surface deformation, but with different maximum vertical and horizontal displacement given the same depth. The model requires eight parameters: length, width, depth, strike, dip, the location (x and y) and opening of the sill.

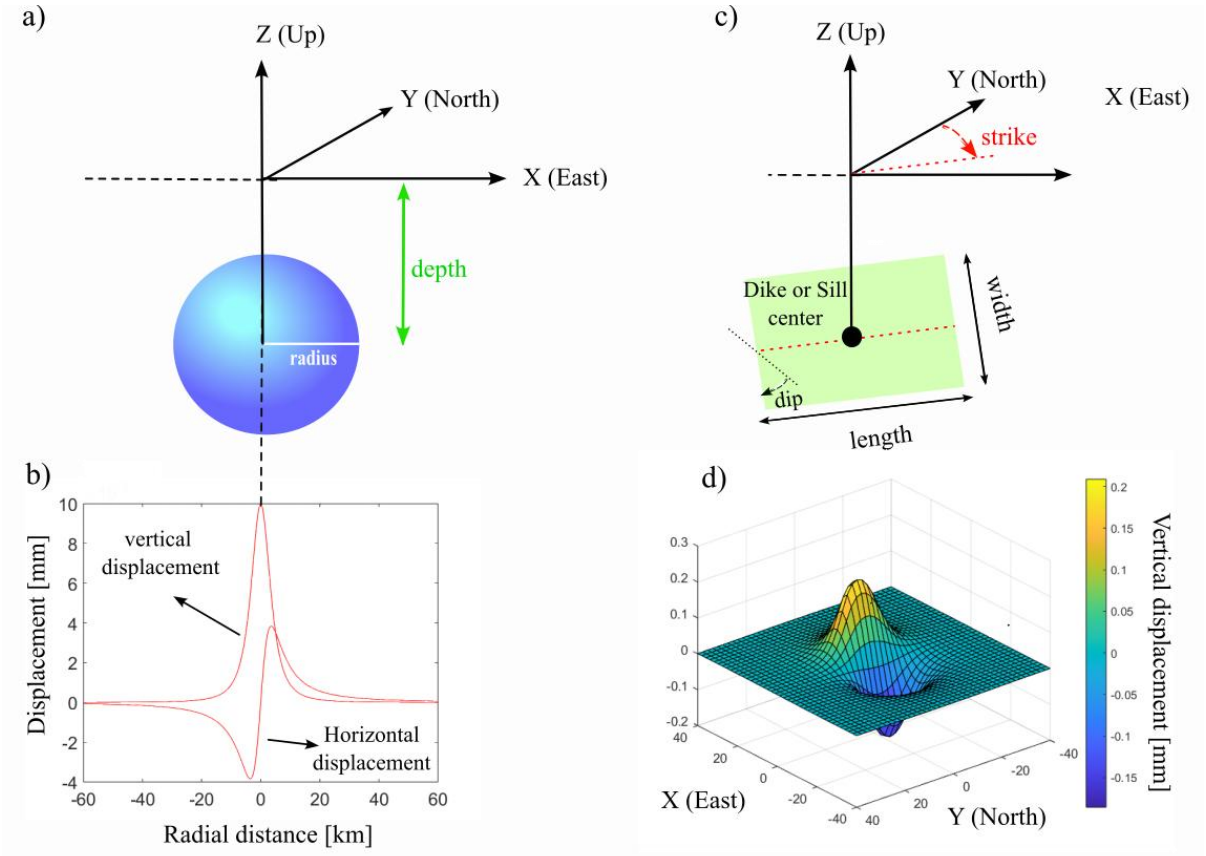

Figure 10. (a) Geometric representation of the point pressure source in an X, Y, Z coordinate system to derive (b) the displacement field (vertical and horizontal) at the surface along a profile crossing the source. (c) Geometric presentation of a dipping Okada solution in an X, Y, Z coordinate system (Beauducel, 2024) to derive (d) the vertical displacement at surface.

Several software packages have been developed to investigate different sources of deformation e.g., dModels (Battaglia et al., 2013); GBIS (Geodetic Bayesian Inversion Software; Bagnardi and Hooper, 2018); GAME (Cannavò, 2019), and VSM (Volcanic and Seismic source Modeling; Trasatti, 2022). These tools usually include several forward models and different inversion methods to infer source parameters (Crozier et al., 2023). In this thesis, the GBIS software has been used to invert GNSS and InSAR geodetic data to infer the source

parameters which best describe the observed deformation. The software is based on a Bayesian approach for the inversion of multiple geodetic data sets that allows characterization of posterior probability density functions (PDFs) of source model parameters. Initially, a given set of a-priori conditions are given. In our case, such conditions are the lower and upper bounds for the values of the source parameters. The inversion algorithm samples posterior PDFs utilizing a Markov chain Monte Carlo method (MCMC), incorporating the Metropolis-Hastings algorithm (e.g., Hastings, 1970), with automatic step size selection, considering the fit of observations to model predictions. The MCMC method relies on the construction of a repeated random sampling to converge to solutions with optimal values for the model parameters. The process further infers a probability density distribution for each of the model parameters.

In the inversion both the GNSS and InSAR LOS datasets are used. The GNSS data file contains: location of the sites (longitude and latitude in decimal degrees), the three components of displacement (north, east and up) and their uncertainties (normally expressed as one standard deviation). The standard version of GBIS, used in the early stages of this project, originally resamples the InSAR LOS data by using a gradient-based quadtree sampling method (Jónsson et al., 2002; Decriem et al., 2010). Such an algorithm divides the data in polygons (squares for regularly spaced data) until the phase variance of the points within each polygon is below a given quadtree threshold variance. If the previously defined variance threshold is exceeded, polygons are further divided into four quadrants. This process goes on until the points within the polygons have variance lower than the selected threshold. As a result, areas with high deformation will be densely sampled. However, if the noise level is relatively high e.g., in far-field areas compared to the actual deformation signal of the LOS dataset, the algorithm may "read" them as high variance zones and iteratively subdivide the regions into smaller ones. To avoid such an effect, in the later stages of the project another sampling method was used. In the modified approach a dense sampling within a circular area is used, with a predefined radius given a reference point (e.g., centered around the deforming area). At distance outside the radius length, the sampling density is reduced to avoid the inversion result to be influenced from noisy data within the far-field.

1.4.2 The Finite Element Method – FEM

The FEM technique seeks an approximate solution to differential equations under examination in a one-, two- or three-dimensional domain, calculating a discrete function rather than continuous, of which values are given only at certain points (Dieterich and Decker, 1975). These points are called the nodes of the calculation grid. The discrete solution of the differential equation is calculated in elementary volumes defined by groups of adjacent nodes, which constitute the finite elements (Figure 11). A contemporary solution in all the elementary volumes in which the domain is subdivided, found by imposing appropriate conditions on the adjacent elements, constitutes the result of the numerical model.

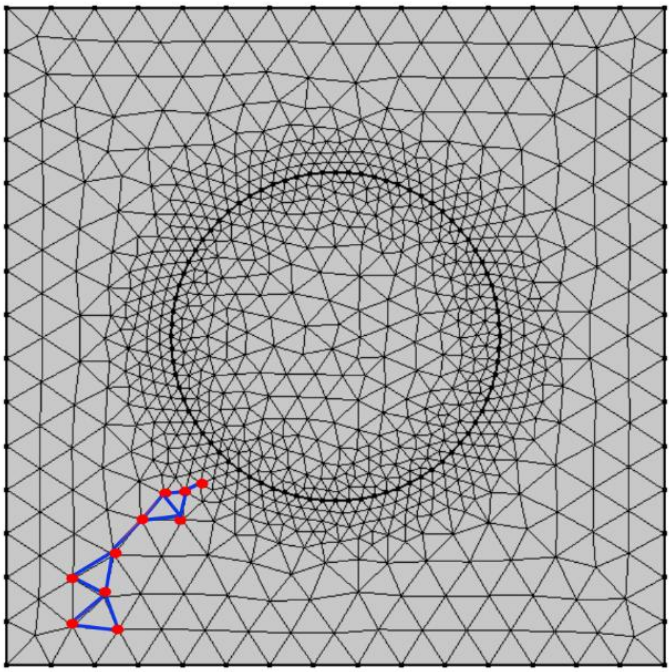

Figure 11. An example of meshing in a two-dimensional finite element model setup in COMSOL Multiphysics: high-density of nodes (red dots) near a hypothesized circular deformation source which results in smaller finite elements area (in blue). The finite elements become larger away from the source of deformation.

Numerical modelling with a finite element analysis approach is comprised of: (1) pre-processing; (2) solution and (3) post-processing phases. (1) In the pre-processing stage, the geometry and conditions of the physical problem are defined. The utilization of an appropriate graphical user interface (GUI) facilitates the creation of a geometric domain that reflects the reality of the study domain as closely as possible by assembling simple geometries like a one-dimensional line element (spring, beam, pipe etc.), a two-dimensional (plane) element (membrane, plate, shell) or a three-dimensional (solid) element. Once the geometry is created, boundary conditions and material properties in agreement with the physical problem can be defined. Some examples of boundary conditions are the stress-free condition, which may be appropriate for the land surface; loads, like external force or pressure applied to a boundary; or a fixed or moving constraint, where it is possible to give motion to some specific part of the geometry. Material properties can be defined in terms of the state of the material: liquid, gas or solid. At this point, the most important step is the discretization (or meshing) of the domain into a system of smaller units - the finite elements - interconnected at points between two or more elements (nodes) (Figure 11). It is important to note that the elements are small volumes, not separate entities and there are no cracks, spaces or surfaces between them. It is possible to choose between three-dimensional (tetrahedra, pyramids, prisms or hexahedra) or two-dimensional (triangular and quadrilateral) meshes. The arrangement of a suitable mesh that

defines the degree of discretization of the domain of interest is a fundamental challenge for designing robust FEM simulations. A common approach to getting a solution as close as possible to what is required, considering appropriate resolution and computing time, is to increase the density of the nodes of the grid in the near-field deformation, where the deformation is expected to be higher or where some boundary condition is acting and decrease it in the far-field. This trade-off approach reduces computational costs but guarantees a sufficiently accurate solution in many cases.

The innovative characteristic of the FEM approach lies in its ability to handle variable density of nodes (such as near irregular areas of the geometry) compared to other techniques like the Finite Difference Methods, FDM (Nishimura and Choet, 2003). The FEM provides the possibility to apply unstructured numerical meshes, while the FDM requires rectangular meshes. The FEM can offer the same numerical accuracy as the FDM, but with less nodes (Frehner et al., 2008). (2) During the solution stage, if the interpolation functions of the physical problem satisfy certain mathematical requirements, a finite element solution for a particular problem converges to an analytical differential solution. A FEM numerical model assembles the governing algebraic equations into matrix form and computes the unknown values of the primary field variables. The basis for the assembly procedure stems from the fact that the elements connected by the same node share the value of the field variable. Field variable (or unknowns) changes according to the physics of the problem, e.g. in a structural problem the field variable are the displacement components; in an electrostatic problem the field variable is the electric potential. Convergence to a solution does not ensure the correct solution. Therefore, it is beneficial to compare FEM models to known analytical or other solutions when available. This process is referred to as benchmarking and is an important step to determine whether a FEM model is working properly (Currenti et al., 2008; Hickey et al., 2014; Pascal, 2013; Greiner, 2024). Benchmarking can typically be done when working with relatively simple initial FEM models, that are then modified to more complex situations. (3) Numerical result visualization and interpretation can be made in the post-processing phase. Most of the FEM solvers provide a log file, which should be searched for warnings or errors.

FEM analyses allow realistic features such as topography, crustal heterogeneities, and thermal variation with depth to be incorporated in volcano deformation models (Lungarini et al., 2005; Ronchin, 2015). However, FEM modeling requires large computational resources and time. Inverse for source model parameters using a FEM approach is typically not suitable for real-time monitoring purposes at present, as it can take hours or days of computation to invert data to estimate the source parameters (Charco et al., 2014; Hickey et al., 2016; O'Hara, 2023). Several software are FEM-based. Some commonly used in Earth Sciences are: Abaqus (Smith, 2009), Pyrit (Bundschuh et al., 2022) and COMSOL Multiphysics (www.comsol.com). COMSOL Multiphysics is the software used in this PhD thesis. This software can solve coupled physics equations simultaneously and can provide a unified workflow for several applications. It is possible to build models by defining the relevant physical quantities, such as material properties, loads, constraints, sources, and fluxes, rather than by defining the underlying equations. These variables, expressions, or numbers can be directly applied to solid domains, boundaries, edges, and points independently of the computational mesh.

Numerical modelling with the FEM approach helps to overcome the limitations forced using the analytical approach. In this thesis I explore how the displacement field due to a near-surface pressurized spherical source is influenced by local elastic properties of the crust within a volcanic area (for more details see Chapter 2). The method was also used to investigate

deformation within a volcanic system located at a divergent plate boundary, contributing to improved understanding of long-term rift evolution (Chapter 3). The model includes an upper elastic part of the (highly fractured and altered) crust above a layer with inelastic properties (viscoelastic rheology). The viscoelastic layer reaches shallower depths beneath the volcanic system, reproducing the magmatic plumbing system. In the last part of the thesis, FEM investigations were carried out to reveal how near-field deformation may be affected by instantaneous emplacing of new lava. Such an effect has been reproduced by simulating a perpendicular loading (utilizing the lava thickness DEM) in the form of $-\rho gz$, where ρ is the density of lava, set to 2900 kg/m^3, g is the gravitational acceleration, 9.81 m^3/s, and z is the thickness of the lava field (for more details see Chapter 4).

1.5 Present study

Crustal deformation at several volcanic systems in Iceland is studied within this thesis, to characterize deformation-driving processes occurring in the subsurface. In Iceland, a dense network of continuous and campaign GNSS, established through the past decades all over the country, and different InSAR missions (Sentinel-1, COSMO-SkyMED and TerraSAR-X), allow good temporal and spatial observations of crustal deformation at active volcanoes. In this thesis I use data from the campaign and continuous GNSS network and the Sentinel-1 satellite to analyse ground deformation observed at three volcanic systems in Iceland: Krafla and Askja volcanic systems in north Iceland, (Figures 1 and 2) and the Fagradalsfjall volcanic system in south-west Iceland (Figures 1 and 3). The observed ground deformation was either inverted to infer parameters of sources of ground deformation or compared to predictions of FEM forward models. In particular, the use of FEM helps gain new insights and constraints on the contribution from different processes and variable rheology to the observed deformation.

The overall objective of the thesis work is to improve understanding of observed small crustal deformation signals, in relation to both short- and long-term processes taking place at several volcanic system in Iceland. In particular, the work undertaken addresses the following research questions:

1. Does crustal heterogeneity in a caldera in combination with changes in a geothermal system influence the observed 2018 ground deformation change and pressure increase in the Krafla caldera?
2. How does the interplay between the regional tectonics and a developed magmatic system beneath calderas influence the decades-long observed deformation at the Krafla and Askja volcanic systems?
3. How did evolution of the magmatic system during and after the 2021 Fagradalsfjall eruption influence the co- and post-eruptive deformation?
4. Given the variety of observed deformation patterns occurring at volcanic systems, can modelling approaches help in discriminating the active processes at work?

Paper one (Chapter 2) focuses on the cause of the recent changes in deformation patterns that occurred during 2018 at the Krafla caldera, in north Iceland, in relation to changes in the geothermal system and geothermal exploitation. GNSS and LOS datasets were inverted to

derive source parameters. A FEM model, taking into consideration realistic crustal characteristics, provides constraints on the elastic moduli of the crust inside the caldera.

In paper two (Chapter 3) a FEM model with both elastic (upper crust) and viscoelastic material (lower crust and in the magmatic plumbing system) is used to study the relationship between local crustal heterogeneity and the plate spreading processes. The plate spreading is reproduced with a uniform velocity applied at the lateral edges of a model domain. Such models are used to investigate decades-long subsidence at Krafla caldera (1989-2018) and at Askja caldera (1983-2021).

In paper three (Chapter 4) the focus is on understanding the evolution of the magmatic plumbing system during the 2021 Fagradalsfjall eruption. In particular, the relationship between ground deformation pattern changes, detected by the continuous GNSS network, and variations in the effusion rate observed at the surface as well as variation in geochemistry of lava samples collected during different time periods is evaluated. The emplacement of new lava was found to locally affect the ground deformation.

2 Paper I: Pressure increase at the magma-hydrothermal interface at Krafla caldera, North-Iceland, 2018–2020: Magmatic processes or hydrothermal changes?

2.1 Summary

A change in the ground deformation was detected at the continuous GNSS KRAC site at the Krafla caldera (North-Iceland) in summer 2018. Time series analysis reveals an initial southern motion up to 10-12 mm/yr, which slowed down to 6-8 mm/yr, about one year after the onset of the change when the vertical component began to show upward motion (Figure 12). GNSS (from annual surveys carried out in the caldera) and LOS difference velocity fields between 2018–2020 and 2015–2018, from summer Sentinel-1 InSAR images, reveal an inflation pattern in the center of the caldera.

The Krafla caldera hosts a geothermal system which has been exploited to produce electricity since 1997. The Leirbotnar geothermal field, in the middle of the Krafla caldera, is the most relevant for geothermal exploitation and is characterized by an upper liquid-dominated (190-220°C) geothermal reservoir, extending down to 1.0-1.4 km depth. A relatively impermeable zone (Gudmundsson and Mortensen, 2015) separates the upper reservoir from a lower reservoir of high-temperature (280–340°C) fluid and steam down to at least ~2.2 km (Stefánsson, 1981; Ármannsson et al., 1987; Mortensen et al., 2014). A monitoring well (not used for extraction and re-injection operations) located in the caldera, shows an increase of the water table level in August 2018 and a pressure measurement in September 2018 also shows an increase. Pressure increase was also observed 2018-2019, but no additional increase was observed in 2020. The total rise of the water table was up ~25 m, and the pressure increase was ~0.2 MPa for the 2018–2020 period. In 2018, the net production (mass extraction minus re-injection) of the Krafla Power Plant was generally higher compared to previous and following years. From 2017 to summer 2018, two re-injection wells were used, but in summer 2018, an additional well, located in the middle of the caldera, became operative, and remained in use until September 2019.

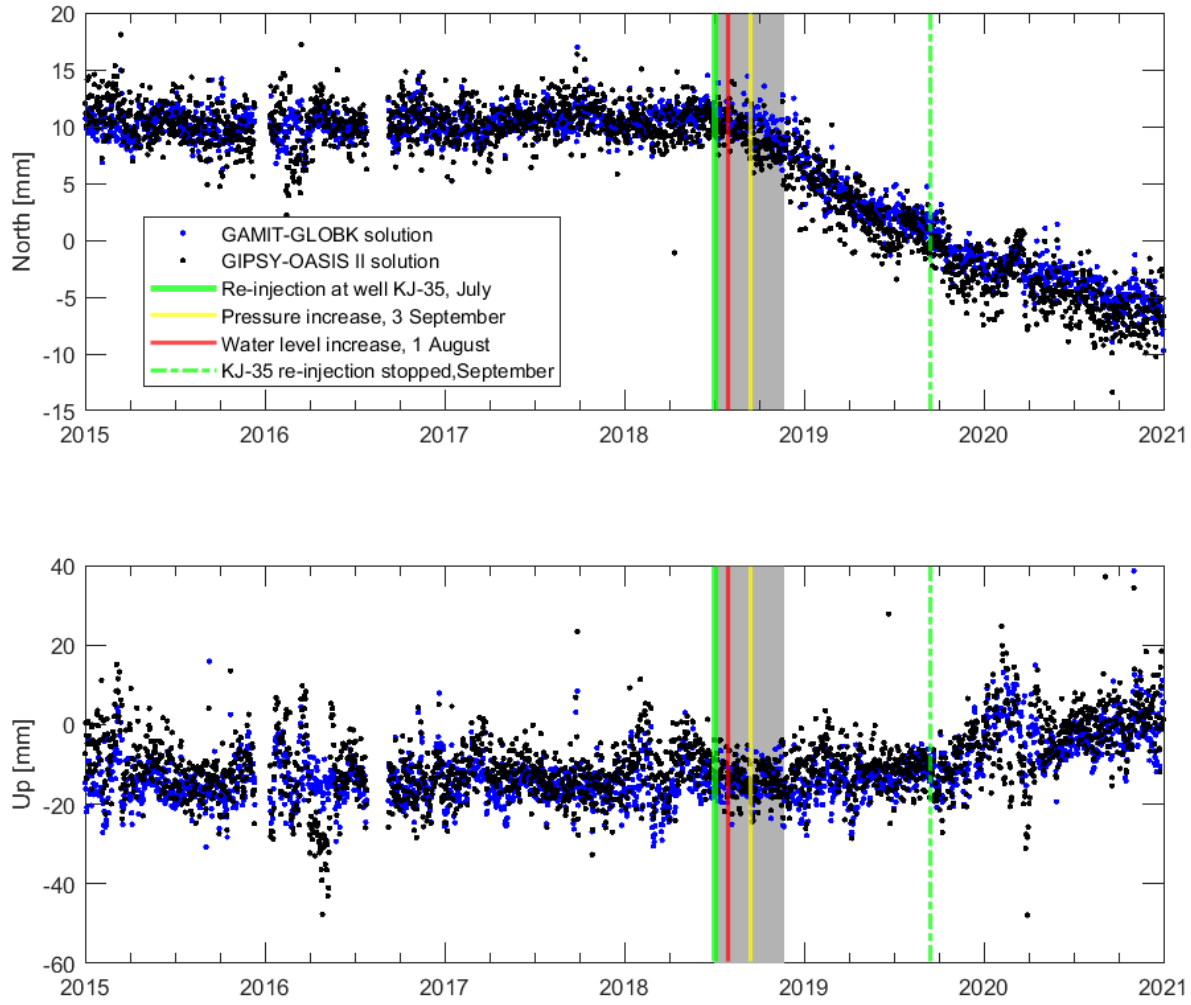

Figure 12. KRAC continuous GNSS station. 2015-2020 time series with a linear, annual and semi-annual modulations removed, for GAMIT-GLOBK solution (blue dots) and GIPSY-OASIS II (black dots). The shaded area indicates the inferred time range of the onset of the deformation, sometime from mid-July 2018 to mid-November 2018. The vertical yellow line shows the timing when a pressure measurement was taken; the vertical red line shows the beginning of the water level increase; the vertical green solid line and the vertical green dotted line show the start and the stop of the re-injection operations at one of the wells in the caldera.

A joint inversion of the GNSS and LOS difference velocity fields locates a Mogi source in the middle of the caldera at 2.1–2.5 km depth (Figure 13). We investigated the influence on deformation pattern of the size of a spherical pressurized source, located at ~2.2 km depth, in relation to the presence of a local geothermally altered crust and intra-caldera deposits (Figure 14), referred to as a low-rigidity volume. A FEM models was built to study the process. The crust surrounding the low-rigidity volume displays elastic Young's modulus according to the crust average estimation based on studies of regional rigidity in Iceland, i.e. 30 GPa (Grapenthin et al., 2006; Auriac et al., 2013; Drouin et al., 2017). Our investigation found that such FEM model where the low-rigidity volume (with Young's modulus = 7 GPa) envelops a pressurized

spherical source of deformation, reproduces broadly the deformation pattern (Figure 13), if the pressure changes in 2017–2019 are representative for the whole geothermal reservoir.

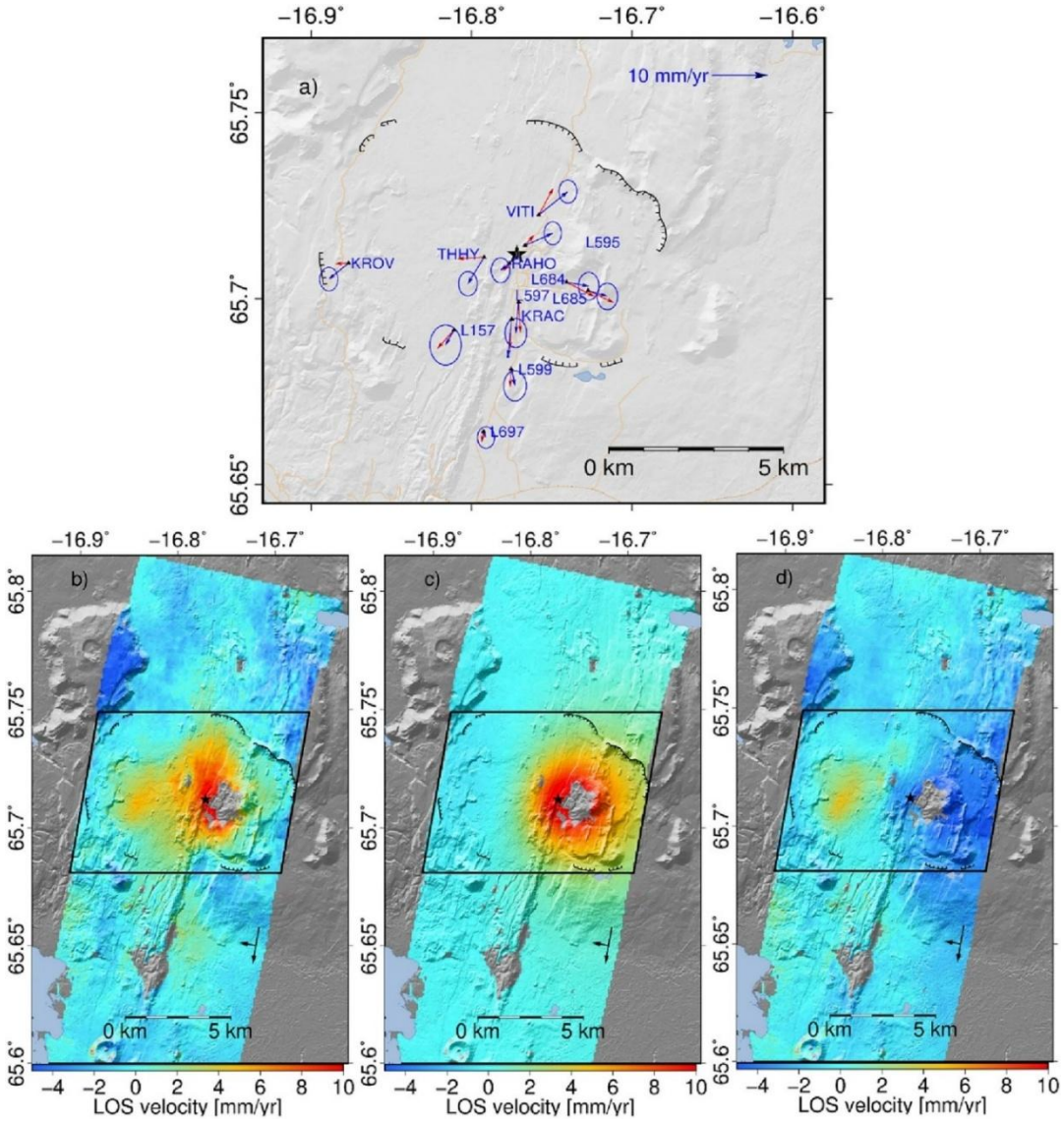

Figure 13. Comparison between observed and predicted displacement from Mogi best-fit GBIS solution. (a) GNSS observed horizonal displacements (blue arrows) and predictions (red arrows) of a best fitting model. The black star indicates the inferred best-fit position for the source centre. (b) LOS data, (c) best fit model predictions and (d) residuals for InSAR track T9. The black polygons mark the area used to evaluate the root mean square of residual value which for this model is = 2.6 mm/yr for the LOS data and 1.1 mm/yr and 9.4 mm/yr for the horizontal and vertical displacements, respectively.

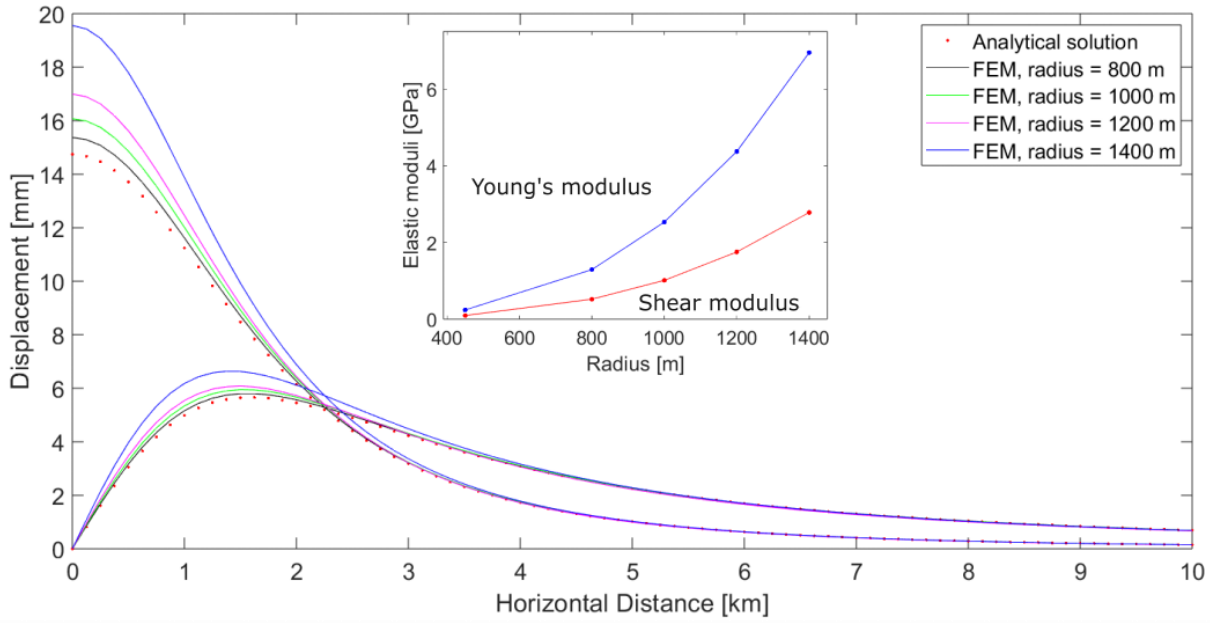

Figure 14. Predicted displacement from the best fit GBIS model (red circles) and numerical solutions from COMSOL for different source radius. The inset shows the elastic moduli, Young's modulus (blue) and shear modulus (red), as a function of the radius.

2.2 Main results

- Continuous GNSS monitoring detected a change in the deformation pattern at the Krafla caldera between mid-July to mid-November 2018. Time series analysis reveals a southern motion (10-12 mm/yr), which slowed down (6-8 mm/yr) approximately one year after the onset of the change, when the vertical component began to show upward motion.
- Yearly pressure measurements in the geothermal system show an increase in September 2018 and in summer 2019, compared to previous years, for a total of ~0.2 MPa. In 2020, no additional increase was observed.
- A joint inversion of geodetic data locates a point-pressure source at 2.1–2.5 km depth, near the magma-hydrothermal interface at the Krafla caldera.
- A FEM model with a pressurized spherical source centered at ~2.2 km depth and radius of ~1.4 km reproduces broadly the observed near-field deformation, using constraints on the intra-caldera Young's modulus value (about 7 GPa), if the pressure change observed in 2018 and 2019 in a monitoring well is representative of the whole geothermal reservoir.

3 Paper II: Strain Localization at Volcanoes Undergoing Extension: Investigation of Long-term Deformation at Krafla and Askja Volcanic Systems in North Iceland

3.1 Summary

Geodetic monitoring by several techniques, e.g., GNSS, InSAR and levelling, reveals deflation at the Krafla caldera from 1989 to 2018 (Tryggvason, 1994; Sturkell et al., 2008; Drouin et al., 2017), and at the Askja caldera from 1983 to 2021 (Sturkell et al., 2006; de Zeeuw-van Dalfsen et al., 2012). Both volcanoes lie at a divergent boundary where extensional processes may play an important role in the observed ground deformation. The high temperatures due to the presence of liquid magma and magma mush (Sparks and Cashman, 2017; Liao et al., 2018) can heat significant volumes of rock, influencing their physical properties, eventually forming a significant local rheological anomaly in the volcano subsurface. Thus, while a fully elastic and homogeneous medium may not suffice to represent the behavior of such deformed rocks, viscoelastic rheology may be a more appropriate way to describe the deformed rocks in a volcanic system. The Krafla and Askja volcanic systems are the most active in the Northern Volcanic Zone of Iceland, and both have historical eruptions attesting the state of activity of the systems. At Krafla, a strong seismic reflector has been mapped at ~2 km depth (Kim et al., 2020), where rhyolitic magma has been encountered in the caldera during the IDDP-1 drilling operations in 2009 (Elders et al., 2011). Similar reflectors were observed at depths ranging from ~4 to ~6 km (Kim et al., 2020). At Askja, tomography shows heavily intruded regions with inferred melt sitting in lenses of low melt fraction or within a mush beneath the caldera at ~5 km and ~9 km depth (Greenfield et al., 2016).

A two-layer three-dimensional FEM model is used to explore the relationship between plate spreading in relation to the presence of viscoelastic material at shallower depth beneath a caldera than regionally (Figure 15). A uniform spreading rate is considered to reproduce the extensional tectonic forces. The model accounts for the presence of a 2 km-thick caldera layer with lowered elastic properties (Young's modulus = 7 GPa as in previous paper), to simulate a geothermally altered area. A series of models has an elastic layer next to the low-rigidity volume reaching a depth of 7, 10 and 15 km, respectively, at 25 km away from the center of the caldera (geometries A1, A2 and A3). This layer has a Young's modulus of 30 GPa, in agreement with average estimation for the Icelandic crust (Grapenthin et al., 2006; Auriac et al., 2013; Drouin et al., 2017). Underlying the low-rigidity volume from 2 km depth to the bottom of the surrounding elastic layer geometry, the model has a viscoelastic material (referred to as up-doming material) to simulate a rheological anomaly beneath the volcano (Figure 15). Within this crustal volume, viscosities in the 10^{13}-10^{19} Pa s range are investigated. We refer to this as the caldera (C-) model. Additionally, two segments (for Krafla) and one segment (for Askja) of

a shallower elastic material and a deeper viscoelastic material were introduced to reproduce the fissure swarms (Figure 15). Their geometry is such that the elastic-viscoelastic interface is located at 2 km depth at the caldera contact and ramps down to 7, 10 or 15 km depth at 50 km distance north of the caldera and 40 km south distance of the caldera in the case of the Krafla volcanic system. For the Askja volcanic system, the model has only one fissure swarm to the north of the caldera. The viscoelastic material in the fissure swarm has a viscosity in the range of 5×10^{17}- 5×10^{19} Pa s, and Young's modulus set to 30 GPa. We refer to this as the Caldera and Fissure Swarm (CFS-) model.

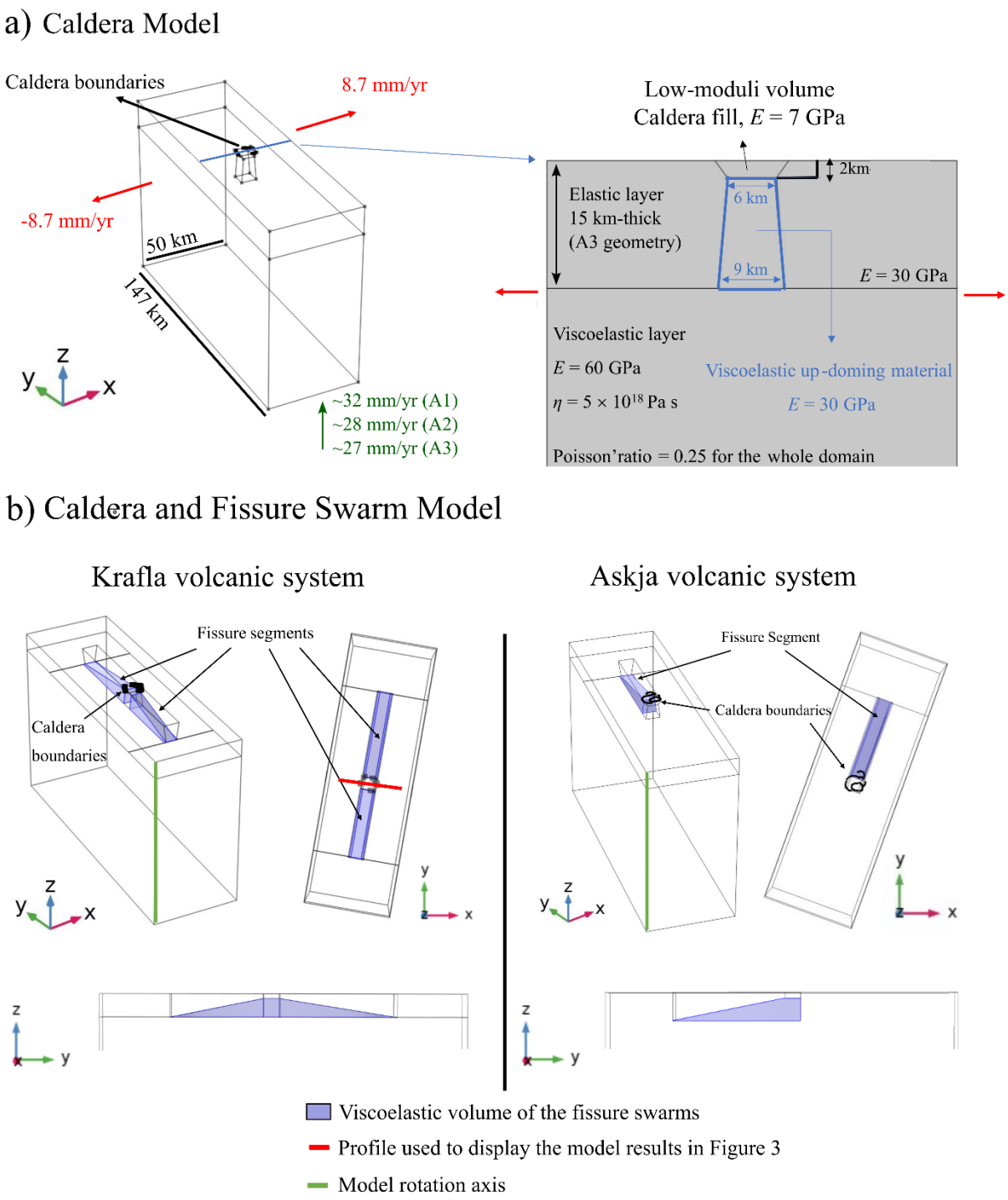

Figure 15. 3D models setup. a) C-model and caldera cross-section showing material properties; b) CFS-model for Krafla (left) and Askja (right) volcanic systems.

The model predictions for ground displacements are compared to inferred vertical displacements 2015-2018, based on InSAR LOS observations from one ascending and one

descending satellite tracks (Drouin and Sigmundsson, 2019). This comparison suggests plate divergence may account for 4-5 mm/yr of observed subsidence at Krafla, which is the bulk of the observed deformation signal there (Figure 16a-c). On the other hand, the model applied to the Askja volcanic system reproduces only 25-20% of the observed deformation (Figure 16d-f), implying the existence of additional causes of deformation (e.g., geothermal activity, magma transport etc.). The modelling results suggest that any magmatic systems undergoing stretching will feature subsidence in relation to the presence of an extensive, rheologically, weak crustal volume beneath volcanic systems.

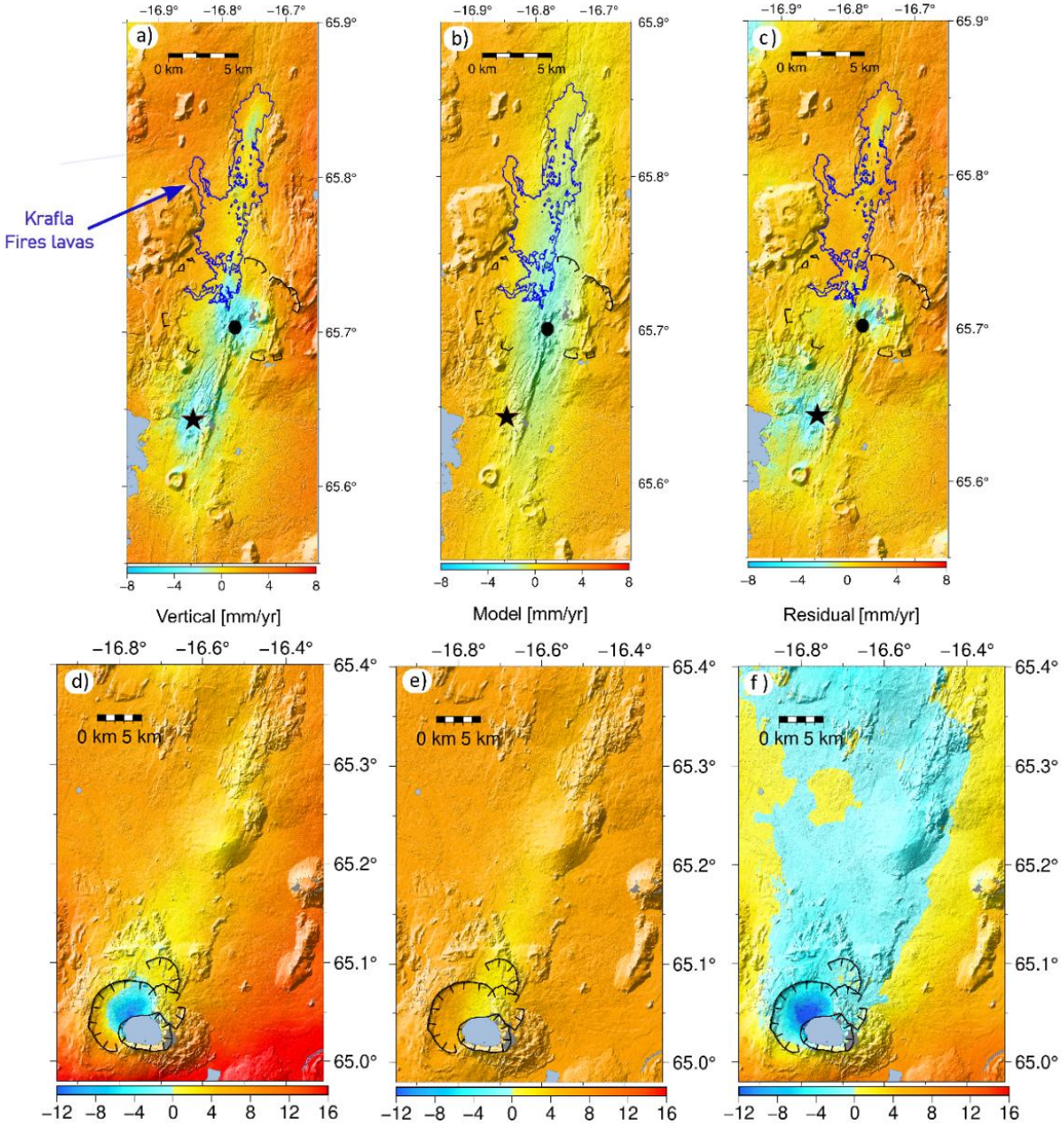

Figure 16. Inferred average vertical velocities from 2015-2018 Sentinel-1 InSAR data (Drouin and Sigmundsson, 2019), model prediction, and residuals in a map view for the Krafla (a- c), and the Askja volcanic systems (d-f). The black circle and black star in panels (a-c) indicate the Krafla and Bjarnarflag power plants, respectively, the blue line shows the Krafla Fires (1975- 1984) lavas extension. The black lines indicate the Krafla (a-c) and Askja (d-f) calderas, respectively.

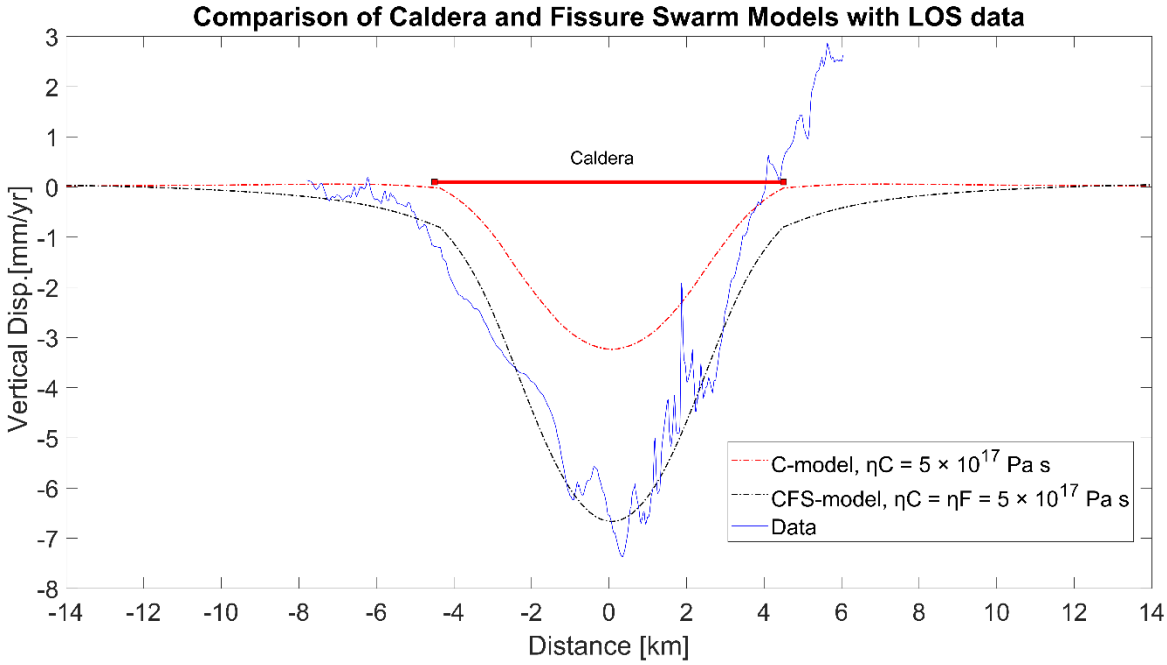

Figure 17. Vertical displacement of the C-model and CFS-model given the same viscosity value in the up-doming material and same elastic layer thickness. The profile is along the red line in X-dimension in Figure 15. ηF = viscosity fissure swarm; ηC = viscosity beneath the caldera.

3.2 Main results

- A plate spreading model, with extensional stretching over a heterogeneous plumbing system symbolizing a caldera (C-model) and a caldera and a fissure swarm geometry (CFS-model), causes subsidence localized in the center of a volcanic system.
- The subsidence rate within a caldera decreases as the viscosity in the heterogeneous magmatic system increases from 5×10^{16} Pa s, to 5×10^{17} Pa s to 5×10^{18} Pa s.
- The comparison of the C-model and CFS-model shows that presence of fissure swarm induces additional subsidence in the caldera compared to the C-model results (Figure 17).
- The CFS-model suggests that plate divergence processes may account for the majority of the observed deformation at Krafla volcanic system during the 2015-2018 period. For the same period, the models reproduce only 25-30% of the observed deformation at Askja volcanic system, suggesting involvement of additional deformation processes (geothermal activity, magma transport).

4 Paper III: Transient ground deformation observed by cGNSS and InSAR during and following the 2021 Fagradalsfjall eruption, Iceland

4.1 Summary

Ground deformation during a volcanic eruption can display particular spatial and temporal patterns that help to interpret physical processes related to the evolution of a magmatic plumbing system. In this paper, the co-eruptive deformation during the 2021 Fagradalsfjall (South-West Iceland, Figure 3) eruption is analyzed. The eruption started after several weeks of intense seismic activity in the area and several inflation-deflation episodes occurring at neighboring volcanoes in Svartsengi and Krýsuvík (e.g, Çubuk-Sabuncu et al., 2021; Geirsson et al., 2021; Flóvenz et al., 2022).

The analysis of spatial and temporal GNSS and InSAR (Sentinel-1) observations of ground deformation identify three geodetic phases in the deformation pattern during the six-month eruptive period (Figure 18): T1, 19 March – 10 May, relatively small deformation occurred; T2, 11 May – 31 July, the highest deformation (up to 30–40 mm in GNSS horizontal components) of the whole eruptive period, followed by a relatively calm phase, T3, 1 August – 18 September, with little or almost null deformation. We jointly inverted GNSS and InSAR data using the GBIS software (Bagnardi and Hooper, 2018) to place constraints on the location and geometry of the source of deformation.

Initial geodetic modelling of the GNSS and LOS data reveal local residuals around the lava deposits. Thus, we integrate the geodetic analysis with a lava loading FEM model by using a digital elevation model of the lava available for the full six-month eruption period (Pedersen et al., 2022). The lava loading model, considering a crustal volume with a Young's modulus set to 30 GPa, reproduces a maximum subsidence of 7-8 cm beneath the lava deposits (Figure 19). The deformation decays rapidly with distance, within 1-2 km away from the lava outline.

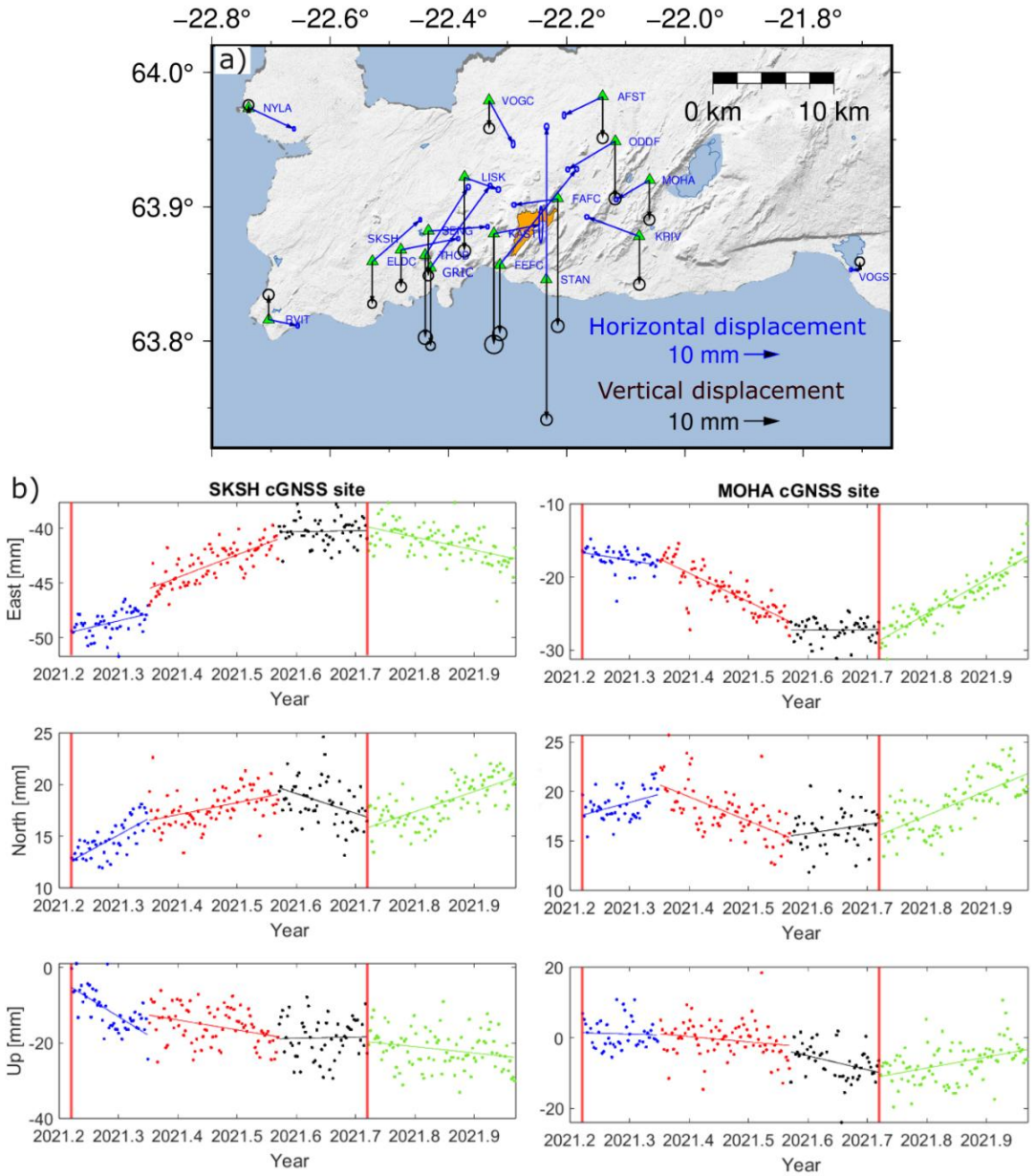

Figure 18. Displacements on the Reykjanes Peninsula from 19 March to 20 December 2021. The upper panel shows GNSS stations (with green triangles) with both vertical and horizontal displacements and the Fagradalsfjall lava field at the end of the eruption (in orange). The lower panels display detrended GNSS time series for stations SKSH (on the left panel) and MOHA (on the right panel) located west and east to the eruption site, respectively. The three co-eruptive deformation periods are marked: T1: 19 March – 10 May (blue dots), T2: 11 May - 31 July (red dots), T3: 1 August – 18 September (black dots), and post-eruptive deformation, 19 September – 20 December (green dots). The vertical red lines indicate the beginning and end of the eruption. The blue, red, black and green lines show the least-square fit for the different geodetic phases. Ocean and lakes are in light blue.

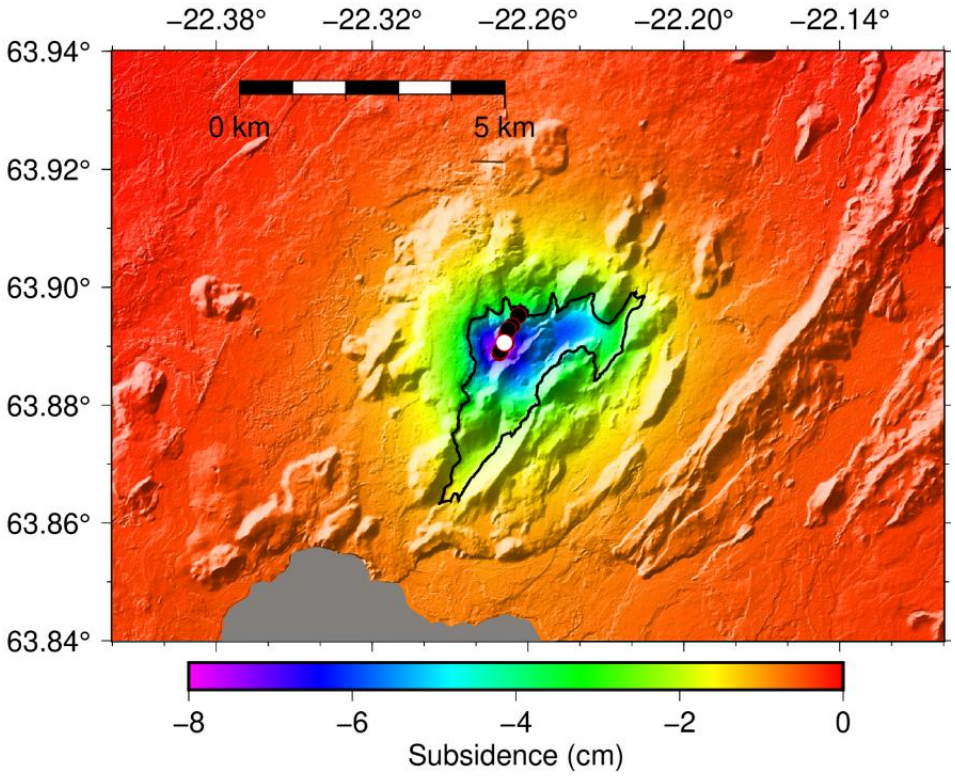

Figure 19. Vertical displacement according to a lava load FEM model (background color) in cm, when the crust has a Young's modulus E = 30 GPa. Grey area is the sea, while the black line marks the lava outline. The white circle indicates the active vent from end of April to 18 September 2021, while the black circles are the vents that opened in the first 5 weeks of the eruption.

After correcting the six-month LOS data for the lava loading signal, the model residuals are reduced, and the fit improves in proximity of the lava field (Figure 20). The preferred model to explain the observed deformation, in addition to the lava loading effects, represents a sill at 12.3–13.5 km depth (sill top), with a deflation volume of 21–27 Mm^3. The best-fit sill location inferred in the T2 geodetic phase is at a slightly shallower 11.1–12.4 depth with a deflating volume of 6–7 Mm^3.

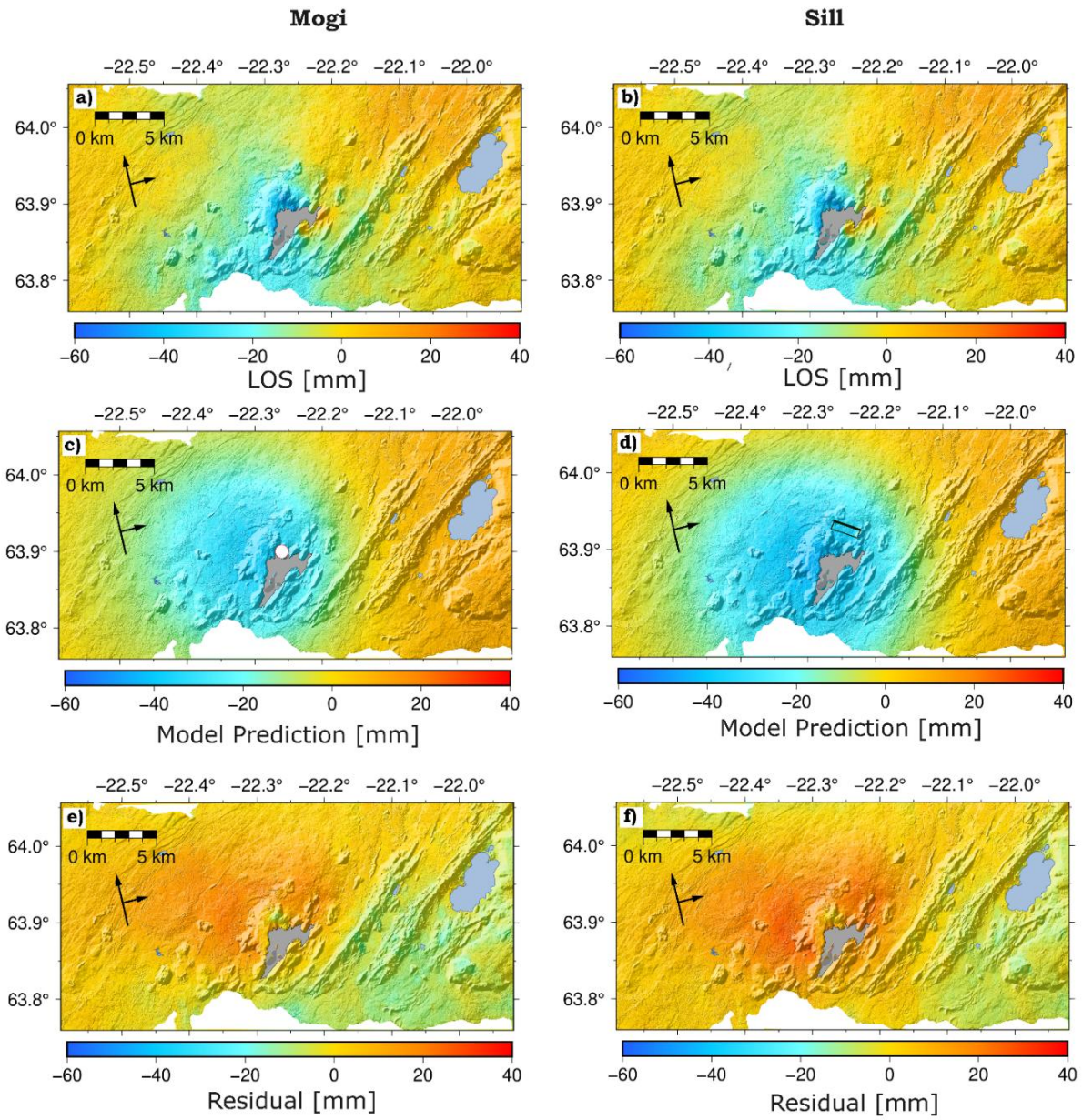

Figure 20. Data and modelling results for the loading corrected six-months LOS change of the T16 InSAR track, for E = 30 GPa. (a) and (b) data – both panels the same, (c) and (d) model prediction, (e) and (f) residuals for a Mogi and a sill geometry, respectively (left and right columns). The white circle in (b) indicates the best-fit solution of the Mogi source at 9 km (95% confidence interval: 8.6-9.5) km depth. Black square in panel d) shows the projection at surface of the modelled deflating sill (thicker line for the top) at a depth of ~12.8 km (95% confidence interval 12.3–13.5 km). Black arrows show the heading and look direction of the satellite. In light grey, the Fagradalsfjall lava field at the end of the eruption and in light blue the lake Kleifarvatn to the east. White indicates the ocean.

Additionally, we evaluate the link between the temporal changes in the displacement pattern with other observables at surface like variations in the effusion rate (Pedersen et al., 2022) and in geochemistry of the time-series of collected lava samples (Halldórsson et al., 2022). These studies, combined with gas analysis, infer input of new magma from a near-Moho depth (approximately ~15 km depth) around the end-April to beginning of May 2021, corresponding to an increase in the extrusion rate at the surface and the beginning of the T2 geodetic phase (Figure 21).

Post-eruptive inflation was detected at the end of the eruption at most of the GNSS stations on the Reykjanes Peninsula. The signal is sourced at a comparable depth to the co-eruptive source, but best-fit location is few kilometers further south.

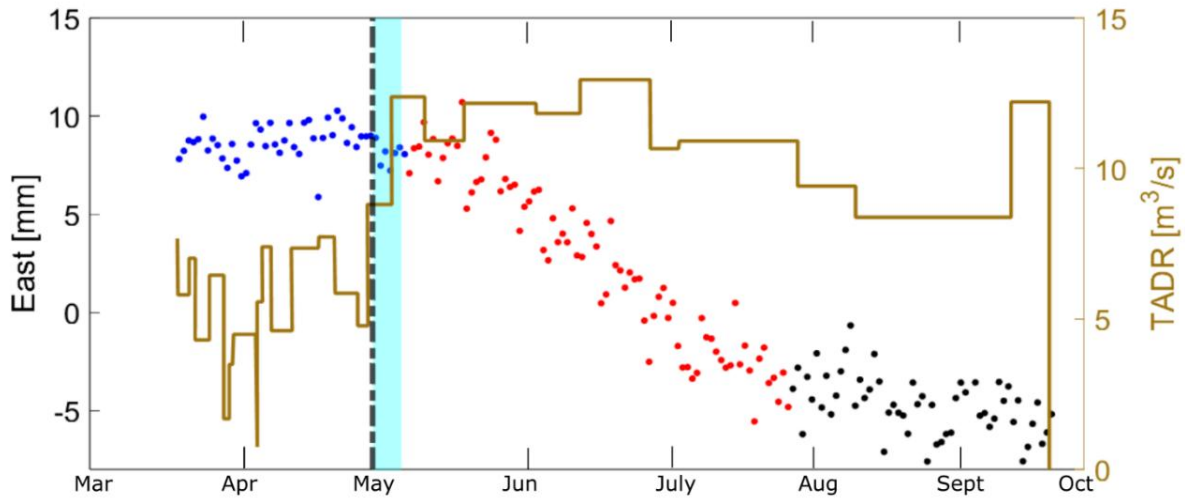

Figure 21. KRIV GNSS east displacement in relation to changes in the effusion rate and eruptive style. T1 geodetic phase, 19 March – 10 May 2021(blue dots), T2 geodetic phase, 11 May – 31 July 2021 (red dots), T3 geodetic phase, 1 August – 18 September 2021 (black dots). The brown line shows the evolution of the time average discharge rate, TADR, during the eruption (Pedersen et al., 2022). The vertical dashed black line indicates the beginning of lava fountain episodes according to seismic tremor observations on 2 May (Eibl et al., 2023), while the cyan shadow marks the acoustic energy increase period observed between 2-8 May 2021 (Lamb et al., 2022).

4.2 Main findings

- Geodetic observations during the six-month 2021 Fagradalsfjall eruption reveal changes in the deformation pattern and allow definition of geodetic phases: T1, 19 March – 10 May; T2,

11 May – 31 July, and T3, 1 August – 18 September. Most of the deformation occurred during the T2 geodetic phase, amounting to up to 30-40 mm in the GNSS horizontal components.

- The modelling strategy includes a joint inversion of InSAR and GNSS data corrected for the lava loading contribution to the deformation. The inferred loading according to our model is up to several centimeters of subsidence near the lava boundary.

- The inversion result infers a best-fit sill source at 12–13 km depth with deflating volume change in the range of (21–27) Mm^3 for the six-month eruptive period.

- The inferred geodetic volume change is about 5-6 times smaller than the estimated bulk volume of the erupted material at the end of the eruption. However, geochemical investigations suggested new magma, possibly from multiple bodies at near-Moho depths (~15 km) reaches the surface with short-lived permanency in the crust, between end-April and beginning of May (Halldórsson et al., 2022; Marshall et al., 2024), resulting in the eventual increase of the effusion rate observed at surface.

5 Conclusions and Outlook

Volcanic areas are home to a significant part of the global population. In 2015, at least 800 million people were estimated to live within a range (~100 km) of potential direct impact of volcanic eruption (Brown et al., 2015), with ~60 million people living within potential evacuation range (~10 km) (Freire et al., 2019). Potential danger may derive from ash dispersion (Jenkins et al., 2015), volcanic gas (Williams-Jone and Rymer, 2015) or pyroclastics and/or lava flow flows (Felpeto et al, 2001; Damiani et al., 2006). Thus, early detection of "anomalous" volcanic behavior is crucial to mitigate the volcanic hazards and issue prompt warnings for communities living near active volcanic zones.

The investigation of ground deformation trends at volcanoes has been widely carried out by using GNSS and InSAR geodetic monitoring techniques in the past decades. These technologies provide continuous point measurements (GNSS) and wide spatial coverage (reaching also remote areas) with periodic measurements (InSAR) of ground deformation. The continuous improvements and the increasing successful algorithms and approaches developed to minimize errors or artifacts in both datasets allow detecting relatively small deformation signals, of mm-scale, previously challenging to investigate, or often masked by possible instrumentation errors or travel path signal delays errors.

A variety of mathematical approaches and models can be used to understand observed geodetic deformation signals, which signatures may relate to very localized deformation source/s, active regional tectonics, or interaction of both. In this project, integration of joint inversion of GNSS and InSAR geodetic data using simple sources of deformation within an elastic halfspace and more complex numerical modelling settings based on the finite element method is carried out to improve understanding of small deformation signals. The results derived in this thesis demonstrate that this is an effective approach, which can be recommended for application in other volcanic areas.

At Krafla caldera, it is found that the inferred deformation source and observed surface displacement may be coupled to effects of intra-caldera crustal heterogeneity and increase of pressure at depth that occurred in the Krafla geothermal reservoir in 2018-2020. From 1989 and until 2018, the Krafla caldera showed subsidence exponentially decreasing from several cm/yr to several mm/yr in 2015-2018 LOS velocities. In the same period, an alike subsidence pattern was observed at the Askja caldera, along the same plate spreading boundary as Krafla, but at a higher rate, 10–15 mm/yr. Modelling results of an elastic and viscoelastic Earth structure beneath both volcanoes, undergoing an uniform extension, suggest that the observed subsidence may relate to the regional tectonics and how extensive the magmatic systems are underneath both volcanic systems. Beyond their immediate implication for improved understanding of the ground deformation processes studied, the methodologies and findings presented here have potential importance for active volcano monitoring in general and for forecasting changes in volcanic behavior, given a known background deformation pattern at a particular volcano.

This project highlights the risk of misinterpreting the true source location and geometry of deformation without a complementary study investigating the impact of various processes on ground displacement. Correcting ground deformation data for external, non-magmatic influences, including small-scale localized effects, is crucial before solving for magmatic source parameters. This became particularly evident in the investigation of the 2021

Fagradalsfjall co-eruptive deformation, where the newly emplaced lava was found to influence the observed deformation.

Additionally, this study demonstrates the importance of interpreting geodetic data in conjunction with other parameters, such as seismicity, pressure variation in the geothermal system (e.g., at Krafla), or changes in effusion rates and geochemical evolution of lavas erupted (e.g., at Fagradalsfjall), providing a broader context for the comprehensive reconstruction of the evolution of conditions in magmatic plumbing systems. Extending the same approach to other areas may offer new opportunities for advancing understanding of crustal deformation taking place at volcanoes around the world. In the event of subsurface changes at depth, ground deformation may serve as a key indicator of these transformations, either used as for early warning or to assess the characteristics of a developing volcanic event. Thus, intensive continuous geodetic monitoring, combined with detailed modelling, is essential for identifying and improving understanding of spatial patterns and temporal variations in surface displacements.

This PhD project has addressed key challenges in understanding volcano-tectonic processes and their subtle, correlated deformation signals, advancing knowledge across multiple volcanic systems in Iceland. It bridges gaps in linking long-term millimeter-scale ground deformation trends to local heterogeneities and regional tectonic influence, while enhancing understanding of transient co-eruptive ground deformation in an evolving magmatic plumbing system. These findings provide a strong foundation for future research, which could further benefit from continued advancements in GNSS, InSAR, and modeling strategies to refine and extend upon this work.

References

Albino, F., Pinel, V., and Sigmundsson, F. (2010). Influence of surface load variations on eruption likelihood: application to two Icelandic subglacial volcanoes, Grímsvötn and Katla. *Geophysical Journal International*. https://doi.org/10.1111/j.1365-246X.2010.04603.x

Altamimi, Z., Rebischung, P., Collilieux, X., Métivier, L., andand Chanard, K. (2023). ITRF2020: an augmented reference frame refining the modeling of nonlinear station motions. *Journal of Geodesy*, *97*(5), 47. https://doi.org/10.1007/s00190-023-01738-w

Amoruso, A., andand Crescentini L. (2013). Analytical models of volcanic ellipsoidal expansion sources. *Annals of Geophysics*, *56*(4), 3. https://doi.org/10.4401/ag-6441

Armannsson, H., Gudmundsson, A., Steingrímsson, B.S. (1987). Exploration and development of the Krafla geothermal area. *Jokull,* 37, 13–30

Árnadóttir, T., Lund, B., Jiang, W., Geirsson, H., Björnsson, H., Einarsson, P., andand Sigurdsson, T. (2009). Glacial rebound and plate spreading: results from the first countrywide GPS observations in Iceland. *Geophysical Journal International*, *177*(2), 691–716. https://doi.org/10.1111/j.1365-246X.2008.04059.x

Árnadóttir, Thóra, Jónsson, S., Pollitz, F. F., Jiang, W., andand Feigl, K. L. (2005). Postseismic deformation following the June 2000 earthquake sequence in the south Iceland seismic zone. *Journal of Geophysical Research: Solid Earth*, *110*(B12), 2005JB003701. https://doi.org/10.1029/2005JB003701

Arnórsson, S. (1995). Geothermal systems in Iceland: Structure and conceptual models—I. High-temperature areas. *Geothermics*, *24*(5–6), 561–602. https://doi.org/10.1016/0375-6505(95)00025-9

Attema, E. P. W., Duchossois, G., andand Kohlhammer, G. (1998). ERS-1/2 SAR land applications: overview and main results. In *IGARSS '98. Sensing and Managing the Environment. 1998 IEEE International Geoscience and Remote Sensing. Symposium Proceedings. (Cat. No.98CH36174)* (pp. 1796–1798 vol.4). Seattle, WA, USA: IEEE. https://doi.org/10.1109/IGARSS.1998.703655

Auriac, A., Spaans, K. H., Sigmundsson, F., Hooper, A., Schmidt, P., andand Lund, B. (2013). Iceland rising: Solid Earth response to ice retreat inferred from satellite radar interferometry and visocelastic modeling. *Journal of Geophysical Research: Solid Earth*, *118*(4), 1331–1344. https://doi.org/10.1002/jgrb.50082

Bagnardi, M., andand Hooper, A. (2018). Inversion of Surface Deformation Data for Rapid Estimates of Source Parameters and Uncertainties: A Bayesian Approach. *Geochemistry, Geophysics, Geosystems*, *19*(7), 2194–2211. https://doi.org/10.1029/2018GC007585

Bamler, R., andand Hartl, P. (1998). Synthetic aperture radar interferometry. *Inverse Problems*, *14*(4), R1–R54. https://doi.org/10.1088/0266-5611/14/4/001

Battaglia, M., Troise, C., Obrizzo, F., Pingue, F., andand De Natale, G. (2006). Evidence for fluid migration as the source of deformation at Campi Flegrei caldera (Italy). *Geophysical Research Letters*, *33*(1), 2005GL024904. https://doi.org/10.1029/2005GL024904

Battagliere, M. L., Daraio, M. G., Sacco, P., Virelli, M., and Coletta, A. (2016). Aerospace technology and Dual Use: COSMO-SkyMed mission status and future

perspectives, *Proceedings of EUSAR 2016: 11th European Conference on Synthetic Aperture Radar*, Hamburg, Germany, 2016, pp. 1-4.

Berardino, P., Fornaro, G., Lanari, R., andand Sansosti, E. (2002). A new algorithm for surface deformation monitoring based on small baseline differential SAR interferograms. *IEEE Transactions on Geoscience and Remote Sensing*, *40*(11), 2375–2383. https://doi.org/10.1109/TGRS.2002.803792

Bertiger, W., Bar-Sever, Y., Dorsey, A., Haines, B., Harvey, N., Hemberger, D., et al. (2020). GipsyX/RTGx, a new tool set for space geodetic operations and research. *Advances in Space Research*, *66*(3), 469–489. https://doi.org/10.1016/j.asr.2020.04.015

Biggs, J., Ebmeier, S. K., Aspinall, W. P., Lu, Z., Pritchard, M. E., Sparks, R. S. J., andand Mather, T. A. (2014). Global link between deformation and volcanic eruption quantified by satellite imagery. *Nature Communications*, *5*(1), 3471. https://doi.org/10.1038/ncomms4471

Biggs, Juliet, andand Wright, T. J. (2020). How satellite InSAR has grown from opportunistic science to routine monitoring over the last decade. *Nature Communications*, *11*(1), 3863. https://doi.org/10.1038/s41467-020-17587-6

Björnsson, H. (2010). Understanding jökulhlaups: From tale to theory. *Journal of Glaciology*, *56*(200), 1002–1010. https://doi.org/10.3189/002214311796406086

Blewitt, G. (1989). Carrier phase ambiguity resolution for the Global Positioning System applied to geodetic baselines up to 2000 km. *Journal of Geophysical Research: Solid Earth*, *94*(B8), 10187–10203. https://doi.org/10.1029/JB094iB08p10187

Bock, Y., andand Melgar, D. (2016). Physical applications of GPS geodesy: a review. *Reports on Progress in Physics*, *79*(10), 106801. https://doi.org/10.1088/0034-4885/79/10/106801

Brander, J. L., Mason, R. G., andand Calvert, R. W. (1976). Precise distance measurements in Iceland. *Tectonophysics*, *31*(3-4), 193-206.

Briole, P., Massonnet, D., andand Delacourt, C. (1997). Post-eruptive deformation associated with the 1986–87 and 1989 lava flows of Etna detected by radar interferometry. *Geophysical Research Letters*, *24*(1), 37–40. https://doi.org/10.1029/96GL03705

Brown, SK, Auker, MR, and Sparks, RSJ. (2025). Populations around Holocene volcanoes and development of a Population Exposure Index. In: Loughlin SC, Sparks RSJ, Brown SK, Jenkins SF, Vye-Brown C, editors. Global Volcanic Hazards and Risk. Cambridge: Cambridge University Press; p. 223–32. B

Buck, W. R., Einarsson, P., and Brandsdóttir, B. (2006). Tectonic stress and magma chamber size as controls on dike propagation: Constraints from the 1975–1984 Krafla rifting episode. *Journal of Geophysical Research: Solid Earth*, *111*(B12), 2005JB003879. https://doi.org/10.1029/2005JB003879

Bundschuh, J., Ruppert, M. G., and Späck-Leigsnering, Y. (2023). Pyrit: A finite element based field simulation software written in Python. *COMPEL - The International Journal for Computation and Mathematics in Electrical and Electronic Engineering*, *42*(5), 1007–1020. https://doi.org/10.1108/COMPEL-01-2023-0013

Bürgmann, R., Rosen, P. A., and Fielding, E. J. (2000). Synthetic Aperture Radar Interferometry to Measure Earth's Surface Topography and Its Deformation.

Annual Review of Earth and Planetary Sciences, *28*(1), 169–209. https://doi.org/10.1146/annurev.earth.28.1.169

Cabaniss, H. E., Gregg, P. M., Nooner, S. L., and Chadwick, W. W. (2020). Triggering of eruptions at Axial Seamount, Juan de Fuca Ridge. *Scientific Reports*, *10*(1), 10219. https://doi.org/10.1038/s41598-020-67043-0

Cannavò, F. (2019). A new user-friendly tool for rapid modelling of ground deformation. *Computers and Geosciences*, *128*, 60–69. https://doi.org/10.1016/j.cageo.2019.04.002

Cao, Y., Jónsson, S., and Hreinsdóttir, S. (2023). Iceland Kinematics From InSAR. *Journal of Geophysical Research: Solid Earth*, *128*(3), e2022JB025546. https://doi.org/10.1029/2022JB025546

Castellazzi, P., Longuevergne, L., Martel, R., Rivera, A., Brouard, C., and Chaussard, E. (2018). Quantitative mapping of groundwater depletion at the water management scale using a combined GRACE/InSAR approach. *Remote Sensing of Environment*, *205*, 408–418. https://doi.org/10.1016/j.rse.2017.11.025

Charco, M., and Galán Del Sastre, P. (2014). Efficient inversion of three-dimensional finite element models of volcano deformation. *Geophysical Journal International*, *196*(3), 1441–1454. https://doi.org/10.1093/gji/ggt490

Chaussard, E. (2016). Subsidence in the Parícutin lava field: Causes and implications for interpretation of deformation fields at volcanoes. *Journal of Volcanology and Geothermal Research*, *320*, 1–11. https://doi.org/10.1016/j.jvolgeores.2016.04.009

Chen, C. W. and Zebker, H. A. (2002). Phase unwrapping for large SAR interferograms: Statistical segmentation and generalized network models. *IEEE Transactions on Geoscience and Remote Sensing*, vol. 40, pp. 1709-1719.

Compton, K., Bennett, R. A., and Hreinsdóttir, S. (2015). Climate-driven vertical acceleration of Icelandic crust measured by continuous GPS geodesy. *Geophysical Research Letters*, *42*(3), 743–750. https://doi.org/10.1002/2014GL062446

Costa, A., Gottsmann, J., Melnik, O., and Sparks, R. S. J. (2011). A stress-controlled mechanism for the intensity of very large magnitude explosive eruptions. *Earth and Planetary Science Letters*, *310*(1–2), 161–166. https://doi.org/10.1016/j.epsl.2011.07.024

Crosetto, M., Monserrat, O., Cuevas-González, M., Devanthéry, N., and Crippa, B. (2016). Persistent Scatterer Interferometry: A review. *ISPRS Journal of Photogrammetry and Remote Sensing*, *115*, 78–89. https://doi.org/10.1016/j.isprsjprs.2015.10.011

Crozier, J., Karlstrom, L., Montgomery-Brown, E., Angarita, M., Cayol, V., Bato, M. G., et al. (2023). Understanding the drivers of volcano deformation through geodetic model verification and validation. *Bulletin of Volcanology*, *85*(12), 74. https://doi.org/10.1007/s00445-023-01687-4

Cubuk-Sabuncu, Y., Jónsdóttir, K., Caudron, C., Lecocq, T., Parks, M. M., Geirsson, H., and Mordret, A. (2021a). Temporal Seismic Velocity Changes During the 2020 Rapid Inflation at Mt. Þorbjörn-Svartsengi, Iceland, Using Seismic Ambient Noise. *Geophysical Research Letters*, *48*(11), e2020GL092265. https://doi.org/10.1029/2020GL092265

Cubuk-Sabuncu, Y., Jónsdóttir, K., Caudron, C., Lecocq, T., Parks, M. M., Geirsson, H., and Mordret, A. (2021b). Temporal Seismic Velocity Changes During the 2020 Rapid Inflation at Mt. Þorbjörn-Svartsengi, Iceland, Using Seismic Ambient Noise.

Geophysical Research Letters, *48*(11), e2020GL092265. https://doi.org/10.1029/2020GL092265

Curlander, J. C., and MacDonough, R. N. (1991). *Synthetic aperture radar: systems and signal processing*. New York, NY: Wiley.

Currenti, G., Del Negro, C., Ganci, G., and Scandura, D. (2008). 3D numerical deformation model of the intrusive event forerunning the 2001 Etna eruption. *Physics of the Earth and Planetary Interiors*, *168*(1–2), 88–96. https://doi.org/10.1016/j.pepi.2008.05.004

Currenti, G., Napoli, R., Coco, A., and Privitera, E. (2017). Effects of hydrothermal unrest on stress and deformation: insights from numerical modeling and application to Vulcano Island (Italy). *Bulletin of Volcanology*, *79*(4), 28. https://doi.org/10.1007/s00445-017-1110-3

Damiani, M. L., Groppelli, G., Norini, G., Bertino, E., Gigliuto, A., and Nucita, A. (2006). A lava flow simulation model for the development of volcanic hazard maps for Mount Etna (Italy). *Computers and Geosciences*, *32*(4), 512–526. https://doi.org/10.1016/j.cageo.2005.08.011

Davis, J. L., Herring, T. A., Shapiro, I. I., Rogers, A. E. E., and Elgered, G. (1985). Geodesy by radio interferometry: Effects of atmospheric modeling errors on estimates of baseline length. *Radio Science*, *20*(6), 1593–1607. https://doi.org/10.1029/RS020i006p01593

Dayton, K., Gazel, E., Wieser, P., Troll, V. R., Carracedo, J. C., La Madrid, H., et al. (2023). Deep magma storage during the 2021 La Palma eruption. *Science Advances*, *9*(6), eade7641. https://doi.org/10.1126/sciadv.ade7641

De Pascale, G. P., Fischer, T. J., Moreland, W. M., Geirsson, H., Hrubcová, P., Drouin, V., et al. (2024). On the Move: 2023 Observations on Real Time Graben Formation, Grindavík, Iceland. *Geophysical Research Letters*, *51*(14), e2024GL110150. https://doi.org/10.1029/2024GL110150

De Zeeuw-van Dalfsen, E., Pedersen, R., Hooper, A., and Sigmundsson, F. (2012). Subsidence of Askja caldera 2000–2009: Modelling of deformation processes at an extensional plate boundary, constrained by time series InSAR analysis. *Journal of Volcanology and Geothermal Research*, *213–214*, 72–82. https://doi.org/10.1016/j.jvolgeores.2011.11.004

Decriem, J., and Árnadóttir, T. (2012). Transient crustal deformation in the South Iceland Seismic Zone observed by GPS and InSAR during 2000–2008. *Tectonophysics*, *581*, 6–18. https://doi.org/10.1016/j.tecto.2011.09.028

Decriem, J., Árnadóttir, T., Hooper, A., Geirsson, H., Sigmundsson, F., Keiding, M., et al. (2010). The 2008 May 29 earthquake doublet in SW Iceland. *Geophysical Journal International*. https://doi.org/10.1111/j.1365-246X.2010.04565.x

Delgado, F., Pritchard, M., Lohman, R., and Naranjo, J. A. (2014). The 2011 Hudson volcano eruption (Southern Andes, Chile): Pre-eruptive inflation and hotspots observed with InSAR and thermal imagery. *Bulletin of Volcanology*, *76*(5), 815. https://doi.org/10.1007/s00445-014-0815-9

Dellino, P., Gudmundsson, M. T., Larsen, G., Mele, D., Stevenson, J. A., Thordarson, T., and Zimanowski, B. (2012). Ash from the Eyjafjallajökull eruption (Iceland): Fragmentation processes and aerodynamic behavior. *Journal of Geophysical Research: Solid Earth*, *117*(B9), 2011JB008726. https://doi.org/10.1029/2011JB008726

DeMets, C., Gordon, R. G., and Argus, D. F. (2010). Geologically current plate motions. *Geophysical Journal International*, *181*(1), 1–80. https://doi.org/10.1111/j.1365-246X.2009.04491.x

Dieterich, J. H., and Decker, R. W. (1975). Finite element modeling of surface deformation associated with volcanism. *Journal of Geophysical Research*, *80*(29), 4094–4102. https://doi.org/10.1029/JB080i029p04094

Dietterich, H. R., Poland, M. P., Schmidt, D. A., Cashman, K. V., Sherrod, D. R., and Espinosa, A. T. (2012). Tracking lava flow emplacement on the east rift zone of Kīlauea, Hawai‘i, with synthetic aperture radar coherence. *Geochemistry, Geophysics, Geosystems*, *13*(5), 2011GC004016. https://doi.org/10.1029/2011GC004016

Drouin, V., Parks, M., Tolpekin, V., Sigmundsson, F., Leeb, D., and Strong, S. (2021, December). Conduits feeding new eruptive vents mapped by high-resolution ICEYE SAR satellite in a daily repeat orbit. In *AGU Fall Meeting Abstracts* (Vol. 2021, pp. G43A-01).

Drouin, V., and Sigmundsson, F. (2019). Countrywide Observations of Plate Spreading and Glacial Isostatic Adjustment in Iceland Inferred by Sentinel-1 Radar Interferometry, 2015–2018. *Geophysical Research Letters*, *46*(14), 8046–8055. https://doi.org/10.1029/2019GL082629

Drouin, V., Heki, K., Sigmundsson, F., Hreinsdóttir, S., and Ófeigsson, B. G. (2016a). Constraints on seasonal load variations and regional rigidity from continuous GPS measurements in Iceland, 1997–2014. *Geophysical Journal International*, *205*(3), 1843–1858. https://doi.org/10.1093/gji/ggw122

Drouin, V. (2016b). Constraints on deformation processes in Iceland from space geodesy: seasonal load variations, plate spreading, volcanoes and geothermal fields. Phd Thesis, University of Iceland, https://hdl.handle.net/1946/25599

Drouin, V., Sigmundsson, F., Verhagen, S., Ófeigsson, B. G., Spaans, K., and Hreinsdóttir, S. (2017). Deformation at Krafla and Bjarnarflag geothermal areas, Northern Volcanic Zone of Iceland, 1993–2015. *Journal of Volcanology and Geothermal Research*, *344*, 92–105. https://doi.org/10.1016/j.jvolgeores.2017.06.013

Ducrocq, C., Geirsson, H., Árnadóttir, T., Juncu, D., Drouin, V., Gunnarsson, G., et al. (2021). Inflation-Deflation Episodes in the Hengill and Hrómundartindur Volcanic Complexes, SW Iceland. *Frontiers in Earth Science*, *9*, 725109. https://doi.org/10.3389/feart.2021.725109

Dzurisin, D. (2006). *Volcano Deformation*. Berlin, Heidelberg: Springer Berlin Heidelberg. https://doi.org/10.1007/978-3-540-49302-0

Dzurisin, D., Lu, Z., Poland, M. P., and Wicks, C. W. (2019). Space-Based Imaging Radar Studies of U.S. Volcanoes. *Frontiers in Earth Science*, *6*, 249. https://doi.org/10.3389/feart.2018.00249

Eibl, E. P. S., Thordarson, T., Höskuldsson, Á., Gudnason, E. Á., Dietrich, T., Hersir, G. P., and Ágústsdóttir, T. (2023). Evolving shallow conduit revealed by tremor and vent activity observations during episodic lava fountaining of the 2021 Geldingadalir eruption, Iceland. *Bulletin of Volcanology*, *85*(2), 10. https://doi.org/10.1007/s00445-022-01622-z

Eibl, E. P. S., Moreland, W. M., Thordarson, T., Höskuldsson, Á., Gudnason, E. Á., Hersir, G. P., and Ágústsdóttir, T. (2024, March 8). Overview of the shallow magma

reservoir, conduit properties and effusion style throughout the 2021 eruption near Fagradalsfjall, Iceland. https://doi.org/10.5194/egusphere-egu24-11019

Einarsson, P. (1978). S-wave shadows in the Krafla Caldera in NE-Iceland, evidence for a magma chamber in the crust. *Bulletin Volcanologique*, *41*(3), 187–195. https://doi.org/10.1007/BF02597222

Einarsson, Páll. (2008). Plate boundaries, rifts and transforms in Iceland. *Jökull*, *58*(1), 35–58. https://doi.org/10.33799/jokull2008.58.035

Einarsson, P. (1991). The Krafla rifting episode 1975-1989, in Náttúra Mývatns, eds A. Garðarsson and A. Einarsson, Reykjavík: Icelandic Nature Science Society, 97–139.

Einarsson, P., and Brandsdottir, B. (1978). *Seismological evidence for Lateral magma intrusion during the July 1978 deflation of the Krafla volcano in NE-Iceland* (No. UI-79-9-7, 890964) (p. UI-79-9-7, 890964). https://doi.org/10.2172/890964

Elders, W. A., Friðleifsson, G. Ó., Zierenberg, R. A., Pope, E. C., Mortensen, A. K., Guðmundsson, Á., et al. (2011). Origin of a rhyolite that intruded a geothermal well while drilling at the Krafla volcano, Iceland. *Geology*, *39*(3), 231–234. https://doi.org/10.1130/G31393.1

Ellis, S. M., Wilson, C. J. N., Bannister, S., Bibby, H. M., Heise, W., Wallace, L., and Patterson, N. (2007). A future magma inflation event under the rhyolitic Taupo volcano, New Zealand: Numerical models based on constraints from geochemical, geological, and geophysical data. *Journal of Volcanology and Geothermal Research*, *168*(1–4), 1–27. https://doi.org/10.1016/j.jvolgeores.2007.06.004

Felpeto, A., Araña, V., Ortiz, R., Astiz, M., and García, A. (2001). Assessment and Modelling of Lava Flow Hazard on Lanzarote (Canary Islands). *Natural Hazards*, *23*(2/3), 247–257. https://doi.org/10.1023/A:1011112330766

Ferretti, A., Prati, C., and Rocca, F. (2000). Nonlinear subsidence rate estimation using permanent scatterers in differential SAR interferometry. *IEEE Transactions on Geoscience and Remote Sensing*, *38*(5), 2202–2212. https://doi.org/10.1109/36.868878

Fialko, Y., Khazan, Y., and Simons, M. (2001). Deformation due to a pressurized horizontal circular crack in an elastic half-space, with applications to volcano geodesy. *Geophysical Journal International*, *146*(1), 181–190. https://doi.org/10.1046/j.1365-246X.2001.00452.x

Flóvenz, Ó. G., Wang, R., Hersir, G. P., Dahm, T., Hainzl, S., Vassileva, M., et al. (2022). Cyclical geothermal unrest as a precursor to Iceland's 2021 Fagradalsfjall eruption. *Nature Geoscience*, *15*(5), 397–404. https://doi.org/10.1038/s41561-022-00930-5

Foulger, G., Bilham, R., Morgan, W. J., and Einarsson, P. (1987). The Iceland GPS Geodetic Field Campain 1986. *Eos, Transactions American Geophysical Union*, *68*(52), 1809–1818. https://doi.org/10.1029/EO068i052p01809-02

Fournier, N., and Chardot, L. (2012). Understanding volcano hydrothermal unrest from geodetic observations: Insights from numerical modeling and application to White Island volcano, New Zealand. *Journal of Geophysical Research: Solid Earth*, *117*(B11), 2012JB009469. https://doi.org/10.1029/2012JB009469

Frehner, M., Schmalholz, S. M., Saenger, E. H., and Steeb, H. (2008). Comparison of finite difference and finite element methods for simulating two-dimensional

scattering of elastic waves. *Physics of the Earth and Planetary Interiors*, *171*(1–4), 112–121. https://doi.org/10.1016/j.pepi.2008.07.003

Freire, S., Florczyk, A., Pesaresi, M., and Sliuzas, R. (2019a). An Improved Global Analysis of Population Distribution in Proximity to Active Volcanoes, 1975–2015. *ISPRS International Journal of Geo-Information*, *8*(8), 341. https://doi.org/10.3390/ijgi8080341

Freire, S., Florczyk, A., Pesaresi, M., and Sliuzas, R. (2019b). An Improved Global Analysis of Population Distribution in Proximity to Active Volcanoes, 1975–2015. *ISPRS International Journal of Geo-Information*, *8*(8), 341. https://doi.org/10.3390/ijgi8080341

Freymueller, J. (2017). Geodynamics. In P. J. G. Teunissen and O. Montenbruck (Eds.), *Springer Handbook of Global Navigation Satellite Systems* (pp. 1063–1106). Cham: Springer International Publishing. https://doi.org/10.1007/978-3-319-42928-1_37

Geirsson, H., Árnadóttir, T., Völksen, C., Jiang, W., Sturkell, E., Villemin, T., et al. (2006). Current plate movements across the Mid-Atlantic Ridge determined from 5 years of continuous GPS measurements in Iceland. *Journal of Geophysical Research: Solid Earth*, *111*(B9), 2005JB003717. https://doi.org/10.1029/2005JB003717

Geirsson, H., Valsson, G., Ófeigsson, B. G., Sturkell, E., Arnadottir, T., LaFemina, P. C., et al. (2020, March 23). Significant temporal changes in glacio isostatic adjustment in Iceland during the 1950s to present. https://doi.org/10.5194/egusphere-egu2020-17390

Geirsson, H., Parks, M., Vogfjörd, K., Einarsson, P., Sigmundsson, F., Jónsdóttir, K., et al. (2021). The 2020 volcano-tectonic unrest at Reykjanes Peninsula, Iceland: stress triggering and reactivation of several volcanic systems. https://doi.org/10.5194/egusphere-egu21-7534

Geirsson, H., Árnadóttir, T., Hreinsdóttir, S., Decriem, J., LaFemina, P. C., Jónsson, S., ... and Sveinbjörnsson, H. (2010). Overview of results from continuous GPS observations in Iceland from 1995 to 2010. *Jökull*, *60*, 3-22.

Geng, J. (2024). Technical aspects of GNSS data processing. Chapter 2 in GNSS Monitoring of the Terrestrial Environment. Editors: Aoki Y., Kreemer C. https://doi.org/10. 1016/ B978-0-323-95507-2. 00013-X

Geng, J., Chen, X., Pan, Y., Mao, S., Li, C., Zhou, J., and Zhang, K. (2019). PRIDE PPP-AR: an open-source software for GPS PPP ambiguity resolution. *GPS Solutions*, *23*(4), 91. https://doi.org/10.1007/s10291-019-0888-1

Giorgi, G., Schmidt, T. D., Trainotti, C., Mata-Calvo, R., Fuchs, C., Hoque, M. M., et al. (2019). Advanced technologies for satellite navigation and geodesy. *Advances in Space Research*, *64*(6), 1256–1273. https://doi.org/10.1016/j.asr.2019.06.010

Goldstein, R. M., and Werner, C. L. (1998). Radar interferogram filtering for geophysical applications. *Geophysical Research Letters*, *25*(21), 4035–4038. https://doi.org/10.1029/1998GL900033

Gottsmann, J., and Odbert, H. (2014). The effects of thermomechanical heterogeneities in island arc crust on time-dependent preeruptive stresses and the failure of an andesitic reservoir. *Journal of Geophysical Research: Solid Earth*, *119*(6), 4626–4639. https://doi.org/10.1002/2014JB011079

Gottsmann, Joachim, and Battaglia, M. (2008). Chapter 12 Deciphering Causes of Unrest at Explosive Collapse Calderas: Recent Advances and Future Challenges of Joint Time-Lapse Gravimetric and Ground Deformation Studies. In *Developments in Volcanology* (Vol. 10, pp. 417–446). Elsevier. https://doi.org/10.1016/S1871-644X(07)00012-5

Grapenthin, R., Sigmundsson, F., Geirsson, H., Árnadóttir, T., and Pinel, V. (2006). Icelandic rhythmics: Annual modulation of land elevation and plate spreading by snow load. *Geophysical Research Letters*, *33*(24), 2006GL028081. https://doi.org/10.1029/2006GL028081

Grapenthin, R., Ófeigsson, B. G., Sigmundsson, F., Sturkell, E., and Hooper, A. (2010). Pressure sources versus surface loads: Analyzing volcano deformation signal composition with an application to Hekla volcano, Iceland. *Geophysical Research Letters*, *37*(20), 2010GL044590. https://doi.org/10.1029/2010GL044590

Greenfield, T., White, R. S., and Roecker, S. (2016). The magmatic plumbing system of the Askja central volcano, Iceland, as imaged by seismic tomography. *Journal of Geophysical Research: Solid Earth*, *121*(10), 7211–7229. https://doi.org/10.1002/2016JB013163

Greiner, S. H. M., and Geirsson, H. (2024). Including a pressure dependent relation between static and dynamic elastic moduli in a Finite Element deformation model of Grímsvötn Volcano, Iceland. *Volcanica*, *7*(2), 907–924. https://doi.org/10.30909/vol.07.02.907924

Grewal, M. S., Andrews, A. P., and Bartone, C. G. (2020). *Global Navigation Satellite Systems, Inertial Navigation, and Integration* (1st ed.). Wiley. https://doi.org/10.1002/9781119547860

Guarnieri, A. M., and Prati, C. (1996). ScanSAR focusing and interferometry. *IEEE Transactions on Geoscience and Remote Sensing*, *34*(4), 1029–1038. https://doi.org/10.1109/36.508420

Gudmundsson, M. T., Larsen, G., Höskuldsson, Á., and Gylfason, Á. G. (2008). Volcanic hazards in Iceland. *Jökull*, *58*(1), 251–268. https://doi.org/10.33799/jokull2008.58.251

Guo, F., Li, X., Zhang, X., and Wang, J. (2017). The contribution of Multi-GNSS Experiment (MGEX) to precise point positioning. *Advances in Space Research*, *59*(11), 2714–2725. https://doi.org/10.1016/j.asr.2016.05.018

Halldórsson, S. A., Marshall, E. W., Caracciolo, A., Matthews, S., Bali, E., Rasmussen, M. B., et al. (2022). Rapid shifting of a deep magmatic source at Fagradalsfjall volcano, Iceland. *Nature*, *609*(7927), 529–534. https://doi.org/10.1038/s41586-022-04981-x

Hanssen, R. F. (2001). *Radar Interferometry: Data Interpretation and Error Analysis* (Vol. 2). Dordrecht: Springer Netherlands. https://doi.org/10.1007/0-306-47633-9

Hastings, W. K. (1970). Monte Carlo sampling methods using Markov chains and their applications. *Biometrika*, *57*(1), 97–109. https://doi.org/10.1093/biomet/57.1.97

Head, M., Hickey, J., Gottsmann, J., and Fournier, N. (2019). The Influence of Viscoelastic Crustal Rheologies on Volcanic Ground Deformation: Insights From Models of Pressure and Volume Change. *Journal of Geophysical Research: Solid Earth*, *124*(8), 8127–8146. https://doi.org/10.1029/2019JB017832

Head, M., Hickey, J., Gottsmann, J., and Fournier, N. (2021). Exploring the Impact of Thermally Controlled Crustal Viscosity on Volcanic Ground Deformation. *Journal*

of Geophysical Research: Solid Earth, *126*(8), e2020JB020724. https://doi.org/10.1029/2020JB020724

Henk, A. (2006). Stress and strain during fault-controlled lithospheric extension—insights from numerical experiments. *Tectonophysics*, *415*(1–4), 39–55. https://doi.org/10.1016/j.tecto.2005.11.006

Herring T., King R., McClusky S. (2010). Introduction to GAMIT/GLOBK, Massachusetts Institute of Technology. www-gpsg.mit.edu/tah/GGMatlab/ Hastings, W. K. (1970).

Hickey, J., and Gottsmann, J. (2014). Benchmarking and developing numerical Finite Element models of volcanic deformation. *Journal of Volcanology and Geothermal Research*, *280*, 126–130. https://doi.org/10.1016/j.jvolgeores.2014.05.011

Hickey, J., Gottsmann, J., Nakamichi, H., and Iguchi, M. (2016). Thermomechanical controls on magma supply and volcanic deformation: application to Aira caldera, Japan. *Scientific Reports*, *6*(1), 32691. https://doi.org/10.1038/srep32691

Hjartardóttir, Á. R., Einarsson, P., and Sigurdsson, H. (2009). The fissure swarm of the Askja volcanic system along the divergent plate boundary of N Iceland. *Bulletin of Volcanology*, *71*(9), 961–975. https://doi.org/10.1007/s00445-009-0282-x

Hjartardóttir, Á., R. (2013). Fissure swarms of the Northern volcanic Rift Zone, Iceland. PhD Thesis, University of Iceland.

Hjartardóttir, Á. R., Einarsson, P., Bramham, E., and Wright, T. J. (2012). The Krafla fissure swarm, Iceland, and its formation by rifting events. *Bulletin of Volcanology*, *74*(9), 2139–2153. https://doi.org/10.1007/s00445-012-0659-0

Hofmann-Wellenhof, Lichtenegger, and Wasle. (2008). *GNSS — Global Navigation Satellite Systems*. Vienna: Springer Vienna. https://doi.org/10.1007/978-3-211-73017-1

Hooper, A., Zebker, H., Segall, P., and Kampes, B. (2004). A new method for measuring deformation on Volcanoes and other natural terrains using InSAR Persistent Scatterers. *Geophyiscal Research Letters*, 31. 1-5. 10.1029/2004GL021737.

Hreinsdóttir S, Einarsson P, Sigmundsson F (2001) Crustal deformation at the oblique spreading Reykjanes Peninsula, SW Iceland: GPS measurements from 1993 to 1998. J Geophys Res 106:13803–13816. https://doi.org/10.1029/2001JB000428

Hreinsdóttir, S., Árnadóttir, T., Decriem, J., Geirsson, H., Tryggvason, A., Bennett, R. A., and LaFemina, P. (2009). A complex earthquake sequence captured by the continuous GPS network in SW Iceland. *Geophysical Research Letters*, *36*(12), 2009GL038391. https://doi.org/10.1029/2009GL038391

Hreinsdóttir, Sigrún, Sigmundsson, F., Roberts, M. J., Björnsson, H., Grapenthin, R., Arason, P., et al. (2014). Volcanic plume height correlated with magma-pressure change at Grímsvötn Volcano, Iceland. *Nature Geoscience*, *7*(3), 214–218. https://doi.org/10.1038/ngeo2044

Hrubcová, P., and Vavryčuk, V. (2023). Tectonic stress changes related to plate spreading prior to the 2021 Fagradalsfjall eruption in SW Iceland. *Tectonophysics*, *851*, 229761. https://doi.org/10.1016/j.tecto.2023.229761

Islam, Md. T., and Sturkell, E. (2015). Temperature-Dependent Newtonian Rheology in Advection-Convection Geodynamical Model for Plate Spreading in Eastern Volcanic Zone, Iceland. *Journal of Geoscience and Environment Protection*, *03*(05), 14–26. https://doi.org/10.4236/gep.2015.35003

Jakobsson, S., Jónasson, K., and Sigurðsson., I. A. (2008). The three igneous rock series of Iceland. *Jökull*, *58*(1), 117–138. https://doi.org/10.33799/jokull2008.58.117

Jin, S., Cardellach, E., and Xie, F. (2014a). Introduction to GNSS. In: GNSS Remote Sensing. Remote Sensing and Digital Image Processing, vol 19. Springer, Dordrecht. https://doi.org/10.1007/978-94-007-7482-7_1

Jin, S., Cardellach, E., and Xie, F. (2014b). GNSS Atmospheric and Multipath Delays. In: GNSS Remote Sensing. Remote Sensing and Digital Image Processing, vol 19. Springer, Dordrecht. https://doi.org/10.1007/978-94-007-7482-7_2

Jin, S., Van Dam, T., and Wdowinski, S. (2013). Observing and understanding the Earth system variations from space geodesy. *Journal of Geodynamics*, *72*, 1–10. https://doi.org/10.1016/j.jog.2013.08.001

Jónasson, K. (1994). Rhyolite volcanism in the Krafla central volcano, north-east Iceland. *Bulletin of Volcanology*, *56*(6–7), 516–528. https://doi.org/10.1007/BF00302832

Jónasson, Kristján. (2007). Silicic volcanism in Iceland: Composition and distribution within the active volcanic zones. *Journal of Geodynamics*, *43*(1), 101–117. https://doi.org/10.1016/j.jog.2006.09.004

Jonsson, S. (2002a). Fault Slip Distribution of the 1999 Mw 7.1 Hector Mine, California, Earthquake, Estimated from Satellite Radar and GPS Measurements. *Bulletin of the Seismological Society of America*, *92*(4), 1377–1389. https://doi.org/10.1785/0120000922

Jonsson, S. (2002b). Fault Slip Distribution of the 1999 Mw 7.1 Hector Mine, California, Earthquake, Estimated from Satellite Radar and GPS Measurements. *Bulletin of the Seismological Society of America*, *92*(4), 1377–1389. https://doi.org/10.1785/0120000922

Jónsson, S., Einarsson, P., and Sigmundsson, F. (1997). Extension across a divergent plate boundary, the Eastern Volcanic Rift Zone, south Iceland, 1967–1994, observed with GPS and electronic distance measurements. *Journal of Geophysical Research: Solid Earth*, *102*(B6), 11913–11929. https://doi.org/10.1029/96JB03893

Juncu, D., Árnadóttir, Th., Geirsson, H., Guðmundsson, G. B., Lund, B., Gunnarsson, G., et al. (2020). Injection-induced surface deformation and seismicity at the Hellisheidi geothermal field, Iceland. *Journal of Volcanology and Geothermal Research*, *391*, 106337. https://doi.org/10.1016/j.jvolgeores.2018.03.019

Kačmařík, M., Douša, J., Zus, F., Václavovic, P., Balidakis, K., Dick, G., and Wickert, J. (2019). Sensitivity of GNSS tropospheric gradients to processing options. *Annales Geophysicae*, *37*(3), 429–446. https://doi.org/10.5194/angeo-37-429-2019

Kaplan, E. D., and Hegarty, C. J. (2006). *Understanding GPS: Principles and Applications* (2nd ed.). Artech House.

Karaoğlu, Ö., Bayer, Ö., Turgay, M. B., and Browning, J. (2020). Thermomechanical interactions between crustal magma chambers in complex tectonic environments: Insights from Eastern Turkey. *Tectonophysics*, *793*, 228607. https://doi.org/10.1016/j.tecto.2020.228607

Keiding, M., Árnadóttir, T., Sturkell, E., Geirsson, H., and Lund, B. (2008). Strain accumulation along an oblique plate boundary: the Reykjanes Peninsula, southwest Iceland. *Geophysical Journal International*, *172*(2), 861–872. https://doi.org/10.1111/j.1365-246X.2007.03655.x

Kim, D., Brown, L. D., Árnason, K., Gudmundsson, Ó., Ágústsson, K., and Flóvenz, Ó. G. (2020). Magma “bright spots” mapped beneath Krafla, Iceland, using RVSP imaging of reflected waves from microearthquakes. *Journal of Volcanology and Geothermal Research*, *391*, 106365. https://doi.org/10.1016/j.jvolgeores.2018.04.022

Kobayashi, T., Morishita, Y., and Munekane, H. (2018). First detection of precursory ground inflation of a small phreatic eruption by InSAR. *Earth and Planetary Science Letters*, *491*, 244–254. https://doi.org/10.1016/j.epsl.2018.03.041

Kouba, J., and Héroux, P. (2001). Precise Point Positioning Using IGS Orbit and Clock Products. *GPS Solutions*, *5*(2), 12–28. https://doi.org/10.1007/PL00012883

LaFemina, P. C., Dixon, T. H., Malservisi, R., Árnadóttir, T., Sturkell, E., Sigmundsson, F., and Einarsson, P. (2005). Geodetic GPS measurements in south Iceland: Strain accumulation and partitioning in a propagating ridge system. *Journal of Geophysical Research: Solid Earth*, *110*(B11), 2005JB003675. https://doi.org/10.1029/2005JB003675

Lamb, O. D., Gestrich, J. E., Barnie, T. D., Jónsdóttir, K., Ducrocq, C., Shore, M. J., et al. (2022). Acoustic observations of lava fountain activity during the 2021 Fagradalsfjall eruption, Iceland. *Bulletin of Volcanology*, *84*(11), 96. https://doi.org/10.1007/s00445-022-01602-3

Lanzi, C., Drouin, V., Sigmundsson, F., Geirsson, H., Hersir, G. P., Ágústsson, K., et al. (2023). Pressure increase at the magma-hydrothermal interface at Krafla caldera, North-Iceland, 2018–2020: Magmatic processes or hydrothermal changes? *Journal of Volcanology and Geothermal Research*, *440*, 107849. https://doi.org/10.1016/j.jvolgeores.2023.107849

Lau, L., and Cross, P. (2007). Development and testing of a new ray-tracing approach to GNSS carrier-phase multipath modelling. *Journal of Geodesy*, *81*(11), 713–732. https://doi.org/10.1007/s00190-007-0139-z

Li, F. K., and Goldstein, R. M. (1990). Studies of multibaseline spaceborne interferometric synthetic aperture radars. *IEEE Transactions on Geoscience and Remote Sensing*, *28*(1), 88–97. https://doi.org/10.1109/36.45749

Li, S., Xu, W., and Li, Z. (2022a). Review of the SBAS InSAR Time-series algorithms, applications, and challenges. *Geodesy and Geodynamics*, *13*(2), 114–126. https://doi.org/10.1016/j.geog.2021.09.007

Li, S., Xu, W., and Li, Z. (2022b). Review of the SBAS InSAR Time-series algorithms, applications, and challenges. *Geodesy and Geodynamics*, *13*(2), 114–126. https://doi.org/10.1016/j.geog.2021.09.007

Li, X., Ge, M., Dai, X., Ren, X., Fritsche, M., Wickert, J., and Schuh, H. (2015). Accuracy and reliability of multi-GNSS real-time precise positioning: GPS, GLONASS, BeiDou, and Galileo. *Journal of Geodesy*, *89*(6), 607–635. https://doi.org/10.1007/s00190-015-0802-8

Li, F.K.; Goldstein, R.M. (1990). Studies of multibaseline spaceborne interferometric synthetic aperture radars, IEEE Trans. Geosci. Remote Sensing, 28, 88–96.

Liao, Y., Soule, S. A., and Jones, M. (2018). On the Mechanical Effects of Poroelastic Crystal Mush in Classical Magma Chamber Models. *Journal of Geophysical Research: Solid Earth*, *123*(11), 9376–9406. https://doi.org/10.1029/2018JB015985

Lisowski, M. (2007). Analytical volcano deformation source models. In D. Dzurisin, *Volcano Deformation* (pp. 279–304). Berlin, Heidelberg: Springer Berlin Heidelberg. https://doi.org/10.1007/978-3-540-49302-0_8

Lu, Z., and Dzurisin, D. (2014). InSAR Imaging of Aleutian Volcanoes. In Z. Lu and D. Dzurisin, *InSAR Imaging of Aleutian Volcanoes* (pp. 87–345). Berlin, Heidelberg: Springer Berlin Heidelberg. https://doi.org/10.1007/978-3-642-00348-6_6

Lu, Z., Masterlark, T., and Dzurisin, D. (2005). Interferometric synthetic aperture radar study of Okmok volcano, Alaska, 1992–2003: Magma supply dynamics and postemplacement lava flow deformation. *Journal of Geophysical Research: Solid Earth*, *110*(B2), 2004JB003148. https://doi.org/10.1029/2004JB003148

Lu, Z., and J. T. Freymueller (1998), Synthetic aperture radar interferometry coherence analysis over Katmai volcano group, Alaska, J. Geophys. Res., 103(B12), 29,887–29,894.

Lungarini, L., Troise, C., Meo, M., and De Natale, G. (2005). Finite element modelling of topographic effects on elastic ground deformation at Mt. Etna. *Journal of Volcanology and Geothermal Research*, *144*(1–4), 257–271. https://doi.org/10.1016/j.jvolgeores.2004.11.031

Lyard, F., Lefevre, F., Letellier, T., and Francis, O. (2006). Modelling the global ocean tides: modern insights from FES2004. *Ocean Dynamics*, *56*(5–6), 394–415. https://doi.org/10.1007/s10236-006-0086-x

Manconi, A., Walter, T. R., and Amelung, F. (2007). Effects of mechanical layering on volcano deformation. *Geophysical Journal International*, *170*(2), 952–958. https://doi.org/10.1111/j.1365-246X.2007.03449.x

Marshall EW, Caracciolo A, Bali E, et al (2024) The Petrology and Geochemistry of the 2021 Fagradalsfjall Eruption, Iceland: An Eruption Sourced From Multiple, Compositionally Diverse, Near-Moho Sills. AGU Advances 5:e2024AV001310. https://doi.org/10.1029/2024AV001310

Massonnet, D., and Feigl, K. L. (1998). Radar interferometry and its application to changes in the Earth's surface. *Reviews of Geophysics*, *36*(4), 441–500. https://doi.org/10.1029/97RG03139

Massonnet, D., Rossi, M., Carmona, C., Adragna, F., Peltzer, G., Feigl, K., and Rabaute, T. (1993a). The displacement field of the Landers earthquake mapped by radar interferometry. *Nature*, *364*(6433), 138–142. https://doi.org/10.1038/364138a0

Massonnet, D., Rossi, M., Carmona, C., Adragna, F., Peltzer, G., Feigl, K., and Rabaute, T. (1993b). The displacement field of the Landers earthquake mapped by radar interferometry. *Nature*, *364*(6433), 138–142. https://doi.org/10.1038/364138a0

McTigue, D. F. (1987). Elastic stress and deformation near a finite spherical magma body: Resolution of the point source paradox. *Journal of Geophysical Research: Solid Earth*, *92*(B12), 12931–12940. https://doi.org/10.1029/JB092iB12p12931

Mitchell, M. A., White, R. S., Roecker, S., and Greenfield, T. (2013). Tomographic image of melt storage beneath Askja Volcano, Iceland using local microseismicity. *Geophysical Research Letters*, *40*(19), 5040–5046. https://doi.org/10.1002/grl.50899

Mogi, K. (n.d.). Relation between the eruption of various volcanoes and the deformation of the ground surface around them. *Bulletin of Earthquake Research Institute*, *36*, 99–134.

Mortensen, A. K., Egilson, Þ., Gautason, B., Árnadóttir, S., and Guðmundsson, Á. (2014). Stratigraphy, alteration mineralogy, permeability and temperature conditions of well IDDP-1, Krafla, NE-Iceland. *Geothermics*, *49*, 31–41. https://doi.org/10.1016/j.geothermics.2013.09.013

Nicholson, H., Condomines, M., Fitton, J. G., Fallick, A. E., Gr Nvold, K., and Rogers, G. (1991). Geochemical and Isotopic Evidence for Crustal Assimilation Beneath Krafla, Iceland. *Journal of Petrology*, *32*(5), 1005–1020. https://doi.org/10.1093/petrology/32.5.1005

Nishimura, T., and Chouet, B. (2003). A numerical simulation of magma motion, crustal deformation, and seismic radiation associated with volcanic eruptions. *Geophysical Journal International*, *153*(3), 699–718. https://doi.org/10.1046/j.1365-246X.2003.01936.x

Dach, R.; Lutz, S.; Walser, P.; and Fridez, P. (2015). Bernese GNSS Software Version 5.2 [Application/pdf]. https://doi.org/10.7892/BORIS.72297

Odbert, H., Taisne, B., and Gottsmann, J. (2015). Deposit loading and its effect on co-eruptive volcano deformation. *Earth and Planetary Science Letters*, *413*, 186–196. https://doi.org/10.1016/j.epsl.2015.01.005

Okada, Y. (1985). Surface deformation due to shear and tensile faults in a half-space. *Bulletin of the Seismological Society of America*, *75*(4), 1135–1154. https://doi.org/10.1785/BSSA0750041135

Okada, Y. (1992). Internal deformation due to shear and tensile faults in a half-space. *Bulletin of the Seismological Society of America*, *82*(2), 1018–1040. https://doi.org/10.1785/BSSA0820021018

O'Hara, C. G. (2023). Estimating deformation source parameters using a 3D elastic finite element model including topography and crustal heterogeniety at Askja, Iceland. MSc thesis, University of Iceland. https://hdl.handle.net/1946/45701f

Osmanoğlu, B., Sunar, F., Wdowinski, S., and Cabral-Cano, E. (2016). Time series analysis of InSAR data: Methods and trends. *ISPRS Journal of Photogrammetry and Remote Sensing*, *115*, 90–102. https://doi.org/10.1016/j.isprsjprs.2015.10.003

Pagli, C., Wright, T. J., Ebinger, C. J., Yun, S.-H., Cann, J. R., Barnie, T., and Ayele, A. (2012). Shallow axial magma chamber at the slow-spreading Erta Ale Ridge. *Nature Geoscience*, *5*(4), 284–288. https://doi.org/10.1038/ngeo1414

Parks, M., Sigmundsson, F., Sigurðsson, Ó., Hooper, A., Hreinsdóttir, S., Ófeigsson, B., and Michalczewska, K. (2020). Deformation due to geothermal exploitation at Reykjanes, Iceland. *Journal of Volcanology and Geothermal Research*, *391*, 106438. https://doi.org/10.1016/j.jvolgeores.2018.08.016

Parks, M., Sigmundsson, F., Drouin, V., Hjartardóttir, Á. R., Geirsson, H., Hooper, A., et al. (2023). Deformation, seismicity, and monitoring response preceding and during the 2022 Fagradalsfjall eruption, Iceland. *Bulletin of Volcanology*, *85*(10), 60. https://doi.org/10.1007/s00445-023-01671-y

Parks, M. M., Sigmundsson, F., Drouin, V., Hreinsdóttir, S., Hooper, A., Yang, Y., et al. (2024). 2021–2023 Unrest and Geodetic Observations at Askja Volcano, Iceland. *Geophysical Research Letters*, *51*(4), e2023GL106730. https://doi.org/10.1029/2023GL106730

Parks M, Drouin V, Sigmundsson F, et al (2025) 2023–2024 inflation-deflation cycles at Svartsengi and repeated dike injections and eruptions at the Sundhnúkur crater

row, Reykjanes Peninsula, Iceland. Earth and Planetary Science Letters 658:119324. https://doi.org/10.1016/j.epsl.2025.119324
Parsons, T., Wu, P. C., Wei, M., and D'Hondt, S. (2023). The weight of New York City: possible contributions to subsidence from anthropogenic sources. Earth's Future, 11(5), e2022EF003465.
Pascal, K. (2013). Interaction between deformation sources and implications for numerica modelling of magma storage. Phd Thesis. University of Leeds.
Pedersen, G. B. M., Belart, J. M. C., Óskarsson, B. V., Gudmundsson, M. T., Gies, N., Högnadóttir, T., et al. (2022). Volume, Effusion Rate, and Lava Transport During the 2021 Fagradalsfjall Eruption: Results From Near Real-Time Photogrammetric Monitoring. *Geophysical Research Letters*, *49*(13), e2021GL097125. https://doi.org/10.1029/2021GL097125
Pedersen, R., Sigmundsson, F., and Masterlark, T. (2009). Rheologic controls on inter-rifting deformation of the Northern Volcanic Zone, Iceland. *Earth and Planetary Science Letters*, *281*(1–2), 14–26. https://doi.org/10.1016/j.epsl.2009.02.003
Peltier, A., Hurst, T., Scott, B., and Cayol, V. (2009). Structures involved in the vertical deformation at Lake Taupo (New Zealand) between 1979 and 2007: New insights from numerical modelling. *Journal of Volcanology and Geothermal Research*, *181*(3–4), 173–184. https://doi.org/10.1016/j.jvolgeores.2009.01.017
Pereira, M. L., Zanon, V., Fernandes, I., Pappalardo, L., and Viveiros, F. (2024). Hydrothermal alteration and physical and mechanical properties of rocks in a volcanic environment: A review. *Earth-Science Reviews*, *252*, 104754. https://doi.org/10.1016/j.earscirev.2024.104754
Petersen, G. N., Bjornsson, H., Arason, P., and Von Löwis, S. (2012). Two weather radar time series of the altitude of the volcanic plume during the May 2011 eruption of Grímsvötn, Iceland. *Earth System Science Data*, *4*(1), 121–127. https://doi.org/10.5194/essd-4-121-2012
Phillipson, G., Sobradelo, R., and Gottsmann, J. (2013). Global volcanic unrest in the 21st century: An analysis of the first decade. *Journal of Volcanology and Geothermal Research*, *264*, 183–196. https://doi.org/10.1016/j.jvolgeores.2013.08.004
Pryor, R. (2011). Multiphysics Modeling using COMSOL®: A First Principles Approach, Jones and Bartlett Publishers, Sudbury, MA.
Ranalli, G. (1995). *Rheology of the earth* (2. ed). London: Chapman and Hall.
Riddick, S. N., and Schmidt, D. A. (2011). Time-dependent changes in volcanic inflation rate near Three Sisters, Oregon, revealed by InSAR: THREE SISTERS TIME-DEPENDENT INFLATION. *Geochemistry, Geophysics, Geosystems*, *12*(12), n/a-n/a. https://doi.org/10.1029/2011GC003826
Rivalta, E., and Segall, P. (2008). Magma compressibility and the missing source for some dike intrusions. *Geophysical Research Letters*, *35*(4), 2007GL032521. https://doi.org/10.1029/2007GL032521
Ronchin, E. (2015). Finite Element Models of Volcano Deformational Systems Having Structural Complexity. PhD Thesis, Universitat de Barcelona. Departament de Geodinàmica i Geofísica.
Sæmundsson, K., Sigurgeirsson, M. Á., and Friðleifsson, G. Ó. (2020). Geology and structure of the Reykjanes volcanic system, Iceland. *Journal of Volcanology and*

Geothermal Research, *391*, 106501. https://doi.org/10.1016/j.jvolgeores.2018.11.022

Sæmundsson K. (1991). Jarðfræði Kröflukerfisins (in Icelandic). In: Garðarsson A, Einarsson Á (eds) Náttúra Mývatns. Icelandic Nature Sci. Soc., Reykjavík, 24-95.

Saemundsson, K., 1978. Fissure swarms and central volcanoes of the neovolcanic zones of Iceland. *In:* Bowes, D.R. and Leake, B.E. (eds), *Crustal Evolution in Northwestern Britain and Adjacent Regions. Geological Journal Special Issue,* ***10,*** *415-432.*

Salvi, S., Atzori, S., Tolomei, C., Allievi, J., Ferretti, A., Rocca, F., et al. (2004). Inflation rate of the Colli Albani volcanic complex retrieved by the permanent scatterers SAR interferometry technique. *Geophysical Research Letters*, *31*(12), +2004GL020253. https://doi.org/10.1029/2004GL020253

Schuler, J., Greenfield, T., White, R. S., Roecker, S. W., Brandsdóttir, B., Stock, J. M., et al. (2015). Seismic imaging of the shallow crust beneath the Krafla central volcano, NE Iceland. *Journal of Geophysical Research: Solid Earth*, *120*(10), 7156–7173. https://doi.org/10.1002/2015JB012350

Segall, P. (2010). *Earthquake and Volcano Deformation:* Princeton: Princeton University Press. https://doi.org/10.1515/9781400833856

Sigmundsson, F. (2006). Iceland Geodynamics. Springer Berlin Heidelberg. https://doi.org/10.1007/3-540-37666-6

Sigmundsson, F., Pinel, V., Lund, B., Albino, F., Pagli, C., Geirsson, H., and Sturkell, E. (2010). Climate effects on volcanism: influence on magmatic systems of loading and unloading from ice mass variations, with examples from Iceland. *Philosophical Transactions of the Royal Society A: Mathematical, Physical and Engineering Sciences*, *368*, 2519–2534. https://doi.org/10.1098/rsta.2010.0042

Sigmundsson, F., Parks, M., Hooper, A., Geirsson, H., Vogfjörd, K. S., Drouin, V., et al. (2022). Deformation and seismicity decline before the 2021 Fagradalsfjall eruption. *Nature*, *609*(7927), 523–528. https://doi.org/10.1038/s41586-022-05083-4

Sigmundsson, F., Parks, M., Geirsson, H., Hooper, A., Drouin, V., Vogfjörd, K. S., et al. (2024a). Fracturing and tectonic stress drive ultrarapid magma flow into dikes. *Science*, *383*(6688), 1228–1235. https://doi.org/10.1126/science.adn2838

Sigmundsson F., Parks M., Geirsson H., Albino F., Schmidt P., Li S., Pálsson F., Ófeigsson B. G., Drouin V., Aðalgeirsdóttir G., Magnússon E., Hooper A., Hreinsdóttir S., Maclennan J., Sturkell E. and Trasatti E., (2024b). Influence of climate change on magmatic processes. What does geodesy and modeling of geodetic tell us? Chapter 15 in GNSS Monitoring of the Terrestrial Environment. Editors: Aoki Y., Kreemer C. https://doi.org/10. 1016/ B978-0-323-95507-2. 00013-X

Sigurdsson, H., and Sparks, R. S. J. (1981). Petrology of rhyolitic and mixed magma ejecta from the 1875 eruption of Askja, Iceland. *Journal of Petrology*, *22*(1), 41-84.

Sigurdsson, H., and Sparks, R. S. J. (1978a). Rifting episode in north iceland in 1874–1875 and the eruptions of askja and sveinagja. *Bulletin Volcanologique*, *41*(3), 149–167. https://doi.org/10.1007/BF02597219

Sigurdsson, Haraldur, and Sparks, S. R. J. (1978b). Lateral magma flow within rifted Icelandic crust. *Nature*, *274*(5667), 126–130. https://doi.org/10.1038/274126a0

Sigurðsson, O. (2005). 10. Variations of termini of glaciers in Iceland in recent centuries and their connection with climate. In *Developments in Quaternary Sciences* (Vol. 5, pp. 241–255). Elsevier. https://doi.org/10.1016/S1571-0866(05)80012-0

Sigvaldason, G. (2002). Volcanic and tectonic processes coinciding with glaciation and crustal rebound: an early Holocene rhyolitic eruption in the Dyngjufjöll volcanic centre and the formation of the Askja caldera, north Iceland. *Bulletin of Volcanology*, *64*(3–4), 192–205. https://doi.org/10.1007/s00445-002-0204-7

Smith, M. (2009). *ABAQUS/Standard User's Manual, Version 6.9*. Dassault Systèmes Simulia Corp.

Soosalu, H., Key, J., White, R. S., Knox, C., Einarsson, P., and Jakobsdóttir, S. S. (2010). Lower-crustal earthquakes caused by magma movement beneath Askja volcano on the north Iceland rift. *Bulletin of Volcanology*, *72*(1), 55–62. https://doi.org/10.1007/s00445-009-0297-3

Sparks, R. S. J., and Cashman, K. V. (2017). Dynamic Magma Systems: Implications for Forecasting Volcanic Activity. *Elements*, *13*(1), 35–40. https://doi.org/10.2113/gselements.13.1.35

Stefánsson, V., 1981. The Krafla geothermal field, Northeast Iceland. In: Geothermal Systems: Principles and Case Histories, pp. 273–293. Chapter 10.

Sturkell E, Sigmundsson F, Einarsson P, Bilham R (1994) Strain accumulation 1986–1992 across the Reykjanes Peninsula Plate Boundary, Iceland, determined from GPS measurements. Geophysical Research Letters 21:125–128. https://doi.org/10.1029/93GL03421

Sturkell, E., Sigmundsson, F., and Slunga, R. (2006). 1983–2003 decaying rate of deflation at Askja caldera: Pressure decrease in an extensive magma plumbing system at a spreading plate boundary. *Bulletin of Volcanology*, *68*(7–8), 727–735. https://doi.org/10.1007/s00445-005-0046-1

Sturkell, E., Sigmundsson, F., Geirsson, H., Ólafsson, H., and Theodórsson, T. (2008). Multiple volcano deformation sources in a post-rifting period: 1989–2005 behaviour of Krafla, Iceland constrained by levelling, tilt and GPS observations. *Journal of Volcanology and Geothermal Research*, *177*(2), 405–417. https://doi.org/10.1016/j.jvolgeores.2008.06.013

Takajo, H., and Takahashi, T., (1988). Least-squares phase estimation from the phase difference. J. Opt. Soc. Am. A **5**, 416-425.

Taylor, N. C., Johnson, J. H., and Herd, R. A. (2021). Making the most of the Mogi model: Size matters. *Journal of Volcanology and Geothermal Research*, *419*, 107380. https://doi.org/10.1016/j.jvolgeores.2021.107380

Tarricone, J., Webb, R. W., Marshall, H. P., Nolin, A. W., and Meyer, F. J. (2022). Estimating snow accumulation and ablation with L-band InSAR. The Cryosphere Discussions, 2022, 1-33.

Teunissen, P. J. G. (1998). GPS Carrier Phase Ambiguity Fixing Concepts. In P. J. G. Teunissen and A. Kleusberg (Eds.), *GPS for Geodesy* (pp. 319–388). Berlin, Heidelberg: Springer Berlin Heidelberg. https://doi.org/10.1007/978-3-642-72011-6_8

Teunissen, P. J. G. (2020). GNSS Precise Point Positioning. In Y. T. J. Morton, F. Diggelen, J. J. Spilker, B. W. Parkinson, S. Lo, and G. Gao (Eds.), *Position, Navigation, and Timing Technologies in the 21st Century* (1st ed., pp. 503–528). Wiley. https://doi.org/10.1002/9781119458449.ch20

Thorarinsson, S., and Sigvaldason, G. E. (1962). The eruption in Askja, 1961; a preliminary report. *American Journal of Science*, *260*(9), 641–651. https://doi.org/10.2475/ajs.260.9.641

Thordarson, T., and Larsen, G. (2007). Volcanism in Iceland in historical time: Volcano types, eruption styles and eruptive history. *Journal of Geodynamics*, *43*(1), 118–152. https://doi.org/10.1016/j.jog.2006.09.005

Thordarson, Thorvaldur, and Höskuldsson, Á. (2008). Postglacial volcanism in Iceland. *Jökull*, *58*(1), 197–228. https://doi.org/10.33799/jokull2008.58.197

Trasatti, E., Giunchi, C., and Bonafede, M. (2003). Effects of topography and rheological layering on ground deformation in volcanic regions. *Journal of Volcanology and Geothermal Research*, *122*(1–2), 89–110. https://doi.org/10.1016/S0377-0273(02)00473-0

Trasatti, Elisa. (2022). Volcanic and Seismic Source Modeling: An Open Tool for Geodetic Data Modeling. *Frontiers in Earth Science*, *10*, 917222. https://doi.org/10.3389/feart.2022.917222

Tryggvason, E. (1994). Surface deformation at the Krafla volcano, North Iceland, 1982–1992. *Bulletin of Volcanology*, *56*(2), 98–107. https://doi.org/10.1007/BF00304105

Tryggvason, E. (1985). Multiple magma reservoirs in a rift zone volcano: Ground deformation and magma transport during the September 1984 eruption of Krafla, Iceland." *Journal of Volcanology and Geothermal Research* 28.1-2 : 1-44

Tryggvason, E. (1973). Seismicity, earthquake swarms, and plate boundaries in the Iceland region. Bulletin of the Seismological Society of America, *63*(4), 1327-1348

Uhlemann, M., Gendt, G., Ramatschi, M., and Deng, Z. (2015). GFZ Global Multi-GNSS Network and Data Processing Results. In C. Rizos and P. Willis (Eds.), *IAG 150 Years* (Vol. 143, pp. 673–679). Cham: Springer International Publishing. https://doi.org/10.1007/1345_2015_120

Vasco, D. W., Rucci, A., Ferretti, A., Novali, F., Bissell, R. C., Ringrose, P. S., et al. (2010). Satellite-based measurements of surface deformation reveal fluid flow associated with the geological storage of carbon dioxide. *Geophysical Research Letters*, *37*(3), 2009GL041544. https://doi.org/10.1029/2009GL041544

Wauthier, C., Cayol, V., Poland, M., Kervyn, F., d'Oreye, N., Hooper, A., et al. (2013). Nyamulagira's magma plumbing system inferred from 15 years of InSAR. *Geological Society, London, Special Publications*, *380*(1), 39–65. https://doi.org/10.1144/SP380.9

Williams-Jones G, Rymer H (2015) Hazards of Volcanic Gases. In: The Encyclopedia of Volcanoes. Elsevier, pp 985–992

Wittmann, W., Sigmundsson, F., Dumont, S., and Lavallée, Y. (2017). Post-emplacement cooling and contraction of lava flows: InSAR observations and a thermal model for lava fields at Hekla volcano, Iceland. *Journal of Geophysical Research: Solid Earth*, *122*(2), 946–965. https://doi.org/10.1002/2016JB013444

Wright, T. J., Sigmundsson, F., Pagli, C., Belachew, M., Hamling, I. J., Brandsdóttir, B., et al. (2012). Geophysical constraints on the dynamics of spreading centres from rifting episodes on land. *Nature Geoscience*, *5*(4), 242–250. https://doi.org/10.1038/ngeo1428

Yang, X., Davis, P. M., and Dieterich, J. H. (1988). Deformation from inflation of a dipping finite prolate spheroid in an elastic half-space as a model for volcanic

stressing. *Journal of Geophysical Research: Solid Earth*, *93*(B5), 4249–4257. https://doi.org/10.1029/JB093iB05p04249

Ye, X., Kaufmann, H., and Guo, X. F. (2004). Landslide Monitoring in the Three Gorges Area Using D-INSAR and Corner Reflectors. *Photogrammetric Engineering and Remote Sensing*, *70*(10), 1167–1172. https://doi.org/10.14358/PERS.70.10.1167

You, X., and Yuan, L. (2021). The sensitivity of ocean tide loading displacements to the structure of the upper mantle and crust of Taiwan Island. *Earth, Planets and Space*, *73*(1), 193. https://doi.org/10.1186/s40623-021-01525-x

Xu, X., Sandwell, D.T., and Smith-Konter, B., (2020). Coseismic Displacements and Surface Fractures from Sentinel-1 InSAR: 2019 Ridgecrest Earthquakes. Seismological Research Letters 91, 1979–1985. https://doi.org/10.1785/0220190275

Zhao, S., McClusky, S., Cummins, P.R., and Miller, M.S. (2024). Co-seismic and post-seismic deformation associated with the 2018 Lombok, Indonesia, earthquake sequence, inferred from InSAR and seismic data analysis. Remote Sensing of Environment 304, 114063. https://doi.org/10.1016/j.rse.2024.114063

Zebker, H.A., and Villasenor, J. (1992). Decorrelation in interferometric radar echoes. *IEEE Transactions on Geoscience and Remote Sensing*, *30*(5), 950–959. https://doi.org/10.1109/36.175330

Zebker, Howard A., Rosen, P. A., Goldstein, R. M., Gabriel, A., and Werner, C. L. (1994). On the derivation of coseismic displacement fields using differential radar interferometry: The Landers earthquake. *Journal of Geophysical Research: Solid Earth*, *99*(B10), 19617–19634. https://doi.org/10.1029/94JB01179

Zumberge, J. F., Heflin, M. B., Jefferson, D. C., Watkins, M. M., and Webb, F. H. (1997). Precise point positioning for the efficient and robust analysis of GPS data from large networks. *Journal of Geophysical Research: Solid Earth*, *102*(B3), 5005–5017. https://doi.org/10.1029/96JB03860

Paper I

Pressure increase at the magma-hydrothermal interface at Krafla caldera, North-Iceland, 2018–2020: Magmatic processes or hydrothermal changes?

Chiara Lanzi, Vincent Drouin, Freysteinn Sigmundsson, Halldór Geirsson, Gylfi Páll Hersir, Kristján Ágústsson, Michelle Maree Parks, Sigrún Hreinsdóttir, Ásgrímur Guðmundsson

Journal of Volcanology and Geothermal Research

https://doi.org/10.1016/j.jvolgeores.2023.107849

Journal of Volcanology and Geothermal Research 440 (2023) 107849

Contents lists available at ScienceDirect

Journal of Volcanology and Geothermal Research

journal homepage: www.journals.elsevier.com/journal-of-volcanology-and-geothermal-research

Pressure increase at the magma-hydrothermal interface at Krafla caldera, North-Iceland, 2018–2020: Magmatic processes or hydrothermal changes?

Chiara Lanzi [a,*], Vincent Drouin [b], Freysteinn Sigmundsson [a], Halldór Geirsson [a], Gylfi Páll Hersir [c,f], Kristján Ágústsson [c,f], Michelle Maree Parks [b], Sigrún Hreinsdóttir [d], Ásgrímur Guðmundsson [e,f]

[a] Nordic Volcanological Center, Institute of Earth Sciences, University of Iceland
[b] Icelandic Meteorological Office, Reykjavik, Iceland
[c] ÍSOR – Iceland GeoSurvey, Reykjavik, Iceland
[d] GNS Science, Lower Hutt, New Zealand
[e] Landsvirkjun, Reykjavik, Iceland
[f] Presently: Independent researcher, Reykjavík, Iceland

ARTICLE INFO

Keywords:
Krafla caldera
Magma-hydrothermal interface
Finite Element Method modelling
Crustal heterogeneity

ABSTRACT

Following volcano deflation since 1989, the deformation pattern in Krafla caldera, North Iceland, changed in 2018. Geodetic measurements reveal a difference in surface velocity fields for 2015–2018 and 2018–2020 periods, reflecting a change in the deformation pattern. The difference velocity field broadly fits deformation caused by a spherical pressure source within a uniform elastic half-space, with a volume change of 2.6–3.8 $\times 10^5$ m^3/yr and centre depth of 2.1–2.5 km, which is close to the brittle-ductile boundary in the area, at a depth of 1.8 to 2.2 km. Potential processes causing the deformation change are evaluated: magmatic processes such as magma inflow or accumulation of volcanic gas, changes in the geothermal area because of change in geothermal production, or a combination of these. In particular, we evaluate if the change in deformation may relate to about 0.1 MPa/yr pressure increase in the geothermal system as measurements in monitoring well KG-10 indicate, eventually due to changes in the geothermal exploitation strategy at the Krafla power plant. Modelling shows that inferred volume change may be due to a spherical source with 1.4 km radius with 0.1 MPa/yr pressure change if the surrounding crust has a Young's modulus E of about 7 GPa. However, the average regional Young's modulus for the upper crust in Iceland has been estimated to be 30 GPa. We use the Finite Element Method (FEM) to assess the influence on the displacement due to the presence of a local crustal volume 5 × 5 × 4 km (horizontal dimensions × depth), which envelops the source (within the Krafla caldera), with $E = 7$ GPa in the central area and 30 GPa in the far field, in a three-dimensional model. Such a model can reproduce significant features of the observed deformation. There are no changes in seismicity in 2018. In late 2019, the earthquake rate increases following a slight decrease over few months. The seismic moment release is relatively steady until the end of 2019, when the rate increases and is relatively constant in 2020. Gravity measurements in late 2019, when compared to limited measurements in 2018, are inconclusive regarding the nature of the deformation, but useful for further monitoring. No noticeable changes have been observed in the chemical composition of fumarole discharge in the Krafla field that relate to new intrusions.

1. Introduction

1.1. Tectonic setting and geology

The Krafla volcanic system in North Iceland is located at the divergent Eurasian North-American plate boundary. The volcanic system consists of a central volcano with a 9 × 7 km wide caldera (Fig. 1), and a transecting fissure swarm, about 5–8 km wide and extending 40 km to the south and 50 km to the north from the caldera (e.g., Hjartardóttir et al., 2012). The caldera, formed about 100,000 years ago (Sæmundsson, 1991), is filled with eruptive products.

The volcanic activity at Krafla has a bimodal behaviour

* Corresponding author.
E-mail address: chl7@hi.is (C. Lanzi).

https://doi.org/10.1016/j.jvolgeores.2023.107849
Received 17 February 2023; Received in revised form 20 June 2023; Accepted 21 June 2023
Available online 24 June 2023

(Sæmundsson, 1991; Nicholson et al., 1991; Jónasson, 1994). The volcanic products are dominantly basalts erupted during rifting episodes. Rhyolitic eruptions also occur and in 2009 such magma was encountered during drilling of the IDDP-1 well of the Iceland Deep Drilling Project (see Fig. 1 for location). The IDDP-1 well was intended to reach the margin of a basaltic magma storage at 4–5 km depth to explore supercritical hydrothermal fluids conditions but was drilled into a hot (900 °C), high-silica (76.5% SiO_2) rhyolite melt at 2.1 km depth (Elders et al., 2011; Pope et al., 2013; Zierenberg et al., 2013; Friðleifsson et al., 2014a, 2014b). In 2008, well KJ-39, located some 2 km south-east of IDDP-1 well, encountered magma as well. During drilling of that well, fresh silicic glass (indicative of quenched liquid magma) was recovered at ~2.5 km depth (Mortensen et al., 2010). Petrology studies inferred that the Krafla rhyolites formed by partial melting of hydrothermally altered crustal rocks (Jónasson, 1994). Zierenberg et al. (2013) came to the same conclusion from studies of major and minor element composition of the IDDP-1 melt samples, whereas Rooyakkers et al. (2021) suggests that stalling and crystallization of evolved basalts at shallow

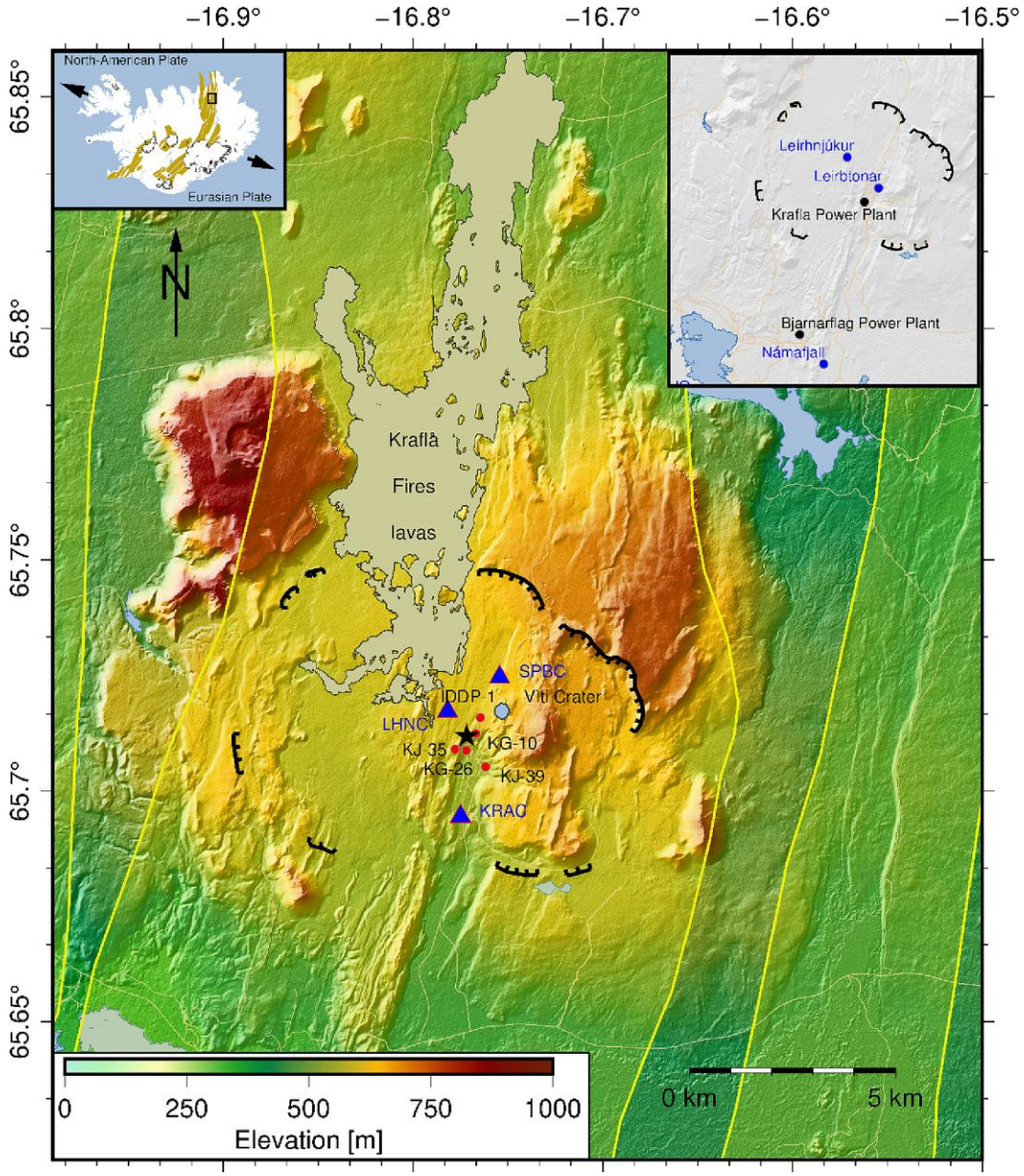

Fig. 1. Study area. Outline of the Krafla caldera (hatched lines) and topography. Location of selected wells are shown with red circles (IDDP-1, KG-10, KJ-35, KG-26 and KJ-39), and blue triangles show locations of continuous GNSS stations at Krafla. The black staris the best-fit location for a point source of pressure consistent with the deformation data. Insert map on upper left shows the location of the Krafla area in North Iceland and the plate boundary (fissure swarms with yellow shading). Insert map on the upper right shows the location of the Bjarnarflag and Krafla power plants, and the Leirhjúkur and Leirbtonar geothermal fields. (For interpretation of the references to colour in this figure legend, the reader is referred to the web version of this article.)

depths forms crystal mush from which evolved melts (e.g., rhyolites) are extracted. The drilling of IDDP-1 showed the existence of a near-liquidus magma body capped by a magma-hydrothermal interface. With an inferred heat flux of ≥16 W/m^2, Eichelberger (2020) predicts a crystallization rate of 0.6 m/yr, but nevertheless no evidence was found for crystallization nor the development of a mush zone at the base of the magma-hydrothermal boundary. On the contrary, it was inferred that the lower part of the magma-hydrothermal boundary is undergoing partial melting. Based on that, it has been suggested that Krafla's rhyolite body is convective and delivering both heat and H_2O but not crystals to its ceiling (Eichelberger, 2020).

The presence of magma in the crust beneath the Krafla caldera was initially inferred from seismic shear wave shadows observed by Einarsson (1978) at 4–7 km depth. Furthermore, the lower crust, 11–14 km depth, beneath the volcano is characterized by a 40 km-wide high velocity dome narrowing upward where an inferred magma chamber lies at ~3 km depth (Brandsdóttir et al., 1997). Earthquakes originating in the Tjörnes Fracture Zone, observed on the local Krafla seismic network, have a steep ray path showing a shear wave shadow but have not been investigated in detail (Ágústsson et al., 2012). Kim et al. (2020) revealed the presence of a strong reflector at depths corresponding to the magma encountered by the IDDP-1 drillhole at a depth of 2.1 km. Similar reflectors are present in the caldera at depths ranging from 4 to 6 km, interpreted as a distributed system of magmatic sills rather than a single large body of magma. A vertical seismic profile (VSP) experiment in wells K-18 and K-26 in Krafla indicates a seismic reflector at 2.3 km depth which may relate to the brittle-ductile transition or the top of a possible magma body, with a zone of low reflectivity below. The bottom of the low reflectivity zone is inferred at 3.3 km depth, which may indicate the bottom of the proposed magma body (Schuler et al., 2015; Kästner et al., 2018; Reiser et al., 2020).

The Krafla volcanic system has two high temperature geothermal systems: the Krafla geothermal area located in the caldera, and the Námafjall geothermal area located about 9 km kilometres SSW of the Krafla geothermal area (Sæmundsson et al., 1971; Ármannsson et al., 1987). The presence of magmatic heat, fluids and permeability led to hydrothermal systems, enabling geothermal utilization. Currently, two power plants are operated in the area by Landsvirkjun, the National Power Company of Iceland. Electricity generation at Námafjall started in 1969 with a capacity of 3 MW. The primary one, the Krafla power plant began operation in 1977 with an initial production of 7 MW, but in 1985 the unit 1 was fulfilled with 30 MW electricity production. In 1996, a second turbine was installed to reach the current capacity of 60 MW (Nielsen et al., 2000). Based on ground resistivity measurements (DC, TEM and MT measurements), the area of the Krafla geothermal field has been estimated to be around 40 km^2 (Árnason and Magnússon, 2001; Mortensen et al., 2014; Árnason, 2020), divided into different sub-fields. The largest one is the Leirbotnar field, in the middle of the Krafla caldera. It has an upper liquid-dominated (190–220 °C) reservoir, extending down to 1.0–1.4 km depth, separated by a relatively impermeable zone (Gudmundsson and Mortensen, 2015) from a lower reservoir of high-temperature (280–340 °C) fluid and steam down to at least 2.2 km (Stefánsson, 1981; Boðvarsson et al., 1984; Ármannsson et al., 1987; Mortensen et al., 2014). Fluid temperature is controlled in the lower reservoir at depth at the boiling temperature, but superheated steam has been encountered in some wells (Guðmundsson et al., 2008; Einarsson et al., 2010; Gudmundsson and Mortensen, 2015).

1.2. Crustal deformation in the Northern Volcanic Zone

Crustal deformation in the Krafla area is influenced by the regional plate spreading processes across the Northern Volcanic Zone (NVZ) of Iceland (e.g., Sigmundsson et al., 2020). Global plate motion models show divergence of the Eurasian plate and the North American plate in the Krafla area at a rate of 18 ± 0.4 mm/yr in the direction N104.5°E (DeMets et al., 2010). Global Navigation and Satellite System (GNSS) geodetic observations in North Iceland in the 1997–2014 period, give a comparable spreading rate and reveal how strain and displacements are distributed across the plate boundary deformation zone (Drouin et al., 2017; Drouin and Sigmundsson, 2019).

During the last 300 years, several major rifting episodes have occurred in the area. The most recent one is known as the Krafla Fires in 1975–1984 (e.g., Björnsson et al., 1977). In summer 1975, an increase in seismicity indicated magma movement below the Krafla caldera (Einarsson, 1991). Between December 1975 and September 1984, about twenty inflation/deflation cycles occurred, nine of which were associated with an eruption (Björnsson et al., 1985; Einarsson and Brandsdóttir, 1980). Each cycle was characterized by gradual inflation, followed by sudden subsidence in the caldera (up to 1–2 m) when dikes propagated laterally, with associated widening of the Krafla fissure swarm in relation to release of tectonic stresses (Buck et al., 2006). The gradual inflation between deflation events of the caldera was up 7–10 mm/day, interpreted to be caused by about 5 m^3/s inflow of magma into a magma chamber with a centre depth of approximately 3 km (e. g., Björnsson et al., 1979).

GNSS measurements in 1987 and 1990 showed a horizontal spreading rate about three times higher than the average spreading rate in North Iceland, attributed to post-rifting stress relaxation following the Krafla Fires (Foulger et al., 1992; Heki et al., 1993; Jónasson, 1994; Pollitz and Sacks, 1996). Additional measurements in 1993 and 1995 found, however, that the rate of spreading was then back to the long-term average of global plate models (Völksen, 2000; Árnadóttir et al., 2009). A deflating signal, in the 1992–1995 period, with modelled source at a depth of 2.4 km in the middle of the caldera, was suggested to be caused by cooling contraction or magma drainage (Sigmundsson et al., 1997; Rymer et al., 1998). An inflating point-pressure source was located about 9 km north of the caldera, at a depth of 21 km, based on interferometric analysis of synthetic aperture radar satellite images (InSAR) from 1993 to 1999 (De Zeeuw-van Dalfsen et al., 2004). It was interpreted as accumulation of magma in a deep source. Alternate interpretation of the same data by Ali et al. (2014) suggests viscoelastic relaxation following the Krafla Fires. Rifting and post-rifting deformation in similar geodynamic setting has been observed at the Dabbahu rift in the Afar region, Ethiopia (Nooner et al., 2009; Wright et al., 2012; Hamling et al., 2014).

The vertical pattern of deformation within the Krafla caldera in the post-eruptive period after the Krafla Fires was consistent with inflation until 1989, followed by deflation for almost three decades (Drouin et al., 2017) until 2018. An exponentially decaying subsidence rate was inferred with a rate of ~5 cm/yr in 1989–1992 (Tryggvason, 1994), declining to about 3 mm/yr in 2005. Sturkell et al. (2008) interpreted the subsidence in terms of the volume contraction of a magma body at ~2.5 km depth below the Leirhjúkur area, caused by cooling and draining of a shallow magma body, and another point-pressure source, at ~1.5 km depth in the Leirbotnar field, due to geothermal exploitation. Drouin et al. (2017) estimated a volume contraction of 6.6×10^5 m^3/yr for a point-source at a similar location as the one found by Sturkell et al. (2008), related to geothermal exploitation in the 1993–2015 period. The deformation pattern at Krafla changed in 2018 (Fig. 2). Hersir et al. (2020) studied seismic, gravity, GNSS and InSAR data in relation to this change, and compared with changes in geothermal utilization. Geothermal processes could either relate to natural processes or be due to changes in the geothermal utilization since the amount of fluid extraction and the amount and locations of fluid re-injection in wells have changed in recent years. Hersir et al. (2020) concluded that the deformation change could be either due to magmatic or geothermal processes or a combination of both.

Here we evaluate the local deformation in the Krafla area during the 2015–2020 period and the processes involved, following the work carried out by Hersir et al. (2020). The observed deformation field is, initially, modelled analytically, considering a point-pressure source within an elastic and homogeneous half-space (Mogi, 1958). Several

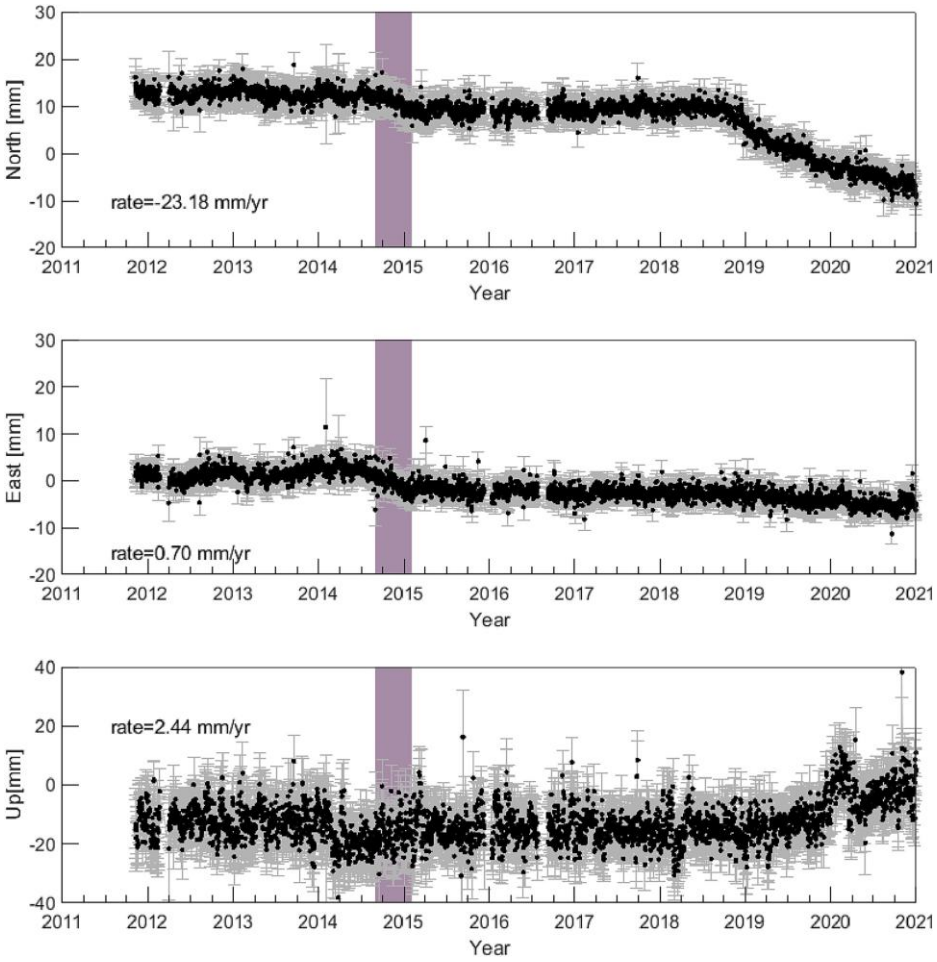

Fig. 2. KRAC GNSS station time series. Linear trends as well as annual and semi-annual terms have been estimated and removed. The station is located directly southwards of the inferred centre of main deformation. The rate of the linear trend removed for each component is indicated on the plot. The purple background shadow indicates when the Bárðarbunga-Holuhraun diking and eruption occurred in 2014–2015. (For interpretation of the references to colour in this figure legend, the reader is referred to the web version of this article.)

studies have investigated how rheological variations in rock properties can strongly influence the interpretation of ground deformation (Trasatti et al., 2003; Masterlark et al., 2010; Del Negro et al., 2009; Hickey and Gottsmann, 2014; Yamasaki et al., 2019). We therefore employ the Finite Element method (FEM) to calculate surface deformation pattern for a pressurized spherical source, at fixed depth, enveloped by a volume to account for eventual low rigidity crustal materials within the Krafla caldera and higher rigidity in the far-field. To model appropriate crustal material properties, we consider earlier studies of regional rigidity in Iceland that found rigidity of ~30 GPa in the 0–15 km depth range based on geodetic and seismological observations (Supplementary Text S1). The aim is to provide new insight in how elastic parameters influence deformation, to improve understanding of magmatic and hydrothermal processes, and their interaction in relation to natural and/or anthropogenic processes.

2. Observed ground deformation, seismic, gravimetric and hydrological changes

2.1. GNSS

A dense local GNSS network was measured at Krafla every few years beginning in 1986 (when the first GNSS survey was carried out in North Iceland) until 2008, and on a yearly basis since 2012 (Drouin et al., 2017 and references therein). The network consists of >25 campaign GNSS stations within or nearby the Krafla caldera. The continuous GNSS KRAC station (see Fig. 1 for location) was installed in 2011 near the Krafla power plant. Two additional continuous GNSS stations were installed in November 2019 within the caldera: LHNC, east of Leirhnjúkur and SPBC north of the Víti crater (Hersir et al., 2020). We analyse the continuous and campaign GNSS data available with the GAMIT/GLOBK software (Herring et al., 2010) and the GIPSY/OASIS II software (Zumberge et al., 1997). Each campaign GNSS station is measured for ~36–48 h, sampling data every 15 s. Site positions are evaluated in the IGb14 reference frame using over 100 worldwide reference stations. The data are corrected for ocean tidal loading using the FES2004 model (Lyard et al., 2006). Velocities were initially estimated in the IGb14 reference frame

and then converted into velocities relative to the Eurasian plate using the plate motion model of Altamimi et al. (2017).

After the time series of KRAC is detrended, and annual and semi-annual variations estimated and removed, a clear change in the north component of displacement in 2018 is evident (Fig. 2). The detrended time series shows southward movement beginning around middle of 2018 with an initial rate of −9 mm/yr until ~2019.7. Thereafter, the rate slows down to about −4.9 mm/yr from ~2019.7 to end-2020. The

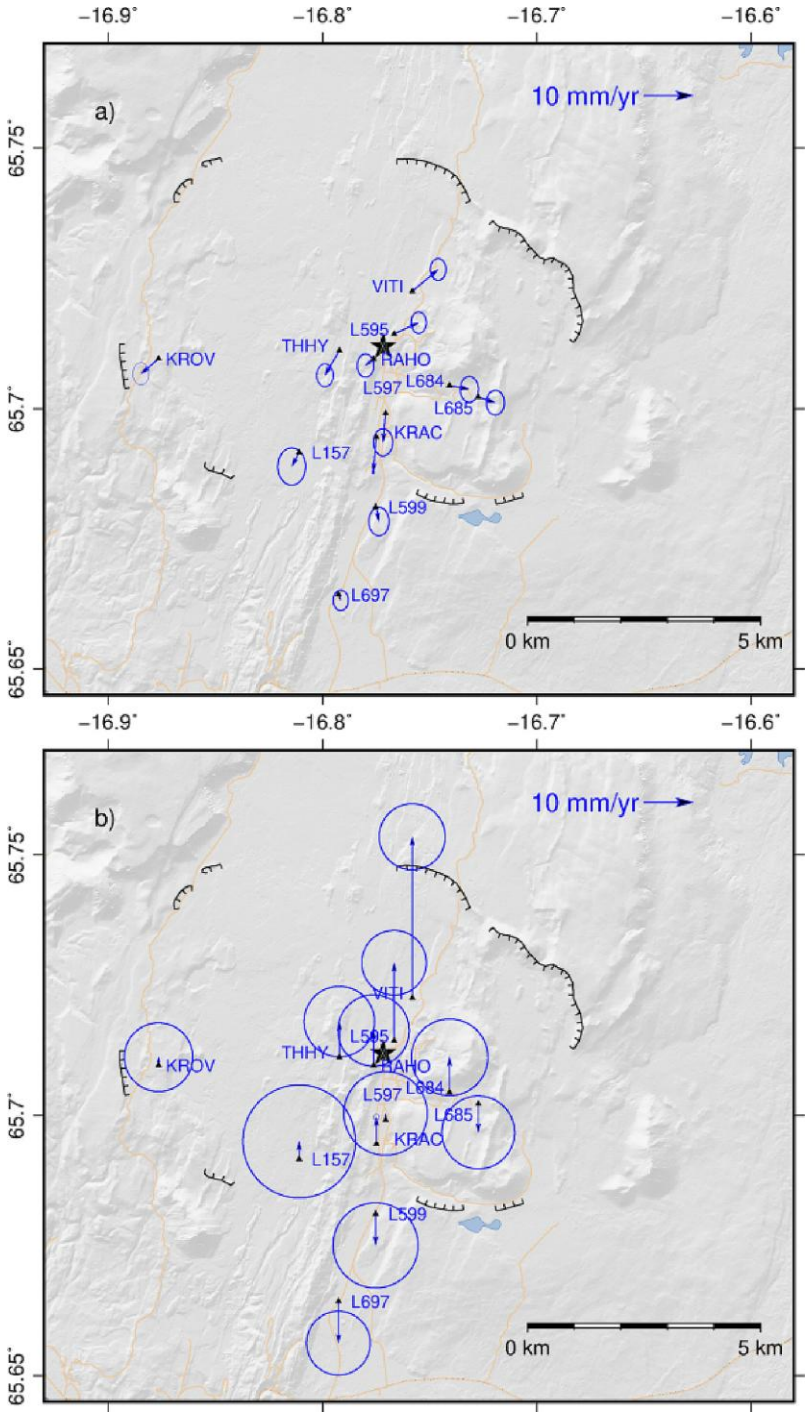

Fig. 3. Horizontal (a) and vertical (b) velocity difference (2018–2020 and 2015–2018). Background shows shaded topography and the Krafla caldera boundaries. The black star is the source centre estimated from modelling. Ellipses indicate velocity uncertainties.

time series also shows a signal in mid-2014 to the beginning of 2015, which may relate to the Bárðarbunga-Holuhraun dike injection and eruption taking place in 2014–2015 (Sigmundsson et al., 2015). The time series for the LHNC and SPBC continuous stations (Supplementary Fig. S1) are broadly consistent with approximately stable velocities since their installation in November 2019.

To make best use of the available data and investigate the change in the deformation pattern, we isolate the signal related to the change in deformation in 2018 by forming the difference of the velocity fields for 2015–2018 and 2018–2020. This we refer to in the following as a difference velocity field. We evaluate it for the 12 GNSS stations with the most complete dataset from 2015 to 2020. This approach is a convenient way to study the change in deformation processes, in relation to changes in deformation trends (Ducrocq et al., 2021). This can reflect either variations in the rate of processes taking place before the change or signify a new process. Deformation due to any processes that remain the same before and after the change in deformation pattern, such as steady crustal cooling, will be cancel out.

The difference velocity field (Fig. 3a) reveals an inflation pattern within the Krafla caldera, witnessed as general horizontal movement away from an area located in the middle of the caldera. The amount of the horizontal displacement is highest for 6 GNSS stations in the central area of the caldera. There the rate is $\sim 6 \pm 2$ mm/yr, while it is smaller ($\sim 3 \pm 2$ mm/yr) for the six stations near or outside the southern caldera boundaries. These rates and uncertainties are the mean and standard deviation of stations in the respective areas. The vertical difference velocity field pattern (Fig. 3b) shows uplift for all the stations inside the caldera, except for L685 station in the south-east part. The uplift in the middle of the caldera occurs at a rate of about 15 ± 6 mm/yr. L599 and L697 GNSS stations, outside the caldera boundaries, show subsidence at a rate of about 7–8 $\pm$ 5 mm/yr. The largest vertical velocity observed at station VITI, 32 mm/yr, is considered an erroneous outlier as it deviates from the pattern observed at nearby stations and InSAR observations show no anomaly at the location of this site. The reason may be site instability; the site is located within an area of loose surface sediments and geothermal alteration and its benchmark may be located on a large boulder rather than solid bedrock.

2.2. InSAR

InSAR interferograms were generated using the InSAR Scientific Computing Environment (ISCE) software version 2.2.0 (Rosen et al., 2012), using SAR images from the Sentinel-1A and Sentinel-1B satellites of the European Space Agency (https://sentinel.esa.int), in the 2015–2020 period. Interferograms are geocoded to a digital elevation model grid with a pixel size of about 90×90 m^2. We use only snow-free images from one ascending (satellite heading northwards) orbit, T147, and two descending (satellite heading southward) orbits, T9 and T111. Line-of-Sight (LOS) velocity fields were derived from time series analysis of interferograms in the same manner as by Drouin and Sigmundsson (2019), with each interferograms measuring displacement in the direction of the line of sight from ground to satellite. For each satellite track, the average difference LOS velocity field was then found by subtracting the LOS 2015–2018 average velocity field from the LOS average velocity field for 2018–2020, in a similar approach as for the GNSS data.

The difference velocity fields for tracks T9, T111 and T147 (Fig. 4) show a clear LOS signal inside the caldera up to maximum values of 8–10 mm/y consistent with a LOS shortening. Ascending track T147 shows similar deformation pattern, but the pattern is wider in the west part of the Krafla caldera. Grey areas shown in Fig. 4 are where data is too noisy, or interferograms were incoherent (no clear signal), resulting in no estimate difference average LOS velocity.

2.3. Seismicity

A local seismic network operating by Landsvirkjun and ÍSOR (Iceland GeoSurvey) since 2006, presently consisting of 21 stations (15 surface instruments and 6 down hole instruments), supplemented with 6 stations from the regional seismic network of the Icelandic Meteorological Office (IMO) in the Krafla, Þeistareykir (few km north-west of Krafla) and Námafjall geothermal areas (Guðnason et al., 2021). Within the Krafla caldera most of the seismic events are located shallower than about 2.4 km, locating the brittle ductile boundary at Krafla caldera at about 1.8–2.4 km depth (Ágústsson and Blanck, 2019). Reanalysis of seismicity in the 2017–2021 interval, using the same procedure for the

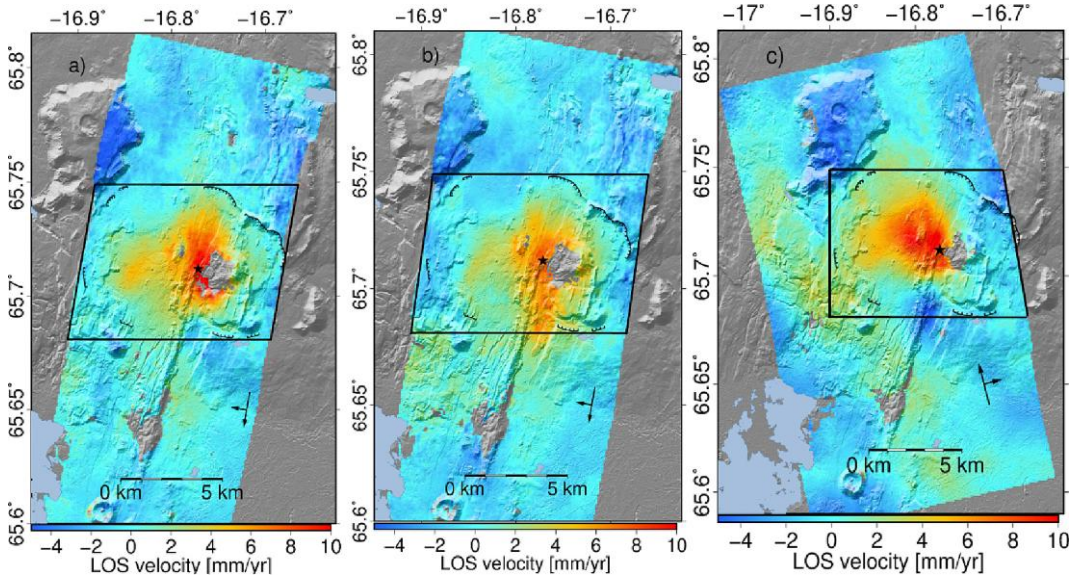

Fig. 4. Difference of average LOS velocities in 2018–2020 and 2015–2018 for Sentinel-1 descending tracks T9 (a) and T111 (b), and the ascending T147 track (c). Black arrows show the heading and look direction of the satellite. The black star is the estimated source centre. The black polygon marks the area we use to evaluate the root mean square values.

location and magnitude estimate for the whole period, shows that the seismicity rate was relatively constant until mid-2019, witnessed as steady linear gradient (~3500 earthquakes/yr) of the curve showing the cumulative number of earthquakes (blue curve in Fig. 5). The rate is slightly lower in August–September 2019 (~3300 earthquakes/yr). The seismicity increases in late 2019-early 2020. The seismic moment release is found by using the formula by Hanks and Kanamori (1979). Cumulative moment (red curve in Fig. 5) is relatively constant until the fall 2019 when a significant change occurs. The moment release increases and is relatively constant thereafter.

No changes in seismicity occurred at the onset of the change in the deformation pattern observed at the north component of KRAC station in mid-2018. The decrease-increase pattern of cumulative numbers of earthquakes and the increase of the seismic moment release correlate, however, relatively well with the later change in rate of the north component at KRAC station and the beginning of the upward motion at this GNSS site in fall 2019 (Fig. 2).

2.4. Gravity

Gravity was measured in Krafla by ÍSOR in November 2019, with a Scintrex CG5 gravimeter, at 21 sites in response to the change in deformation pattern. Earlier measurements at most of these sites were carried out in 2017 and 2018 by Portier et al. (2018). Measurement procedure and the processing of the data was done in the same manner as described by Magnússon (2016). The gravity values (Hersir et al., 2020) from the 2019 campaign are relative to a base station located 1–2 km east form the Bjarnarflag Power Plant. A free-air gravity correction was applied using elevation changes inferred from InSAR. The VITI site (same as the VITI GNSS site) and site 5672 (a few kilometres north-east of VITI site) show a negative gravity change (−11 μGal and − 14 μGal, respectively) between 2018 and 2019 while most of the other sites, located south of the Krafla power plant, show a positive gravity change from 10 μGal to 30 μGal. As described in Chapter 2, paragraph 2.1, the VITI benchmark eventually has local instability. However, the free-air correction does not take this into account, and the height correction inferred by InSAR may be inaccurate.

2.5. Hydrothermal changes

Pressure and water level measurements have been carried out yearly by ÍSOR in monitoring well KG-10 (see Fig. 1 for location), in the centre of the caldera (Egilson, 2020). The well, which is not used for production, is cased down to about 850 m depth and pressure is measured at a depth of 800 m. The water table showed overall stability from 2015 to mid-2018, with a range of variability of 5–10 m until August 2018 (Fig. 6a). Thereafter, the water table increased until beginning of 2019, for a total of 25 m rise. Pressure measurements from 2015 until 2017 showed a slightly declining pattern (Fig. 6a). In 2018 the pressure began to increase and continued in 2019. The increase in the two years period is about 0.2 MPa. This change coincides with the increase of the water level. It remains uncertain how widespread these changes are in the geothermal system. After 2019 the changes have been minor; pressure in well KG-10 increased by 0.01 MPa from 2019 to 2020.

The yearly extraction of mass via utilized boreholes for the Krafla power plant has varied in the study period (Fig. 6b). The decrease after 2017 is due to closure of water-rich wells (Hauksson, 2019; Hersir et al., 2020). Fluid has been re-injected into three wells at Krafla: KG-26, KJ-39, and KJ-35 (Fig. 6c). During the study period, re-injection into well KG-26 was rather stable, while changes occur in the re-injection into the other two wells. Re-injection begins in well KJ-35 in July 2018, continuing episodically until September 2019. Re-injection rate at well KJ-39 decreases in August 2018 by half of the rate in 2017. It decreases further in 2019 and 2020. The total re-injection rate is rather constant until mid-2019 but decreases in the second half of 2019. The net production (the difference between extraction and re-injection) shows an increase each year from 2015 to 2018, reaching a maximum of 5900 ktons/year. After that, the net production decreases. The overall net extraction of fluid for the second half of 2020 was the lowest for the past 40 years, while one of the turbines of the Krafla power plant was stopped in mid-2020 due to maintenance.

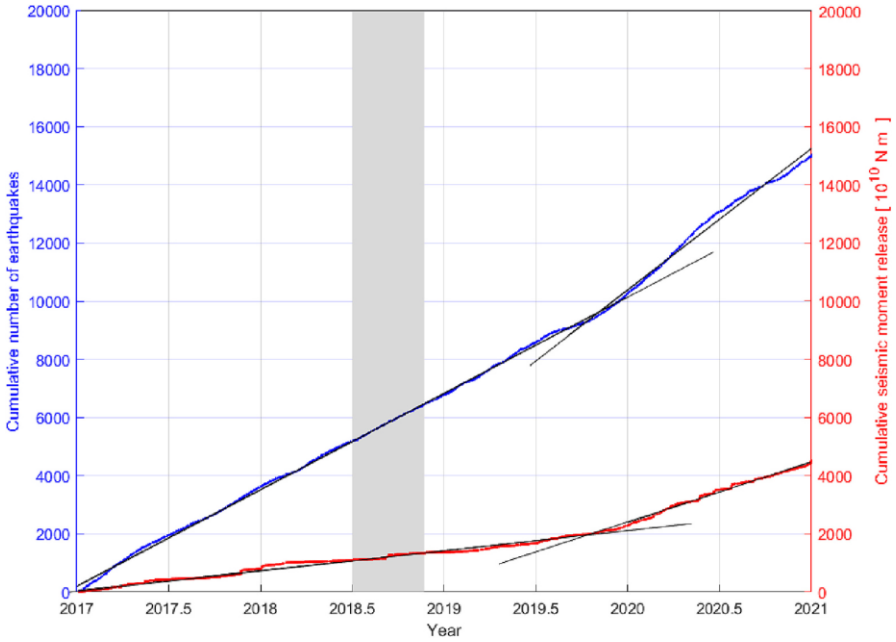

Fig. 5. Cumulative number of earthquakes and cumulative seismic moment release for the 2017–2020 period. The black lines show linear fit to segments of the cumulative number of earthquakes evaluated from 2017 to end-2019 and end-2019 to end-2020 time periods and linear trends for the moment release evaluate from 2017 to mid-2019 and mid-2019 to end-2020 time periods. The shaded area shows the time frame of the change in deformation pattern observed at the KRAC GNSS station.

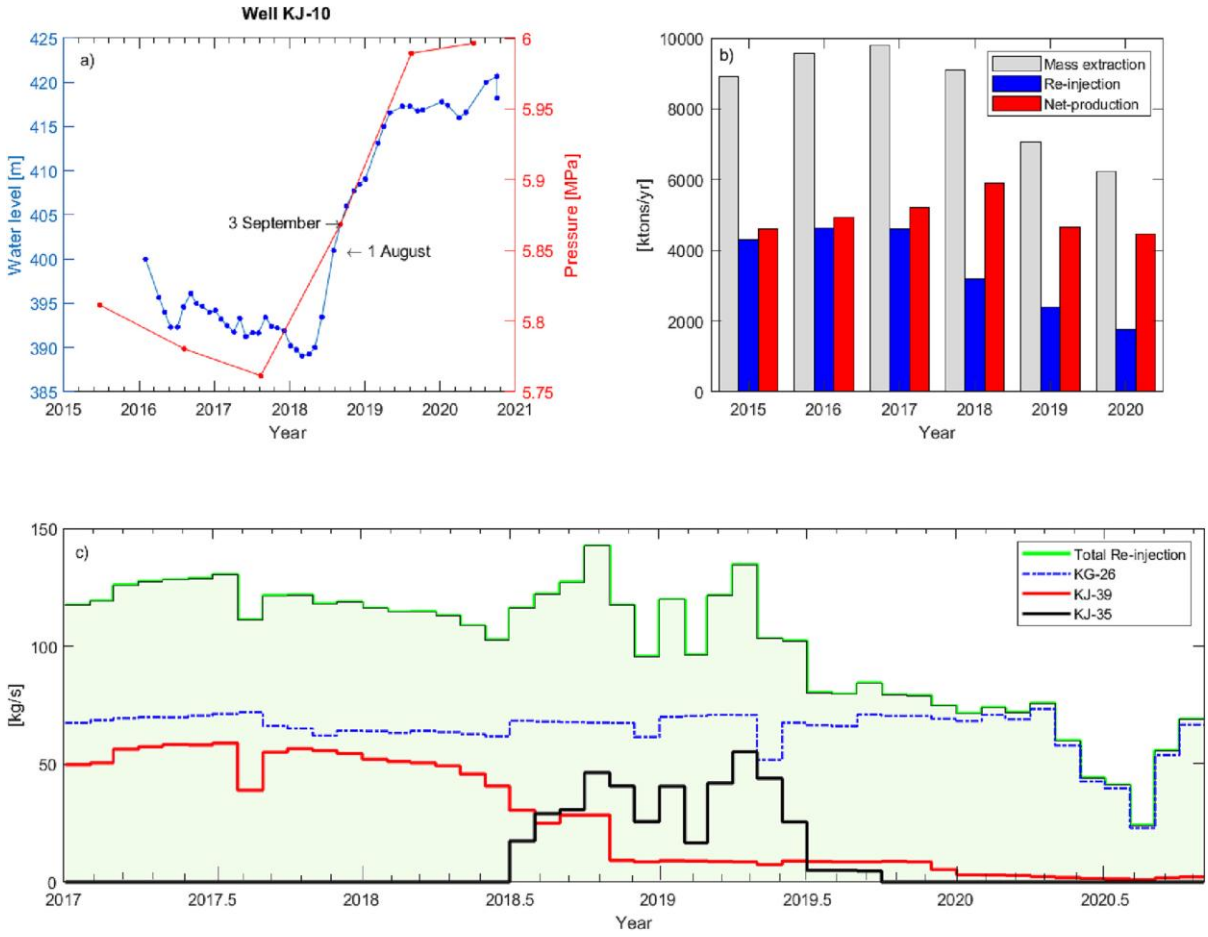

Fig. 6. a) Water level and pressure measurements at 800 m depth in monitoring well KG-10. See Fig. 1 for location. Data from Egilson (2020). b) Total mass extraction, re-injection and net-production (ktons/yr), at the Krafla power plant between 2015 and 2020. c) Monthly average rate of re-injection into wells KG-26, KJ-35 and KJ-39, and the total re-injection rate from 2017 to 2020. Data in panel b) and c) provided by Landsvirkjun.

3. Modelling of geodetic data

3.1. Model Parameters and analytical solution

The GBIS open-source Geodetic Bayesian Inversion Software (Bagnardi and Hooper, 2018) was used to evaluate how well a joint inversion of the GNSS and InSAR difference velocity fields (presented in Chapter 2) fit to predicted surface displacements due to a localized source with volume change within an elastic half-space. The InSAR difference velocity field were down sampled as described in Supplementary Text S2. The inversion algorithm samples posterior probability density function through a Markov chain Monte Carlo method, incorporating the Metropolis-Hastings algorithm. Different source geometries were considered: a point source of pressure (Mogi, 1958), a horizontal rectangular sill with uniform opening (Okada, 1985), and an increase in pressure in a prolate spheroid source (Yang et al., 1988).

3.2. Finite Element Method (FEM)

We carry out FEM modelling using the Structural Mechanics module of COMSOL Multiphysics v5.5 (www.comsol.com). The initial model (Supplementary Fig. S2a) is a "small sphere model", with a spherical pressure source with a radius of 450 m, embedded in a three-dimensional 100 × 100 km domain, with a free (no constraints and no loads acting on the boundary) flat surface. The source radius has been set to 450 m, sufficiently small to avoid effects on surface displacement, and large enough to reduce the need for too high pressure being applied at the source boundary. Other boundary conditions are applied similarly as in Hickey et al. (2014) for a spherical cavity in a homogeneous elastic half-space. The average pressure change per year in 2017–2019 in well KG-10, $\Delta P = 0.1$ MPa, is applied uniformly to the boundaries of the spherical source. Considering the size of the source and this pressure change, we find the elastic moduli that give the same best-fit source strength and the same best-fit displacement field as obtained from the GBIS inversion. The aim is to test if the pressure change recorded at KG-10 may be representative for pressure change in the whole geothermal reservoir. We validated the FEM model by comparing the ground deformation in the small sphere model to predictions of the Mogi source analytical model.

We also considered FEM models in a uniform elastic half-space model with a larger spherical source. We explore the relationship between source radius, and rigidity/Young's modulus values to evaluate the source parameter combination that gives similar surface displacement fields for a fixed value of the source strength parameter (Supplementary Text S3). We explore the most suitable result (according to expected elastic properties of the Icelandic crust) and highlight

limitations of the assumptions of the point source of pressure model.

We finally consider a "two-domain model" to account for deviation of the homogeneous medium, different values of elastic parameters within and outside the caldera. This model geometry (Supplementary Fig. S2b) is divided into two domains: domain 1 (regional) and domain 2 (local). The local domain roughly corresponds to the caldera area, in a simplified manner. It is a 9 × 10 km wide and 4 km deep rectangular volume (360 km^3). The idea to introduce a local domain with different elastic features is to study eventual effects of different rigidity material within the Krafla caldera, where elastic parameters may have a different value than regionally.

4. Results

4.1. GBIS models

Results of the inversion with the difference velocity fields with the GBIS software for the point source of pressure are shown in Table 1, Fig. 7, and Supplementary Fig. S3. Results for the sill-like geometry and spheroid source results are presented in Supplementary Figs. S4 and S5. Probability density functions (Supplementary Figs. S6, S7, and S8) are estimated for each model parameter, thereby providing estimates of model parameter uncertainties, considering the data and their uncertainties, assuming the model assumptions are correct. The inferred centre of the point-source is at 2.1–2.3 km depth beneath surface near the middle of the caldera, and the volume change is 2.6–3.8 × 10^5 m^3/yr (95% confidence intervals). The observed and modelled GNSS difference in velocity fields are similar (Fig. 7a). However, the point source model over-predicts LOS displacements at large distances from the source, and therefore we explored if other source geometries could provide a better fit. A horizontal rectangular sill with uniform opening and pressurized prolate spheroid source provided a worse fit. The Root Mean Square (RMS) of LOS residual evaluated for the point source model is 2.58 mm/yr, for the spheroid it is 2.89 mm/yr and for the sill it is 4.01 mm/yr (Supplementary Table S1). The sill and prolate spheroid models are not considered further in the following.

4.2. Relationship between source size and elastic moduli

The GBIS point source modelling results optimal depth and source location have been used to build a numerical model, with a pressure increase of 0.1 MPa applied to a spherical source. The FEM solution shows the same displacement field as the analytical solution for a point source that best fits the observed ground deformation. The comparison (Supplementary Fig. S9) shows a good match between the analytical and the FEM solution for a spherical source with a 450 m radius. However, the values of the elastic parameters that model (E = 0.238 GPa; μ = 0.093 GPa) are much lower than the regional values inferred for the Icelandic crust. We therefore consider models with a larger radius (800, 1000, 1200 and 1400 m; Fig. 8a). We explore the value of elastic parameters that can produce the same displacement field for the same source strength (7.6 × 10^4 m^3, according to eq. 4 in Supplementary Text S3) if the pressure change is 0.1 MPa. For equal pressure change, the increase of the radius of the source must be matched by an increase in values for the rigidity/Young's modulus (Fig. 8b and c), to result in the same source strength and equal fit of the data. A constant scaling factor between rigidity and Young's modulus follows from eq. 5 in Supplementary Text S3. The results show, however, that the vertical and the horizontal displacements at the free surface due to a pressurized spherical source are somewhat different as the source radius becomes larger, despite modification of the elastic parameters. These results show the limitations of one of the assumptions in the point source model, which is valid when $(a/d)^5 << 1$, where a is smaller in relation to its depth d (McTigue, 1987). As source radius increases, the source top is closer to the surface, causing larger ground displacements above the source. The horizontal displacement is less sensitive to the proximity to the surface than the vertical displacement.

Table 1
Results from GBIS inversion for a point source model based on 2015–2018 and 2018–2020 difference velocity fields from GNSS and InSAR. Columns show model parameters, the optimal fit, and the 2.5 and 97.5 percentiles of posterior probability density functions. The range spanned by the 2.5 and 97.5 percentiles is the 95% confidence interval.

Model parameter	Optimal	2.5%	97.5%
Longitude	−16.77°	−16.77°	−16.77°
Latitude	65.71°	65.71°	65.71°
Depth (m)	2254	2077	2492
ΔV (m^3/yr)	3.2 × 10^5	2.6 × 10^5	3.8 × 10^5
Source Strength (m^3)	7.6 × 10^4	6.4 × 10^4	9.1 × 10^4

4.3. Effect of low-rigidity area

Modelling in section 4.2 shows that a spherical source within elastic half-space, with 1.4 km radius and 0.1 MPa/yr pressure change, can only reproduce the observed deformation if E = 6.95 GPa. This value is significantly lower than what is expected for Iceland as a whole (E = 30 GPa). It is not realistic to consider larger values for the radius as the source top for r = 1400 m is close to the surface, and for smaller radii the values of the elastic parameters are too low for the average values of the Icelandic crust. Relaxing the assumptions of the homogeneity in the elastic half-space may allow a better match between observations, data, and available constraints. For that purpose, we evaluate how the presence of a localized crustal volume, with different elastic moduli around the source affects the deformation field.

Fig. 9 shows the derived displacement field assuming E = 6.95 GPa in Domain 2 and E = 20, 30 and 40 GPa in the far field and the deeper crust. A spherical source is within Domain 2, with centre at 2.2 km depth and radius 1.4 km. The modelled surface displacements broadly fit the vertical and horizontal components of displacement, showing a similar pattern of deformation as for the homogenous elastic medium solution. The near-field solutions for both components show though larger displacements compared to the analytical due to the violation of the point source assumption discussed in paragraph 4.2. Also, near 5 km radial distance, the horizontal displacement shows an abrupt change compared to the analytical solution, due to the boundary of low-rigidity domain and the far field domain. At distances larger than 5 km from the source centre, the difference between the two-domain solution and the other solutions diminishes.

4.4. Root mean square (RMS)

To quantify the goodness of fit of the models, the RMS residual for all FEM models, as well as the RMS for $GNSS_{obs}$ ($_{obs}$ = observation) and LOS_{obs} only are presented in Table 2. The GNSS RMS residual values, for both the vertical and horizontal components, are significantly smaller than the RMS $GNSS_{obs}$ value. For GNSS, the RMS residual results are comparable for the FEM models. The LOS RMS residual values for the FEM models show also an improvement compared to the RMS evaluated for LOS_{obs} only. The use of RMS is a simple way to quantify the goodness of fit when comparing displacement from FEM models to observations. However, a comparison of RMS of different models does not consider the varying degree of complexity of models, for example if the model domain is divided into sub-domains with varying properties (like in our case for the two-domain model compared to the others). Nevertheless, all our models have the same number of varied parameters: radius and Young's modulus. Furthermore, we compare our models to each type of observation separately.

The small sphere model provides mathematically the best fit, given the GNSS and LOS RMS evaluation. However, if the model is used to explain the deformation with the hypothesis that the pressure change in monitoring well KG-10 is representative for the whole geothermal

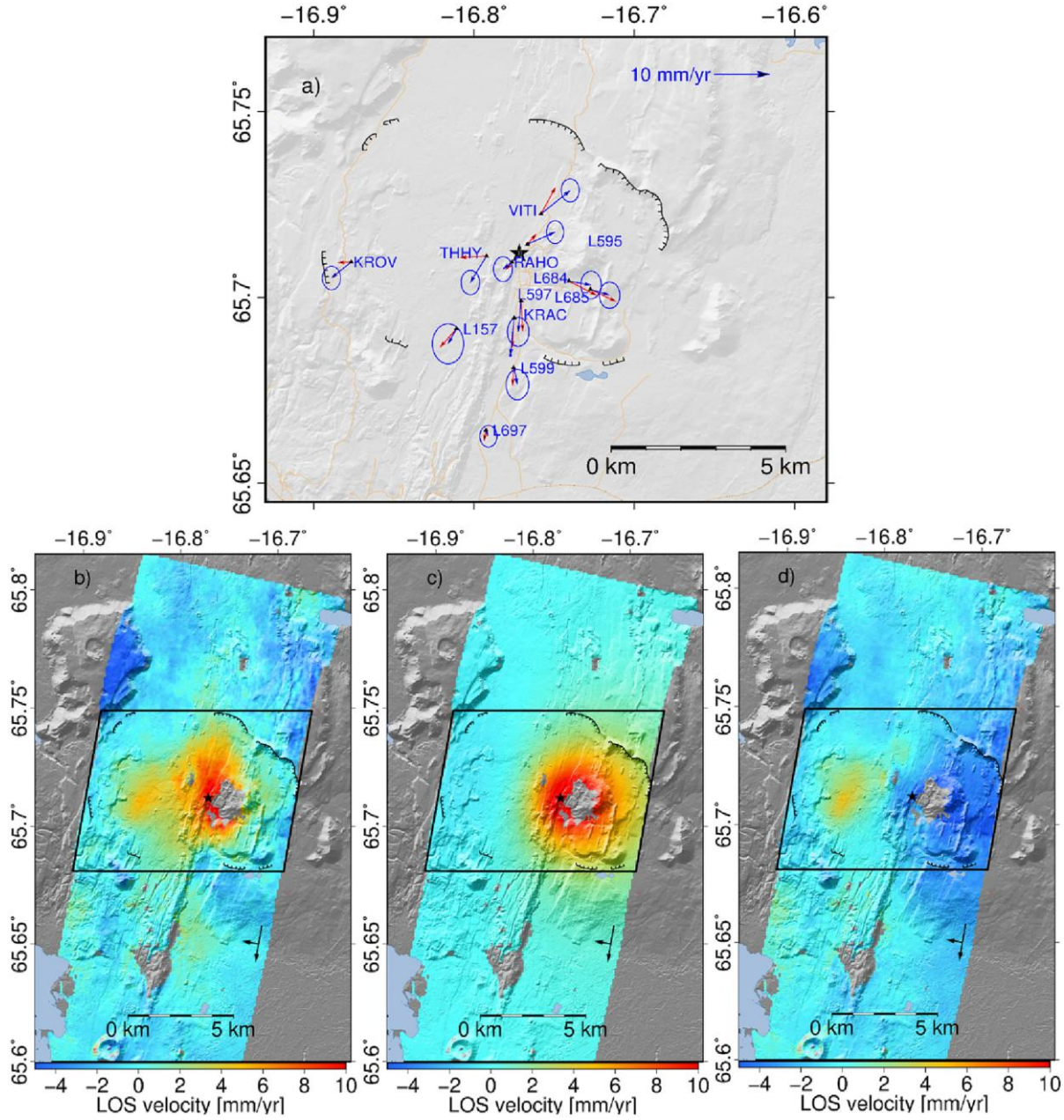

Fig. 7. Comparison between the predicted displacement from Mogi best-fit result (GBIS) and observations. Panel (a) GNSS horizonal data (blue arrows) and predictions (red arrows) of a best fitting model. The black star indicates the inferred best-fit position for the source centre. Panel (b) LOS data, (c) best fit model predictions and (d) residuals for InSAR track T9. The black polygons marks the area used to evaluate the root mean square value. (For interpretation of the references to colour in this figure legend, the reader is referred to the web version of this article.)

reservoir, then the model requires unrealistically low elastic moduli compared to earlier findings for Iceland. Therefore, the two-domain model, with a low-rigidity crustal volume confined to the near-field in the caldera, may provide a better explanation.

5. Discussion

Inversion of geodetic data during 2018–2020 from the Krafla caldera shows that the time difference velocity fields can be explained by a spherical pressure source at 2.1–2.5 km depth, located <1 km south to the location of the IDPP-1 well (Fig. 1). Compared to the previously found deformation sources, our source depth is about 0.6–1 km deeper and roughly ~0.5 km to the north-west of a deflating Mogi source under Leirbotnar and roughly ~1–1.5 km to the east of a second deflating Mogi source under Leirhnjúkur but of comparable depth (Sturkell et al., 2008, for 1989–2005, and Drouin et al., 2017, for 1993–2015,

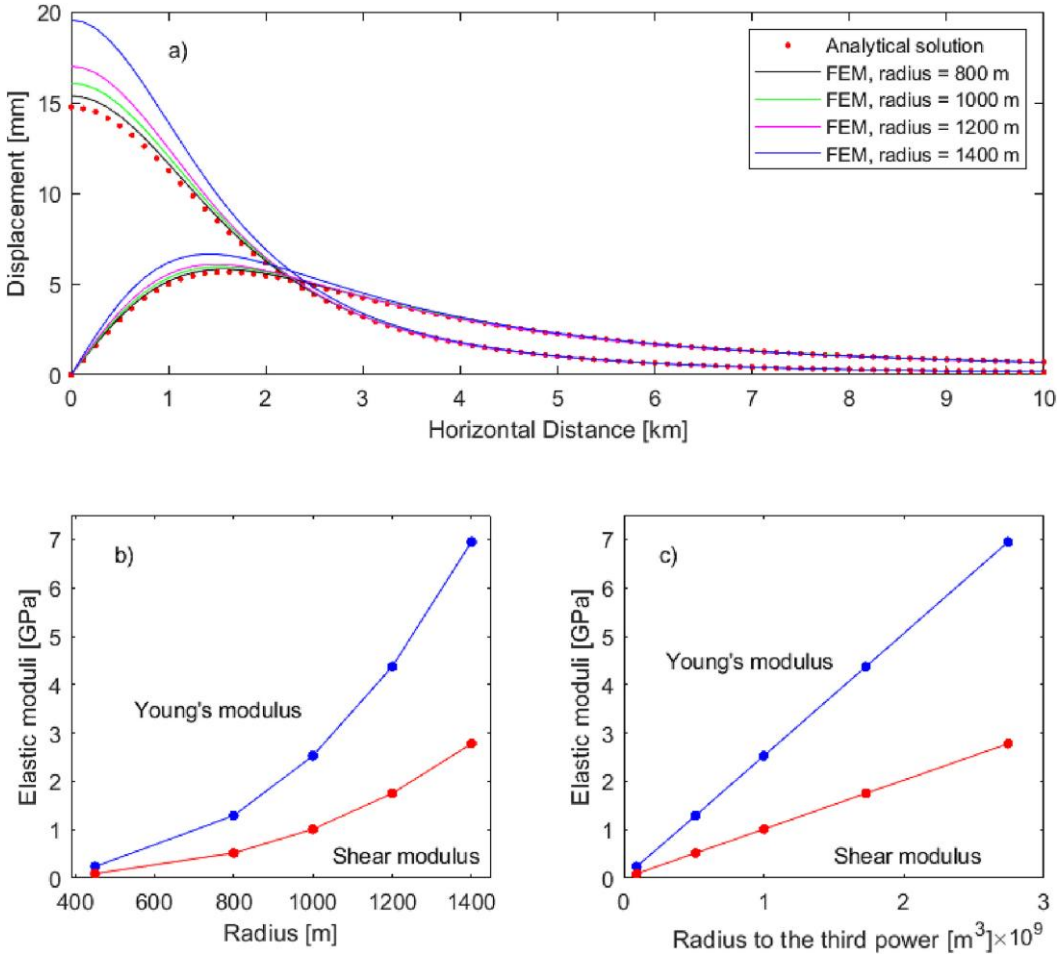

Fig. 8. (a) Predicted displacement from the best fit GBIS model (red circles) and numerical solutions from COMSOL for different source radius. Combinations of Young's modulus (blue) and shear modulus (red) with source radius that can broadly explain observed deformation at Krafla. Panel (b) shows elastic moduli as a function of the radius. Panel (c) shows elastic moduli as a function of the radius to the third power. (For interpretation of the references to colour in this figure legend, the reader is referred to the web version of this article.)

Supplementary Fig. S10 and Table S2). The centre of the deformation source we found is close to the location where the IDDP-1 drillhole intersected magma. Its depth is also at the brittle-ductile boundary and where the lower geothermal reservoir is located. Therefore, there is need to consider both magmatic and hydrothermal processes as a potential cause of deformation. Seismic tomography at Krafla (Schuler et al., 2015) has revealed a distinct east-west trending low V_p zone at 1.5–2.5 km depth b.s.l. beneath the IDDP-1 borehole, extending 4 km east and west of the well. The low V_p zone, with V_p values as low as 4.4 km/s, extends between 3.0 and 3.5 depth b.s.l. between Leirhnjúkur and Víti crater and matches the locations of two attenuating bodies found by Einarsson (1978). Underneath the Leirbotnar geothermal field, very low-V_p/V_s values ($\leq$1.65) are found at 2–3 km depth b.s.l. beneath Víti, close to the IDDP-1 borehole which was drilled into rhyolitic magma. Schuler et al. (2015) suggested that the low V_p/V_s zone observed might be linked to a superheated steam zone overlying the rhyolitic melt.

The deformation source may therefore originate from pressure changes, either in the geothermal system or in a magma body. Variations in the geothermal system may relate to the variations in geothermal utilization. Change in the ground deformation at KRAC sites begins at a similar time as the re-injection in well KJ-35 began in July 2018 (Fig. 10). The inversion result indicates that the best fitting location of a point-source is located in-between the KJ-35 re-injection well (~1.2 km west of it), and the monitoring well, KG-10 (~0.2 km east of it). In addition to changes in fluid re-injection strategy, there was also a change in mass extraction in the system for the geothermal production. The total amount of mass extraction was lower in 2018 than the previous years (Fig. 6). There is uncertainty about the exact beginning of the deformation at the KRAC site considering uncertainties of the GNSS observations. The suggested onset time of the deformation change is shown with the grey shading in Fig. 10. This time interval overlaps with beginning of the pressure increase in the geothermal reservoir, the beginning of re-injection at well KJ-35 and the reduced amount of re-injection at well KJ-39. Furthermore, a change in the rate of the deformation occurs when the re-injection at well KJ-35 stopped in fall 2019. Deformation prior to and after 2018 may relate to change in one common process. Since 2004, geodetic observations indicate relatively steady rate of subsidence, ~5 mm/yr, in the caldera, eventually related to geothermal exploitation (Drouin et al., 2017). If processes before and after 2018 both relate mainly to the geothermal system, then the change after 2018 can be described as rebound of ground deformation and pressure following changes in the geothermal utilization, relating to

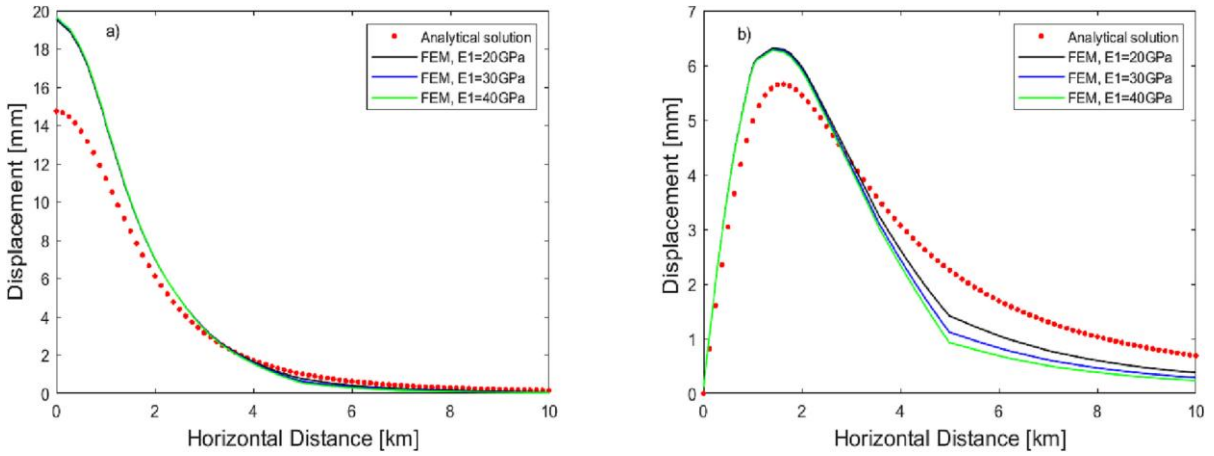

Fig. 9. a) Vertical and b) horizontal displacement results for two-domain model with different Young's modulus values. Red dots show the analytical solution from GBIS (uniform and elastic half space) compared against the new model configuration. (For interpretation of the references to colour in this figure legend, the reader is referred to the web version of this article.)

Table 2
Statistical evaluation of the different FEM models. The RMS corresponds to the root mean square (Supplementary Text S4).

RMS	GNSS stations (mm/yr)	LOS (mm/yr)	Small sphere model (mm/yr)	Large sphere model (mm/yr)	Two-domain model (mm/yr)
Horizontal displacement	3.41		1.08	1.05	1.13
Vertical displacement	11.83		8.98	9.39	9.43
LOS (all tracks)		2.74	2.18	2.59	2.56

changes in rates of extraction and re-injection, as well as changes in where re-injection takes place and what wells are used to extract geothermal fluids.

Inflow of new magma, gas accumulation or crystallization in shallow magma bodies are often suggested to explain ground motion around volcanoes (Bellucci et al., 2006; Dzurisin et al., 2009; Chang et al., 2010; Parks et al., 2012). In map view, our inferred source is located ~0.5 km south-west of the IDDP-1 well and ~0.5 km north-west of the KJ-39 well, at a similar depth as the magma has been intersected at the two wells. Kim et al. (2020) mapped an unusually strong reflector at the same depth where the magma has been encountered by the IDDP-1 drillhole and near-offset source VSP experiments indicate a reflector at 2.3 km depth (Kästner et al., 2018; Millett et al., 2018; Reiser et al., 2020). If the 2018–2020 deformation source is of magmatic origin, the most likely candidate process is pressure increase in the IDDP-1 rhyolite magma body. There is a need to consider the value of the volumetric flow rate inferred from the inversion result: $\sim 3.1 \times 10^5$ m^3/yr or 0.01 m^3/s. Such very low flow rate for liquid magma may not be realistic, as if liquid magma flows in channel at this rate it may solidify because of cooling due to heat transfer into the host rock. Also, unrest periods at volcanoes in similar geodynamic setting are typically associated with magma transfer at a much higher rate.

A potential magmatic origin of the increased pressure may relate to volcanic gas. For example, ongoing deformation could be a delayed response to magma degassing events that commenced earlier than the deformation changes. At Campi Flegrei, Italy, Chiodini et al. (2016) hypothesize that periods of intense magma degassing may drive injection of volatiles into an overlying hydrothermal system and lead to extensive heating and expansion, causing ground deformation. Since 1985 a decrease in N_2/He and N_2/CO_2 ratios has been observed at Campi Flegrei caldera, paralleled by an increase in He/CO_2, at least up to 2016 (Calino et al., 2014). It has also been proposed that the uplift in early 2020 in Svartsengi on the Reykjanes Peninsula, SW-Iceland, the harbinger of the Fagradalsfjall eruption in March 2021, was driven by magmatic fluid ingress (Flóvenz et al., 2022). Eventually, the inferred pressure increase at Krafla may relate to gas accumulation in the IDDP-1 magma body or in the superheated steam zone overlying melt. However, the concentration of carbon dioxide (C_20), hydrogen sulfide (H_2S), and hydrogen, H_2, in vapor from fumaroles in Leirhnjúkur has decreased in recent years, even quite sharply since 2017 (Óskarsson and Óladóttir, 2020). Measurements of methane (CH_4), nitrogen (N_2) and argon (Ar) soil at Leirhnjúkur in the autumn of 2020 do not indicate changes in gas flux through the surface (Óskarsson and Óladóttir, 2020).

Unusual seismicity around volcanic area is often linked to magma movement in the subsurface and, together with ground deformation and gas variation, represents one of the commonly geophysical precursors used to signal an impeding eruption (e.g., Druitt and Kokelaar, 2002; Cervelli et al., 2006; De la Cruz-Reyna et al., 2008; Fischer et al., 2022; Sigmundsson et al., 2022). Changes in seismicity activity may also be caused by anthropogenic geothermal activity (Flóvenz et al., 2015; Juncu et al., 2018). In both hypotheses, magmatic or geothermal, it is natural to assume that the local stress field would be perturbed when ground deformation occurs (Feuillet et al., 2006). At Krafla, no changes in seismicity were observed at the onset of the ground deformation pattern change in 2018. Changes occurred later in mid-2019, displaying a decrease followed both by an increase pattern in the number of earthquakes and an increase of moment release at the end of 2019.

Gravity measurements may eventually discriminate between magma intrusion and inflow of liquid or gas at shallow depths as the density of magma differs from the density of superheated vapor, gas or liquid (Rymer, 1994; Gottsmann and Rymer, 2002; De Zeeuw-van Dalfsen et al., 2006; Flóvenz et al., 2022). The result of the gravity campaign carried out in 2019 (Hersir et al., 2020) compared to previous measurements in 2017 and 2018 (Portier et al., 2018) show positive gravity changes, between 10 and 38 μGal, in an area south of the Krafla power plant, but do not cover the main area of deformation. These changes may, e.g., be related to an increase in groundwater level by 3 to 4 m with 20% porosity, or 6 to 8 m with 10% porosity (Hersir et al., 2020). The series of gravity measurements in 2019 at permanent sites are valuable as baselines in the future, for a further understanding of the subsurface

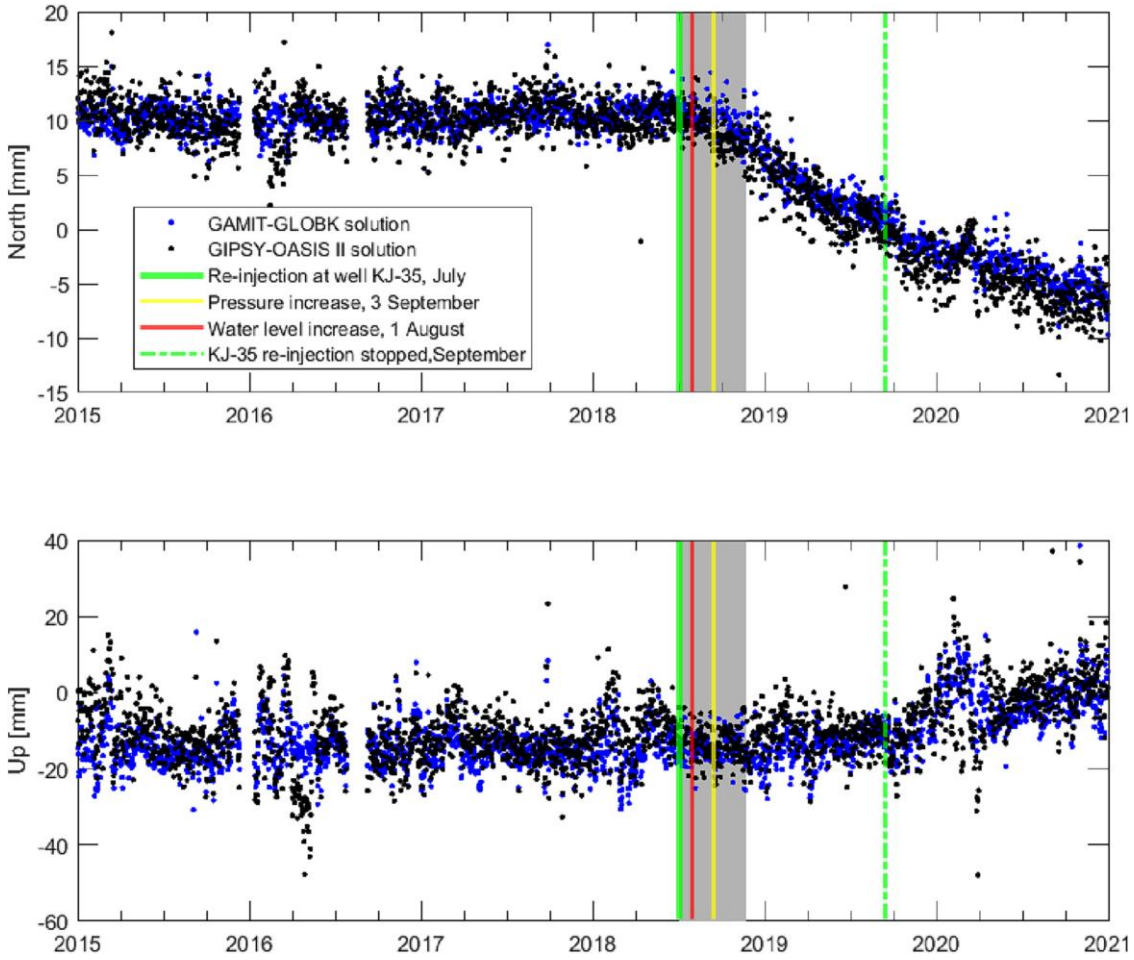

Fig. 10. KRAC continuous GNSS station. 2015–2020 time series is showing 2015–2020 with a linear, annual and semi-annual trends removed for GAMIT-GLOBK solution (blue dots) and GIPSY-OASIS II (black dots). The shaded area shows the time range of the onset of the deformation, mid-July 2018 to mid-November 2018; the vertical yellow line is showing the pressure measurement; the vertical red line shows the beginning of the water level increase; the vertical green line and the vertical green dotted line show the start and the stop of the re-injection operations at KJ-35 well. At similar time, October–November 2019, re-injection at KJ-39 well decreased significantly. (For interpretation of the references to colour in this figure legend, the reader is referred to the web version of this article.)

processes in the Krafla area.

The inferred source depth (2.1–2.5 km) suggests pressure increase at or near the magma-hydrothermal boundary at Krafla. Because of the relatively small volume estimate (and small rate), a sole magmatic origin for the 2018 change does not correspond well with the estimated range of magma flow rates in comparable geodynamic setting. Alternatively, processes in the hydrothermal reservoir beneath the Krafla caldera may play an important role in the deformation change commencing in 2018. Hydrothermal processes can have a significant effect on rock strength and rigidity of the uppermost crust due to presence of fluids, high temperatures, and alteration of minerals (Hill et al., 2006; Frolova et al., 2014). One could also consider the possibility that changes in the hydrothermal system in 2017–2019 may be a direct response to changes within the magmatic system. The pressure changes in well KG-10 are related to one part of the geothermal reservoir and, thus, it is not clear if the observed changes relate to conditions in the whole reservoir.

6. Conclusions

Difference of average ground velocities in 2018–2020 and 2015–2018 observed by GNSS and InSAR reveal a change in ground deformation pattern at Krafla caldera in 2018, after decades of subsidence. A point source of increase pressure model fits the time difference velocity field, with source centre depth at 2.1–2.5 km. This is close to the brittle-ductile boundary, where magma has been intersected during previous drilling operations in 2009 at the IDDP-1 well and in 2008 at the KJ-39 well. The inferred rate of volume increase, 2.7–3.8 $\times$ 10^5 m^3/yr, is minor compared to many magma intrusion events. Gravity changes are small, but no measurements exist within the main deformation area. They do not reveal evidence for large-scale magma, gas or fluid transfer. The deformation change may be a result of changes in the geothermal system. Both the amount of fluid extraction and the amount of fluid re-injection into wells changed in 2018. The onset of the change in deformation in the caldera begins at similar time as pressure increases in well KG-10 (0.2 MPa in 2017–2019) and re-injection strategy changes, suggesting a possible link between the geothermal exploitation, ground deformation and pressure changes. Numerical FEM modelling with low-

rigidity crust in the Krafla subsurface demonstrates that the observed ground deformation may be caused by pressure increase at similar level as observed in well KG-10, assuming the increase as representative for the whole geothermal reservoir. A pressurized source centre at 2.2 km depth and radius of 1.4 km reproduces the observed near-field deformation, if a local Young's modulus value is about 7 GPa, while its value is larger in the far-field domain (20–40 GPa).

Author contributions

C.L. and F.S. led the development of the ideas and modelling framework presented in this paper. The interpretation and comparison with other data sets were done by G.P.H., F.S., K.Á. and C.L. Analytical modelling with GBIS software was carried out by C.L. and M.M.P. Numerical modelling with the COMSOL Multiphysics software was carried out by C.L. Collection and analyses of geodetic data (GNSS and InSAR) was carried out by C.L, F.S., H.G., S.H., V.D, S.H. Seismic data were collected from the local seismic network operated by Iceland GeoSurvey (ÍSOR)/Landsvirkun and with stations operated by the Icelandic Meteorological Office (IMO), interpretation was led by K.Á. Gravity measurement analysis was carried out by G.P.H. and K.Á. All the authors contributed to evaluation of the modelling, discussion of the results and the writing of the paper.

Declaration of Competing Interest

The authors declare that they have no known competing financial interests or personal relationships that could have appeared to influence the work reported in this paper.

Data availability

Data will be made available on request.

Acknowledgements

We thank two anonimous reviewers and the editor Tobias P. Fischer for comments that helped us to improve the manuscript. We thank collaboration on the GNSS surveying in Krafla 2012-2019 with Delft University of Technology, through their summer course program for geodesy students, led by Sandra Verhagen, Paco Lopez Dekker, Hans van Der Marel, Ramon Hansen, and others. At University of Iceland, we thank technician Sveinbjörn Steinþórsson for excellent field support for the GNSS measurements, and Siqi Li for overseeing measurements in 2017-2020 during her Ph.D. Cécile Ducrocq is thanked for advice on GNSS operations and analysis. We thank Iceland GeoSurvey (ÍSOR) and Icelandic Met Office (IMO) and various staff members of these institutions, for the support and collaboration making this research possible. In particular we thank Ingvar Þór Magnússon for his part in acquiring and processing the gravity data. We thank Anette Kærgaard Mortensen for the helpful comments on the manuscript. We thank Landsvirkjun for providing the data regarding the geothermal power plant operations used in this work. The Generic Mapping Tools software (Wessel et al., 2013) and Matlab package (2021) were used to produce the figures in this paper.

Appendix A. Supplementary data

Supplementary data to this article can be found online at https://doi.org/10.1016/j.jvolgeores.2023.107849.

References

Ágústsson, K., Blanck, H., 2019. Krafla – Jarðskjálftar og niðurdæling. In: Iceland GeoSurvey, Report ÍSOR-2019/022.

Ágústsson, K., Árnadóttir, S., Flóvenz, Ó.G., 2012. Skjálftamælingar í Kröflu, Staðan í apríl 2012. In: Iceland GeoSurvey, Report ÍSOR-2012/18, LV-2012/058. In Icelandic.

Ali, S.T., Feigl, K.L., Carr, B.B., Masterlark, T., Sigmundsson, F., 2014. Geodetic measurements and numerical models of rifting in northern Iceland for 1993–2008. Geophys. J. Int. 196 (3), 1267–1280. https://doi.org/10.1093/gji/ggt462.

Altamimi, Z., Métivier, L., Rebischung, P., Rouby, H., Collilieux, X., 2017. ITRF2014 plate motion model. Geophys. J. Int. 209 (3), 1906–1912.

Ármannsson, H., Gudmundsson, Á., Steingrímsson, B.S., 1987. Exploration and development of the Krafla geothermal area. Jökull 37, 13–30.

Árnadóttir, T., Lund, B., Jiang, W., Geirsson, H., Björnsson, H., Einarsson, P., 2009. Glacial rebound and plate spreading: results from the first countrywide GPS observations in Iceland. Geophys. J. Int. 177, 691–716. https://doi.org/10.1111/j.1365-246X.2008.04059.x.

Árnason, K., 2020. New conceptual model for the magma-hydrothermal-tectonic system of Krafla, NE Iceland. Geosciences 2020 (10), 34. https://doi.org/10.3390/geosciences10010034.

Árnason, K., Magnússon, I.Th., 2001. *Niðurstöður Viðnámsmælinga í Kröflu* (in Icelandic). In: Report for Landsvirkjun, OS-2001/062.

Bagnardi, M., Hooper, A., 2018. Inversion of surface deformation data for rapid estimates of source parameters and uncertainties: a Bayesian approach. Geochem. Geophys. Geosyst. 19 (7), 2194–2211.

Bellucci, F., Woo, J., Kilburn, C.R., Rolandi, G., 2006. Ground deformation at Campi Flegrei, Italy: implications for hazard assessment. Geol. Soc. Spec. Publ. 269 (1), 141–157.

Björnsson, A., Saemundsson, K., Einarsson, P., Tryggvason, E., Grönvold, K., 1977. Current rifting episode in north Iceland. Nature 266, 318–323. https://doi.org/10.1038/266318a0.

Björnsson, A., Johnsen, G., Sigurdsson, S., Thorbergsson, G., Tryggvason, E., 1979. Rifting of the plate boundary in north Iceland 1975–1978. J. Geophys. Res. 84 (B6), 3029–3038.

Björnsson, A., Björnsson, G., Gunnarsson, Á., Þorbergsson, G., 1985. Breytingar á landhæð við Kröflu 1974–1984. (In Icelandic) In: Orkustofnun, Report OS-85019/JHD-05.67 s.

Boðvarsson, G.S., Pruess, K., Stefansson, V., Eliasson, E.T., 1984. The Krafla geothermal field, Iceland: 2. The natural state of the system. Water Resour. Res. 20, 1531–1544.

Brandsdóttir, B., Menke, W., Einarsson, P., White, R.S., Staples, R.K., 1997. Faroe-Iceland ridge experiment 2. Crustal structure of the Krafla central volcano. J. Geophys. Res. 102 (B4), 7867–7886.

Buck, W.R., Einarsson, P., Brandsdóttir, B., 2006. Tectonic stress and magma chamber size as controls on dike propagation: constraints from the 1975–1984 Krafla rifting episode. J. Geophys. Res. Solid Earth 111, B12404.

Cervelli, P.F., Fournier, T., Freymueller, J., Power, J.A., 2006. Ground deformation associated with the precursory unrest and early phases of the January 2006 eruption of Augustine Volcano. Alaska. Geophys. Res. Lett. 33, L18304. https://doi.org/10.1029/2006GL027219.

Chang, W.L., Smith, R.B., Farrell, J., Puskas, C.M., 2010. An extraordinary episode of Yellowstone caldera uplift, 2004–2010, from GPS and InSAR observations. Geophys. Res. Lett. 37, L23302.

Chiodini, G., Paonita, A., Aiuppa, A., et al., 2016. Magmas near the critical degassing pressure drive volcanic unrest towards a critical state. Nat. Commun. 7, 13712.

De la Cruz-Reyna, S., Yokoyama, I., Martinez-Bringas, A., Ramos, E., 2008. Precursory seismicity of the 1994 eruption of Popocatepetl Volcano, central Mexico. Bull. Volcanol. 70, 753–767.

De Zeeuw-van Dalfsen, E., Pedersen, R., Sigmundsson, F., Pagli, C., 2004. Satellite radar interferometry 1993–1999 suggests deep accumulation of magma near the crust-mantle boundary at the Krafla volcanic system. Iceland. Geophys. Res. Lett. 31, L13611.

De Zeeuw-van Dalfsen, E., Rymer, H., Williams-Jones, G., Sturkell, E., Sigmundsson, F., 2006. Integration of micro-gravity and geodetic data to constrain shallow system mass changes at Krafla Volcano, N Iceland. Bull. Volcanol. 68 (5), 420–431.

Del Negro, C., Currenti, G., Scandura, D., 2009. Temperature-dependent viscoelastic modeling of ground deformation: Application to Etna volcano during the 1993–1997 inflation period. Phys. Earth Planet. Inter. 172 (3), 299–309.

DeMets, C., Gordon, R.G., Argus, D.F., 2010. Geologically current plate motions. Geophys. J. Int. 181, 1–80. https://doi.org/10.1111/j.1365-246X.2009.04491.x.

Drouin, V., Sigmundsson, F., 2019. Countrywide observations of plate spreading and glacial isostatic adjustment in iceland inferred by Sentinel-1 radar interferometry, 2015–2018. Geophys. Res. Lett. 46, 8046–8055. https://doi.org/10.1029/2019GL082629.

Drouin, V., Sigmundsson, F., Ofeigsson, B.G., Hreinsdóttir, S., Sturkell, E., Einarsson, P., 2017. Deformation in the Northern Volcanic Zone of Iceland 2008–2014: an interplay of tectonic, magmatic, and glacial isostatic deformation. J. Geophys. Res. Solid Earth 122, 3158–3178.

Druitt, T.H., Kokelaar, B.P., 2002. The eruption of Soufriere Hills volcano, Montserrat, from 1995 to 1999. Geol. Soc. London 21, 45–69.

Ducrocq, C., Geirsson, H., Árnadóttir, T., Juncu, D., Drouin, V., Gunnarsson, G., Kristjánsson, B.R., Sigmundsson, F., Hreinsdóttir, S., Tómasdóttir, S., Blanck, H., 2021. Inflation-deflation episodes in the Hengill and Hrómundartindur volcanic complexes, SW Iceland. Front. Earth Sci. 9, 725109 https://doi.org/10.3389/feart.2021.725109.

Dzurisin, D., Lisowski, M., Wicks, C.W., 2009. Continuing inflation at Three Sisters volcanic center, central Oregon Cascade Range, USA, from GPS, leveling, and InSAR observations. Bull. Volcanol. 71 (10), 1091–1110. L045451.

Egilson, Þ., 2020. Eftirlitsmælingar í Kröflu, Bjarnarflagi og á Þeistareykjum árið 2020. Íslenskar orkurannsóknir. (In Icelandic). In: Report ÍSOR-2020/088, Landsvirkjun, LV-2020-038.
Eichelberger, J., 2020. Distribution and transport of thermal energy within magma–hydrothermal systems. Geosciences 10 (6), 212.
Einarsson, P., 1978. S-wave shadows in the Krafla caldera in NE-Iceland, evidence for a magma chamber in the crust. Bull. Volcanol. 41, 187–195.
Einarsson, P., 1991. The Krafla rifting episode 1975–1989. In: Garðarsson, A., Einarsson, A. (Eds.), Náttúra Mývatns. Icelandic Nature Science Society, Reykjavík, pp. 97–139.
Einarsson, P., Brandsdóttir, B., 1980. Seismological evidence for lateral magma intrusion during the July 1978 deflation of the Krafla volcano in NE-Iceland. J. Geophys. 47, 160–165.
Einarsson, K., Pálsson, B., Gudmundsson, Á., Hólmgeirsson, S., Ingason, K., Mattíasson, J., Hauksson, T., Ármannsson, H., 2010. Acid wells in the Krafla Geothermal Field. In: Proceedings World Geothermal Congress 2010, Bali, Indonesia, 25–29 April 2010, 2731, pp. 1–6.
Elders, W.A., Friðleifsson, G.Ó., Zierenberg, R.A., Pope, E.C., Mortensen, A.K., Guðmundsson, Á., Lowenstern, J.B., Marks, N.E., Owens, L., Bird, D.K., Reed, M., Olsen, N.J., Schiffman, P., 2011. Origin of a rhyolite that intruded a geothermal well while drilling at the Krafla volcano, Iceland. Geology 39, 231–234.
Feuillet, N., Cocco, M., Musumeci, C., Nostro, C., 2006. Stress interaction between seismic and volcanic activity at Mt Etna. Geophys. J. Int. 164, 697–718.
Fischer, T., Hrubcová, P., Salama, A., Doubravová, J., Ágústsdóttir, T., Gudnason, E.Á., Horálek, J., Hersir, G.P., 2022. Swarm seismicity illuminates stress transfer prior to the 2021 Fagradalsfjall eruption in Iceland. Earth Planet. Sci. Lett. 594, 117685.
Flóvenz, Ó.G., Ágústsson, K., Guðnason, E.Á., Kristjánsdóttir, S., 2015. Reinjection and induced seismicity in geothermal fields in Iceland. In: Proceedings World Geothermal Congress, Melbourne, Australia, 19–25 April 2015.
Flóvenz, Ó.G., Wang, R., Hersir, G.P., Dahm, T., Hainzl, S., Vassileva, M., Drouin, V., Heimann, S., Isken, M.P., Gudnason, E.Á., Ágústsson, K., Ágústsdóttir, T., Horálek, J., Motagh, M., Walter, T.R., Rivalta, E., Jousset, P., Krawczyk, C.M., Milkereit, C., 2022. Cyclical geothermal unrest as a precursor to Iceland's 2021 Fagradalsfjall eruption. Nat. Geosci. 15 (5), 397–404.
Foulger, G., Jahn, C.H., Seeber, G., et al., 1992. Post-rifting stress relaxation at the divergent plate boundary in Northeast Iceland. Nature 358, 488–490.
Friðleifsson, G.Ó., Ármannsson, H., Guðmundsson, Á., Árnason, K., Mortensen, A.K., Pálsson, B., Einarsson, G.M., 2014a. Site selection for the well IDDP-1 at Krafla. Geothermics 49, 9–15. https://doi.org/10.1016/j.geothermics.2013.06.001.
Friðleifsson, G.Ó., Elders, W.A., Albertsson, A., 2014b. The concept of the Iceland deep drilling project. Geothermics 49, 2–8.
Frolova, J., Ladygin, V., Rychagov, S., Zukhubaya, D., 2014. Effects of hydrothermal alterations on physical and mechanical properties of rocks in the Kuril–Kamchatka island arc. Eng. Geol. 183, 80–95.
Gottsmann, J., Rymer, H., 2002. Deflation during caldera unrest; constraints on subsurface processes and eruption prediction from gravity-height data. Bull. Volcanol. 64, 338–348.
Gudmundsson, Á., Mortensen, A.K., 2015. Well locations consideration of purpose objectives and achievement with emphasis on recent drilling in the Krafla geothermal area. In: Proc. World Geothermal Congress 2015. Melbourne, Australia, pp. 19–25.
Guðmundsson, Á., Steingrímsson, B., Ármannsson, H., Thórhallsson, S., 2008. An estimate of the state of well KJ-36, Krafla at the beginning of the year 2008. In: ÍSOR Memo,, 3 pp.
Guðnason, E.Á., Magnússon, R., Vilhjálmsson, A., Ágústsdóttir, T., Gunnarsson, K., 2021. Seismic Monitoring in Krafla, Þeistareykir and Námafjall. In: Report for Landsvirkjun. Report ÍSOR-2021/049.
Hamling, I.J., Wright, T.J., Calais, E., Lewi, E., Fukahata, Y., 2014. InSAR observations of post-rifting deformation around the Dabbahu rift segment, Afar, Ethiopia. Geophys. J. Int. 197, 33–49. https://doi.org/10.1093/gji/ggu003.
Hanks, T.C., Kanamori, H., 1979. A Moment Magnitude Scale. J. Geophys. Res. 84, 2348–2350.
Hauksson, T., 2019. Þeistareykir, Krafla og Bjarnarflag, Afköst borhola og efnainnihald vatns og gufu í borholum og vinnslurás árið 2018. Report LV-2019-026 (In Icelandic).
Heki, K., Foulger, G.R., Julian, B.R., Jahn, C.H., 1993. Plate dynamics near divergent boundaries: geophysical implications of post-rifting crustal deformation in NE Iceland. J. Geophys. Res. 98, 14279–14297.
Herring, T., King, R., McClusky, S., 2010. Introduction to GAMIT/GLOBK, Massachusetts Institute of Technology www-gpsg.mit.edu/tah/GGMatlab/.
Hersir, G.P., Sigmundsson, F., Ágústsson, K., Magnússon, I.Þ., Drouin, V., Vilhjálmsson, A.M., Lanzi, C., Li, S., Geirsson, H., Hreinsdóttir, S., 2020. Geodetic observation and surface deformation at Krafla in late 2019–2020. In: Report for Landsvirkjun LV-2020-036; report for ÍSOR-2020/037.
Hickey, J., Gottsmann, J., 2014. Benchmarking and developing numerical Finite Element models of volcanic deformation. J. Volcanol. Geotherm. Res. 280, 126–130.
Hill, D.P., Troise, C., De Natale, G., Kilburn, C.R.J., 2006. Unrest in Long Valley Caldera, California, 1978–2004. In: Mechanisms of activity and unrest at large calderas. Geol. Soc. Spec. Publ. 269, 1–24.
Hjartardóttir, Á., Einarsson, P., Bramham, E., Wright, T., 2012. The Krafla fissure swarm, Iceland, and its formation by rifting events. Bull. Volcanol. 74 (9), 2139–2153.
Jónasson, K., 1994. Rhyolite volcanism in the Krafla central volcano, Northeast Iceland. Bull. Volcanol. 56, 516–528.
Juncu, D., Árnadóttir, T., Geirsson, H., Guðmundsson, G.B., Lund, B., Gunnarsson, G., Hooper, A., Hreinsdottir, S., Michalczewska, K., 2018. Injection-induced surface deformation and seismicity at the Hellisheidi geothermal field, Iceland. J. Volcanol. Geotherm. Res. 391 https://doi.org/10.1016/j.jvolgeores.2018.03.019.
Kästner, F., Giese, R., Planke, S., Millett, J.M., Flóvenz, Ó.G., 2018. Seismic imaging in the Krafla high-temperature geothermal field, NE Iceland, using zero- and far-offset vertical seismic profiling (VSP) data. J. Volcanol. Geotherm. Res. 391, 106315.
Kim, D., Brown, L., Árnason, K., Gudmundsson, O., Ágústsson, K., Flovenz, O., 2020. Magma "bright spots" mapped beneath Krafla, Iceland, using RVSP imaging of reflected waves from microearthquakes. J. Volcanol. Geotherm. Res. 391, 106365.
Lyard, F., Lefevre, F., Letellier, T., Francis, O., 2006. Modelling the global ocean tides: modern insights from FES2004. Ocean Dyn. 56, 394–415.
Magnússon I.Þ., 2016. Þyngdarmælingar á Þeistareykjum í júlí til september 2015 og þyngdarkort af Kröflusvæði. Iceland GeoSurvey, Reykjavík, report, ÍSOR-2016/013 (In Icelandic).
Masterlark, T., Haney, M., Dickinson, H., Fournier, T., Searcy, C., 2010. Rheologic and structural controls on the deformation of Okmok Volcano, Alaska: FEMs, InSAR, and ambient noise tomography. J. Geophys. Res. 115, B02409.
McTigue, D.F., 1987. Elastic stress and deformation near a finite spherical magma body: resolution of the point source paradox. J. Geophys. Res. 92 (B12), 12931.
Millett, J.M., Planke, S., Kästner, F., Blischke, A., Hersir, G.P., Halldórsdóttir, S., Flóvenz, Ó.G., et al., 2018. Sub-surface geology and velocity structure of the Krafla high temperature geothermal field, Iceland: Integrated ditch cuttings, wireline and zero offset vertical seismic profile analysis. J. Volcanol. Geotherm. Res. 391, 106342.
Mogi, K., 1958. Relations between the eruptions of various volcanoes and the deformations of the ground surface around them. Bull. Earthq. Res. Inst., Univ. Tokyo 36, 99–134.
Mortensen, A.K., Grönvold, K., Guðmundsson, Á., Steingrímsson, B., Egilson, Þ., 2010. Quenched Silicic Glass from Well KJ-39 in Krafla, North-Eastern Iceland. In: Proceedings of the World Geothermal Congress 2010, Bali, Indonesia, 25–29 April 2010, pp. 1–6.
Mortensen, A.K., Egilson, Th., Gautason, B., Árnadóttir, S., Gudmundsson, Á., 2014. Stratigraphy, alteration mineralogy, permeability and temperature conditions of well IDDP-1, Krafla, NE-Iceland. Geothermics 49, 31–41.
Nicholson, H., Condomines, M., Fitton, J.G., Fallick, A.E., Grönvold, K., Rogers, G., 1991. Geochemical and isotopic evidence for crustal assimilation beneath Krafla, Iceland. J. Petrol. 32, 1005–1020.
Nielsen, G., Maack, R., Gudmundsson, Á., Gunnarsson, G.I., 2000. Completion of Krafla geothermal power plant. In: Proc. World Geothermal Congress 2000, Kyushu-Tohoku, Japan, May 28–June 10, 2000, pp. 3259–3264.
Nooner, S.L., Bennati, L., Calais, E., Buck, W.R., Hamling, I.J., Wright, T.J., Lewi, E., 2009. Post-rifting relaxation in the Afar region, Ethiopia. Geophys. Res. Lett. 36 (21), L21308.
Okada, Y., 1985. Surface deformation to shear and tensile faults in a halfspace. Bull. Seismol. Soc. Am. 75 (4), 1135–1154.
Óskarsson, F., Óladóttir, A.A., 2020. Leirhnjúkur: Gasstyrkur í gufu og gasflæði um jarðveg. (In Icelandic). In: Iceland GeoSurvey. Report ÍSOR/Landsvirkjun, ÍSOR-2004.
Parks, M., Biggs, J., England, P., Mather, T., Nomikou, P., Palamartchouk, K., Papanikolaou, X., et al., 2012. Evolution of Santorini Volcano dominated by episodic and rapid fluxes of melt from depth. Nat. Geosci. 5 (10), 749–754.
Pollitz, F., Sacks, I.S., 1996. Viscosity structure beneath northeast Iceland. J. Geophys. Res. 101 (B8), 17771–17793.
Pope, E.C., Bird, D.K., Arnorsson, S., 2013. Evolution of low- ^{18}O Icelandic crust. Earth Planet. Sci. Lett. 374, 47–59.
Portier, N., Hinderer, J., Bernard, J.D., 2018. Report on the 2017–2018 Relative (Scintrex CG5) Micro-Gravity Measurements at the Theistareykir Geothermal Plant. IPGS (Institut de Physique du Globe de Strasbourg), Université de Strasbourg/CNRS, France.
Reiser, F., Schmelzbach, C., Sollberger, D., Maurer, H., Greenhalgh, S., Planke, S., Kästner, F., Flóvenz, Ó., Giese, R., Halldórsdóttir, S., Hersir, G.P., 2020. Imaging the high-temperature geothermal field at Krafla using vertical seismic profiling. J. Volcanol. Geotherm. Res. 391, 106474.
Rooyakkers, S., Stix, J., Berlo, K., Petrelli, M., Hampton, R.L., Barker, S.J., Morgavi, D., 2021. The origin of rhyolitic magmas at Krafla central Volcano (Iceland). J. Petrol. 62 (8), 1–27.
Rosen, P.A., Gurrola, E., Sacco, G.F., Zebker, H., 2012. The InSAR scientific computing environment. In: Proceedings of the 9th European Conference on Synthetic Aperture Radar, pp. 730–733.
Rymer, H., 1994. Microgravity change as a precursor to volcanic activity. J. Volcanol. Geotherm. Res. 61, 311–328. https://doi.org/10.1016/0377-0273(94)90011-6.
Rymer, H., Cassidy, J., Locke, C.A., Sigmundsson, F., 1998. Post-eruptive gravity changes from 1990 to 1996 at Krafla volcano, Iceland. J. Volcanol. Geotherm. Res. 87 (1–4), 141–149.
Sæmundsson, K., 1991. Jarðfræði Kröflukerfisins (in Icelandic). In: Garðarsson, A., Einarsson, Á. (Eds.), Náttúra Mývatns. Icelandic Nature Sci. Soc, Reykjavík, pp. 24–95.
Sæmundsson, K., Gudmundsson, G., Pálmason, G., Grönvold, K., Ragnars, K., Arnórsson, S., 1971. Námafjall – Krafla, preliminary investigations of the high temperature areas. (in Icelandic). In: Orkustofnun Report 121p.
Schuler, J.T., Greenfield, R.S., White, S.W., Roecker, B., Brandsdóttir, J.M., Stock, J., Tarasewicz, H., Martens, H.R., Pugh, D., 2015. Seismic imaging of the shallow crust beneath the Krafla central volcano, NE Iceland. J. Geophys. Res. Solid Earth 120, 7156–7173.
Sigmundsson, F., Vadon, H., Massonnet, D., 1997. Readjustment of the Krafla spreading segment to crustal rifting measured by satellite radar interferometry. Geophys. Res. Lett. 24 (15), 1843–1846.

Sigmundsson, F., Hooper, A., Hreinsdóttir, S., et al., 2015. Segmented lateral dyke growth in a rifting event at Bárðarbunga volcanic system, Iceland. Nature 517 (7533), 191–195.
Sigmundsson, F., Einarsson, P., Hjartardóttir, Á., Drouin, V., Jonsdottir, K., Árnadóttir, T., Geirsson, H., Hreinsdottir, S., Li, S., Ófeigsson, B., 2020. Geodynamics of Iceland and the signatures of plate spreading. J. Volcanol. Geotherm. Res. 391, 106436.
Sigmundsson, F., Parks, M., Hooper, A., et al., 2022. Deformation and seismicity decline before the 2021 Fagradalsfjall eruption. Nature 609, 523–528.
Stefánsson, V., 1981. The Krafla geothermal field, Northeast Iceland. In: Geothermal Systems: Principles and Case Histories, pp. 273–293. Chapter 10.
Sturkell, E., Sigmundsson, F., Geirsson, H., Ólafsson, H., Theodórsson, T., 2008. Multiple volcano deformation sources in a post-rifting period: 1989–2005 behaviour of Krafla, Iceland constrained by levelling, tilt and GPS observations. J. Volcanol. Geotherm. Res. 177, 405–417.
Trasatti, E., Giunchi, C., Bonafede, M., 2003. Effects of elastic and rheological layering on ground deformation in volcanic regions. J. Volcanol. Geotherm. Res. 122, 89–110.
Tryggvason, E., 1994. Surface deformation at the Krafla volcano, North Iceland, 1982–1992. Bull. Volcanol. 56, 98–107.
Völksen, C., 2000. Die Nutzung von GPS für die Deformationsanalyse in regionalen Netzen amn Beispiel Islands. Ph.D. thesis,. In: Wissenschaftliche Arbeiten der Fachrichtung Vermessungswesen der Universität Hannover, Nr. 237, Hannover, Germany.
Wessel, P., Smith, W.H.F., Scharroo, R., Luis, J., Wobbe, F., 2013. Generic mapping tools: Improved version released. EOS Trans. Am. Geophys. Union 94 (45), 409–410.
Wright, T., Sigmundsson, F., Pagli, C., et al., 2012. Geophysical constraints on the dynamics of spreading centres from rifting episodes on land. Nat. Geosci. 5, 242–250.
Yamasaki, T., Sigmundsson, F., Iguchi, M., 2019. Viscoelastic crustal response to magma supply and discharge in the upper crust: Implications for the uplift of the Aira caldera before and after the 1914 eruption of the Sakurajima volcano. Earth Planet. Sci. Lett. 531, 115981.
Yang, X.M., Davis, P.M., Dieterich, J.H., 1988. Deformation from inflation of a dipping, finite, prolate ellipsoid in an elastic half-space. J. Geophys. Res. 93, 4249–4258.
Zierenberg, R.A., Schiffman, P., Barfod, G.H., Lesher, C.E., Marks, N.E., Lowenstern, J.B., Mortensen, A.K., Pope, E.C., Bird, D.K., Reed, M.H., Fridleifsson, G.O., Elders, W.A., 2013. Composition and origin of rhyolite melt intersected by drilling in the Krafla geothermal field, Iceland. Contrib. Mineral. Petrol. 165, 327–347.
Zumberge, J.F., Heflin, M.B., Jefferson, D.C., Watkins, M.M., Webb, F.H., 1997. Precise point positioning for the efficient and robust analysis of GPS data from large networks. J. Geophys. Res. 102, 5005–5017.

Supplementary material for

Pressure increase at the magma-hydrothermal interface at Krafla caldera, North-Iceland, 2018-2020: magmatic processes or hydrothermal changes?

Chiara Lanzi (1), Vincent Drouin (2), Freysteinn Sigmundsson (1), Halldór Geirsson (1), Gylfi Páll Hersir (3, 6), Kristján Ágústsson (3, 6), Michelle Maree Parks (2), Sigrún Hreinsdóttir (4), Ásgrímur Guðmundsson (5, 6)

(1) Nordic Volcanological Center, Institute of Earth Sciences, University of Iceland, (2) Icelandic Meteorological Office, Reykjavik, Iceland, (3) ÍSOR – Iceland GeoSurvey, Reykjavik, Iceland, (4) GNS Science, Lower Hutt, New Zealand, (5) Landsvirkjun, Reykjavik, Iceland, (6) Presently: Independent researcher, Reykjavík, Iceland

*Corresponding author
Email address: chl7@hi.is

Table of content:

Text S1. Studies on regional rigidity in Iceland

Different quantitative estimates of the elastic parameters for the Icelandic crust are available from geodetic observations. Grapenthin et al. (2006) found a correlation between annual variation of land elevation in continuous GNSS time series and the predicted ground response to annual snow load. They derive an Earth model to explain their observations with Young's modulus $E = 40 \pm 15$ GPa, assuming the Earth behaves as a uniform elastic half-space with a Poisson's ratio, $\nu = 0.25$. Auriac et al. (2014) studied ground deformation induced by a glacier surge (sudden surface load changes associated with ice transfer). They solve for the best-fitting values of E and ν by comparing observed deformation from InSAR data and deformation field calculated from a finite element model. Their favoured model has two elastic layers, an upper 1 km-thick layer with $\nu = 0.17$ and $\nu = 0.25$ for the lower layer. They found best-fitting values of $E = 12.9$-15.3 GPa in the upper layer and $E = 67.3$-81.9 GPa in the lower layer (95% confidence intervals). Drouin et al. (2016) used a similar approach as Grapenthin et al. (2006) but with a larger network of GNSS sites all over Iceland and evaluated the annual and semi-annual components of the cycle in the horizontal and vertical components. They used elastic parameters inferred from the preliminary reference Earth model (PREM, Dziewonski and Anderson, 1981) derived from seismological observations. They found there was a need to apply a scaling factor of 2.3 ± 0.6 to the PREM elastic parameters, to produce a fit between observed and predicted annual change in land elevation in Iceland. The PREM model provides values of elastic parameters for the whole Earth, but our modelling depends only on their values close to the surface. The scaled PREM Young's modulus values found by Drouin et al. (2016) for the topmost 15 km of the crust is 29.7 GPa.

Text S2. InSAR down sampling

Prior to the inversion with GBIS, the InSAR data were subsampled using a gradient-based quadtree sampling method (Jónsson et al., 2002; Decriem et., 2010). The algorithm divides the data in sets of

$$U_z = C\ \frac{d}{(r^2+d^2)^{3/2}}$$

$$U_{\mathrm{r}} = C\ \frac{\mathrm{r}}{(\mathrm{r}^2+\mathrm{d}^2)^{3/2}}$$

Δ

pressure change, Δ

$$C = \frac{1-v}{\pi}\ \Delta V$$

$$C = \frac{1-v}{\mu} a^3\ \Delta P \qquad C = \frac{2(1-v^2)}{\mathrm{E}} a^3\ \Delta P$$

μ is the Young's modulus and is the Poisson's ratio

assumed to be 0.25 in our models). The Young's modulus is related to the shear modulus through:

$$E = 2\mu(1+v)$$

$$RMS = \sqrt{\frac{\sum(d_{obs} - d_{pre})^2}{N}}$$

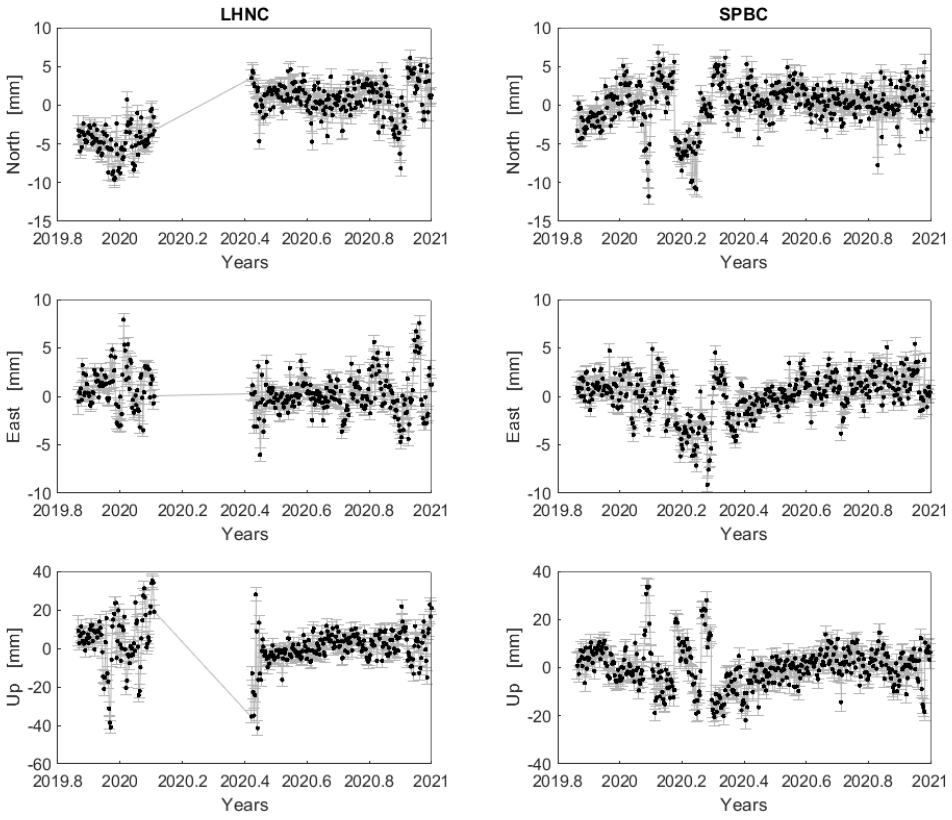

Fig. S1. GNSS time series for LHNC (left) and SPBC (right) stations in Krafla in the IGS 2014 reference frame. Linear trends are only removed, as the time series are too short to estimate their seasonal signals. Part of the LHNC times series has been excluded when the antenna was buried by snow.

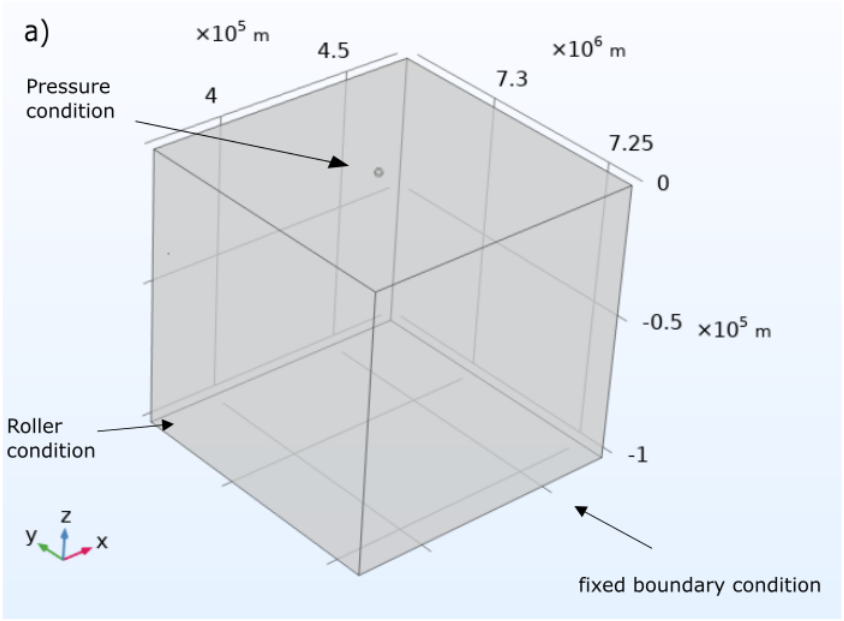
a)
×10^5 m
4.5
×10^6 m
7.3
Pressure condition
4
7.25
0
-0.5
×10^5 m
Roller condition
-1
z
y
x
fixed boundary condition

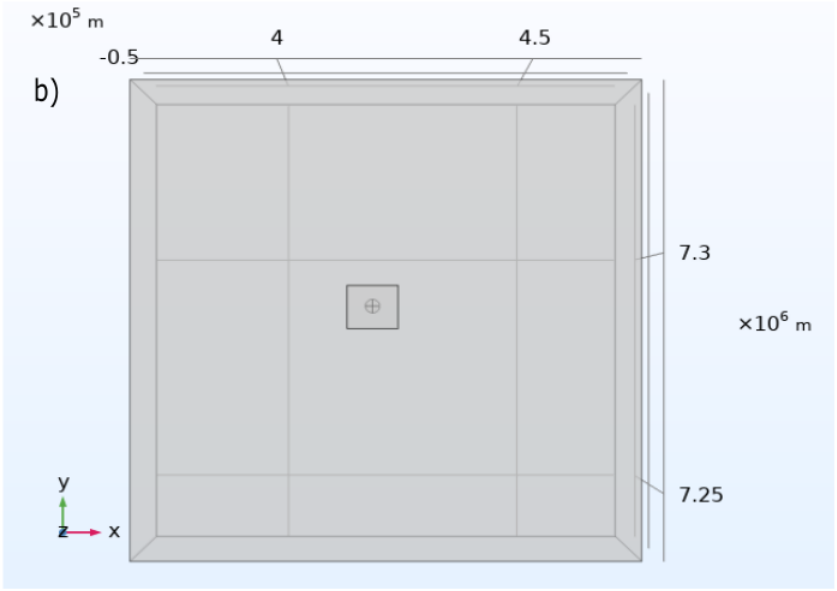
×10^5 m
4
4.5
-0.5
b)
7.3
×10^6 m
y
z
x
7.25

× ×

ΔP

7

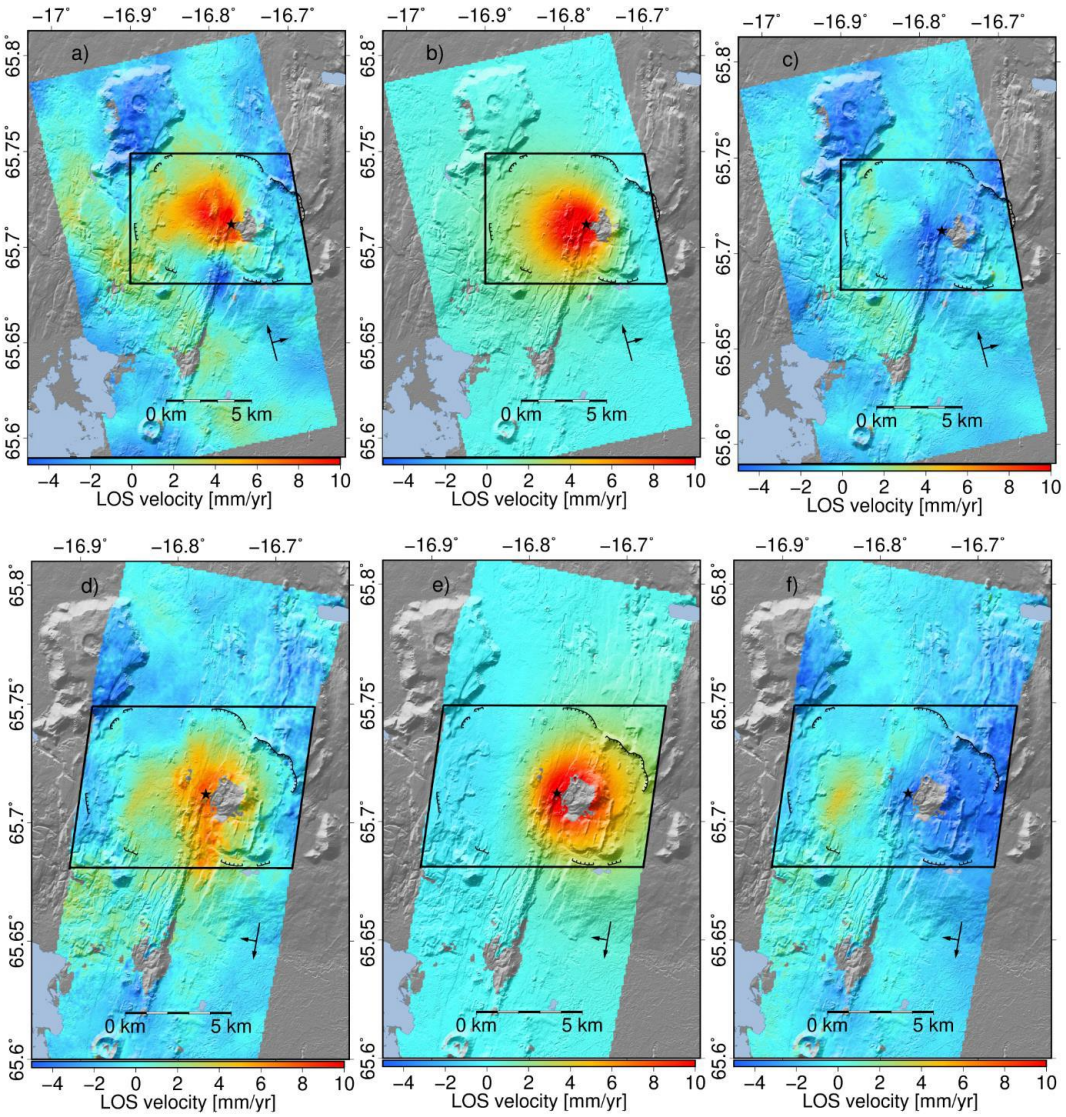

Fig. S3. LOS difference velocity data (a, d), predicted best-fit model results from GBIS (b, e) and residuals (c, f) for track T147 (upper panels) and track T111 (lower panels). The black polygons marks the area used to evaluate the root mean square value. The black star indicates the inferred best-fit position for the centre source.

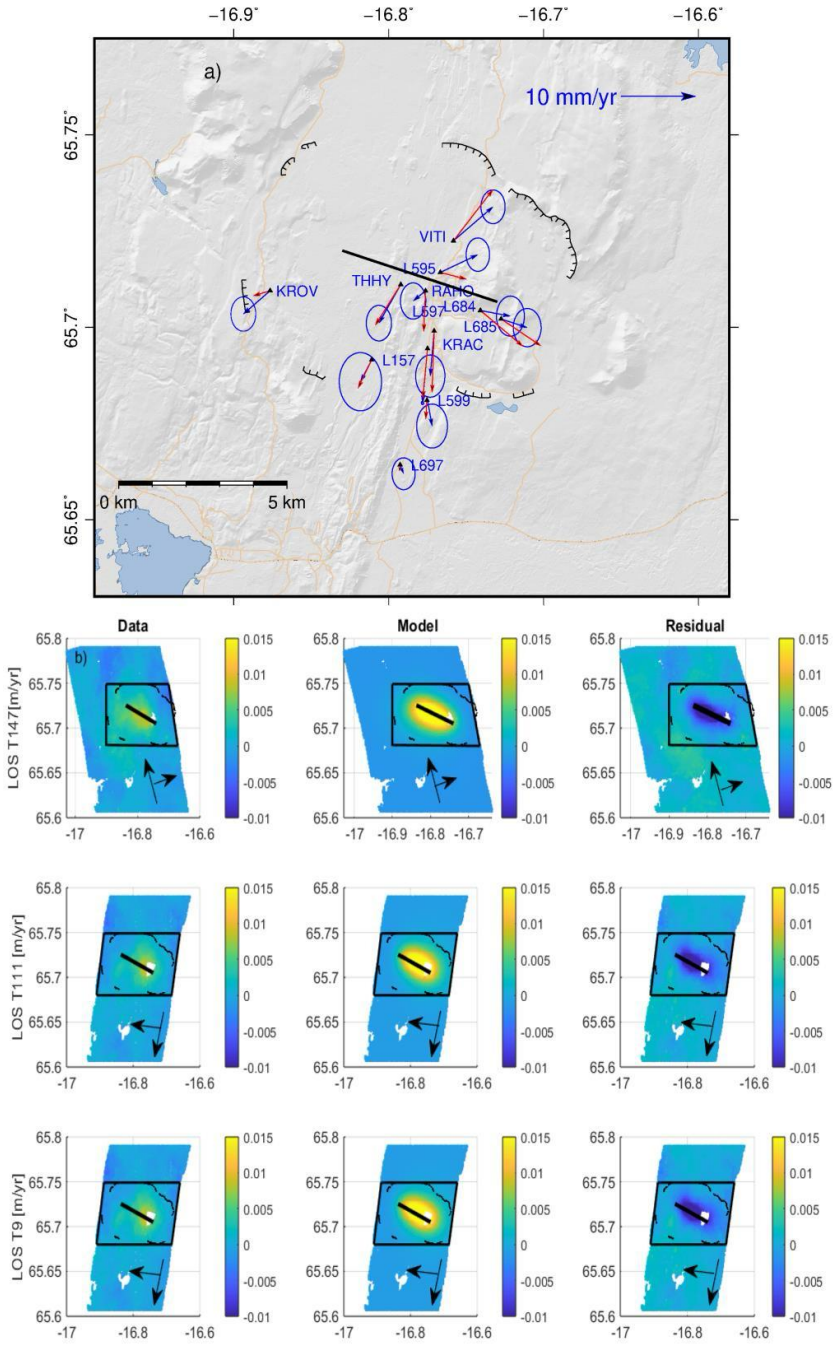

Fig. S4. Comparison between predicted displacements for a best fitting sill model and observations. (upper) GNSS horizonal displacements (blue arrows) and model predictions (red arrows). The black star indicates the inferred best-fit position for the source. (lower) InSAR LOS change (left), best fit model predictions (middle) and residuals (right) for InSAR tracks T147, T111, T9. The black polygons marks the area used to evaluate the root mean square value.

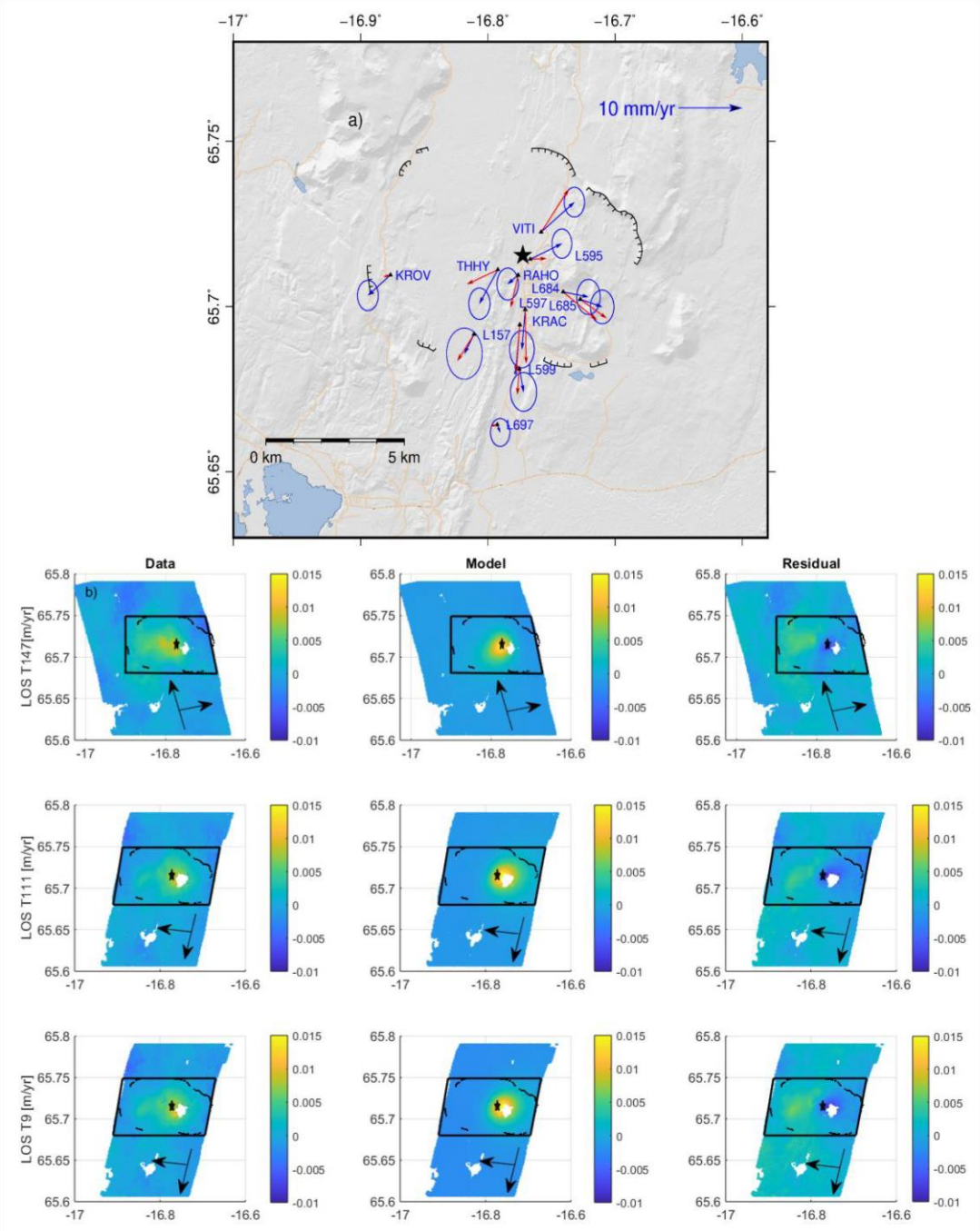

Fig. S5. Comparison between predicted displacements for a best fitting sill model and observations. (upper) GNSS horizonal data (blue arrows) and model predictions (red arrows). The black star indicates the inferred best-fit position for the source. (lower) InSAR LOS change (left), best fit model predictions (middle) and residuals (right) for InSAR tracks T147, T111, T9. The black polygons marks the area used to evaluate the root mean square value.

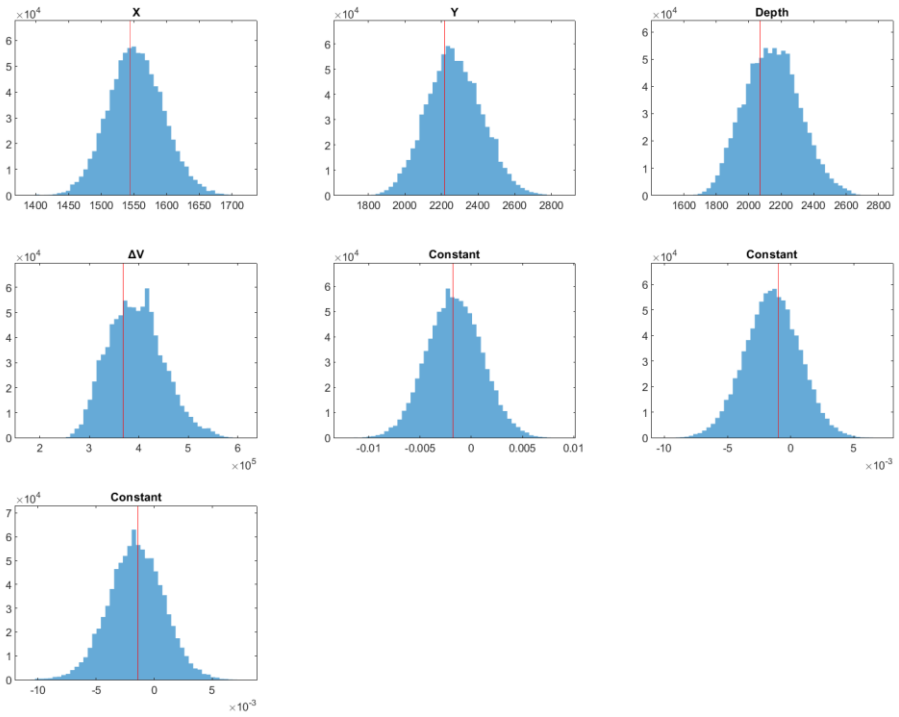

Fig. S6. Inferred probability density functions for Mogi best fit model parameters (GBIS). Source location (X and Y), depth and volume change (ΔV). Also inferred are three offset parameters (InSAR Const.) for each of the InSAR satellite tracks used, as the input velocity fields may have an arbitrary offset.

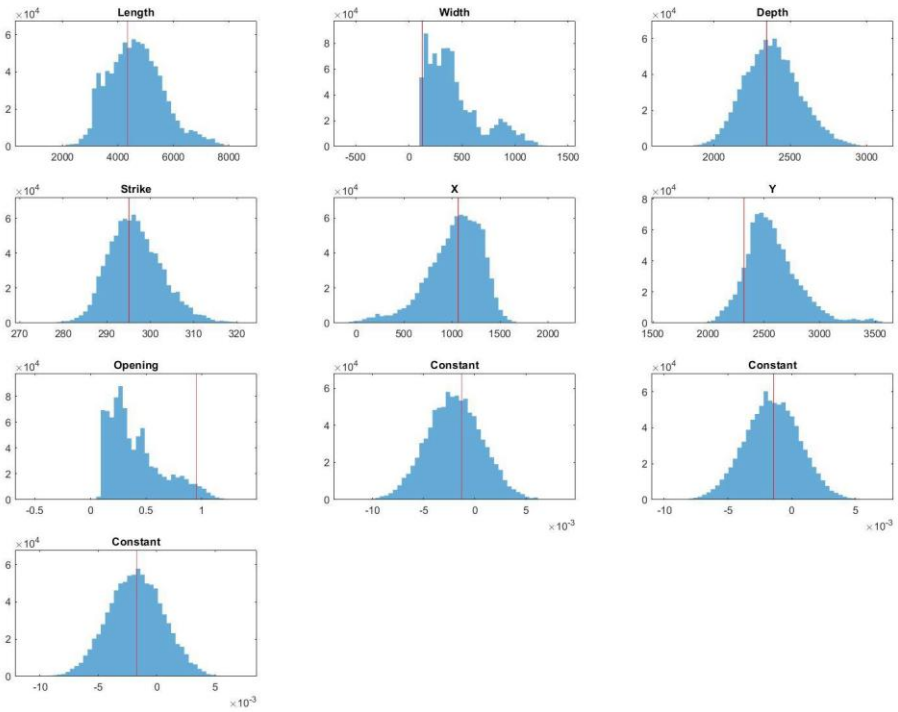

Fig. S7. Inferred probability density functions for sill best fit model parameters (GBIS). Source location (X and Y), source depth, length, width and opening of the sill. Also inferred are three offset parameters (InSAR Const.) for each of the InSAR satellite tracks used, as the input velocity fields may have an arbitrary offset.

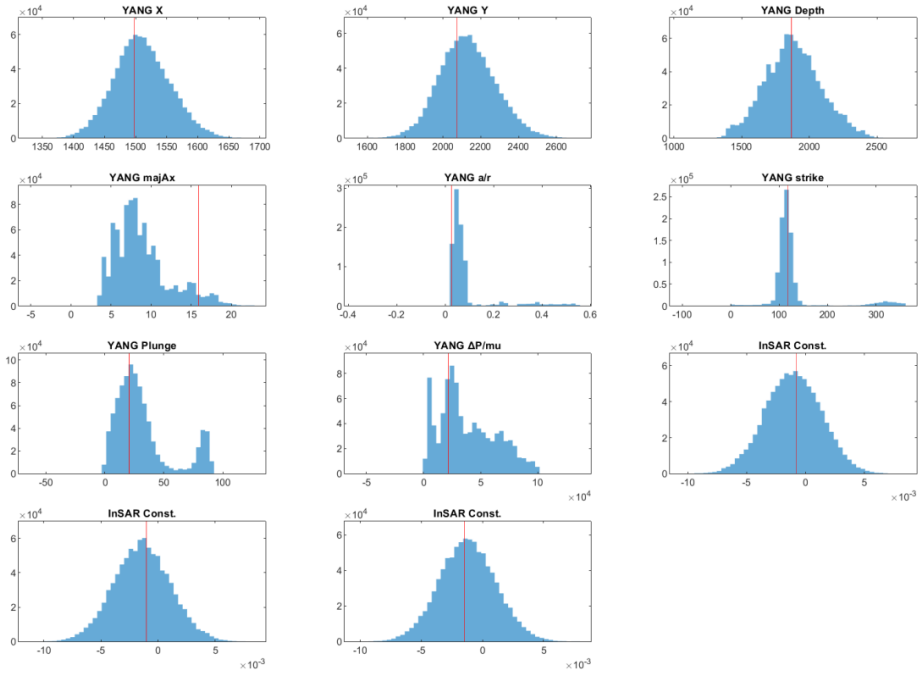

Fig. S8. Inferred probability density functions for prolate spheroid best fit source model parameters (GBIS). Source location (X and Y), source depth, length of major semi-axis in meters and dimensionless aspect ratio between semi-axes (minor/major, A and A/B); strike angle of major semi-axis with respect to North in degrees; plunge, inclination angle of major semi-axis with respect to horizontal in degrees (0° = horizontal; 90° = vertical); ΔP/mu, dimensionless excess pressure (pressure change/shear modulus). Also inferred are three offset parameters (InSAR Const.) for each of the InSAR satellite tracks used, as the input velocity fields may have an arbitrary offset.

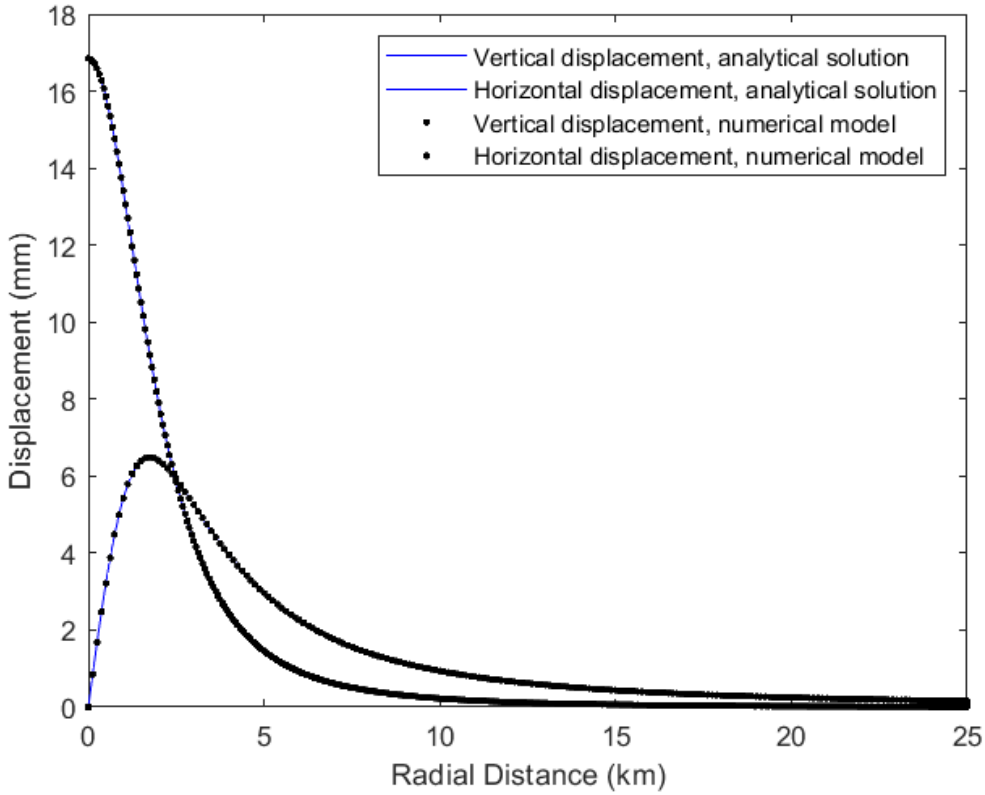

Fig. S9. Displacement according to Mogi best fit solution (blue lines, GBIS). Also shown is a numerical solution from the COMSOL software (black circles).

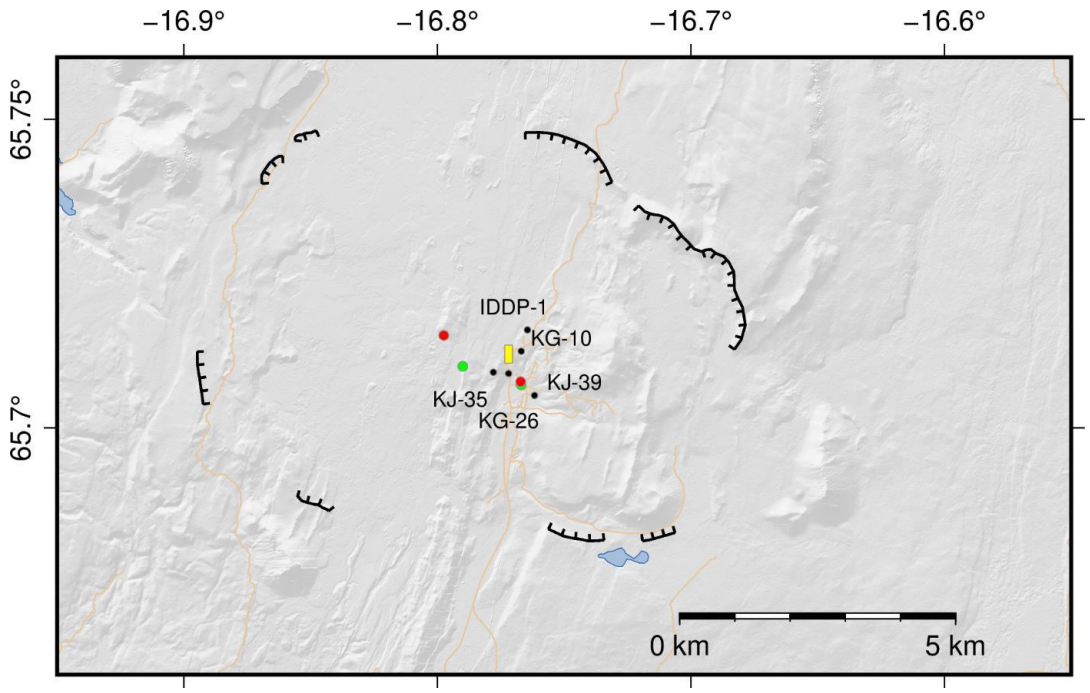

Fig. S10. Estimated location of Mogi deformation source from GBIS inversion (yellow rectangle). The area of the rectangle shows the 95% confidence interval for horizontal location. Green circles show Mogi sources from Sturkell et al. (2008) and red from Drouin et al. (2017). Black circles show the re-injected well KJ-35, KG-26 and KJ-39, the IDDP-1 borehole, and the monitoring well, KG-10.

Table S1. Root mean square evaluation (RMS) for the best fit GBIS point-pressure, sill and spheroid source.

LOS RMS (mm/yr)	Point-pressure	Spheroid	Sill-like
with predicted displacements=0	2.74	2.74	2.74
Residual	2.56	2.89	4.01

Table S2. Location of the Mogi best fit result (GBIS) in the Krafla area from this and previous studies.

Model parameter	Lon (°)	Lat (°)	Depth (km)
This study	-16.77	65.71	2.1-2.5
Sturkell et al. (2008) Leirhnjúkur area	-16.79	65.71	~ 2.5
Drouin et al. (2017) Leirhnjúkur area	-16.79	65.72	~ 2.5
Sturkell et al. (2008) Leirbotnar area	-16.76	65.72	~ 1.5
Drouin et al. (2017) Leirbotnar area	-16.76	65.70	~ 1.5

Supplementary references

Auriac, A., Spaans, K. H., Sigmundsson, F., Hooper, A., Schmidt, P., Lund, B., 2014. Iceland rising: Solid Earth response to ice retreat inferred from satellite radar interferometry and viscocelastic modeling. Journal of Geophysical Research: Solid Earth, 118, 1331– 1344.

Decriem, J., Árnadóttir, T., Hooper, A., Geirsson, H., Sigmundsson, F., Keiding, M., Ófeigsson, B. G., Hreinsdóttir, S., Einarsson, P., LaFemina, P., Bennett, R. A., 2010. The 2008 May 29 earthquake doublet in SW Iceland. Geophysical Journal International, 181 (2), 1128–1146.

Drouin, V., Heki, K., Sigmundsson, F., Hreinsdóttir, F., Ofeigsson, B. G., 2016. Constraints on seasonal load variations and regional rigidity from continuous GPS measurements in Iceland, 1997–2014. Geophysical Journal International, 205 (3), 1843– 1858.

Dziewonski A.M., Anderson D. L., 1981. Preliminary reference Earth model, Physics of the Earth and Planetary Interiors, 25, 297-356, ISSN 0031-9201.

Grapenthin R., Sigmundsson F., Geirsson H., Árnadóttir T., Pinel, V., 2006. Icelandic rhythmics: annual modulation of land elevation and plate spreading by snow load. Geophys. Res. Lett., 33, L24305. doi:10.1029/2006GL028081

Jónsson, S., 2002. Fault Slip Distribution of the 1999 Mw 7.1 Hector Mine, California, Earthquake, Estimated from Satellite Radar and GPS Measurements. Bull. Seismol. Soc. Amer., 92. 1377-1389.

Mogi K., 1958. Relations between the eruptions of various volcanoes and the deformations of the ground surface around them. Bull. Earthquake Res. Inst. Univ. Tokyo, 36, 99–134.

Lisowski M., 2007. Analytical Volcano Deformation Source Models. Berlin, Heidelberg: Springer Praxis Books, 279–304. chap. 8. doi:10.1007/978-3-540- 49302-0_8

Sigmundsson F., 2006. Iceland Geodynamics, Crustal Deformation and Divergent Plate Tectonics. Springer Verlag and Praxis Publishing, 209 pp.

Paper II

Strain Localization at Volcanoes Undergoing Extension: Investigation of Long-term Deformation at Krafla and Askja Volcanic Systems in North Iceland

Chiara Lanzi, Freysteinn Sigmundsson, Michelle Maree Parks, Halldór Geirsson, Vincent Drouin

Geophysical Research Letters

https://doi.org/10.1029/2024GL110299

AGU ADVANCING EARTH AND SPACE SCIENCES

Geophysical Research Letters®

RESEARCH LETTER
10.1029/2024GL110299

Strain Localization at Volcanoes Undergoing Extension: Investigation of Long-Term Deformation at Krafla and Askja Volcanic Systems in North Iceland

Chiara Lanzi[1], **Freysteinn Sigmundsson**[1], **Michelle Maree Parks**[2], **Halldór Geirsson**[1], **and Vincent Drouin**[2]

[1]Nordic Volcanological Center, Institute of Earth Sciences, University of Iceland, Reykjavík, Iceland, [2]Icelandic Metereological Office, Reykjavík, Iceland

Key Points:

- Gradual deflation (mm to cm per year) over decades has been observed at the Krafla and Askja volcanic systems in Iceland
- Numerical models show that deflation is induced by stretching across volcanic systems and dependent on their crustal rheological anomalies
- For the 2015–2018 period, an extensional model can broadly explain observed deflation at Krafla, but only ~25%–30% at the Askja caldera

Supporting Information:

Supporting Information may be found in the online version of this article.

Correspondence to:

C. Lanzi,
chl7@hi.is

Citation:

Lanzi, C., Sigmundsson, F., Parks, M. M., Geirsson, H., & Drouin, V. (2024). Strain localization at volcanoes undergoing extension: Investigation of long-term deformation at Krafla and Askja volcanic systems in North Iceland. *Geophysical Research Letters*, *51*, e2024GL110299. https://doi.org/10.1029/2024GL110299

Received 16 MAY 2024
Accepted 20 SEP 2024

Abstract Volcanoes in extensional environments may show gradual subsidence over decades during quiescent periods, due to various processes such as magma withdrawal, cooling, contraction, plate spreading and viscoelastic response. If significant rheological anomalies reside in volcano roots, due to the presence of magma and hot rock, they can influence the style of deformation. We use Finite Element Method (FEM) models to explore how strain localization due to extension can lead to volcano deflation. We apply rheological models comprising an elastic layer overlying a viscoelastic domain and include local up-doming regions of low viscosity material beneath volcanic centers. The models reveal a localized subsidence above the rheological anomaly, influenced by the tectonic extension, and by the up-doming volume and its viscosity. The models suggest that plate divergence may account for 4–5 mm/yr of observed subsidence at Krafla and Askja volcanic systems (KVS and AVS, respectively) in North Iceland.

Plain Language Summary Extensional stretching may have an important effect on the ground deformation observed at volcanic systems located along a divergent boundary. The physical properties of the crust are altered by the presence of hot material and/or geothermal activity at central volcanoes, compared to the surrounding rocks. We use a two-layer model consisting of an elastic crustal volume overlying a viscoelastic layer, which locally reaches shallower depth (referred to up-doming material), to investigate such crustal properties beneath volcanic systems. We explore a wide range of viscosity values in the up-doming material and elastic layer thickness. The models, applied to investigate observed ground deformation at the Krafla and Askja volcanic systems, suggests that regional stretching with realistic material properties in the crust beneath the volcanic system, fits quite well the observed deformation satellite data at Krafla volcanic system in the 2015–2018 observations, but only a minor contributor to the Askja deformation pattern in the same period. Our modeling approach suggests that any extensive magmatic system undergoing stretching should feature subsidence in relation to the presence of hot material/magma mush beneath volcanic systems.

1. Introduction

Extensional zones occur in different tectonic settings: continental rifts, back-arc basins, and divergent plate boundaries on mid-oceanic ridges. Although rifting events have been instrumentally monitored on the ocean floor (e.g., Chadwick et al., 2016; Tolstoy et al., 2006), it is difficult to monitor the deformation associated with the whole process of spreading. Studies at subaerial extensionalzones are therefore important, such as in Iceland (e.g., Árnadóttir et al., 2009; Drouin & Sigmundsson, 2019) and in Afar, East Africa (e.g., Biggs et al., 2009; Cattin et al., 2006).

Magmatic activity in these areas is focused at volcanic systems, often composed of narrow zones of extensive faulting in fissure swarms and central volcanoes with calderas and geothermal activity (e.g., Ayele et al., 2007; Einarsson & Brandsdóttir, 2021). High-temperature rheological anomalies in the subsurface, due to the presence of liquid magma and magma mush (Liao et al., 2018; Sparks & Cashman, 2017) heat significant volumes of rock, influencing physical properties. Thus, viscoelastic rheology may be appropriate to describe the crustal behavior at depth in volcanic systems, rather than an elastic approach. Different modeling approaches have been used to incorporate viscoelastic response of the crust, including focusing on the effects of a viscoelastic shell, surrounding a magmatic source (Del Negro et al., 2009); a horizontally layered medium with for example, an elastic plate over a uniform viscoelastic half-space (e.g., Yamasaki et al., 2018); and a temperature-dependent viscosity structure

(Hickey et al., 2016). Predicted ground deformation of such models compared to geodetic measurements have been used to evaluate best-fit solutions at different volcanoes. Viscosities in the range of 10^{16}–10^{19} Pa s are usually employed in the viscoelastic shell approach (Currenti & Williams, 2014; Newman et al., 2001, 2006). Two-layer models have found viscosity in the range of $\sim10^{17}$–10^{19} Pa s for the lower viscoelastic layer (Grapenthin et al., 2010; Hamling et al., 2014; Pearse & Fialko, 2010); while, thermo-mechanical models derive a lower viscosity, in the range of $\sim10^{14}$–10^{16} Pa s, around the magmatic source and at deeper levels in such models (>25–30 km), where temperatures are estimated in the range of 800°C–1,300°C (Gottsmann & Odbert, 2014). Newman et al. (2001), from laboratory experiments on partially crystallized silicate melt (Lejeune & Richet, 1995) and partially melted granites (van der Molen and Paterson, 1979) inferred that viscosity for crystallized rhyolite at or near the solidus temperature (~670°) is in the range of $\sim10^{15}$–10^{17} Pa s and viscosities for quartz-bearing crystalline rock around a liquid magma body, heated to ~500°C–600°C, in the range of 10^{17}–10^{19} Pa s.

We investigate here the ground deformation at volcanic systems undergoing extensional stretching with three-dimensional (3D) FEM models, considering material properties of volcanic plumbing systems. We evaluate how rheological anomalies undergoing extension may lead to surface deflation. We fit model predictions to observed long-term deformation at the KVS and AVS in Iceland, inferred from Interferometric Synthetic Aperture Radar (InSAR) time series covering the 2015–2018 period (Drouin & Sigmundsson, 2019).

2. Geological Setting and Ground Deformation

The Northern Volcanic Zone (NVZ) of Iceland (Figure 1) is a part of the Eurasian–North American divergent plate boundary, with a spreading rate of ~17.4 mm/yr in direction N104.5°E, according to plate motion models (DeMets et al., 2010). Global Navigation Satellite System (GNSS) geodetic observations in the 1993–2004 and the 2008–2014 periods give a comparable spreading rate (Árnadóttir et al., 2009; Drouin, Sigmundsson, Ófeigsson, et al., 2017). The plate divergence is accommodated by ~50 km-wide zone (Drouin, Sigmundsson, Ófeigsson, et al., 2017). The volcanic systems are (north to south): Theistareykir, Krafla, Fremrinámar, Askja, and Kverkfjöll (Figure 1). Several plate spreading models in Iceland attempt to explain deformation using horizontal crustal layers (e.g., Jónsson et al., 1997; LaFemina et al., 2005). On the other hand, Pedersen et al. (2009), with FEM models, link the observed inter-rifting deformation field to rheological variations within the en-echelon arrangement of the fissure swarms in the NVZ. In Iceland, glacial isostatic adjustment (GIA) produces also regional deformation (Árnadóttir et al., 2009). InSAR-based analysis shows a maximum GIA uplift rate of 31 ± 4 mm/yr at the edge of Vatnajökull, during 2004–2009 (Auriac et al., 2013). The rate decays with distance from the ice cap (Drouin & Sigmundsson, 2019).

The KVS (Figure 1) consists of a central volcano with a 9 × 7 km caldera, formed ~100,000 years ago (Sæmundsson, 1991), later filled with eruptive products, and ~5–8 km-wide transecting fissure swarm, extending ~40 km to the south and ~50 km to the north from the caldera (e.g., Hjartardóttir et al., 2012). The KVS hosts the Krafla geothermal field in the caldera and the Bjarnarflag geothermal area, ~10 km south of the caldera, both exploited for energy production. After a rifting episode in 1975–1984 (Einarsson, 1991; Wright et al., 2012), inflation occurred until 1989 in the caldera, followed by deflation until 2018. Difference velocity fields (between 2015–2018 and 2018–2020) reveal minor inflation inside the caldera with an inferred 2.1–2.5 km-deep point-source (Lanzi et al., 2023). During 1989–1992, a subsidence rate of ~5 cm/yr was recorded (Tryggvason, 1994), exponentially decaying to ~3–5 mm/yr in 1995–2015 (Drouin, Sigmundsson, Verhagen, et al., 2017; Sturkell et al., 2008). Zones of seismic attenuation at 3–7 km depth have been identified inside the caldera and interpreted as shallow magma storage (Einarsson, 1978). A 40 km-wide high velocity dome extends from the lower crust (11–14 km depth) beneath the volcano narrowing upward where a magma body has been inferred at ~3 km depth (Brandsdóttir et al., 1997). Low V_p/V_s zones (≤1.65), located underneath the geothermal system at 2–3 km depth bsl (Schuler et al., 2015), close to a borehole (IDDP-1) that was drilled into rhyolitic magma at 2.1 km depth in 2009 (Elders et al., 2011), may be associated with a superheated steam layer, at the boundary between host rock and felsic melt. Vertical seismic profiling mapped a reflector at the same depth as the bottom of IDDP-1 drillhole, and at depths ranging from 4 to 6 km, interpreted as a distributed system of magmatic sills (Kim et al., 2020).

The AVS (Figure 1) has a central volcano with several calderas where geothermal activity occurs, and a transecting 20 km-wide and 150 km-long fissure swarm (Hjartardóttir et al., 2009). The main Askja caldera has a

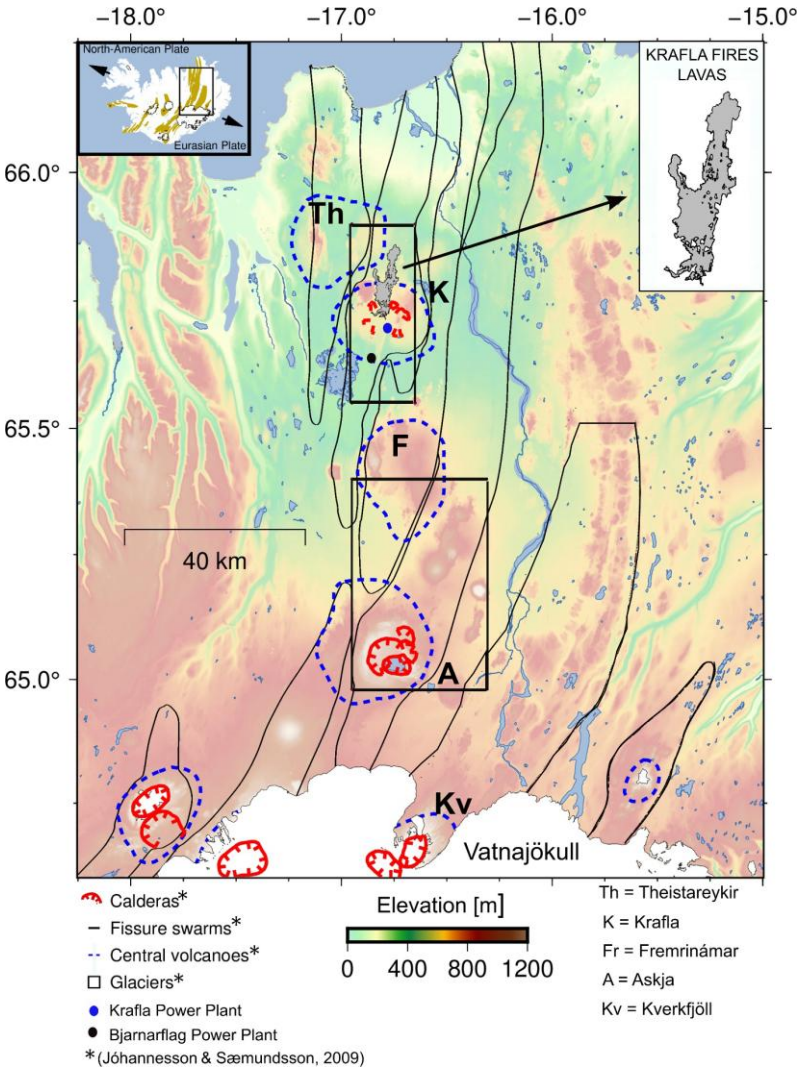

Figure 1. Volcanic systems in the NVZ of Iceland. Inset maps show the location of the NVZ and fissure swarms in Iceland (on the left) and the Krafla Fires lavas outline (on the right). Black rectangles mark the areas shown in Figure 4.

diameter of ∼8 km, and the most recent eruption occurred in 1961 when a fissure opened at its north-eastern boundary (Thorarinsson & Sigvaldason, 1962). Leveling (since 1983), GNSS (since 1993), and InSAR (since the early 1990s) show maximum deflation in the middle of the caldera at an initial rate of ∼5 cm/yr (Sturkell et al., 2006), exponentially decaying to 2.5–3 cm/yr in 2000–2009 (de van Zeeuw-Dalfsen et al., 2012). Inflation began centered in the caldera in summer 2021. In 2 years, the uplift amounted to ∼70 cm due to inferred pressure increase at ∼2.8 km depth (Parks et al., 2024). Tomography studies identified low seismic velocity at ∼6–11 km bsl beneath Askja caldera (Mitchell et al., 2013) with two major regions of high V_p/V_s ratio, involving a volume of ∼100 km^3, at ∼5 and ∼9 km bsl (Greenfield et al., 2016). These were interpreted as heavily intruded regions with melt sitting in lenses of low melt fraction (∼10%) or within a mush (Greenfield et al., 2016). In the lower crust, the seismic ray coverage is not as good as above, but low V_s and high V_p/V_s areas can be identified, suggesting areas of melt storage and melt transported from a deeper source (Greenfield et al., 2016; Soosalu et al., 2010).

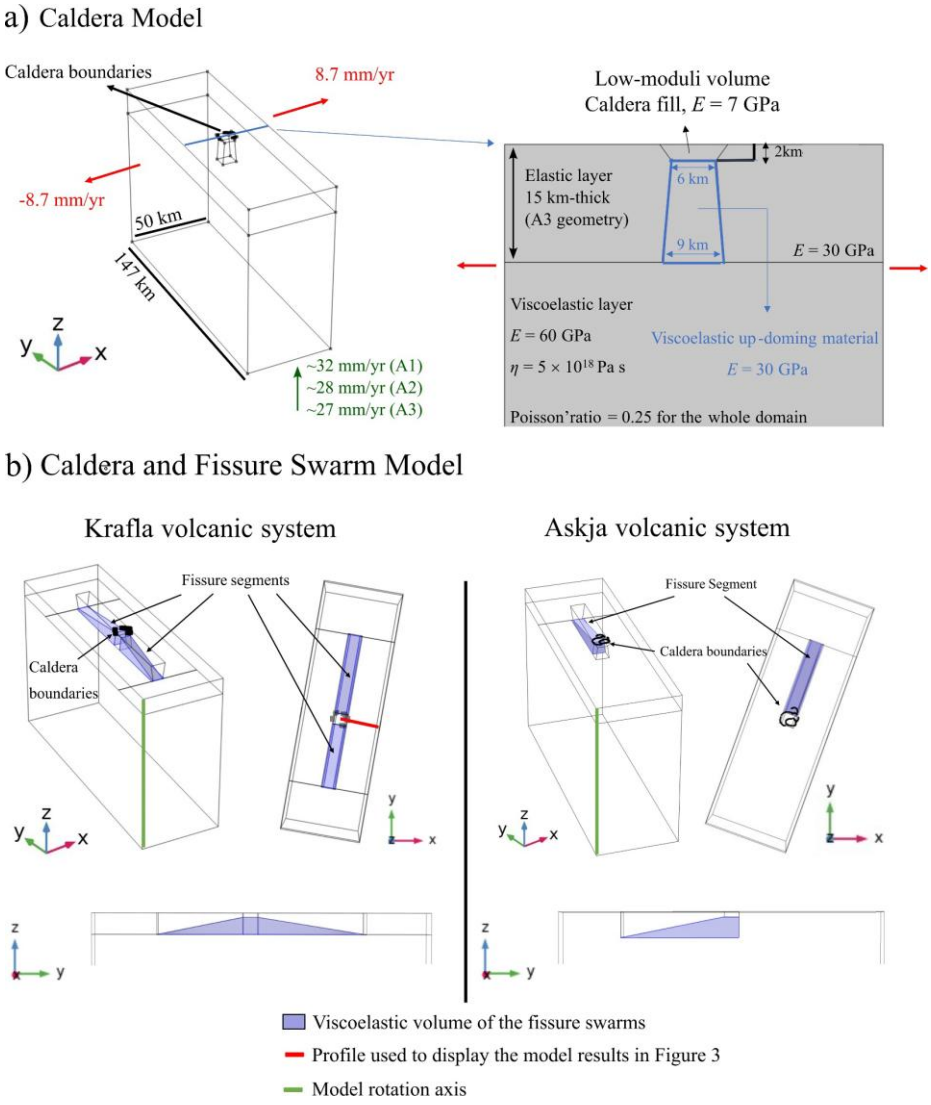

Figure 2. 3D models setup. (a) C-model and caldera cross-section showing material properties; (b) CFS-model for KVS (left) and AVS (right).

3. Numerical Modeling Set-Up

We use 3D numerical FEM models with COMSOL Multiphysics (v5.6) software to investigate the effects of vertical and lateral variations in multi-layered geometry, and the effect of variable elastic properties and a viscoelastic rheology on strain localization, in extensional settings. The models are 50 km-wide (X-dimension, approximately East-West), 147 km-long (Y-dimension, approximately North-South), and 100 km-deep (Z-dimension). They consist of two 70 km-long volumes, representing fissure swarm, north and south of a 7 km-wide caldera block (Figure 2). Extension is reproduced by imposing an uniform velocity, 8.7 mm/yr on the right side and −8.7 mm/yr on the left side of the domain, respectively, in the *X*-direction over 200 years. At the model edges in the Y-dimension, horizontal movement is fixed to zero, but vertical movement is allowed. The bottom of the model was initially fixed resulting in an overall subsidence of the whole domain due to the stretching. To balance that, we apply an upward velocity at the bottom, equal to the total thinning of the crust (estimated by an initial

model) divided by the runtime of the simulation. Thus, the model results are such that the far-field has about zero vertical displacement.

First, we consider a fully elastic model and investigate the influence of a local low-moduli elastic material near the surface in a central volcano, that corresponds for example, to a caldera in-fill. Such an approach to evaluate the effect of volcanoclastic fill has been used at Taupo volcano (e.g., Ellis et al., 2007; Peltier et al., 2009). We develop a one-layer elastic model (Figure S1 in Supporting Information S1) where the model domain has Young's modulus $E = 30$ GPa (inferred value for the average Icelandic crust, e.g., Grapenthin et al., 2006; Drouin et al., 2016), except for a 2 km-thick layer with $E = 7$ GPa which reproduces the caldera-infill volume properties (Lanzi et al., 2023), that is 9×7 km-wide at surface and 6 km at the bottom, in the X-direction.

We next consider effects of thermal anomalies due to the presence of magma storage zones and hot rock where a ductile response of the crust may occur. Selection of rheological behavior of crustal material and implementation of tectonic forcing will have a fundamental influence on model predictions (Head et al., 2019; Text S1 in Supporting Information S1). We here model a mixture of liquid, magma mush, and hot rock to behave effectively with Maxwell rheology, with lowered crustal viscosity, η, compared to the surroundings. We introduce a two-layer model (Figure 2a), the caldera (C) model (Table S1 in Supporting Information S1), where a regional viscoelastic layer ($E = 60$ GPa and viscosity, $\eta = 5 \times 10^{18}$ Pa s) underlies an elastic layer. The viscoelastic layer is not uniform: it reaches shallower levels under the low-moduli volume previously introduced. We refer to the locally shallow volume as up-doming material, simulating a viscoelastic zone beneath a caldera. There we test viscosity ranging from 5×10^{14} to 5×10^{19} Pa s. Most of the seismicity in the Krafla caldera is shallower than 2.4 km, and the brittle-ductile boundary has been located there at ∼1.8–2.4 km depth (Ágústsson & Blanck, 2019). In accordance with this study, we fixed the top of the up-doming material at 2 km depth. Different regional elastic layer thicknesses are considered: 7, 10 and 15 km, referred to as A1, A2 and A3 geometries, respectively. The base of the elastic layer and the up-doming volume coincide (Figure 2). As the elastic layer thickness increases, the volume of the up-doming viscoelastic material is larger.

Additionally, we introduce a 9 km-wide (X-dimension) fissure swarm geometry (Figure 2b) where the 2 km-deep elastic-viscoelastic interface at the caldera ramps down to 7, 10 or 15 km depth at 50 and 40 km distance north and south, respectively, of the Krafla caldera The ramping is consistent with the overall earthquake depth distribution that shows deepening (toward 6–7 km depth) within the northern fissure swarm of the KVS (Guðnason et al., 2023). The AVS model has only one fissure swarm to the north of the caldera. The elastic layer ($E = 10$ GPa, Gudmundsson, 2011; Pedersen et al., 2009), of the fissure swarm linearly thickens away from the caldera and the viscoelastic layer thins from the caldera to the end of the fissure swarm. The viscoelastic material in the fissure swarm has a viscosity in the range of 5×10^{17}–5×10^{19} Pa s, and $E = 30$ GPa. We refer to this model as the caldera and fissure swarm (CFS) model.

We applied the CFS-model to the NVZ. To reproduce the strike of the Krafla and Askja fissure swarm, the model was rotated N10°E and N20°E, respectively (Figure 2b). Caldera and fissure swarm geometry are constrained by structural data (Hjartardóttir et al., 2009, 2012). GIA studies reveal a regional viscosity in the range 2–10×10^{18} Pa s and elastic layer thickness, ranging from 7 to 10 km (Árnadóttir et al., 2009; Fleming et al., 2007; Pagli et al., 2007) to 15–40 km (Auriac et al., 2013) for the NVZ.

4. Model Results

4.1. Caldera (C) and Caldera and Fissure Swarm (CFS) Models

The one-layer model displacements with localized shallow low elastic-moduli volume has no significant surface subsidence after 200 years of stretching (Figure S2 in Supporting Information S1). When we incorporate the viscoelastic layer and the up-doming volume (the C-model) the ground subsidence is tightly focused above the caldera decreasing to zero in the far-field (Figure 3; Figure S3 in Supporting Information S1). The model outputs for $\eta = 5 \times 10^{19}$ Pa s in the up-doming material show the smallest subsidence rate, ∼0.1, 0.25, and 0.4 mm/yr for A1, A2 (Figure S3 in Supporting Information S1) and A3 geometries, respectively. The localized subsidence rate is ∼3.5–4.7 mm/yr (A1 and A3 geometries), 3.2–4.4, 1.8–2.3 mm/yr, for viscosity in the range of 10^{16}, 10^{17}, 10^{18} Pa s (Table S2 in Supporting Information S1). The lowest viscosity leads to the largest subsidence rate. When a viscosity lower than 10^{16} Pa s is applied, there is no further increase in the subsidence rate (Figure S3 in Supporting Information S1). Another feature revealed by the models is that an increase of the elastic layer

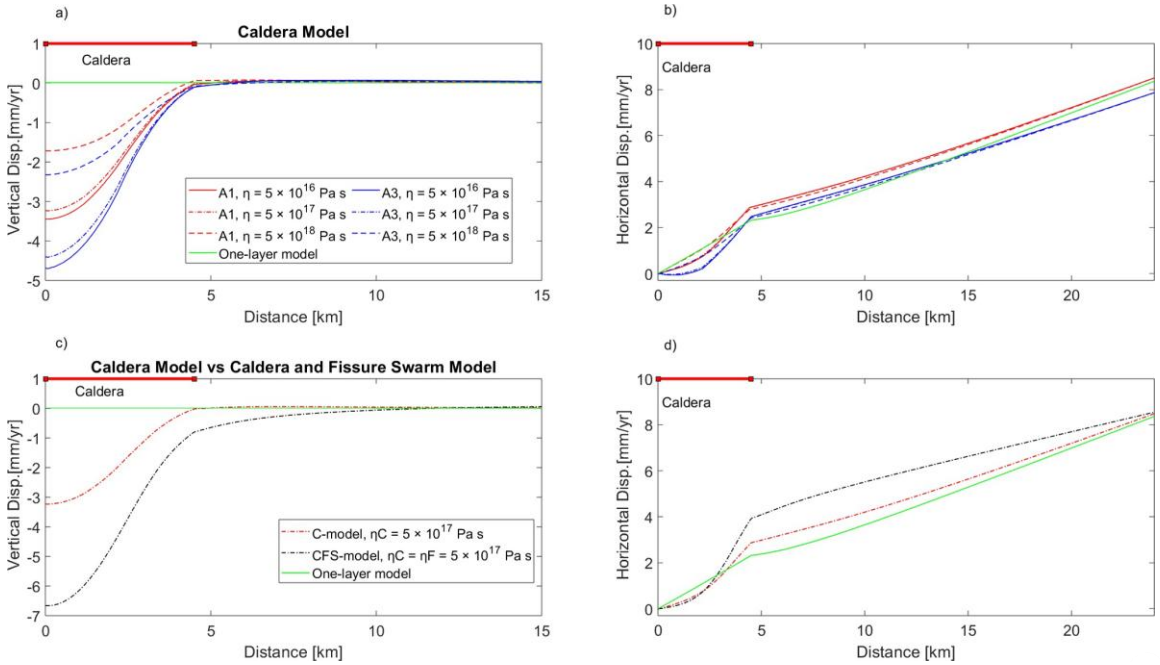

Figure 3. (a) Vertical and (b) horizontal displacements in C-model result for A1 and A3 geometries and one-layer model shown along the red line in the positive X-dimension in Figure 2b (approximately east-west profile). (c) Vertical and (d) horizontal displacements of the one-layer model, the C-model,and the CFS-model given the same viscosity and elastic layer thickness. ηF = viscosity fissure swarm; ηC = viscosity beneath the caldera.

thickness, and thus the larger viscoelastic volume involved beneath the caldera (Figure 2a), leads to higher subsidence rate, given the same viscosity in the up-doming volume (Figure 3a). The horizontal component (Figure 3b) shows less variability as the viscosity changes. The solutions for model A1 and A3 when the viscosity is 10^{16} Pa s and 10^{17} Pa s overlap and display only a slight difference when the viscosity is 10^{18} Pa s.

The CFS-model predicts localized deformation both above the caldera and along the fissure swarm (Figures 3c and 3d; Figure S4 in Supporting Information S1). The caldera area has larger subsidence rates, ~7 mm/yr, given the same geometry and viscosity of the C-model, where the subsidence rate is ~3 mm/yr (Figures 3c and 3d; Table S1 in Supporting Information S1). In the fissure swarm, the subsidence rates are lower (~3 mm/yr) than in the caldera (Figure S4 in Supporting Information S1).

The model results are presented as surface velocities after 200 years (longer time evolution is provided in Figure S5 in Supporting Information S1), corresponding to about half of the average time between rifting events at KVS, that has experienced six eruptive episodes in the last 2800 years (Sæmundsson, 1991).

4.2. Application to KVS and AVS

The 2015–2018 inferred vertical displacement estimates from InSAR data (Drouin & Sigmundsson, 2019), are used in the evaluation of the best-fit CFS-model for the KVS and AVS based on Root Mean Square (RMS) analysis (Text S2 in Supporting Information S1). Maximum observed subsidence rates are ~4 mm/yr in the Krafla caldera, ~1–2 mm/yr along the northern fissure swarm, and ~5 mm/yr in the southern fissure swarm (Figures 4a–4e). The Askja caldera displays a higher subsidence rate, ~15–20 mm/yr, and ~6–7 mm/yr along the Askja northern fissure swarm (Figures 4f–4l). The RMS of residuals (inferred velocities minus model predictions) is lower than the RMS evaluated for the inferred velocity, ~2.7 mm/yr (Text S2 in Supporting Information S1). The lowest RMS value for the KVS, 1.3 mm/yr, is obtained for the A2 geometry with ηF (viscosity fissure swarm) = ηC (viscosity beneath the caldera) = 5×10^{18} Pa s (Figures 4a–4e) and for the A1 geometry with ηF = 5×10^{18} Pa s and ηC = 5×10^{17} Pa s beneath the caldera (Figures S6–S12 in Supporting Information S1).

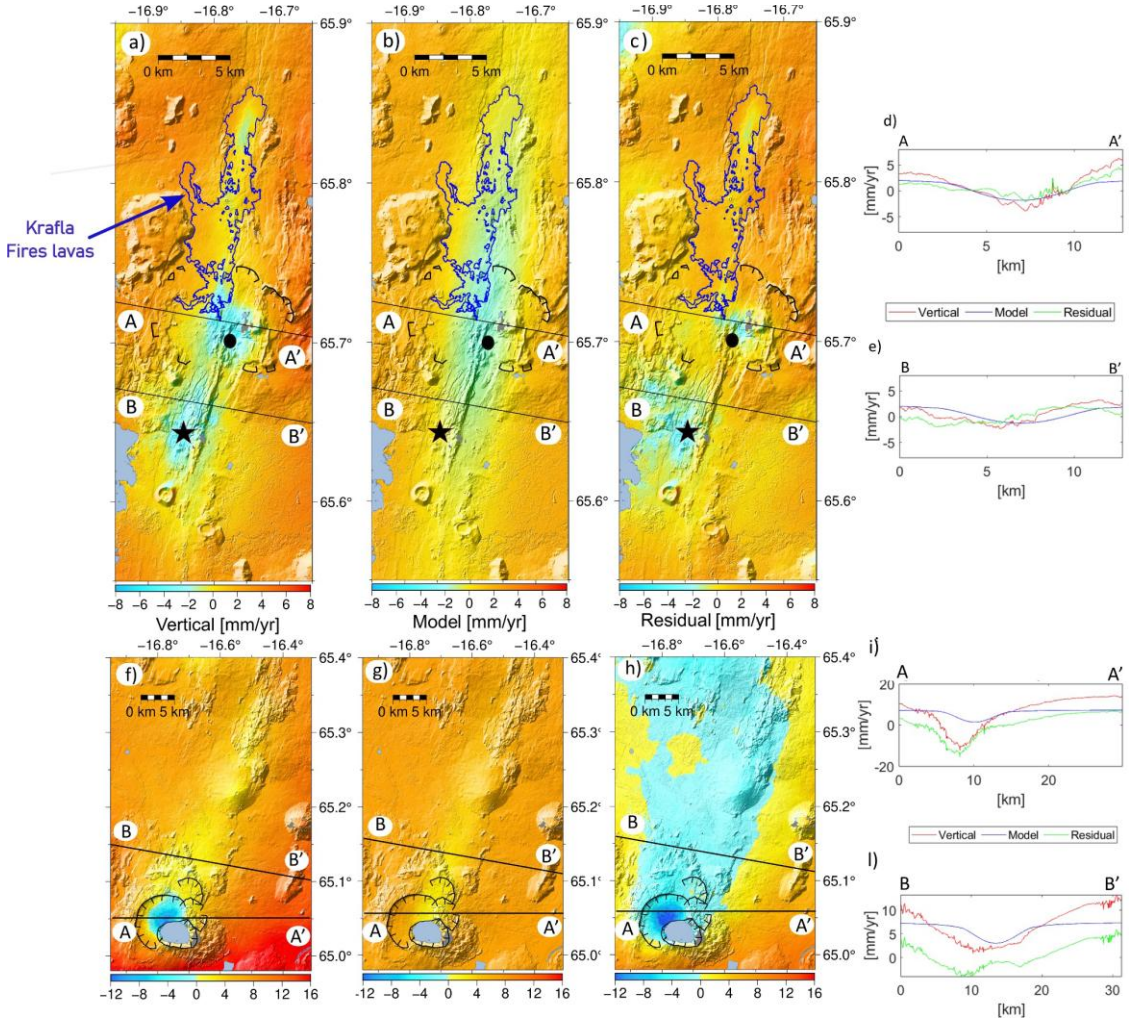

Figure 4. Inferred average vertical velocities 2015–2018 (see text), model prediction, and residuals in a map view and profiles along caldera (A-A') and fissure segment (B-B') for the KVS (a)–(e), and the AVS (f–l). The black circle and black star indicate the Krafla and Bjarnarflag power plants, respectively.

Both the A2 and A1 geometries, applied to the KVS, reproduces the subsidence in the caldera reasonably well, with the largest misfit around ∼1.8 mm/yr, after a correction for ongoing GIA in Iceland is applied The correction is the average of expected uplift magnitude over the KVS (3.5 mm/yr) and AVS (7.5 mm/yr) (Drouin & Sigmundsson, 2019, Text S3 in Supporting Information S1). Actually, the GIA uplift pattern is more complex, contributing to residual when comparing models and observations.

Predicted subsidence in the fissure swarms is wider than observed, and a narrow elongated residual zone is present around 10 km north from the caldera. In the southern fissure swarm, the model underpredicts the observed deformation over a wide area, between the Krafla caldera and the lake (blue area in Figure 4). Similar RMS evaluation for the AVS finds A1 geometry with $\eta F = \eta C = 5 \times 10^{17}$ Pa s to be the best-fit model with RMS equal to 3.4 mm/yr, against the 8.3 mm/yr for the estimated velocity (Figures 4f–4l; Figures S13–S19 in Supporting Information S1). However, the residuals are quite large (>8–10 mm/yr) and the model reproduces only 25%–30% of the deformation signal.

5. Discussion

FEM models considering local up-doming of viscoelastic material (η in the 10^{16}–10^{18} Pa s range) and a variable depth of the elastic-viscoelastic interface of a fissure swarm, extending from a caldera, can reproduce a significant part of the observed 2015–2018 vertical velocity pattern at KVS (Figures 4a–4e), but only a minor component of subsidence at the AVS (Figures 4f–4l).

Several studies attribute most of the recent subsidence at the Krafla caldera to a combined effect of geothermal exploitation, and cooling of and/or melt withdrawal from a shallow reservoir (1995–2006 period, Sturkell et al., 2008; 1995–2015 period, Drouin, Sigmundsson, Verhagen, et al., 2017). We demonstrate that rates observed in the 2015–2018 period may be strongly influenced by strain localization effects in relation to plate movements, although residuals are still evident (Figure 4c). The simple shape of the viscoelastic volume assumed in our model (to demonstrate the effects of strain localization) is likely to deviate from the true shape of such crustal volumes. Improved fit could be achieved by varying for example, width, depth or length of viscoelastic crustal volume, as exact shape of such volumes has an influence on model predictions (Figure S20 in Supporting Information S1). Other unmodelled processes may also contribute. A wide region of residual occurs around the Bjarnarflag geothermal power plant, where previous studies inferred several mm/yr of surface subsidence due toa ∼1.5 km-deep source of pressure decrease (Drouin, Sigmundsson, Verhagen, et al., 2017). The Krafla Fires lavas may still be undergoing some thermal contraction where it is thickest, as inferred first from 1992 to 1995 InSAR observations (Sigmundsson et al., 1997). Our model shows a narrow area of ∼3 mm/yr residuals over the northern part of the lava field. Wittmann et al. (2017) show that subsidence of ∼2 mm/yr may occur ∼23 after the emplacement of a lava deposit with thickness comparable to the last Krafla Fires event (Rossi, 1997). Other processes contributing to the residuals may include continued post-rifting relaxation (Ali et al., 2014), cooling of the dike complex formed in 1975–1984 causing rift subsidence (Sigmundsson et al., 1997), or effects of loading from the Krafla Fires lavas (e.g., Odbert et al., 2015).

The best-fit rheological model, A1 geometry, applied to AVS (Figures 4f–4l) suggests strain localization due to regional stretching is not the only origin (or indeed the most significant) of the observed deformation. Cooling and contraction of a shallow magma body (possibly combined with magma outflow) has been proposed to cause the ground deformation. Sturkell et al. (2006) modeled the deformation in the caldera using two deflating Mogi sources (at ∼3 km and at ∼16 km depth). A small low-velocity anomaly resides at 13–19 km depth (Mitchell et al., 2013), close to clusters of deep earthquakes that have been associated with movement of magma within the lower crust (Soosalu et al., 2010) supporting the deeper source modeled by Sturkell et al. (2006). The KVS and AVS are located along the same divergent margin and deep lateral pressure-connection through a partial zone at mantle level has been suggested to connect the two plumbing systems at depth, based on correlation of magmatic activities, and coupled ground deformation events observed in the NVZ (de van Zeeuw-Dalfsen, 2013; Sturkell et al., 2006; Tryggvason, 1989; Yang et al., 2023). Coupling activity between adjacent volcanic systems has been observed at Campi Flegrei and Vesuvius volcanoes (Walter et al., 2014) and Kīlauea and Mauna Loa (Gonnermann et al., 2012), though on a shorter distance (<30 km). Reduction of elastic layer thickness under rifts and associated subsidence is in agreement with the study of Islam (2016) of the Western Volcanic Zone in South Iceland, based on thermal modeling.

Our model suggests that any extensive magmatic system undergoing stretching should display subsidence, like the KVS and AVS, related to the presence of magma and hot material/magma mush beneath calderas. By integrating our models with additional sources of deformation (e.g., activity in the geothermal system, magma transfer, etc.), a more complete understanding of deformation patterns at volcanoes can be achieved. We note that the Fremrinámar volcanic system in the NVZ is also subsiding (∼2 mm/yr in 2015–2018, Figure S21 in Supporting Information S1), but at a lower rate than Krafla and Askja. This may be indicative of a weak rheological anomaly there, consistent with no eruption in the area in the last 3,000 years (Sæmundsson, 2019).

6. Conclusions

We present FEM numerical models to investigate the relationship between subsidence and crustal structure at volcanic systems undergoing extension, during quiescent periods. Long-term model subsidence rates are up to 5–6 mm/yr for rheological models of magmatic systems in Iceland. For the 2015–2018 period, they can account for most of the observed subsidence at the KVS and 25%–30% of the observed subsidence at the AVS. The patterns and magnitude of local heterogeneity in extensional volcanic settings contribute to the strain localization,

providing a bottom-up control on the behavior of the deformation pattern. A better understanding of processes contributing to long-term subsidence of volcanoes provides improved insights of magma plumbing systems, long-term trends of volcanoes and forecasting changes in volcanic behavior given a known background deformation pattern.

Data Availability Statement

The 2015–2018 Sentinel-1 crustal velocities over the Northern Volcanic Zone of Iceland are available at Drouin (2024).

Acknowledgments
We thank Matthew Head and an anonymous reviewer for comments that helped to greatly improve the manuscript. Support provided by MaDRe Project (RANNIS Grant 228933–051) and Icelandic Research Fund ISVOLC project (Grant 239615–051) is acknowledged. We thank the European Space Agency for their open access for Sentinel data. Figures were produced with Matlab (MathWorks, 2002) and GMT software (Wessel et al., 2013). We thank Yilin Yang for assistance with the GMT scripts.

References

Ágústsson, K., & Blanck, H. (2019). Krafla – Jarðskjálftar og niðurdæling. *Iceland GeoSurvey, Report ÍSOR-2019/022*.
Ali, S. T., Feigl, K. L., Carr, B. B., Masterlark, T., & Sigmundsson, F. (2014). Geodetic measurements and numerical models of rifting in Northern Iceland for 1993–2008. *Geophysical Journal International*, *196*(3), 1267–1280. https://doi.org/10.1093/gji/ggt462
Árnadóttir, T., Lund, B., Jiang, W., Geirsson, H., Einarsson, P., & Sigurdsson, T. (2009). Glacial rebound and plate spreading: Results from the first countrywide GPS observations in Iceland. *Geophysical Journal International*, *177*(2), 691–716. https://doi.org/10.1111/j.1365-246X.2008.04059.x
Auriac, A., Spaans, K. H., Sigmundsson, F., Hooper, A., Schmidt, P., & Lund, B. (2013). Iceland rising: Solid Earth response to ice retreat inferred from satellite radar interferometry and viscoelastic modeling. *Journal of Geophysical Research: Solid Earth*, *118*(4), 1331–1344. https://doi.org/10.1002/jgrb.50082
Ayele, A., Jacques, E., Kassim, M., Kidane, T., Omar, A., Tait, S., et al. (2007). The volcano–seismic crisis in Afar, Ethiopia, starting September 2005. *Earth and Planetary Science Letters*, *255*(1–2), 177–187. https://doi.org/10.1016/j.epsl.2006.12.014
Biggs, J., Anthony, E., & Ebinger, C. (2009). Multiple inflation and deflation events at Kenyan volcanoes, East African Rift. *Geology*, *37*(11), 979–982. https://doi.org/10.1130/G30133A.1
Brandsdóttir, B., Menke, W., Einarsson, P., White, R. S., & Staples, R. K. (1997). Faroe-Iceland ridge experiment 2. Crustal structure of the Krafla central volcano. *Journal of Geophysical Research*, *102*(B4), 7867–7886. https://doi.org/10.1029/96jb03799
Cattin, R., Doubre, C., Chabalier, J., King, G., Vigny, C., Avouac, J., et al. (2006). Numerical modelling of Quaternary deformation and post-rifting displacement in the Asal-Ghoubbet rift (Djibouti, Africa). *Earth and Planetary Science Letters*, *239*, 352–367. https://doi.org/10.1016/j.epsl.2005.07.028
Chadwick, W. W., Jr., Paduan, J. B., Clague, D. A., Dreyer, B. M., Merle, S. G., Bobbitt, A. M., et al. (2016). Voluminous eruption from a zoned magma body after an increase in supply rate at Axial Seamount. *Geophysical Research Letters*, *43*(23). https://doi.org/10.1002/2016GL071327
Currenti, G., & Williams, C. (2014). Numerical modeling of deformation and stress fields around a magma chamber: Constraints on failure conditions and rheology. *Physics of the Earth and Planetary Interiors*, *226*, 14–27. https://doi.org/10.1016/j.pepi.2013.11.003
Del Negro, C., Currenti, G., & Scandura, D. (2009). Temperature-dependent viscoelastic modeling of ground deformation: Application to Etna volcano during the 1993–1997 inflation period. *Physics of the Earth and Planetary Interiors*, *172*(3), 299–309. https://doi.org/10.1016/j.pepi.2008.10.019
DeMets, C., Gordon, R. G., & Argus, D. F. (2010). Geologically current plate motions. *Geophysical Journal International*, *181*, 1–80. https://doi.org/10.1111/j.1365-246X.2009.04491.x
de van Zeeuw-Dalfsen, E., Pedersen, R., Hooper, A., & Sigmundsson, F. (2012). Subsidence of Askja caldera 2000–2009: Modelling of deformation processes at an extensional plate boundary, constrained by time series InSAR analysis. *Journal of Volcanology and Geothermal Research*, *213–214*, 72–82. https://doi.org/10.1016/j.jvolgeores.2011.11.004
de van Zeeuw-Dalfsen, E., Rymer, H., Sturkell, E., Pedersen, R., Hooper, A., Sigmundsson, F., & Ófeigsson, B. (2013). Geodetic data shed light on ongoing caldera subsidence at Askja, Iceland. *Bulletin of Volcanology*, *75*(5), 709. https://doi.org/10.1007/s00445-013-0709-2
Drouin, V. (2024). 2015-2018 Sentinel-1 velocities over Iceland. *OSF*. [Dataset]. https://doi.org/10.17605/OSF.IO/7UXZT
Drouin, V., Heki, K., Sigmundsson, F., Hreinsdóttir, F., & Ofeigsson, B. G. (2016). Constraints on seasonal load variations and regional rigidity from continuous GPS measurements in Iceland, 1997–2014. *Geophysical Journal International*, *205*(3), 1843–1858. https://doi.org/10.1093/gji/ggw122
Drouin, V., & Sigmundsson, F. (2019). Countrywide observations of plate spreading and glacial isostatic adjustment in Iceland inferred by sentinel-1 radar interferometry, 2015–2018. *Geophysical Research Letters*, *46*(14), 8046–8055. https://doi.org/10.1029/2019GL082629
Drouin, V., Sigmundsson, F., Ófeigsson, B. G., Hreinsdóttir, S., Sturkell, E., & Einarsson, P. (2017). Deformation in the Northern Volcanic Zone of Iceland 2008–2014: An interplay of tectonic, magmatic, and glacial isostatic deformation. *Journal of Geophysical Research: Solid Earth*, *122*(4), 3158–3178. https://doi.org/10.1002/2016JB013206
Drouin, V., Sigmundsson, F., Verhagen, S., Ófeigsson, B. G., Spaans, K., & Hreinsdóttir, S. (2017). Crustal deformation studies at Krafla and Bjarnarflag geothermal areas, northern volcanic zone of Iceland, 1993–2015. *Journal of Volcanology and Geothermal Research*, *344*, 92–105. https://doi.org/10.1016/j.jvolgeores.2017.06.013
Dziak, R. P., Bohnenstiehl, D. R., Cowen, J. P., Baker, E. T., Rubin, K. H., Haxel, J. H., & Fowler, M. (2007). Rapid dike emplacement leads to eruptions and hydrothermal plume release during seafloor spreading events. *Geology*, *35*(7), 579–582. https://doi.org/10.1130/G23476A.1
Einarsson, P. (1978). S-wave shadows in the Krafla caldera in NE-Iceland, evidence for a magma chamber in the crust. *Bulletin of Volcanology*, *41*(3), 187–195. https://doi.org/10.1007/BF02597222
Einarsson, P. (1991). In N. Mývatns, A. Garðarsson, & A. Einarsson (Eds.), *The Krafla rifting episode 1975-1989* (pp. 97–139). Reykjavík: Icelandic Nature Science Society.
Einarsson, P., & Brandsdóttir, B. (2021). Seismicity of the northern volcanic zone of Iceland. *Frontiers in Earth Science*, *9*, 628967. https://doi.org/10.3389/feart.2021.628967
Elders, W. A., Friðleifsson, G. Ó., Zierenberg, R. A., Pope, E. C., Mortensen, A. K., Guðmundsson, Á., et al. (2011). Origin of a rhyolite that intruded a geothermal well while drilling at the Krafla volcano, Iceland. *Geology*, *39*(3), 231–234. https://doi.org/10.1130/G31393.1
Ellis, S. M., Wilson, C. J. N., Bannister, S., Bibby, H. M., Heise, W., Wallace, L., & Patterson, N. (2007). A future magma inflation event under the rhyolitic Taupo volcano, New Zealand: Numerical models based on constraints from geochemical, geological, and geophysical data. *Journal of Volcanology and Geothermal Research*, *168*(1–4), 1–27. https://doi.org/10.1016/j.jvolgeores.2007.06.004

Fleming, K., Martinec, Z., & Wolf, D. (2007). Glacial-isostatic adjustment and the viscosity structure underlying the Vatnajökull Ice Cap, Iceland. *Pure and Applied Geophysics*, *164*(4), 751–768. https://doi.org/10.1007/s00024-007-0187-6

Gonnermann, H., Foster, J., Poland, M., Wolfe, C. J., Brooks, B. A., & Miklius, A. (2012). Coupling at Mauna Loa and Kīlauea by stress transfer in an asthenospheric melt layer. *Nature Geoscience*, *5*(11), 826–829. https://doi.org/10.1038/ngeo1612

Gottsmann, J., & Odbert, H. (2014). The effects of thermo-mechanical heterogeneities in island-arc crust on time-dependent pre-eruptive stresses and the failure of an andesitic reservoir. *Journal of Geophysical Research: Solid Earth*, *119*(6), 4626–4639. https://doi.org/10.1002/2014JB011079

Grapenthin, R., Ófeigsson, B. G., Sigmundsson, F., Sturkell, E., & Hooper, A. (2010). Pressure sources versus surface loads: Analyzing volcano deformation signal composition with an application to Hekla volcano, Iceland. *Geophysical Research Letters*, *37*(20). https://doi.org/10.1029/2010gl044590

Grapenthin, R., Sigmundsson, F., Geirsson, H., Árnadóttir, T., & Pinel, V. (2006). Icelandic rhythmics: Annual modulation of land elevation and plate spreading by snow load. *Geophysical Research Letters*, *33*(24), L24305. https://doi.org/10.1029/2006GL028081

Greenfield, T., White, R., & Roecker, S. (2016). The magmatic plumbing system of the Askja central volcano, Iceland as imaged by seismic tomography: The magmatic plumbing system of Askja. *Journal of Geophysical Research: Solid Earth*, *121*(10), 7211–7229. https://doi.org/10.1002/2016JB013163

Gudmundsson, A. (2011). *Rock fractures in geological processes*. Cambridge University Press.

Guðnason, E. Á., Ágústsdóttir, Þ., Magnússon, R. L., & Gunnarsson, K. (2023). Seismic monitoring in Krafla, þeistareykir and námafjall. Reprocessing of the entire 2006-2022 catalogue. ÍSOR 2023/009 Project number no.: 22-0021; LV 2023-021.

Hamling, I. J., Wright, T. J., Calais, E., Lewi, E., & Fukahata, Y. (2014). InSAR observations of post-rifting deformation around the Dabbahu rift segment, Afar, Ethiopia. *Geophysical Journal International*, *197*(1), 33–49. https://doi.org/10.1093/gji/ggu003

Head, M., Hickey, J., Gottsmann, J., & Fournier, N. (2019). The influence of viscoelastic crustal rheologies on volcanic ground deformation: Insights from models of pressure and volume change. *Journal of Geophysical Research: Solid Earth*, *124*(8), 8127–8146. https://doi.org/10.1029/2019jb017832

Hickey, J., Gottsmann, J., Nakamichi, H., & Iguchi, M. (2016). Thermomechanical controls on magma supply and volcanic deformation: Application to Aira caldera, Japan. *Scientific Reports*, *6*(1), 32691. https://doi.org/10.1038/srep32691

Hjartardóttir, Á., Einarsson, P., Bramham, E., & Wright, T. (2012). The Krafla fissure swarm, Iceland, and its formation by rifting events. *Bulletin of Volcanology*, *74*(9), 2139–2153. https://doi.org/10.1007/s00445-012-0659-0

Hjartardóttir, Á., Einarsson, P., & Sigurdsson, H. (2009). The fissure swarm of the Askja volcanic system along the divergent plate boundary of N Iceland. *Bulletin of Volcanology*, *71*(9), 961–975. https://doi.org/10.1007/s00445-009-0282-x

Islam, M. Q. (2016). *Rheological response to tectonic and volcanic deformation in Iceland*. Doctoral dissertation. Department of Earth Sciences, University of Gothenburg. Retrieved from https://gupea.ub.gu.se/handle/2077/42079

Jónsson, S., Einarsson, P., & Sigmundsson, F. (1997). Extension across a divergent plate boundary, the Eastern Volcanic Rift Zone, south Iceland, 1967–1994, observed with GPS and electronic distance measurements. *Journal of Geophysical Research*, *102*(B6), 11913–11929. https://doi.org/10.1029/96JB03893

Kim, D., Brown, L., Árnason, K., Gudmundsson, O., Ágústsson, K., & Flovenz, O. (2020). Magma "bright spots" mapped beneath Krafla, Iceland, using RVSP imaging of reflected waves from microearthquakes. *Journal of Volcanology and Geothermal Research*, *391*, 106365. https://doi.org/10.1016/j.jvolgeores.2018.04.022

LaFemina, P. C., Dixon, T. H., Malservisi, R., Árnadóttir, T., Sturkell, E., Sigmundsson, F., & Einarsson, P. (2005). Geodetic GPS measurements in South Iceland: Strain accumulation and partitioning in a propagating ridge system. *Journal of Geophysical Research*, *110*(B11), B11405. https://doi.org/10.1029/2005JB003675

Lanzi, C., Drouin, V., Sigmundsson, F., Geirsson, H., Hersir, G. P., Ágústsson, K., et al. (2023). Pressure increase at the magma-hydrothermal interface at Krafla caldera, North-Iceland, 2018–2020: Magmatic processes or hydrothermal changes? *Journal of Volcanology and Geothermal Research*, *440*, 107849. https://doi.org/10.1016/j.jvolgeores.2023.107849

Lejeune, A. M., & Richet, P. (1995). Rheology of crystal-bearing silicate melts: An experimental study at high viscosities. *Journal of Geophysical Research*, *100*(B3), 4215–4229. https://doi.org/10.1029/94JB02985

Liao, Y., Soule, S. A., & Jones, M. (2018). On the mechanical effects of poroelastic crystal mush in classical magma chamber models. *Journal of Geophysical Research: Solid Earth*, *123*(11), 9376–9406. https://doi.org/10.1029/2018JB015985

MathWorks. (2022). MATLAB [Software]. *MathWorks*. Retrieved from https://www.mathworks.com/products/matlab.html?s_tid=hp_products_matlab

Mitchell, M. A., White, R. S., Roecker, S. W., & Greenfield, T. (2013). Tomographic image of melt storage beneath Askja Volcano, Iceland using local microseismicity. *Geophysical Research Letters*, *40*(19), 5040–5046. https://doi.org/10.1002/grl.50899

Newman, A. V., Dixon, T. H., & Gourmelen, N. (2006). A four-dimensional viscoelastic deformation model for Long Valley Caldera, California, between 1995 and 2000. *Journal of Volcanology and Geothermal Research*, *150*(1–3), 244–269. https://doi.org/10.1016/j.jvolgeores.2005.07.017

Newman, A. V., Dixon, T. H., Ofoegbu, G. I., & Dixon, J. E. (2001). Geodetic and seismic constraints on recent activity at long valley caldera, California: Evidence for viscoelastic rheology. *Journal of Volcanology and Geothermal Research*, *105*(3), 183–206. https://doi.org/10.1016/S0377-0273(00)00255-9

Odbert, H., Taisne, B., & Gottsmann, J. (2015). Deposit loading and its effect on co-eruptive volcano deformation. *Earth and Planetary Science Letters*, *413*, 186–196. https://doi.org/10.1016/j.epsl.2015.01.005

Pagli, C., Sigmundsson, F., Lund, B., Sturkell, E., Geirsson, H., Einarsson, P., et al. (2007). Glacio-isostatic deformation around the Vatnajökull ice cap, Iceland, induced by recent climate warming: GPS observations and finite element modeling. *Journal of Geophysical Research*, *112*(B8), B08405. https://doi.org/10.1029/2006JB004421

Parks, M., Sigmundsson, F., Drouin, V., Hreinsdóttir, S., Hooper, A., Yang, Y., et al. (2024). 2021-2023 unrest and geodetic observations at Askja volcano, Iceland. *Geophysical Research Letters*, *51*(4), e2023GL106730. https://doi.org/10.1029/2023GL106730

Pearse, J., & Fialko, Y. (2010). Mechanics of active magmatic intraplating in the rio grande rift near socorro, New Mexico. *Journal of Geophysical Research*, *115*(B7). https://doi.org/10.1029/2009JB006592

Pedersen, R., Sigmundsson, F., & Masterlark, T. (2009). Rheologic controls on inter-rifting deformation of the northern volcanic zone, Iceland. *Earth and Planetary Science Letters*, *281*(1–2), 14–26. https://doi.org/10.1016/j.epsl.2009.02.003

Peltier, A., Hurst, T., Scott, B., & Cayol, V. (2009). Structures involved in the vertical deformation at Lake Taupo (New Zealand) between 1979 and 2007: New insights from numerical modelling. *Journal of Volcanology and Geothermal Research*, *181*(3–4), 173–184. https://doi.org/10.1016/j.jvolgeores.2009.01.017

Rossi, M. J. (1997). Morphology of the 1984 open-channel lava flow at Krafla volcano, northern Iceland. *Geomorphology*, *20*(1–2), 95–112. https://doi.org/10.1016/s0169-555x(97)00007-x

Sæmundsson, K. (1991). Jarðfræði kröflukerfisins (in Icelandic). In A. Garðarsson, Á. Einarsson, & N. Mývatns (Eds.), Icelandic nature sci. Soc., *reykjavík* (pp. 24–95).

Sæmundsson, K. (2019). Fremrinamar. In B. Oladottir, G. Larsen, & M. T. Guðmundsson (Eds.), *Catalogue of Icelandic volcanoes*. IMO, UI and CPD-NCIP. Retrieved from https://icelandicvolcanos.is/?volcano=FRE#

Schuler, J., Greenfield, T., White, R. S., Roecker, S. W., Brandsdóttir, B., Stock, J. M., et al. (2015). Seismic imaging of the shallow crust beneath the Krafla central volcano, NE Iceland. *Journal of Geophysical Research: Solid Earth*, *120*(10), 7156–7173. https://doi.org/10.1002/2015JB012350

Sigmundsson, F., Vadon, H., & Massonnet, D. (1997). Readjustment of the Krafla spreading segment to crustal rifting measured by satellite radar interferometry. *Geophysical Research Letters*, *24*(15), 1843–1846. https://doi.org/10.1029/97gl01934

Soosalu, H., Key, J., White, R. S., Knox, C., Einarsson, P., & Jakobsdóttir, S. S. (2010). Lower-crustal earthquakes caused by magma movement beneath Askja volcano on the north Icelandic rift. *Bulletin of Volcanology*, *72*(1), 55–62. https://doi.org/10.1007/s00445-009-0297-3

Sparks, R. S. J., & Cashman, K. V. (2017). Dynamic magma systems: Implications for forecasting volcanic activity. *Elements*, *13*(1), 35–40. https://doi.org/10.2113/gselements.13.1.35

Sturkell, E., Sigmundsson, F., Geirsson, H., Ólafsson, H., & Theodórsson, T. (2008). Multiple volcano deformation sources in a post-rifting period: 1989–2005 behaviour of Krafla, Iceland constrained by levelling, tilt and GPS observations. *Journal of Volcanology and Geothermal Research*, *177*(2), 405–417. https://doi.org/10.1016/j.jvolgeores.2008.06.013

Sturkell, E., Sigmundsson, F., & Slunga, R. (2006). 1983–2003 decaying rate of deflation at Askja caldera: Pressure decrease in an extensive magma plumbing system at a spreading plate boundary. *Bulletin of Volcanology*, *68*(7–8), 727–735. https://doi.org/10.1007/s00445-005-0046-1

Thorarinsson, S., & Sigvaldason, G. E. (1962). The eruption in Askja, 1961 a preliminary report. *American Journal of Science*, *260*(9), 641–651. https://doi.org/10.2475/ajs.260.9.641

Tolstoy, M., Cowen, J. P., Baker, E. T., Fornari, D. J., Rubin, K. H., Shank, T. M., et al. (2006). A sea-floor spreading event captured by seismometers. *Science*, *314*(5807), 1920–1922. https://doi.org/10.1126/science.1133950

Tryggvason, E. (1989). Ground deformation in Askja, Iceland: Its source and possible relation to flow of the mantle plume. *Journal of Volcanology and Geothermal Research*, *39*(1), 61–67. https://doi.org/10.1016/0377-0273(89)90021-8

Tryggvason, E. (1994). Surface deformation at the Krafla volcano, north Iceland, 1982–1992. *Bulletin of Volcanology*, *56*(2), 98–107. https://doi.org/10.1007/BF00304105

van der Molen, I., & Paterson, M. S. (1979). Experimental deformation of partially-melted granite. *Contributions to Mineralogy and Petrology*, *70*, 299–318. https://doi.org/10.1007/BF00375359

Walter, T. R., Shirzaei, M., Manconi, A., Solaro, G., Pepe, A., Manzo, M., & Sansosti, E. (2014). Possible coupling of Campi Flegrei and Vesuvius as revealed by InSAR time series, correlation analysis and time dependent modeling. *Journal of Volcanology and Geothermal Research*, *280*, 104–110. https://doi.org/10.1016/j.jvolgeores.2014.05.006

Wessel, P., Smith, W. H., Scharroo, R., Luis, J., & Wobbe, F. (2013). Generic mapping tools: Improved version released. *Eos, Transactions American Geophysical Union*, *94*(45), 409–410. https://doi.org/10.1002/2013eo450001

Wittmann, W., Sigmundsson, F., Dumont, S., & Lavallée, Y. (2017). Post-emplacement cooling and contraction of lava flows: InSAR observations and a thermal model for lava fields at hekla volcano, Iceland. *Journal of Geophysical Research: Solid Earth*, *122*(2), 946–965. https://doi.org/10.1002/2016jb013444

Wright, T., Sigmundsson, F., Pagli, C., Belachew, M., Hamling, I. J., Brandsdóttir, B., et al. (2012). Geophysical constraints on the dynamics of spreading centres from rifting episodes on land. *Nature Geoscience*, *5*(4), 242–250. https://doi.org/10.1038/ngeo1428

Yamasaki, T., Sigmundsson, F., & Iguchi, M. (2018). Viscoelastic crustal response to magma supply and discharge in the upper crust: Implications for the uplift of the Aira caldera before and after the 1914 eruption of the Sakurajima volcano. *Earth and Planetary Science Letters*, *531*, 115981. https://doi.org/10.1093/gji/ggaa440

Yang, Y., Sigmundsson, F., & Geirsson, H. (2023). Joint bayesian modeling of velocity break points, noise characteristics, and their uncertainties in GNSS time series: Far-field velocity anomalies concurrent with magmatic activity in Iceland. *Geophysical Research Letters*, *50*(14), e2023GL103432. https://doi.org/10.1029/2023GL103432

References From the Supporting Information

Cabaniss, H. E., Gregg, P. M., Nooner, S. L., & Chadwick, W. W., Jr. (2018). Triggering of eruptions at axial seamount, Juan de Fuca ridge. *Scientific Reports*, *10*(1), 10219. https://doi.org/10.1038/s41598-020-67043-0

Currenti, G. (2018). Viscoelastic modeling of deformation and gravity changes induced by pressurized magmatic sources. *Journal of Volcanology and Geothermal Research*, *356*, 264–277. https://doi.org/10.1016/j.jvolgeores.2018.03.020

Costa, A., Gottsmann, J., Melnik, O., & Sparks, R. S. J. (2011). A stress-controlled mechanism for the intensity of very large magnitude explosive eruptions. *Earth and Planetary Science Letters*, *310*(1–2), 161–166. https://doi.org/10.1016/j.epsl.2011.07.024

Jóhannesson, H., & Sæmundsson, K. (2009). Jarðfræðikort af íslandi 1: 600 000, höggun: Geological map of Iceland 1: 600 000–tectonics. *Icelandic Institute of Natural History, Reykjavík*.

Karaoğlu, Ö., Bayer, Ö., Turgay, M. B., & Browning, J. (2020). Thermomechanical interactions between crustal magma chambers in complex tectonic environments: Insights from Eastern Turkey. *Tectonophysics*, *793*, 228607. https://doi.org/10.1016/j.tecto.2020.228607

Head, M., Hickey, J., Thompson, J., Gottsmann, J., & Fournier, N. (2021). Rheological controls on magma reservoir failure in a thermo-viscoelastic crust. *Journal of Geophysical Research: Solid Earth*, *127*(7), e2021JB023439. https://doi.org/10.1029/2021jb023439

Henk, A. (2006). Stress and strain during fault-controlled lithospheric extension—Insights from numerical experiments. *Tectonophysics*, *415*(1–4), 39–55. https://doi.org/10.1016/j.tecto.2005.11.006

Trasatti, E., Giunchi, C., & Bonafede, M. (2003). Effects of topography and rheological layering on ground deformation in volcanic regions. *Journal of Volcanology and Geothermal Research*, *122*(1–2), 89–110. https://doi.org/10.1016/s0377-0273(02)00473-0

Geophysical Research Letters

Supporting Information for

Strain Localization at Volcanoes Undergoing Extension: Investigation of Long-term Deformation at Krafla and Askja Volcanic Systems in North Iceland

Chiara Lanzi (1), Freysteinn Sigmundsson (1), Michelle Maree Parks (2), Halldór Geirsson (1), Vincent Drouin (2)

(1) Nordic Volcanological Center, Institute of Earth Sciences, University of Iceland,

(2) Icelandic Meteorological Office, Reykjavik, Iceland

Contents of this file

Introduction

This supporting information provides text on the different approaches in formulating plate spreading and viscoelastic rheology (Text S1), our implementation of the Root Mean Square analysis (Text S2) and the consideration of Glacial isostatic Adjustment (GIA) in our models (Text S3). Figure S1 displays the one-layer model configuration, and Figure S2 shows the one-layer model result. Figures S3 and S4 display the result for the Caldera (C) model, with elastic thickness = 10 km. Figure S4 shows the result for the Caldera and

Fissure Swarm (CFS) model. Figure S5 shows the total vertical displacement over 1000 yr. Figures S6 - S12 display the model prediction and residual of the Caldera and Fissure Swarm model compared to the observation data for Krafla volcanic system. Figures S13 - S19 display model predictions and residuals for the Caldera and Fissure Swarm model compared to the observation data for Askja volcanic system. Figure S20 shows the comparison of the caldera model (CM) and the vertical column model (VCM). Figure S21 shows the inferred rate of vertical displacement in 2015-2018 for the Northern Volcanic Zone of Iceland. Table S1 provides model characteristics and Table S2 gives the numerical values of the subsidence rate for the Caldera model and Caldera and Fissure Swarm model.

Text S1. Viscoelastic rheology and crustal extension modelling approaches

Assessment of strain partitioning at volcanoes or calderas in various regional or local extensional tectonic regime has been addressed with numerical simulations with different methodology and model geometries. Many of the studies simulate tectonic extension with either a uniform velocity (Pedersen et al., 2009; Peltier et al., 2009; Cabaniss et al., 2018) or, alternatively, a constant rate of external stress (Costa et al., 2011; Karaoğlu et al., 2020) applied on the sides of a numerical model domain. Furthermore, different approaches have been developed to account for the ductile rheology of the crust in modelling simulations (e.g., Trasatti et al., 2003; Del Negro et al., 2009; Hickey et al., 2016; Currenti, 2018).

In elastic rheology, the modes of deformation, including pressurization/depressurization (stress-based models, e.g., Currenti, 2014) and volume changes, either expansion or contraction, (strain-based models, Head et al., 2019) are overall considered equivalent. However, the choice of the boundary condition in a viscoelastic regime (e. g., Maxwell or Standard Linear Solid rheology) affects differently the stress and strain patterns in space and time (Head et al., 2019). The ground deformation involving viscoelastic rheology is also influenced by the imposed thermal constraints (Henk, 2006; Head et al., 2021).

In a comprehensive overview on the influence of Maxwell and Standard Linear Solid rheology, where both stress-based and strain-based methodology and thermal constrain has been included, Head et al. (2019 and 2021) demonstrate that the Maxwell rheology, though widely used, may not in all cases provide a good approximation for volcanic systems investigations due to its fluid response and its relation to the duration of the perturbation applied, favoring the SLS solution. However, the strain response of the SLS rheology may be limited (Head et al., 2019).

Text S2. Root mean square (RMS)

To quantify the prediction capability of the models, we use the RMS value of residuals between observations and the different model predications:

$$RMS = \sqrt{\frac{\sum\left((d_{obs}-d_{pre})-mean(d_{obs}-d_{pre})\right)^2}{N}} \quad (1)$$

where $d_{obs,}$ are observation data, d_{pre}, are predicted displacements from a model and N is the number of observations. We decided to subtract the mean of the residual to the difference between the observation and model prediction. Mean subtraction may help in centering the data around zero, while the data distribution itself remains unchanged. The RMS values can be compared to the RMS of the observations themselves (equation 1 with predicted displacements = 0). We evaluate separately the RMS for the Near-up data (d_{obs}). The RMS for d_{obs} has been evaluated by using Near-up observations, which fall inside or nearby the area presented in Figure 4. The number of observations in the Near-Up observations depends on the quality of the InSAR data over the study area, if incoherent zones are present or not, 275560 for Krafla volcanic system and 275560 for Askja volcanic system.

Text S3. Effects of Glacial Isostatic Adjustment (GIA)

Correction for ongoing GIA in Iceland has been applied considering the modelling results by Drouin and Sigmundsson (2019). The correction applied was 3.5 mm/yr uplift for Krafla volcanic system and 7.5 mm/yr uplift for Askja volcanic system. The values were taken as average value of the GIA effect in both the volcanic systems and simply added to the FEM model predictions and compared against the observations. However, such one-value correction did not consider the complexity of the GIA pattern in the Northern Volcanic Zone of Iceland where the GIA signal increases with distance from the Vatnajökull ice cap. In particular, a significant increase of the GIA signal occurs south of the Askja caldera causing the inflation observed in Figure 4f.

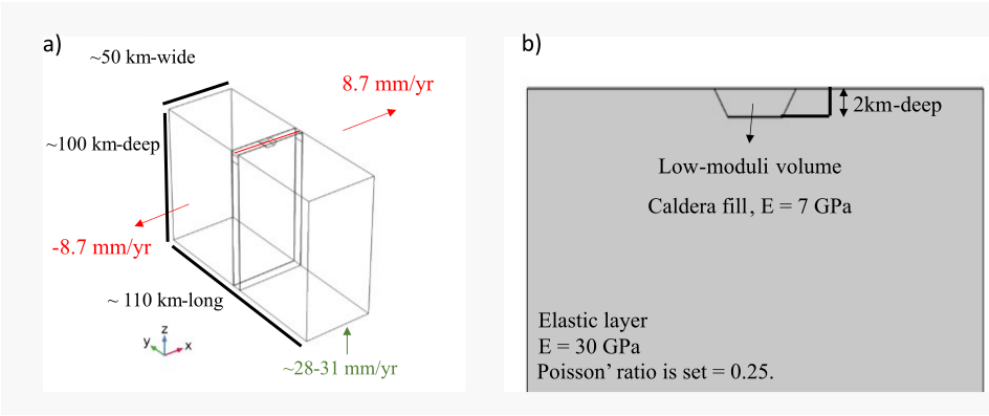

Figure S1. One-layer model configuration. a) 3D view with the main boundary conditions and west-east profile (in blue) through the central caldera. The upward velocity, applied at the bottom of the model, range from 28 to 31 mm/yr according to the different elastic layer geometries tested. b) Shallower domain cross-section of the profile defined in S1a**.** Material properties of the crust are defined.

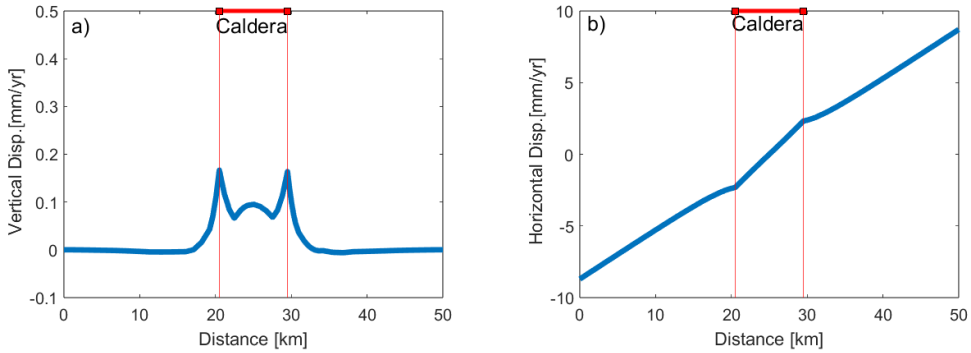

Figure S2. a) Vertical and b) horizontal one layer surface deformation. Profile as shown in blue in Supplementary Figure S1a.

5

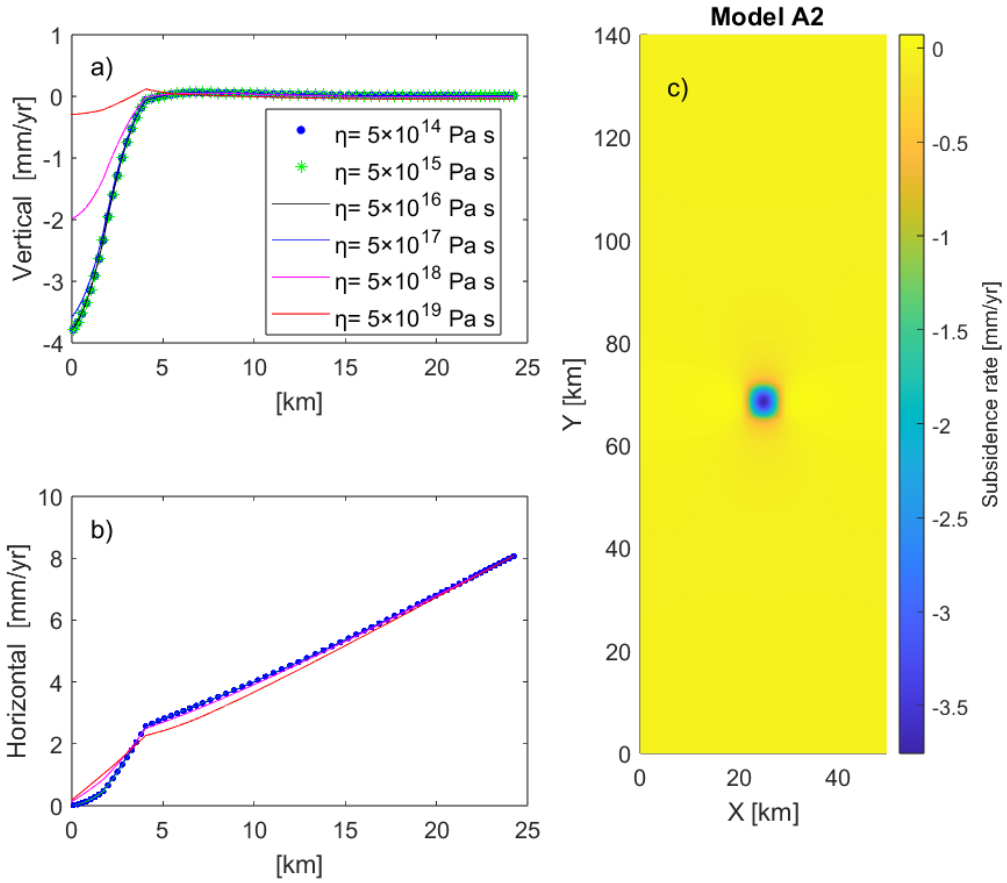

Figure S3. Result for the two-layer model, the caldera (C) model, with elastic layer thickness = 10 km (A2) a) Vertical and b) horizontal displacement along profile as defined in red in Figure 2a for all viscosities values tested, η = 5×(10^{14} -10^{19}) Pa s; c) Vertical displacement at surface in map view for η = 5×10^{17} Pa s.

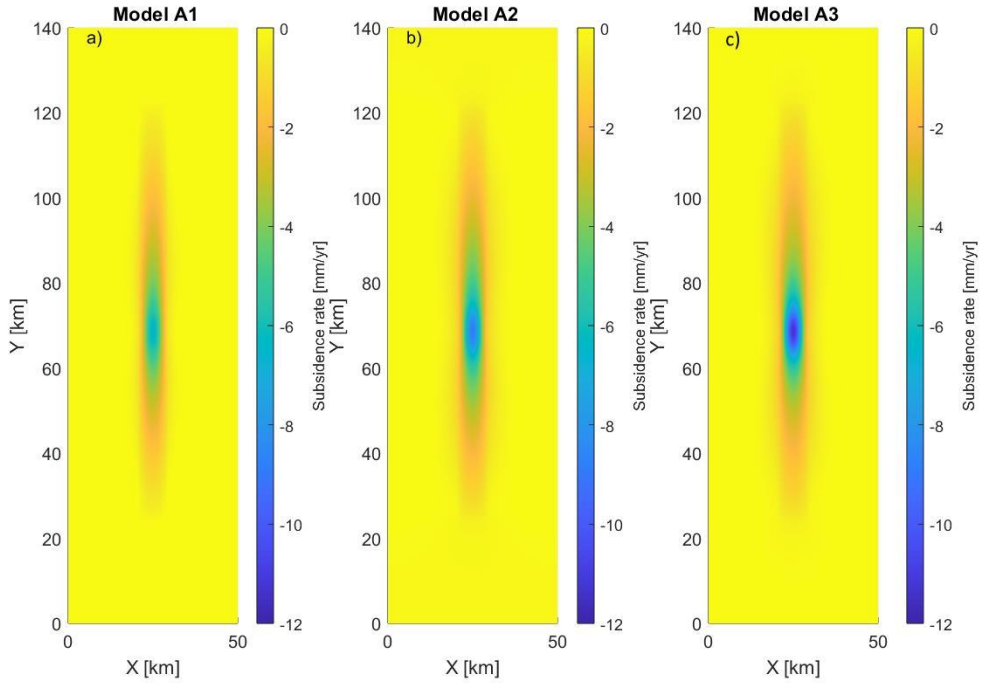

Figure S4. Result for the two-layer model, the Caldera and Fissure Swarm (CFS) model. a) Model A1, b) A2 and c) A3 in map view.

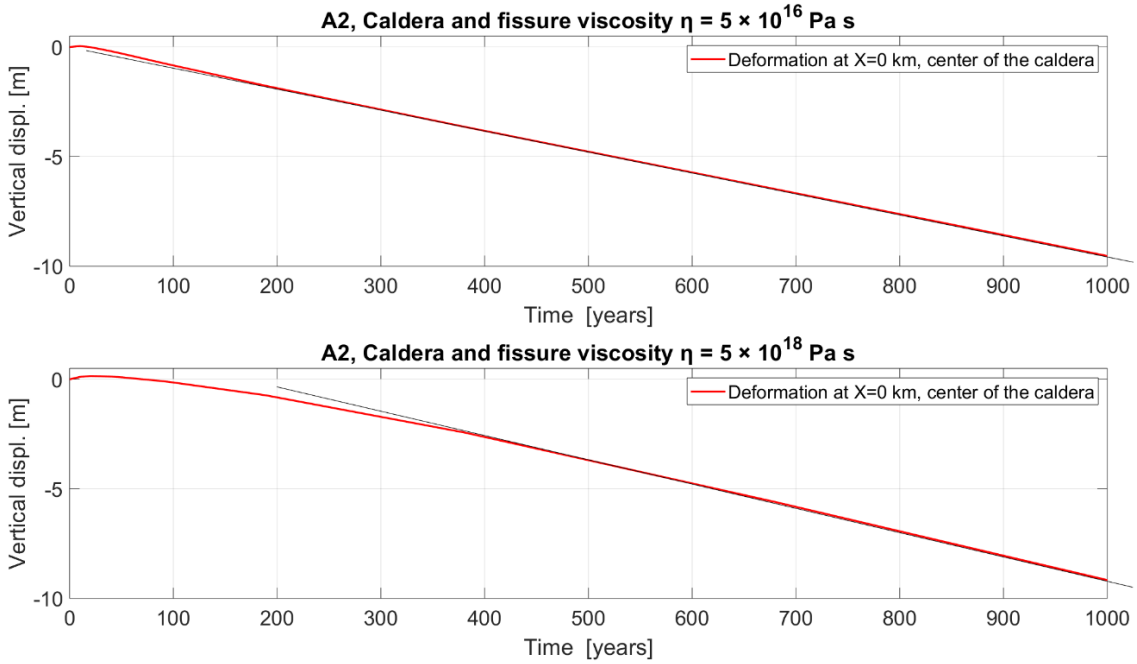

Figure S5. Total vertical displacement after 1000-year runtime for an elastic layer 10 km thick

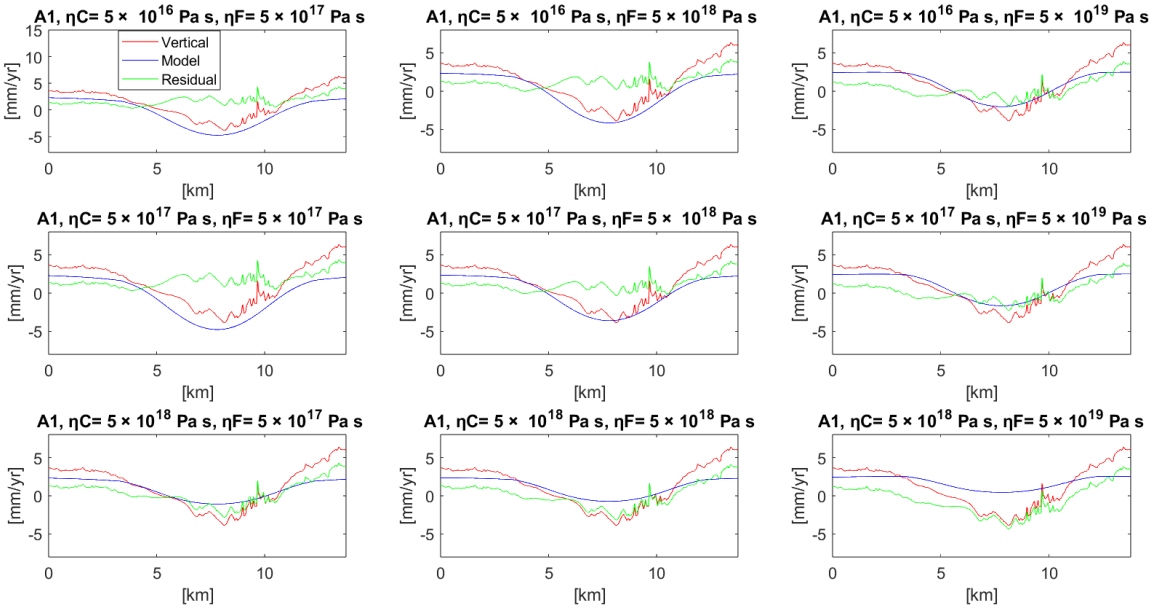

Figure S6. Caldera and Fissure Swarm model results for Krafla volcanic system. Profile AA' defined as in Figure 4a along caldera. All model combinations (in blue), in terms of viscosity values in the caldera, $\eta C = 5 \times (10^{16}\text{-}10^{18})$ Pa s, and in the viscoelastic fissure segment, $\eta F = 5\times(10^{17}\text{-}10^{19})$ Pa s, are compared against the observation (in red) and display the residual (in green), when the elastic layer is 7 km thick.

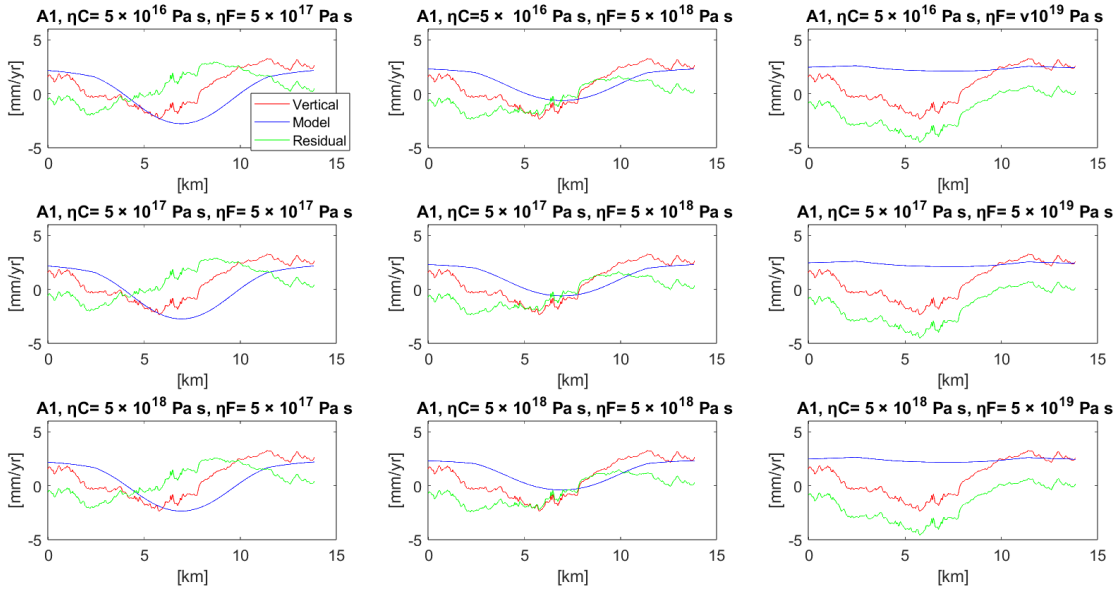

Figure S7. Caldera and Fissure Swarm model results for Krafla volcanic system. Profile BB' defined as in Figure 4a along the fissure segment. All model combinations (in blue), in terms of viscosity values in the caldera, $\eta C = 5\times(10^{16} - 10^{18})$ Pa s, and in the viscoelastic fissure segment, $\eta F = 5\times(10^{17} - 10^{19})$ Pa s, are compared against the observation (in red) and display the residual (in green), when the elastic layer is 7 km thick.

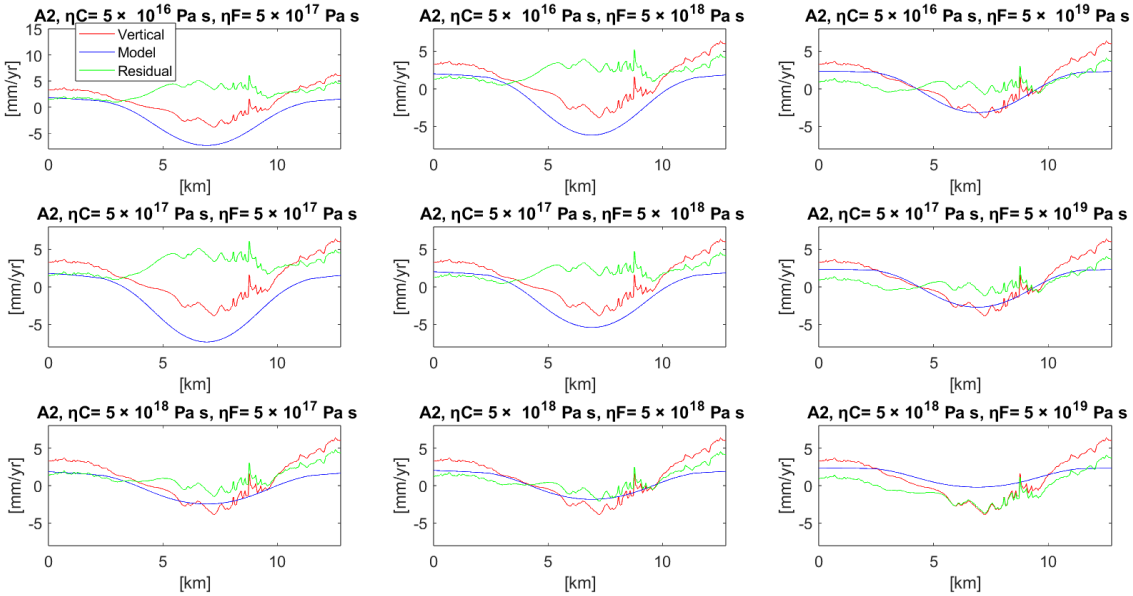

Figure S8. Caldera and Fissure Swarm model results for Krafla volcanic system. Profile AA' defined as in Figure 4a. All model combinations, in terms of viscosity values in the caldera, $\eta C = 5\times(10^{16} - 10^{18})$ Pa s, and in the viscoelastic fissure segment, $\eta F = 5\times(10^{17} - 10^{19})$ Pa s, are compared against the observation (in red) and display the residual (in green), when the elastic layer is 10 km thick.

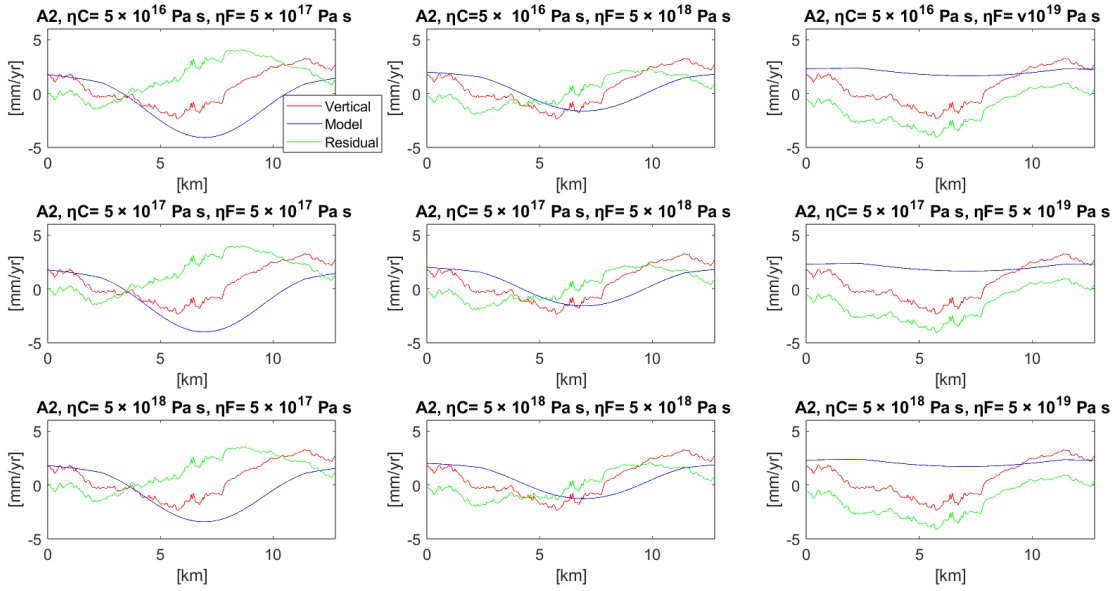

Figure S9. Caldera and Fissure Swarm model results for Krafla volcanic system. Profile BB' defined as in Figure 4a along the fissure segment. All model combinations (in blue), in terms of viscosity values in the caldera, ηC = 5×(10^{16} -10^{18}) Pa s, and in the viscoelastic fissure segment, ηF = 5×(10^{17} -10^{19}) Pa s, are compared against the observation and display the residual, when the elastic layer is 10 km thick.

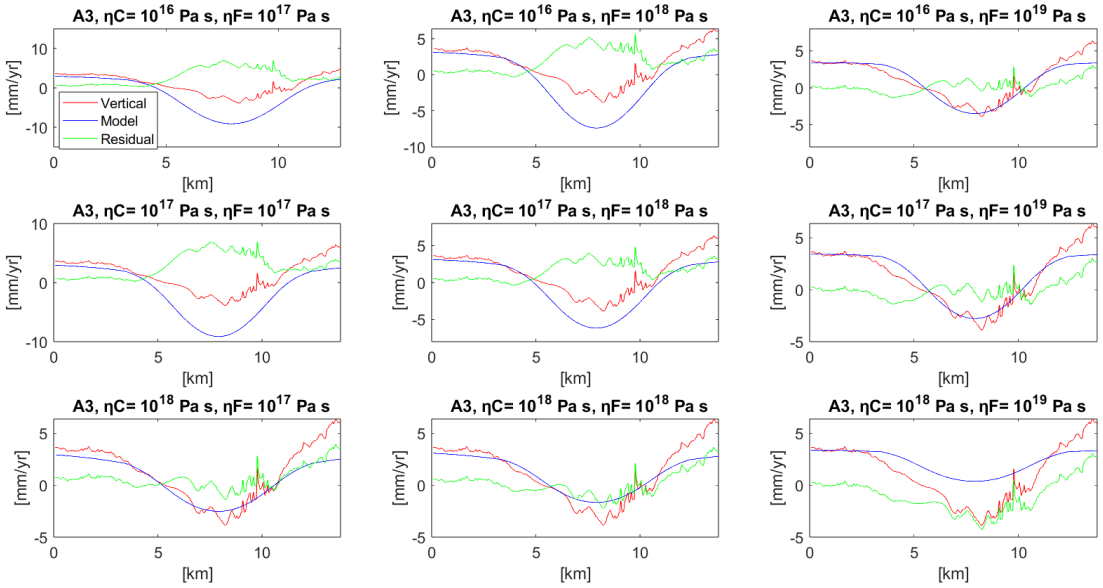

Figure S10. Caldera and Fissure Swarm model results for Krafla volcanic system as the profile AA' defined in Figure 4a along caldera. All model combinations (in blue), in terms of viscosity values in the caldera, ηC = 5×(10^{16} -10^{18}) Pa s, and in the viscoelastic fissure segment, ηF = 5×(10^{17} -10^{19}) Pa s, are compared against the observation and display the residual, when the elastic layer is 15 km thick.

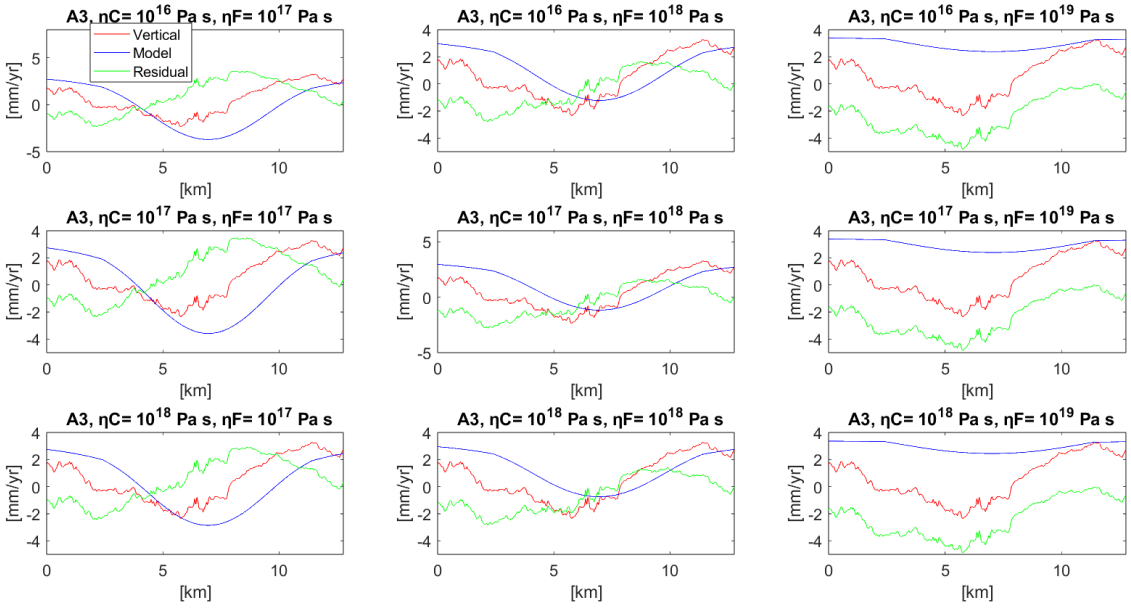

Figure S11. Caldera and Fissure Swarm model results for Krafla volcanic system as the profile BB' defined in Figure 4a along the fissure segment. All model combinations (in blue), in terms of viscosity values in the caldera, $\eta C = 5\times(10^{16} - 10^{18})$ Pa s, and in the viscoelastic fissure segment, $\eta F = 5\times(10^{17} - 10^{19})$ Pa s, are compared against the observation and display the residual, when the elastic layer is 15 km thick.

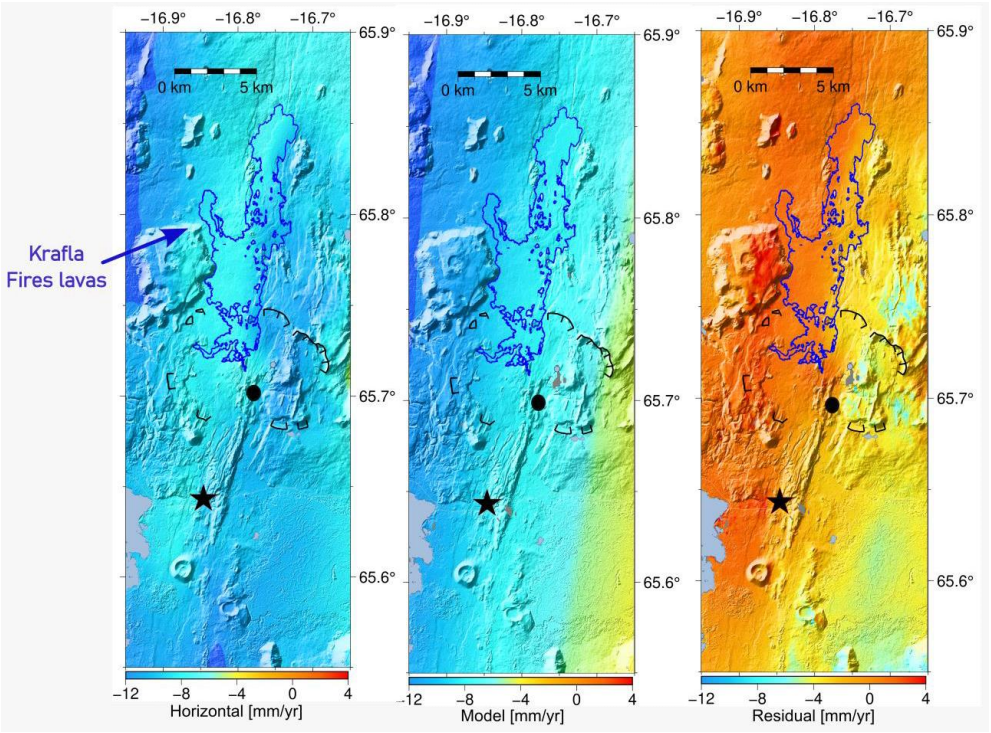

Figure S12. Inferred rate of horizontal displacements 2015-2018, model prediction, residuals in a map view for the Krafla volcanic system. The black circle and black star indicate the Krafla and Bjarnarflag power plants, respectively.

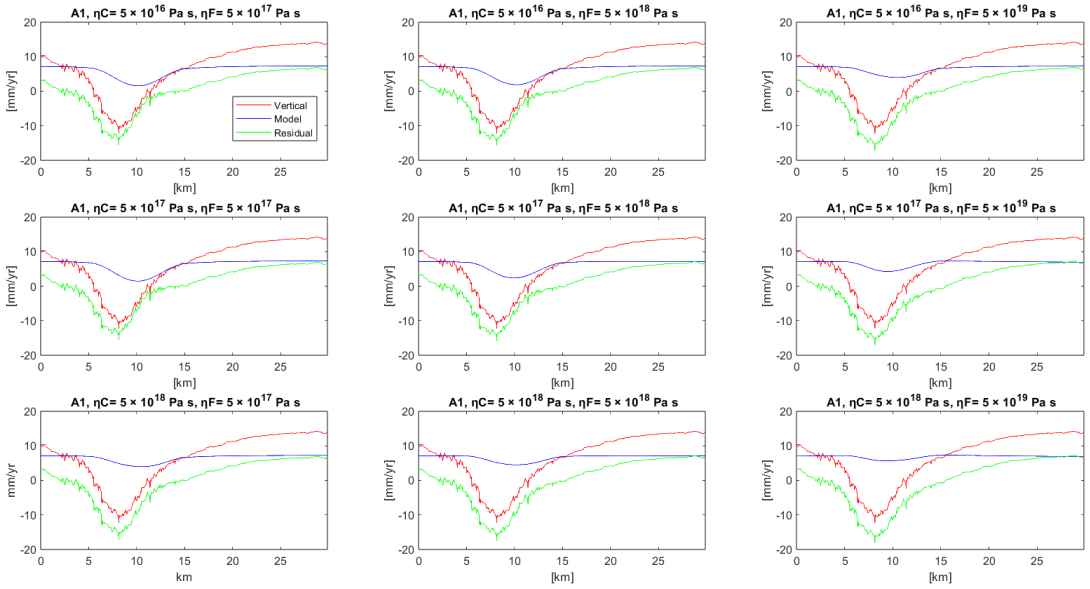

Figure S13. Caldera and Fissure Swarm model results for Askja volcanic system as the profile AA' defined in Figure 4f along caldera. All model combinations (in blue), in terms of viscosity values in the caldera, ηC = 5×(10^{16} -10^{18}) Pa s, and in the viscoelastic fissure segment, ηF = 5×(10^{17} -10^{19}) Pa s, are compared against the observation and display the residual, when the elastic layer is 7 km thick.

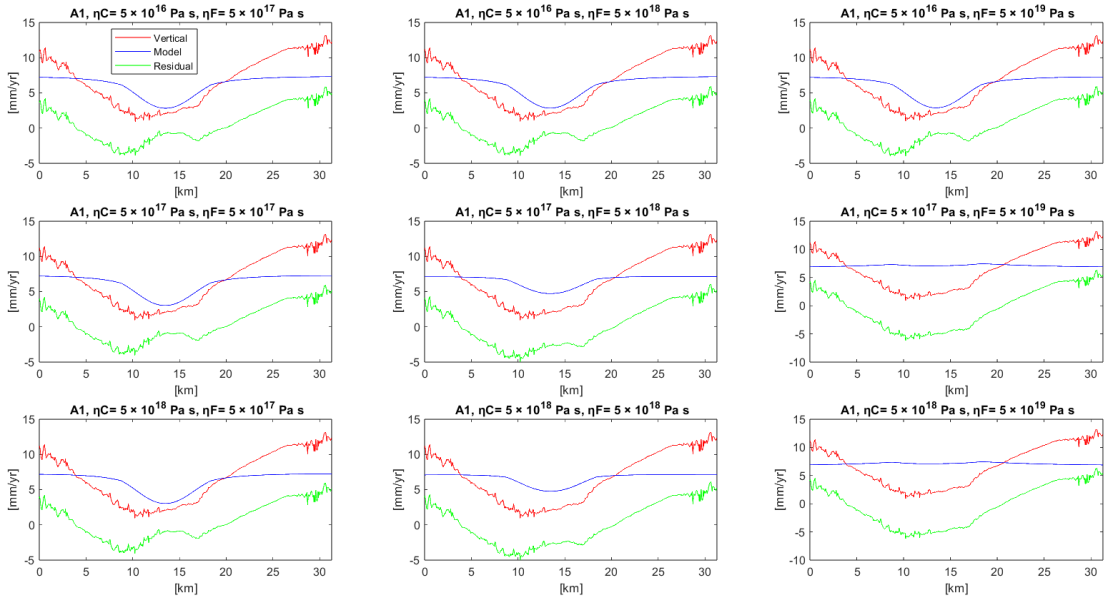

Figure S14. Caldera and Fissure Swarm model results for Askja volcanic system as the profile BB' defined in Figure 4f along caldera. All model combinations (in blue), in terms of viscosity values in the caldera, ηC = 5×(10^{16} -10^{18}) Pa s, and in the viscoelastic fissure segment, ηF = 5×(10^{17} -10^{19}) Pa s, are compared against the observation (in red) and display the residual (in green), when the elastic layer is 7 km thick.

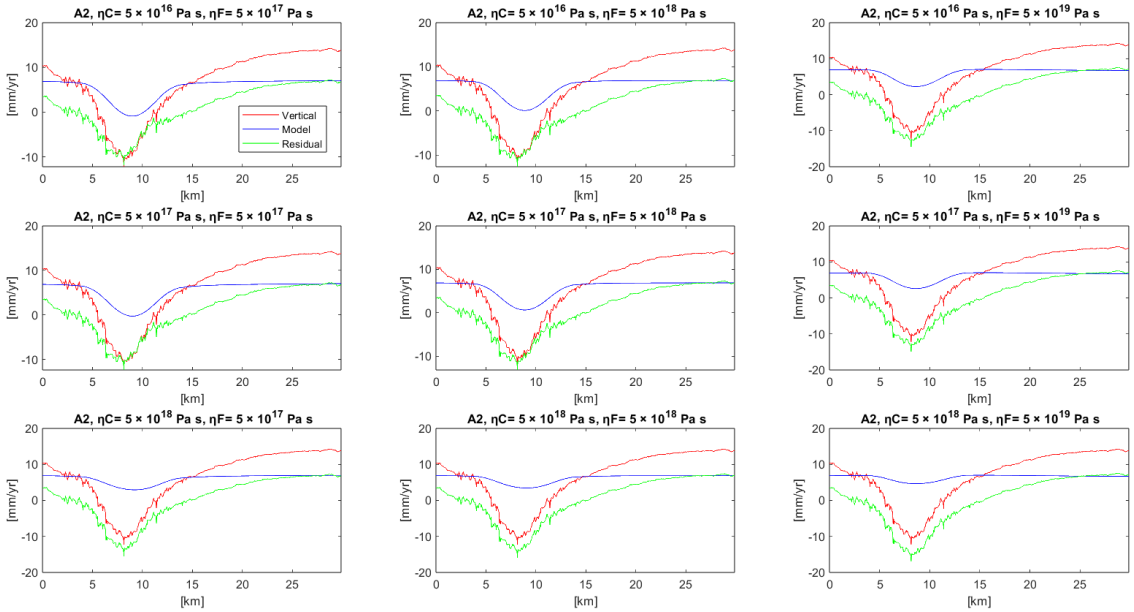

Figure S15. Caldera and Fissure Swarm model results for Askja volcanic system as the profile AA' defined in Figure 4f along caldera. All model combinations (in blue), in terms of viscosity values in the caldera, $\eta C = 5\times(10^{16} - 10^{18})$ Pa s, and in the viscoelastic fissure segment, $\eta F = 5\times(10^{17} - 10^{19})$ Pa s, are compared against the observation (in red) and display the residual (in green), when the elastic layer is 10 km thick.

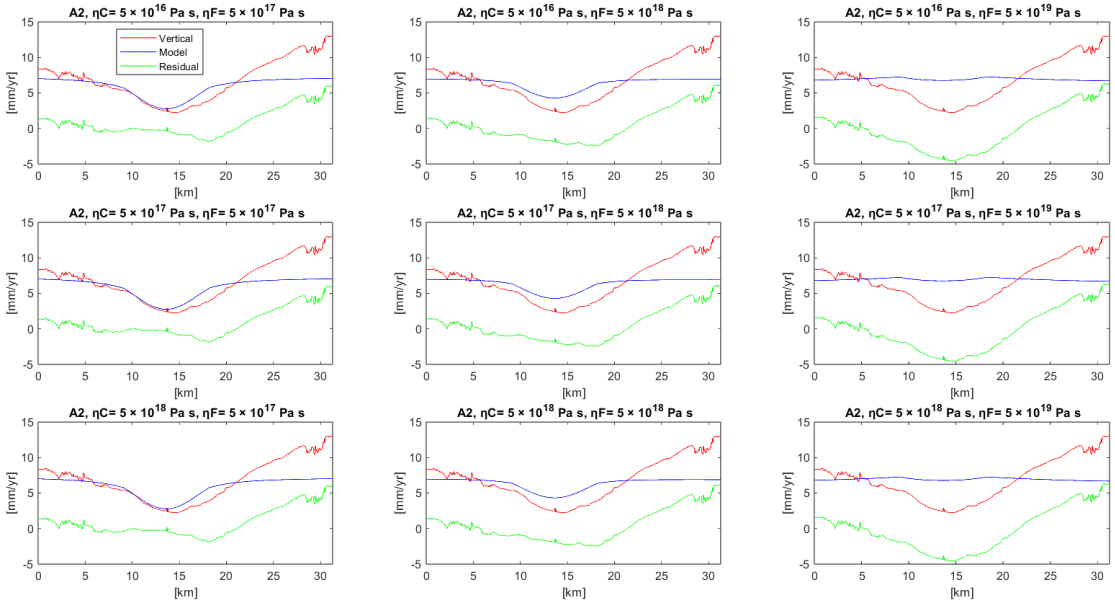

Figure S16. Caldera and Fissure Swarm model results for Askja volcanic system as the profile BB' defined in Figure 4f along caldera. All model combinations (in blue), in terms of viscosity values in the caldera, $\eta C = 5\times(10^{16} - 10^{18})$ Pa s, and in the viscoelastic fissure segment, $\eta F = 5\times(10^{17} - 10^{19})$ Pa s, are compared against the observation (in red) and display the residual (in green), when the elastic layer is 10 km thick.

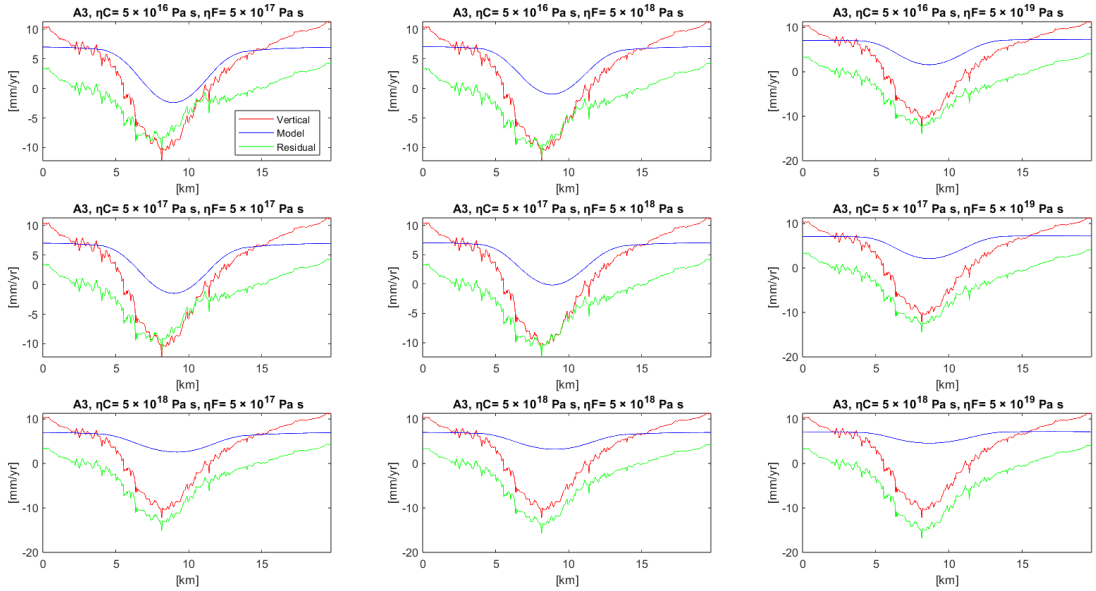

Figure S17. Caldera and Fissure swarm model results for Askja volcanic system as the profile AA' defined in Figure 4f along caldera. All model combinations (in blue), in terms of viscosity values in the caldera, ηC = 5×(10^{16} -10^{18}) Pa s, and in the viscoelastic fissure segment, ηF = 5×(10^{17} -10^{19}) Pa s, are compared against the observation (in red) and display the residual (in green), when the elastic layer is 15 km thick.

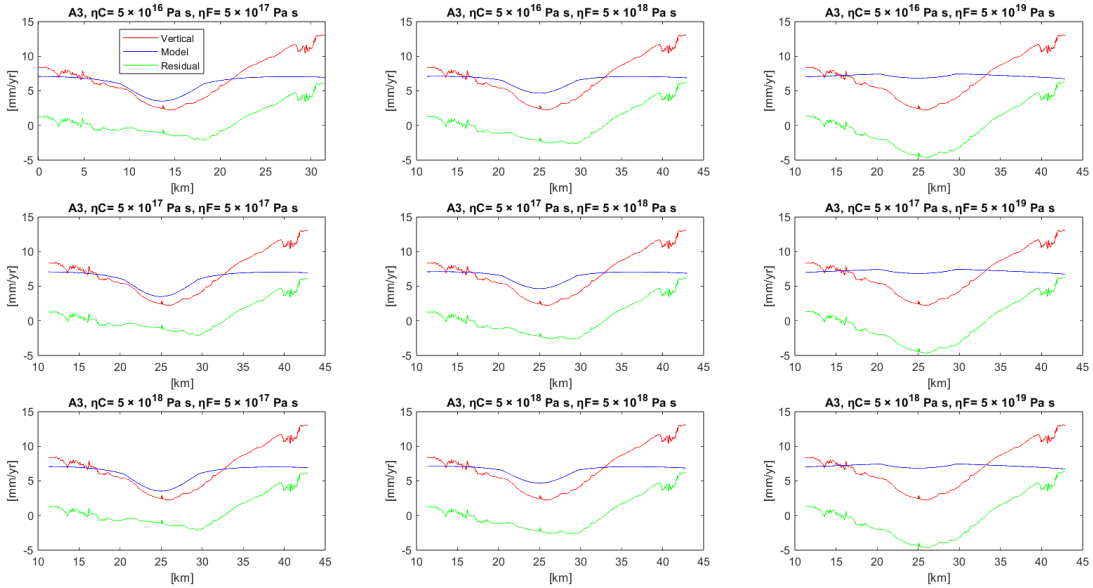

Figure S18. Caldera and Fissure swarm model results for Askja volcanic system as the profile BB' defined in Figure 4f along caldera. All model combinations (in blue), in terms of viscosity values in the caldera, ηC = 5×(10^{16} -10^{18}) Pa s, and in the viscoelastic fissure segment, ηF = 5×(10^{17} -10^{19}) Pa s, are compared against the observation (in red) and display the residual (in green), when the elastic layer is 15 km thick.

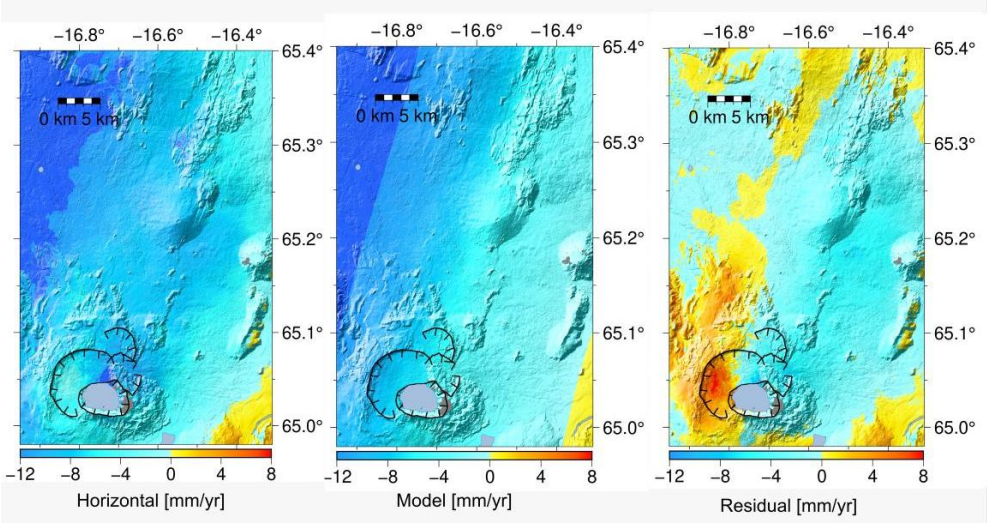

Figure S19. Inferred rate of horizontal displacements 2015-2018, model prediction, residuals in a map view for the Askja volcanic system.

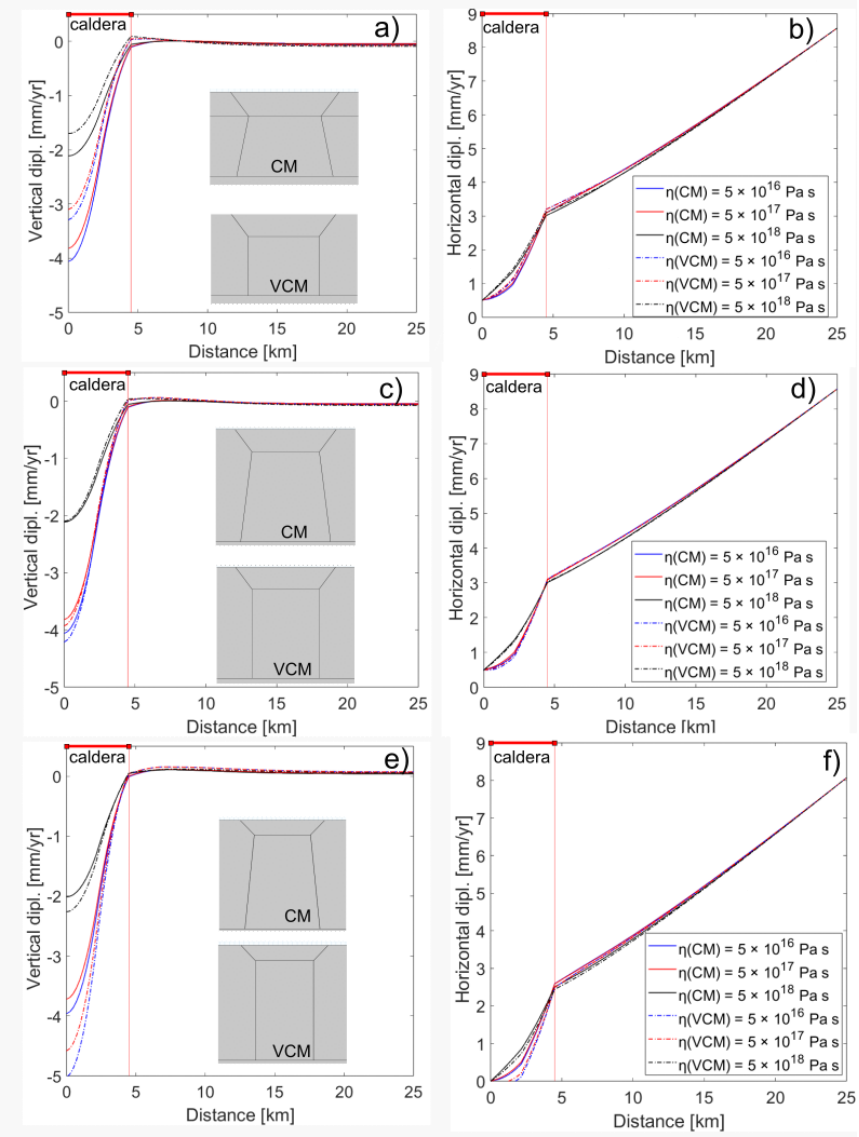

Figure S20. Comparison of the caldera model (CM) and the vertical column model (VCM), with elastic layer thickness = 7 km (A1) in a) vertical and b) horizontal displacements, with elastic layer thickness = 10 km (A2) in c) vertical and d) horizontal displacements and with elastic layer thickness = 15 km (A3) in e) vertical and f) horizontal displacements, along profile as defined in red in Figure 2a for viscosities values, η = 5×(10^{16}-10^{17}-10^{18}) Pa s. The CM and the VCM differs about a maximum subsidence of 1 mm/yr in the A1 and A3 geometries when the lowest viscosity, η = 5×10^{16} Pa s is used. The A2 geometry and the horizontal deformation in all geometry tested do not show a significant difference between the CM and VCM models. A second feature between the two sets of models is a small uplift signal at the caldera and surrounding elastic layer boundary at surface in the VCM. The signal is more pronounced in the A1 and A2 geometries and subdued in A3.

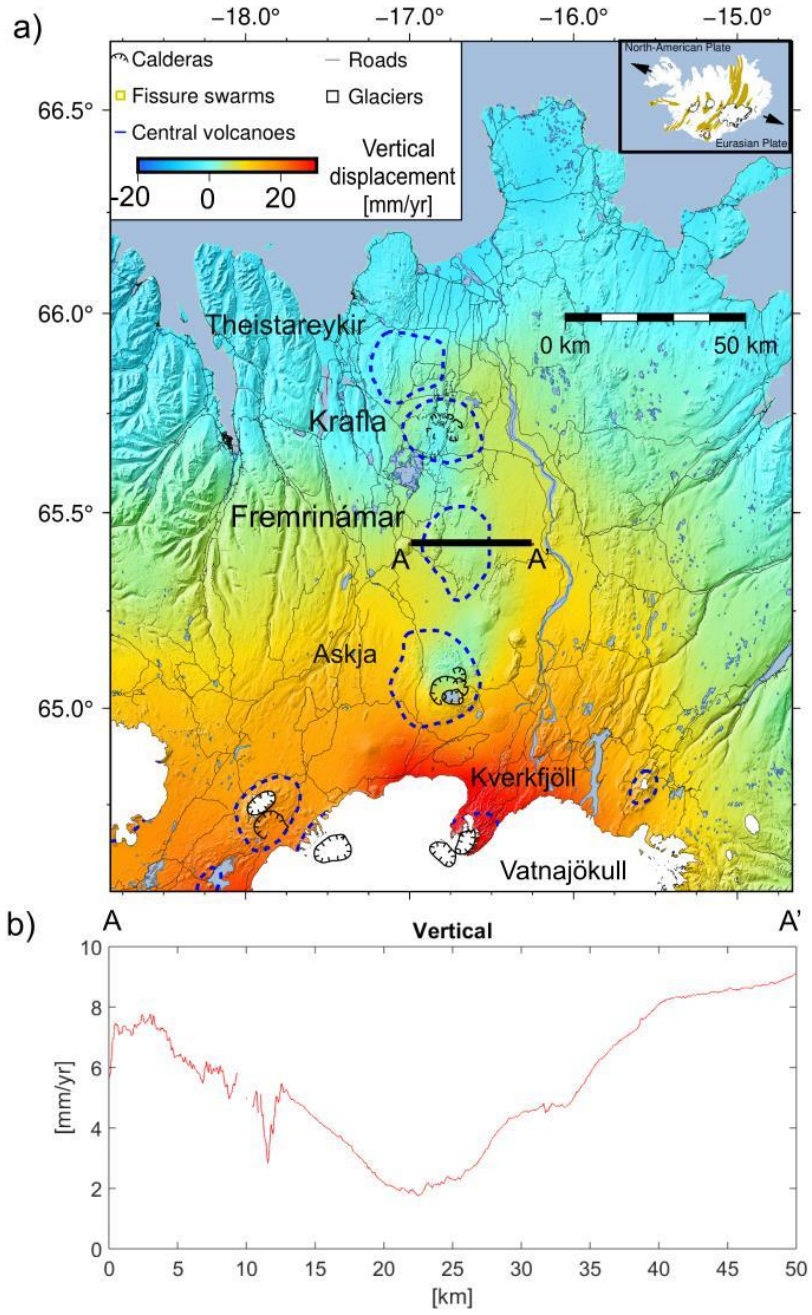

Figure S21. a) Inferred rate of vertical displacements 2015-2018, for the NVZ. b) Vertical displacements as defined in the AA' west-east profile in panel a) at the Fremrinámur volcanic system. Calderas, central volcanoes, and fissure swarm are by Jóhannesson et al. (2009).

Table S1. Model characteristics.

Model Name	Elastic layer thickness	Caldera Model	Caldera and Fissure Swarm model
A1	7 km	Viscoelastic rheology present beneath the caldera	Viscoelastic rheology present beneath the caldera and the fissure segments
A2	10 km		
A3	15 km		

Table S2. Subsidence rate for the Caldera (C) model and Caldera and Fissure Swarm (CFS) model.

	C model			CFS model		
Viscosity in the caldera	A1 mm/yr	A2 mm/yr	A3 mm/yr	A1* mm/yr	A2* mm/yr	A3* mm/yr
5×10^{16} Pa s	3.5	3.9	4.7	6.5	10	13
5×10^{17} Pa s	3.2	3.7	4.3	5.9	9.0	11
5×10^{18} Pa s	1.8	2.0	-2.1	3.0	5.0	6.0

*viscosity in the fissure segment = 5×10^{17} Pa s

Paper III

Transient ground deformation observed by cGNSS and InSAR during and following the 2021 Fagradalsfjall eruption, Iceland

Chiara Lanzi, Halldór Geirsson, Michelle Maree Parks, Vincent Drouin, Freysteinn Sigmundsson

Submitted to Bulletin of Volcanology

Transient ground deformation observed by GNSS and InSAR during and following the 2021 Fagradalsfjall eruption, Iceland

Chiara Lanzi (1, 2), Halldór Geirsson (1), Michelle Maree Parks (2), Vincent Drouin (2), Freysteinn Sigmundsson (1)

(1) Nordic Volcanological Center, Institute of Earth Sciences, University of Iceland, Reykjavik, Iceland
(2) Icelandic Meteorological Office, Reykjavik, Iceland

Abstract

Geodetic observations, coupled with modelling of the detected signals, can help discriminate between different processes contributing to measured surface deformation during a volcanic eruption, providing insight into its evolution, the associated magma transport, and processes occurring in the subsurface. We use Global Navigation Satellite System (GNSS) geodesy and Interferometric analysis of Synthetic Aperture Radar (InSAR) satellite images to map overall gradual deflation during the six-month-long 2021 eruption in Geldingadalir at Mt. Fagradalsfjall, in SW-Iceland. The co-eruptive deflation shows three temporal phases: T1, 19 March – 10 May; T2, 11 May – 31 July; T3, 1 August – 18 September, correlating with changes in the effusion rate, eruptive style, and geochemistry of the erupted basalt. Effects of lava loading are evident in the geodetic observations. We remove this signal with a Finite Element Method (FEM) model and infer geodetic sources responsible for the observed ground deformation. Our observations are best explained by a deflating sill-shaped source at ~12–14 km depth with volume contraction of 21–27 Mm^3, around 4-5 times lower than the estimated bulk volume of the erupted material. Inflation was detected after the eruption and can be modelled at a similar depth as the co-eruptive source. Understanding co- and post-eruptive ground deformation

patterns and their correlation with other observables at volcanoes e.g., effusion rate and geochemistry is essential to unveil the architecture of the underlying magmatic plumbing system and hazard assessment, considering also the possibility of reactivation of neighboring volcanic systems, known from earlier volcanic activity periods on the Reykjanes Peninsula (RP).

1 Introduction

Volcanic eruptions are commonly associated with pre-, co- and/or post-eruptive ground deformation, but the style, magnitude and occurrence of surface displacements in the different phases of a volcanic cycle varies significantly (e.g., Lanari et. al, 1998; Dzurisin, 2006; Lu et al. 2007). GNSS and InSAR techniques are commonly applied to investigate volcano deformation patterns providing maps of high spatial and temporal resolution of ground movements (e.g., Mann et al. 2002; Di Traglia et al. 2014; Poland and Zebker, 2022; Hamling, 2021). Regional processes that require consideration include plate motion and Glacial Isostatic Adjustment (GIA) (e.g., Árnadóttir et al. 2009; Drouin and Sigmundsson, 2019). Local processes other than magmatic include pre- co- and post-seismic deformation (Pagli et al. 2003; Árnadóttir et al. 2004; Árnadóttir et al. 2005), geothermal deformation (Juncu et al. 2017), landslide deformation (Makabayi et al. 2021), and loading effects (Briole et al. 1997; Lucas et al. 2022).

Here we provide an analysis of ground deformation patterns observed during the six-month (19 March - 18 September 2021) Fagradalsfjall eruption, the first eruption of the current period of high volcanic activity on the Reykjanes Peninsula in Southwest Iceland (Fig. 1). Using detrended GNSS time series and InSAR observations, and analytical models, we constrain location, geometry and volume change of the deforming source causing the observed deflation for the whole co-eruptive period, as well as parameters for different stages of the eruption. Additionally, we find that accounting for lava loading is important when modeling the deformation signal. We study the correlation between temporal changes in ground displacements and variations in effusion rates and

time-series of geochemical analysis of lava samples. Furthermore, we investigate the evolution of the post-eruptive deformation, from end-September to mid-December 2021.

1.1 Tectonic background

The RP is a zone of oblique spreading at the Eurasian and North-American plates (Fig. 1). The central axis of the plate boundary deformation is aligned to ~N77°E, whereas the direction of plate spreading is ~N105°E, at a rate of ~18-19 mm/yr, according to global plate motion models (e.g., DeMets et al. 2010) and GNSS and InSAR observations (Árnadóttir et al. 2009; Drouin and Sigmundsson, 2019). The RP is the on-land continuation of the Mid-Atlantic Reykjanes Ridge to the west, and to the east it connects to the South Iceland Seismic Zone (SISZ) and the Western Volcanic Zone (WVZ) of Iceland at the Hengill triple junction (approximately 64°N, 21.4°W; Fig. 1). From west to east, the Reykjanes, Svartsengi, Fagradalsfjall Krýsuvík, Brennisteinsfjöll and Hengill volcanic systems can be identified (Fig. 1; Sæmundsson et al. 2020). They are spaced ~5 km apart, with fissure swarms striking N40°E in average (Clifton and Kattenhorn 2006; Hjartardóttir et al. 2023) and characterized by eruptive fissures with crater rows and extensive normal faulting. N-S trending arrays of strike-slip faults, mostly displaying right-lateral movement, also cut across the plate boundary (Einarsson, 2008). All the volcanic systems, except Fagradalsfjall, have geothermal areas, and the Reykjanes, Svartsengi, and Hengill high-temperature geothermal fields are exploited for energy production (Parks et al. 2020; Juncu et al. 2020).

The geological history for the latter half of the Holocene shows episodic eruptive periods, each lasting a few hundred years, separated by relatively long intervals (800-1000 years) of quiescence (Sæmundsson et al. 2020). Effusive eruptions have typically occurred on several kilometers-long fissures, with minor ash produced (Gudmundsson et al. 2008). During each eruptive period, volcanism jumps from one system to another (Sæmundsson et al. 2020). A previous period of volcanic activity on the RP occurred 800-1240 AD, and included eruptions at the Reykjanes, Svartsengi, Krýsuvík and Brennisteinsfjöll volcanic systems, while at Fagradalsfjall the last eruption occurred ~7000 yr ago (Sæmundsson et al. 2016).

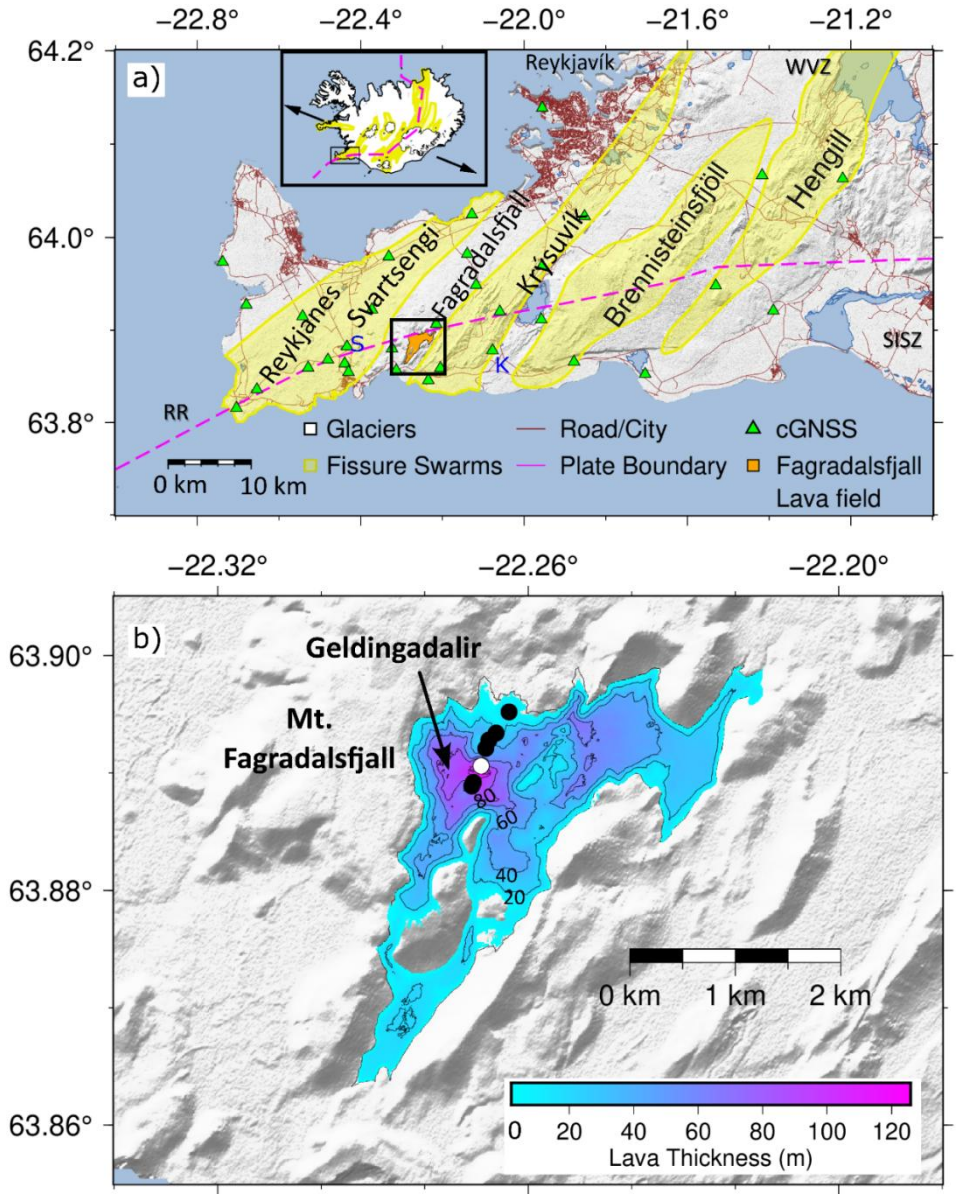

Figure 1. a) Map of the Reykjanes Peninsula showing the location of the Fagradalsfjall 2021 lava field (Pedersen et al. 2022), the continuous GNSS network and the central axis of the plate boundary deformation (Sigmundsson et al. 2022). Fissure swarms from Jóhannesson et al. (2009) are shown in yellow. Sæmundsson et al. (2020) identified also the Fagradalsfjall system between Svartsengi and Krýsuvík. SISZ = South Iceland Seismic Zone, RR= Reykjanes Ridge and WVZ = Western Volcanic Zone. In blue uppercase letters, S = SENG and K = KRIV: two GNSS sites, shown in Figure 2. Ocean and lakes in light blue. Inset shows Iceland with fissure swarms, glaciers, and the plate boundary axis (Árnardottir et al. 2009). The arrows indicate relative plate motion. Reykjanes Peninsula is marked by a black rectangle. The black square in (a) indicates the region of panel (b), which shows a thickness map (isopachs spaced at 20 m) of the lava field at Fagradalsfjall on 30 September 2021 (Pedersen et al. 2022).The white and black circles are locations of the vents that opened between March-April 2021, with the white circle indicating the only active vent from 27 April to the end of the eruption (Barsotti et al. 2022).

Seismic monitoring on the RP prior the current phase showed episodic activity with periods of elevated seismicity lasting about a decade (1929-1935, mid-1950s, 1967-1977 and 1997-2006) every 20-25 years (Klein et al. 1977; Einarsson et al. 1991; Árnadóttir et al. 2004; Björnsson et al, 2020). Mainshock-aftershock sequences occur predominantly in the eastern RP (east of 22.4° longitude, Keiding et al. 2008), associated with strike-slip faulting on N-S striking faults, mainly in the Krýsuvík and Hengill areas (Tryggvason, 1973; Árnadóttir et al. 2004; Keiding et al. 2008; Hreinsdóttir et al. 2009). Earthquake swarms are more typical in the western part (Tryggvason, 1973; Einarsson, 1991). Pronounced swarm activity, at 2-6 km depth, was observed at Fagradalsfjall and Krýsuvík volcanic systems in 1997-2006 (Keiding et al. 2008; 2009). Seismicity was observed again in 2017 along the plate boundary at Fagradalsfjall in a 9 km-long cluster directed WSW-ENE with strike ~N67°E (Hrubcová and Vavryčuk, 2023). In the central part of this cluster, an aseismic gap was observed at depths of 3–6 km and interpreted by Hrubcová and Vavryčuk (2023) as a zone of crustal weakening with stress changes because of plate spreading and upcoming fluid flow during a preparatory phase which led to the 2021 Fagradalsfjall volcanic eruption. Seismic tomography, based on 2014-2015 data, locates a horizontal low-velocity anomaly at 5–8 km depth extending along the whole Peninsula, except beneath the Svartsengi and Krýsuvík geothermal fields, where the anomaly reaches 4-6 km depth, suggesting that all the volcanic systems on the RP are connected to some degree (Rahimi-Dalkhani et al. 2023).

The plate boundary deformation field was mapped by GNSS measurements in 1986-1992, showing left-lateral strain accumulation across the RP (Sturkell et al. 1994). This was later confirmed by 1992-1995 InSAR data, with an inferred plate boundary locking depth of ~5 km (Vadon and Sigmundsson, 1997) and by 1993-1998 GNSS measurements (Hreinsdóttir et al. 2001). Keiding et al. (2008) re-modeled the observations of Hreinsdóttir et al. (2001), along with newer data, and found that deformation during non-magmatic periods on the RP agrees well with shear and extension according to global plate motion models. Stress inversions of seismicity are further in agreement with plate motion models (Keiding et al. 2009). Continuous GNSS monitoring on the RP shows overall constant deformation rates prior to 2021, except due to mainshock-aftershock activity, e.g., in 2000 (Árnadóttir et al. 2004), 2003 (Keiding et al.

2008) and 2008 (Sigbjörnsson et al. 2009), or inflation/deflation cycles due to geothermal activity at Svartsengi, Krýsuvík and Hengill geothermal areas (Vadon and Sigmundsson, 1997; Eysteinsson, 2000; Keiding et al. 2009; Gudjónsdóttir et al. 2020; Ducrocq et al. 2021), until end-2019 (Sigmundsson et al. 2024).

1.2 The 2019 -2021 volcano-tectonic unrest and the 2021 Fagradalsfjall eruption

In December 2019, seismicity increased above the previous background level in the Fagradalsfjall area. Three inflation episodes were detected in the Svartsengi area, ~10 km to the west of Fagradalsfjall, by geodetic monitoring in January, March-to-April and May-to-July 2020, with uplift rates of 3–4 mm/d (Geirsson et al. 2021), coinciding with the onset of an earthquake swarm (Flóvenz et al. 2022). Each inflation was followed by deflation and decreasing seismicity (Çubuk-Sabuncu et al. 2021; Flóvenz et al. 2022; Fig. 2). The cumulative uplift (~10 cm) has been attributed to intrusion of sills at 3.2–4.3 km depth with a total volume of 9–11 Mm^3 (million cubic meters) (Çubuk-Sabuncu et al. 2021; Geirsson et al. 2021), either driven by injection of magma-derived gas into the shallow crust (Flóvenz et al. 2022), or injection of magma into a previously existing magma domain (Sigmundsson et al. 2024).

In mid-July 2020, inflation started in the Krýsuvík volcanic system (Fig. 2), ~10 km to the east of Fagradalsfjall, and a M_w 5.6 earthquake occurred there on 20 October (Geirsson et al. 2021; Flóvenz et al. 2022). An overall seismicity migration to the east was observed across the peninsula in 2020 (Ducrocq et al. 2024). From December 2019 and until the Fagradalsfjall dike started forming on 24 February 2021, TerraSAR-X interferometry shows surface fault movements, on hundreds of unknown fractures in the western and central part of the RP, mostly coinciding with the earthquake at Krýsuvík and the Svartsengi inflations (Ducrocq et al. 2024). Furthermore, movement was observed between 11 July and 22 October 2020 on a ~2 km-long N45°E striking fracture at Fagradalsfjall, with location coinciding with the longest lasting volcanic vent of the subsequent 2021 eruption (Ducrocq et al. 2024) and partially coinciding with the 2017 seismicity observed by Hrubcová and Vavryčuk (2023). Although no inflation-deflation episodes are known at Fagradalsfjall prior to the 2021 eruption, a localized strain anomaly

was observed there in 2015-2018 (Sigmundsson et al. 2022), a seismic swarm in 2017 (Hrubcová and Vavryčuk, 2023), as well as deep seismicity (~10-12 km depth) since June 2020 (Greenfield et al. 2022).

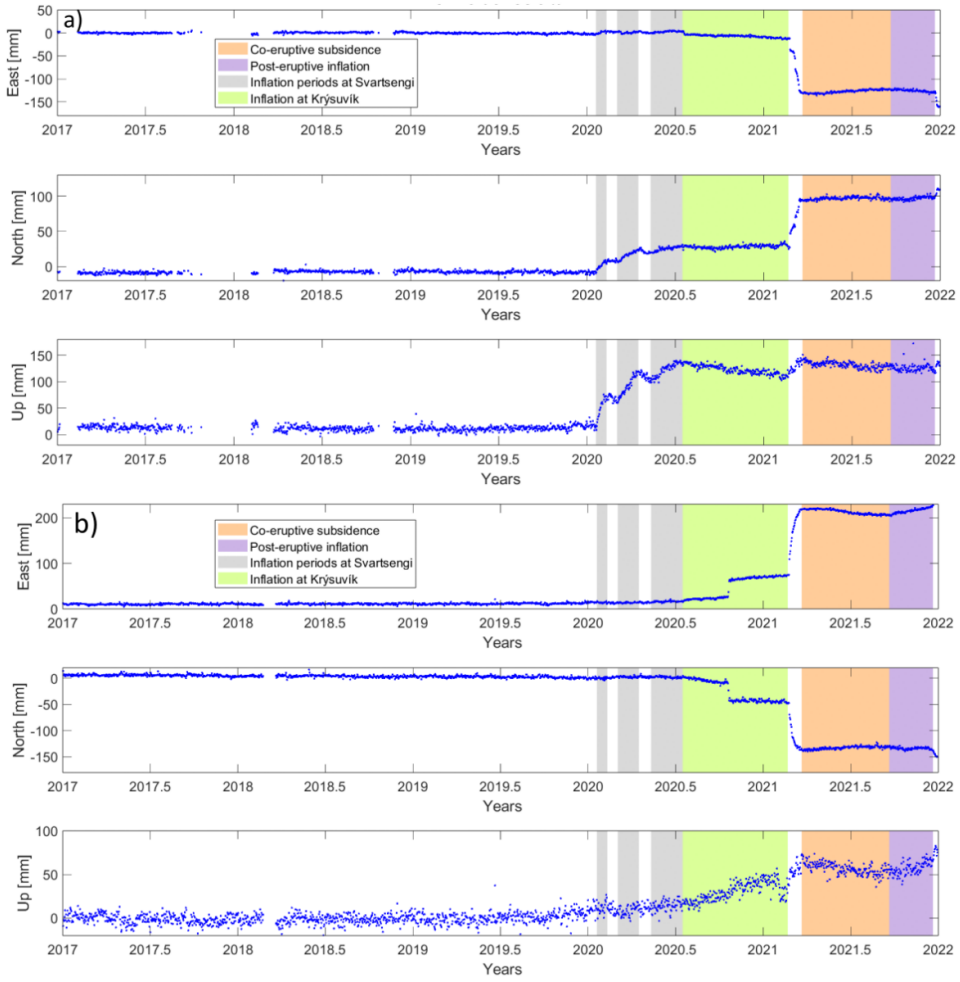

Figure 2. Continuous GNSS detrended time series from 2017 to end of 2021 at stations SENG (a) and KRIV (b). Linear trend as well as annual and semi-annual terms have been estimated (for 2015-2020) and removed. Inflation periods in 2020 at Svartsengi are shown with grey background shadow are: 21 January – early February, 6 March – 17 April and 15 May – 22 July (Cubuk-Sabuncu et al. 2021). The Krýsuvík inflation, started on 15 July is marked in light green until the M_w 5.6 earthquake on 20 October. According to the north component on KRIV station, the inflation slowed down before earthquake occurred at Krýsuvík on 20 October 2020, causing the observed discontinuity in the north and east component. Afterwards, very small signal, possibly related to post-seismic deformation, is observed. On 24 February 2021, a dike intrusion started beneath Fagradalsfjall marking the rapid following change observed in the time series. The 2021 Fagradalsfjall co-eruptive deformation is from 19 March to 18 September 2021; initial post-eruptive inflation period occurred from 19 September to 20 December 2021.

On 24 February 2021, a M_w 5.64 earthquake occurred at the Fagradalsfjall volcanic system, preceded by a three-hour-long intense but small magnitude seismic swarm. High seismicity and high deformation rates (from continuous GNSS and InSAR observations) followed during the formation of an evolving dike intrusion until 19 March 2021, when an effusive lava eruption began. Seismicity was located on and around both the Fagradalsfjall growing dike intrusion and the many approximately north–south oriented strike-slip faults triggered by the intrusion (Sigmundsson et al. 2022). The high rates of deformation and seismicity observed during the initial phase of the dike intrusion declined to almost null at the eruption onset (Sigmundsson et al. 2022), while continued movements on the previously detected fractures were observed by InSAR at least until end-April (Ducrocq et al. 2024). The February-March 2021 Fagradalsfjall dike consisted of a southern segment (strike N24°E) and a northern segment (strike N45°E), with a total length of ~9 km and volume intruded around 26–34 Mm^3 between the surface and ~8 km depth (Sigmundsson et al. 2022).

The behavior of the 2021 Fagradalsfjall eruption varied with time, for example with respect to the time-average discharge rate (TADR). The initial TADR was up to 4.9 m^3/s until 5 April, when lava production concentrated on two vents spaced ~500 m apart (Pedersen et al. 2022). Afterwards, several short-lived additional fissures opened between the two vents (Barsotti et al. 2022), but then the activity stabilized at one vent on 27 April (Fig. 1b). At the beginning of May, the eruption displayed episodic intense lava emplacement followed by inactive periods, with TADR around 13-11 m^3/s until early September. Each period of lava fountaining, compared to repose time, was characterized by higher acoustic amplitudes and an inferred increase in gas bubble radii between early and late-May, suggesting a widening of the upper conduit (Lamb et al. 2022). Eibl et al. (2023) proposed that the dimension of the eruptive vent and the widening of the crater controlled the observed larger seismic amplitudes at the beginning of May. The duration and intermittency of the lava fountaining events are suggested to relate to pressure cycles within a shallow magma-filled cavity (~100 m), where CO_2 degassing during the magma ascent in the upper crust, is followed by further gas-liquid separation (Scott et al. 2023). After a 9-day long pause in early-September, the eruption resumed on 11 until it ended on 18 September (Pedersen et al. 2022). Post-eruptive inflation followed until 21

December 2021 when a new diking event occurred beneath Fagradalsfjall (Parks et al. 2023).

Geochemical analysis of eruptive products (from the beginning of the eruption to end of April) reveal compositional diversity of the erupted lava, consistent with extraction of magma from aggregation of melts from separate magma bodies initially located within the shallowest part of the mantle, which become gradually increasingly dominated by magmas generated at greater depths (Halldórsson et al. 2022; Marshall et al. 2024). Thermobarometry analysis on tephra glass collected 28 April-6 May confirmed such evolution (Bali et al. 2021), indicating that prior to erupting the magma last equilibrated at a depth of more than 15 km, near the Moho discontinuity (Weir et al. 2001). Furthermore, the longest time scales inferred by diffusion chronometry shows that a phase of deep magma accumulation (without geodetic detection) and mush disaggregation was ongoing on the RP at least one to two years before the eruption occurred (Kahl et al. 2022).

2 Geodetic data acquisition and time series analysis

2.1 GNSS

At the time of the 2021 eruption, a local network of continuous GNSS (cGNSS) stations was present throughout the RP (Fig. 1). Some of the stations had been installed during the decade prior to the unrest to investigate inflation-deflation episodes occurring at different volcanic systems and geothermal utilization-related deformation in the area. In 2020, additional cGNSS sites were installed near Svartsengi to monitor the ongoing unrest, and at the beginning of the 2021 Fagradalsfjall diking event more stations were added (Fig. 3).

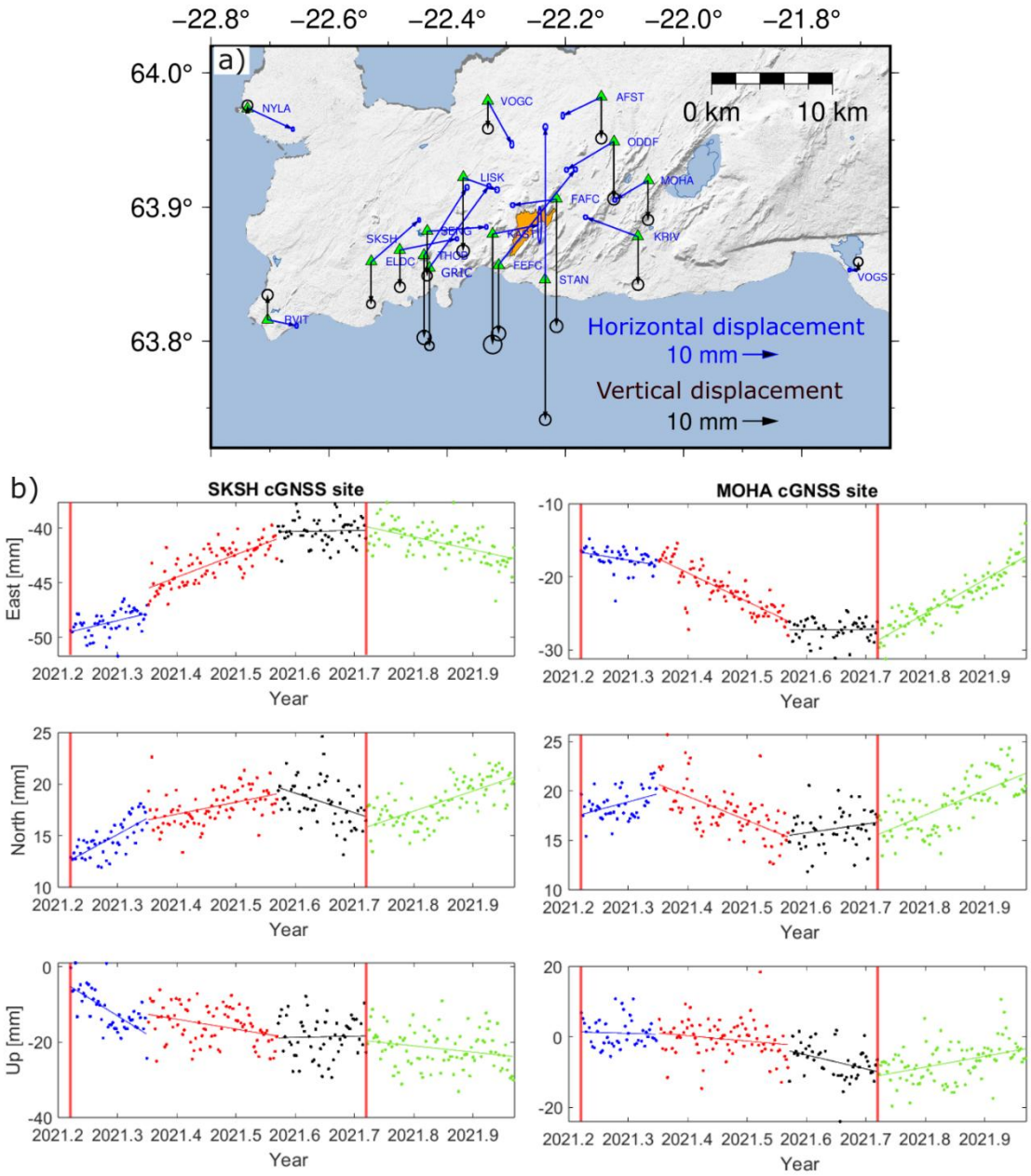

Figure 3. Displacements from 19 March to 20 December 2021. The upper panel shows GNSS stations (in green triangles) with inferred vertical and horizontal displacements (arrows) and associated one standard deviation (1σ) uncertainties (ellipses). Also shown is the Fagradalsfjall lava field at the end of the eruption in orange, and ocean and lakes in light blue. The lower panels display detrended GNSS time series for stations SKSH (on the left panel) and MOHA (on the right panel) located west and east to the eruption site, respectively. The three co-eruptive deformation periods are marked: T1: 19 March – 10 May (blue dots), T2: 11 May - 31 July (red dots), T3: 1 August – 18 September (black dots), and post-eruptive deformation, 19 September – 20 December (green dots). The vertical red lines indicate the beginning and end of the eruption. The blue, red, black and green lines show the least-square fit for the different geodetic phases.

We processed the cGNSS data available for precise daily positioning with both the GAMIT/GLOBK software (version 10.7, Herring et al. 2018) and the GIPSY/OASIS II software (Zumberge et al. 1997). The GAMIT/GLOBK site positions are evaluated in the ITRF14 reference frame using over 100 worldwide reference stations (Altamimi et al. 2017). The data are corrected for ocean tidal loading using the FES2004 model (Lyard et al. 2006). The GIPSY/OASIS II analysis uses the same ocean tidal loading model and ITRF14 reference frame. The time series resulting from the GAMIT/GLOBK and GIPSY/OASIS II processing are comparable; here we present only the results from the GIPSY/OASIS II processing.

For cGNSS time series longer than 5 years prior to the unrest period that began in December 2019, we estimated and removed linear, annual, and semiannual variation in the years from 2015 to end-2019 (Supplementary Table S1). We use this specific period as time series were not significantly affected by volcanic and seismic deformation. We fit the following equation to the geodetic times series:

$$\mathrm{y(t)} = a + b\mathrm{t} + c\cos\left(\frac{2\pi t}{T}\right) + d\sin\left(\frac{2\pi t}{T}\right) + e\cos\left(\frac{4\pi t}{T}\right) + f\sin\left(\frac{4\pi t}{T}\right) \qquad (1)$$

The parameters a-f are constant and indicate: *a,* linear component intercept with *y*-axis at $t = 0$, *b* is the linear component rate, *c*, *d* are the amplitude of annual (12 months) periodic perturbations and *e* and f are the corresponding semiannual (6 months) amplitudes. *T* is equal to the period of 1 year. We estimated the *a-f* parameters for each of the east, north and up components using the Tsview software (Herring, 2003). Then, we subtracted the resulting fitted equation from each time series over its entire time span. We refer to these as detrended long time series. For time series, from stations installed in 2020 and 2021, shortly prior to the eruption, we could not apply equation 1. Instead, we first applied an ITRF-EU rotation (to a fixed Eurasian plate) to the time series, and then we subtracted the expected plate boundary deformation motion using a plate boundary model by Drouin and Sigmundsson (2019). We refer to these as detrended short time series. For both the short and long detrended time series, we estimate the co-eruptive deformation and uncertainties by calculating the co-eruptive deformation rate using the least squares method and then multiply the rate by the total time length of the eruption

(19 March – 18 September). Uncertainties are presented as ellipses with 1σ sigma standard deviation (Fig. 3). Several GNSS times series have repeated gaps (often one week-long) in the co-eruptive period. Data from such time-series were not shown in Fig. 3 and not included in the modelling for the six-month eruptive period. However, they were used if they had a continuous recording during a specific period of modelling interest (Section 3).

The full co-eruptive period (CP) deformation shows horizontal displacements aligned inward towards the eruption site, and general subsidence (Fig. 3; Supplementary Figs. S1-S5). The average inward horizontal displacement is ~15–20 mm and maximum value around ~40 mm at station STAN. The maximum observed subsidence is about ~30–40 mm at STAN and FAFC stations (Fig. 3). The time-series reveal several velocity changes during the CP (Fig. 3b; Supplementary Figs. S1–S5). Visual inspection of the time series and the definition of linear trends where the variance of the data shows a sense of consistency e.g., the highest and lowest data points remain approximately constant over time, spotted upward or downward trends common in all the deformation components, establishing three geodetic phases: T1, 19 March – 10 May, with relatively small displacements, up to ~6 mm in horizontal and ~8 mm, and subsidence; T2, 11 May – 31 July, with the fastest displacement rate of the CP, with maximum horizontal displacement of ~25 mm at STAN site (south of the eruptive site). Maximum subsidence was ~23 mm at FAFC and STAN stations (Supplementary Fig. S4) and average value around ~10 mm; T3, 1 August – 18 September (end of the eruption), with small displacements again. The displacements in the geodetic phases are estimated in a similar manner as the CP displacement: by multiplying the estimated displacement rates for T1, T2 and T3 periods by the time length of each geodetic phase. In the 5 weeks following the onset of the eruption, ~10 vents opened at different times, with most of them ceasing activity within 10–30 days of their opening. With each new vent opening, 1-day interferograms observed local ground deformation within ~1 km distance from the vent opening (Drouin et al. 2021). The GNSS sites are relatively far from the vent opening area; however, some of the variability in the ground deformation observed in the GNSS time-series in T1 (e.g., FEFC, Supplementary Fig. S2) may relate to the opening of more vents. The changes from T1 to T2 and T2 to T3 are clearly defined in the east and north components while

the vertical change is more subdued (Fig. 3b; Supplementary Figs. S1-S5). During the T2 phase, there is clear horizontal motion towards the eruptive site at cGNSS stations across the RP. For the vertical displacement, the pattern is more variable. Both near-field (<10–12 km from the eruption site) and the far-field (>12 km from the eruption site) stations on the east side of Fagradalsfjall show subsidence, while the westernmost stations show no significant movement (e.g., NYLA, RVIT in the Reykjanes volcanic system, Supplementary Fig. S1).

After 18 September, many times-series show inflation until 20 December 2021 (Fig. 3), although lack of data at some GNSS stations in November, due to loss of electric power, makes the continuous analysis difficult. We refer to 18 September to 20 December as the post-eruptive period. The sites on the westernmost part of the peninsula have different patterns though, showing almost null deformation (Supplementary Figs. S3 and S5). The stations on the east side of the peninsula show quite well an inflation pattern, more pronounced at the near-field stations (Fig. 3; Supplementary Figs. S2 and S4). Although the cGNSS data is limited, a general constant inflation rate is suggested (e.g., FEFC and ODDF stations, Supplementary Fig. S2; ELDC and STAN Supplementary Figs. S3-S4).

2.2 InSAR

InSAR interferograms were generated using the InSAR Scientific Computing Environment (ISCE) software version 2.2.0 (Rosen et al. 2012), using SAR images from the Sentinel-1 satellites of the European Space Agency (https://sentinel.esa.int). We use images between 20 March to 22 September 2020 from one ascending (satellite heading northwards) orbit, T16, and one descending (satellite heading southward) orbit, T155, for the CP and between 22 September and 17 December 2021 for the post-eruptive period. In total, 44 T16 images and 44 T155 images were used in the analysis. Interferograms were corrected for topography and geocoded using the IslandsDEM v1 digital elevation model (10×10 m^2 resolution) (LMI, 2021)._Line-of-Sight (LOS) displacement were derived from time series analysis of interferograms using an in-house implementation of the Small Baseline approach (SBAS, Berardino et al. 2002). Resulting displacements

grids have a pixel size of about 50×50 m^2. LOS displacements for both orbits were estimated for the CP, as well as for the T1-T3 periods and the post-eruptive phase.

LOS displacements in the CP (Fig. 4a-b) are dominated by LOS lengthening consistent with deflation, in broad agreement with the cGNSS observations. The strongest signal is within a zone within ~1-2 km of the lava field, ~50-60 mm in track T16 at the northern-western edge of the new lava field (Fig. 4a). The LOS displacements decrease with distance from the lava field but are still observable ~10 km away from the eruptive center. Track T155 also shows the largest displacements around the northern part of the lava field, but the signal is more widespread to the eastern areas of the peninsula (Fig. 4b). Similar spatial displacement pattern, for both tracks, is observed during the T2 geodetic phase (Fig. 4c-d), but on a smaller scale: the LOS maximum displacement around the northern part of the lava field is ~30-35 mm, and then decreases with distance. The LOS data for the T1 and T3 geodetic phases are significantly affected by noise (Supplementary Fig. S6), but in T1 a subsidence signal is discernible mostly around the northern edge of the Fagradalsfjall lava field, in a similar location as the six-month period and T2 geodetic phase LOS data.

Post-eruptive deformation between 22 September and 20 December 2021, shows ~20-25 mm LOS shortening surrounding the lava field, geographically like a 'mirror-image' of co-eruptive subsidence for the T16 track (Fig. 4e). The signal in track T155 (Fig. 4f) is not equally well defined, most likely affected by noise, though LOS shortening is seen mostly in the area located south-east of the lava field.

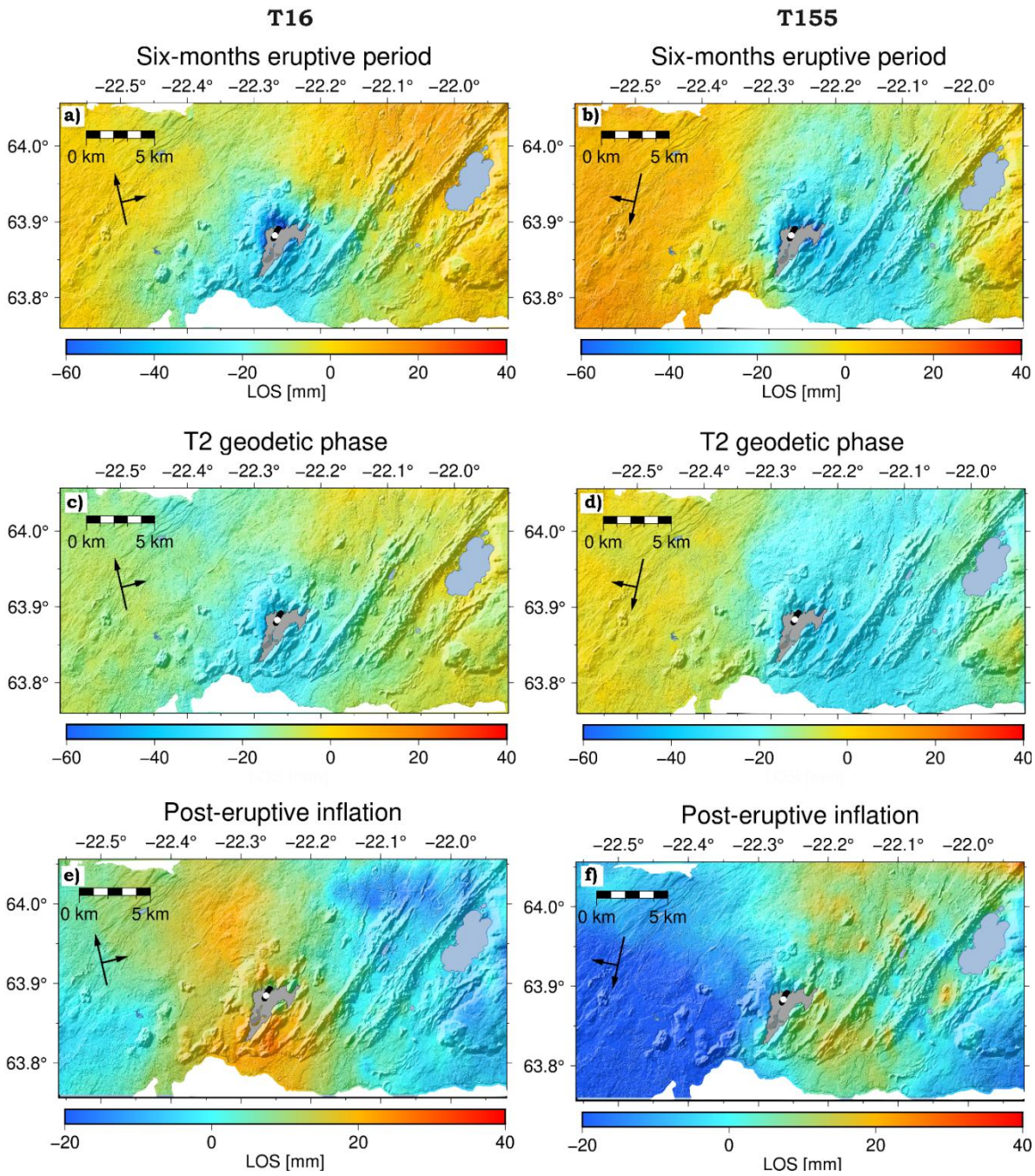

Figure 4. LOS displacements for two Sentinel-1 tracks, T16 (on the left) and T155 (on the right). The whole eruptive period deformation is presented in (a) and (b), the T2 geodetic phase in (c) and (d), and the post-eruptive deformation until 17 December in (e) and (f). Black arrows show the heading and look direction of the satellite. In light grey, the Fagradalsfjall lava field at the end of the eruption and in light blue the ocean. The black and white circles indicate the vent opened between March and April 2021. The white circle is the long-lived eruptive vent from 27 April to 18 September.

3 Modelling approaches

3.1 Geodetic source modelling

To determine the sources of the deflation (19 March – 18 September) and inflation (19 September – 20 December) periods, we model the observed deformation with solutions for magmatic sources embedded in an elastic, isotropic and homogeneous half-space. We estimate source depth, volume change, and location (longitude and latitude) for a point source of pressure change, approximating a spherical deformation source (Mogi, 1958). Additionally, we consider a rectangular dislocation source, also referred to as sill, with uniform opening (Okada, 1985) where eight parameters were inferred: longitude and latitude, length, width, depth, strike, dip and opening of the source. We use a modified version of the GBIS software (Geodetic Bayesian Inversion Software, Bagnardi and Hooper, 2018; Parks et al. 2024). The GBIS inversion algorithm samples the posterior probability density function (pdf) for each model parameter through a Markov chain Monte Carlo method, incorporating the Metropolis-Hastings algorithm. An initial set of model parameters is selected with random step within the range of manually defined *a priori* distribution bounds of the source parameters.

The LOS displacement fields were down-sampled such that observations in a "near-field area" (defined as a circular area with 10-km radius from a reference point ~2 km west to the lava field, with coordinate -22.34°E and 63.89°N) were sampled with one pixel every ~400 m in both the longitude and latitude. At distance larger than 10 km from the reference point, the sampling density was reduced to one pixel every ~800 m, to reduce effects of the far-field noise. The inverted data are cGNSS and LOS displacements for the CP, and for T1, T2 and T3 geodetic phases as described in Section 2. To quantify uncertainties in the GNSS data, the variance associated with each displacement component is included. Such values constitute the diagonal of the variance-covariance matrix, which has all remaining off-diagonal elements set to 0, assuming that no covariance exists between the three components of displacement. The InSAR errors are considered the same (isotropic and stationary) between both deforming and non-deforming areas. We calculate experimental semi-variograms by masking the deforming areas and using the remaining data points to estimate the spatial variability of the dataset. A weighting is applied to both the GNSS and LOS data used in the inversion. In this case

the weighting ratio of the GNSS with respect to LOS is a factor of 1:5. Thus, the LOS data weighed 5 times more compared to the GNSS.

In the CP and T2 periods, we use both Sentintel-1 InSAR tracks, while for the post-eruptive deformation modelling, we use only T16 track as the other dataset is affected by noise.

3.2 Lava loading modelling

Initial inversion modelling results for CP show a narrow zone of residual subsidence around the thicker part of the 2021 Fagradalsfjall lava field (see Results). This suggested that the load of the lava emplaced on the Earth's surface caused observable ground displacements, as several studies have documented (e.g., Briole et al. 1997; Ebmeier et al. 2012; Odbert et al. 2015). The 2021 Fagradalsfjall lava was emplaced inside a valley and was characterized by several episodic overflows into the nearby valleys, leading to uneven lava thickness. Over the northern part of the lava field, the thickness reaches up to 50–60 m, with a rapid increase to almost ~120 m near the main vent (Fig. 1b). In the southern deposit area, the lava is ~20–30 m thick (Pedersen et al. 2022). The observed ground deformation signal (Fig. 4; Supplementary Fig. S6) increases rapidly in amplitude on approaching the northern thicker part of the lava field. Thus, we carried out an evaluation of the lava loading effects to quantify the ground deformation due to the newly emplaced lava. We used the COMSOL Multiphysics v5.6 software (www.comsol.com), based on the FEM. Elastic deformation due to the lava load was evaluated for the observed lava thickness at the end of the eruption (Fig. 1b).

We use a three-dimensional (3D) Digital Elevation Model (DEM) of the lava field overlying a flat, homogeneous, elastic and isotropic half-space approximating the Earth's crust (Pedersen et al. 2022). The lava DEM (2×2 m resolution) was generated from measurements collected on 30 September 2021 with pre-eruptive topography subtracted. The FEM model is 20 km-wide (east-west or X-direction), 14 km-long (north-south or Y-direction) and 50 km-deep (Supplementary Fig. S7). The loading is simulated by applying a vertical volume force (a force per unit volume) equal to $-rg$, where r is the density of the erupted material, which has been estimated around 2600±50 kg/m^3 (Bjarnason, 2024), and g is the gravitational acceleration (set to 9.81 m^2/s). At the bottom of the lava field,

the force over area becomes *-rgz*. The lava DEM does not end at 0 thickness; thus, to ensure one connected model domain of the lava field and the half-space beneath, for implementation in COMSOL, we added a layer to the lava field and later removed the effect of such layer by subtracting deformation due to it (Supplementary S7). The loading is applied as a static condition and does not consider variation over time. However, elastic properties at volcanoes may be quite variable and uncertain due to the heterogeneity (Heap et al. 2020; Supplementary Text S1). We tested static Young's modulus (E) equal to 15 and 30 GPa, to span the range of most likely values in the volcanic context in Iceland (Supplementary Text S1).

4 Results

We first present the results of the lava loading modelling, followed by the geodetic modelling result for the uncorrected and corrected (for the lava loading signal) deformation data for CP and T2 phase. The T1 and T3 data have too low signal-noise ratio to yield meaningful inversion results. Finally, the post-eruptive inferred sources are presented.

4.1 Lava Loading LOS deformation

The lava loading models have widespread subsidence beneath and around the 2021 Fagradalsfjall lava field (Fig. 5). Maximum model subsidence reaches 15–16 cm for E =15 GPa and ~7–8 cm when E = 30 GPa (Fig. 5). The largest displacement is beneath the thickest deposit, in the northern part of the lava field and where the active vent was located from end of April 2021 (white circle in Fig. 5). The modelled signals decrease rapidly with distance from the lava field: the vertical displacement is less than 2 mm at more than 4-5 km distance from the lava edge for E = 15 GPa, and at ~2 km for E = 30 GPa. In the southern part of the lava field, where thickness deposits are below ~50 m, the modelled deformation shows around 4 cm and 2 cm of subsidence for E = 15 GPa and E = 30 GPa, respectively.

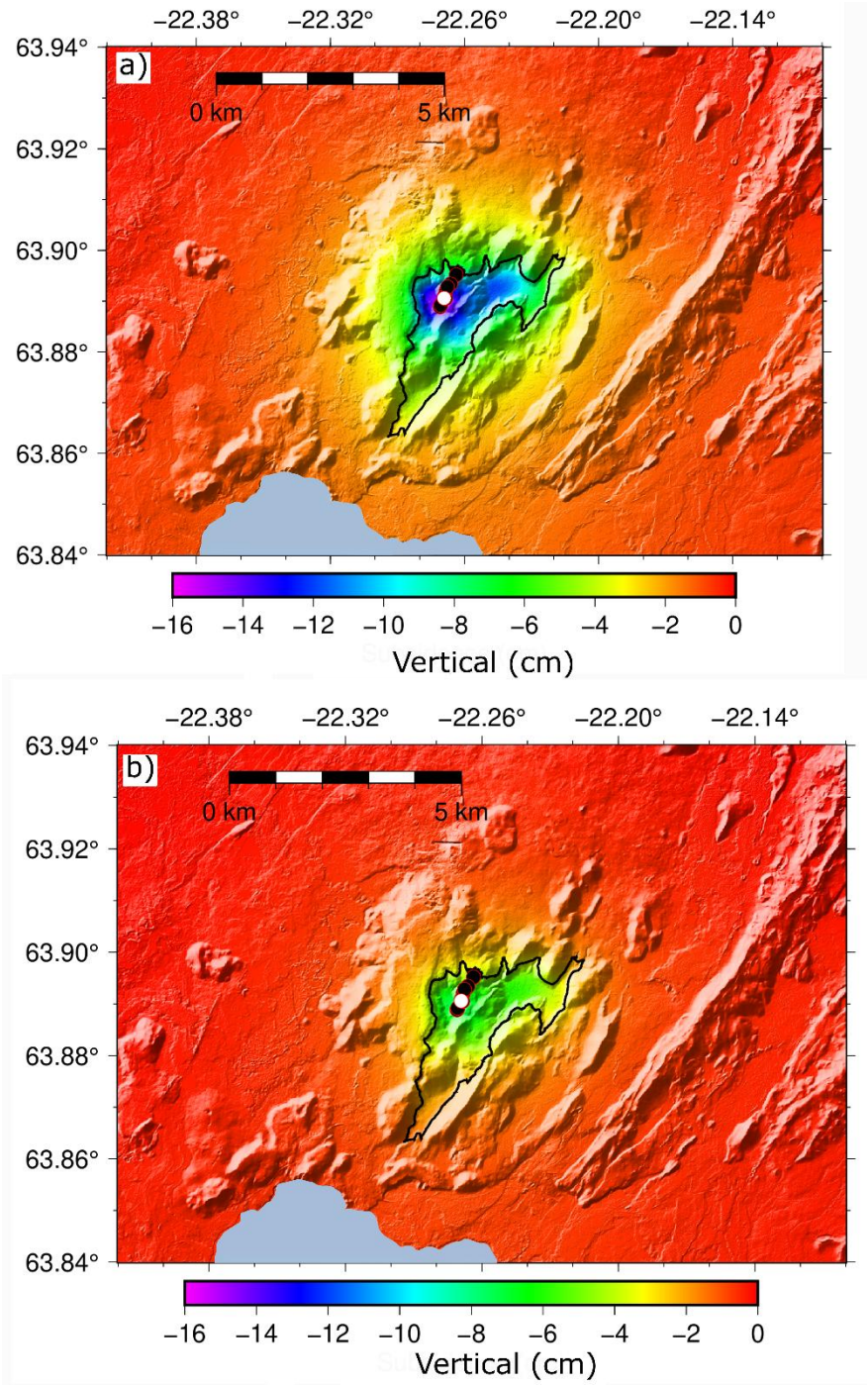

Figure 5. Vertical displacements according to the lava load COMSOL model in cm. a) Vertical displacement when the crust has a Young's modulus E = 15 GPa; b) Same as (a) for E = 30 GPa. Light blue area is the sea, while the black line indicates the Fagradalsfjall lava outline. The black and white circles indicate the eruptive vents which opened between March and April 2021. The white circle is the long-lived eruptive vent from 13 April to 18 September.

We convert the three components of displacement to LOS and remove the lava loading response with E equal to 15 GPa and 30 GPa to create two sets of lava loading corrections to use in the inversion approach. We focus only on the CP and do not consider lava loading deformation in T2. Given the geographical extension of the loading signal and location of the GNSS sites, we only apply the loading correction to the InSAR data.

4.2 Co-eruptive deformation source (19 March – 18 September)

We modeled the co-eruptive deformation with a joint inversion of GNSS and both the original LOS data (uncorrected data) and the lava-loading corrected LOS data, considering either a pressurized point-source (Mogi source) or a sill with uniform opening. The LOS data corrected with E = 15 GPa are referred to as Mogi-A and sill-A models and for E = 30 GPa as Mogi-B and sill-B models.

The inversion results for CP using the uncorrected LOS data show a Mogi source at 8.3–9.2 km depth (d), with a negative volume change (ΔV) of 16–19 Mm^3, located under the northern part of the Fagradalsfjall lava field (Fig. 6, Table 1, Supplementary Figs. S8–S9). Alternatively, the inversion result finds a sill source with bottom depth at 11.9–13.1 km, a deflating ΔV of 19–27 Mm^3, a strike of -(63 – 76) and dip of -(20 – 26), located 1–2 km north to the lava field (Fig. 6; Supplementary Figs. S8–S9, Table 1; pdf in Supplementary Figs. S10-S11). The goodness of fit evaluated with the Weighted Residual Sum of Square, WRSS, displays comparable value, ~0.30 for both source's geometries, with a narrow zone of residual mostly within ~1 km from the northern and eastern boundary of the lava field (Figs. 7; Supplementary Figs. S8-S9).

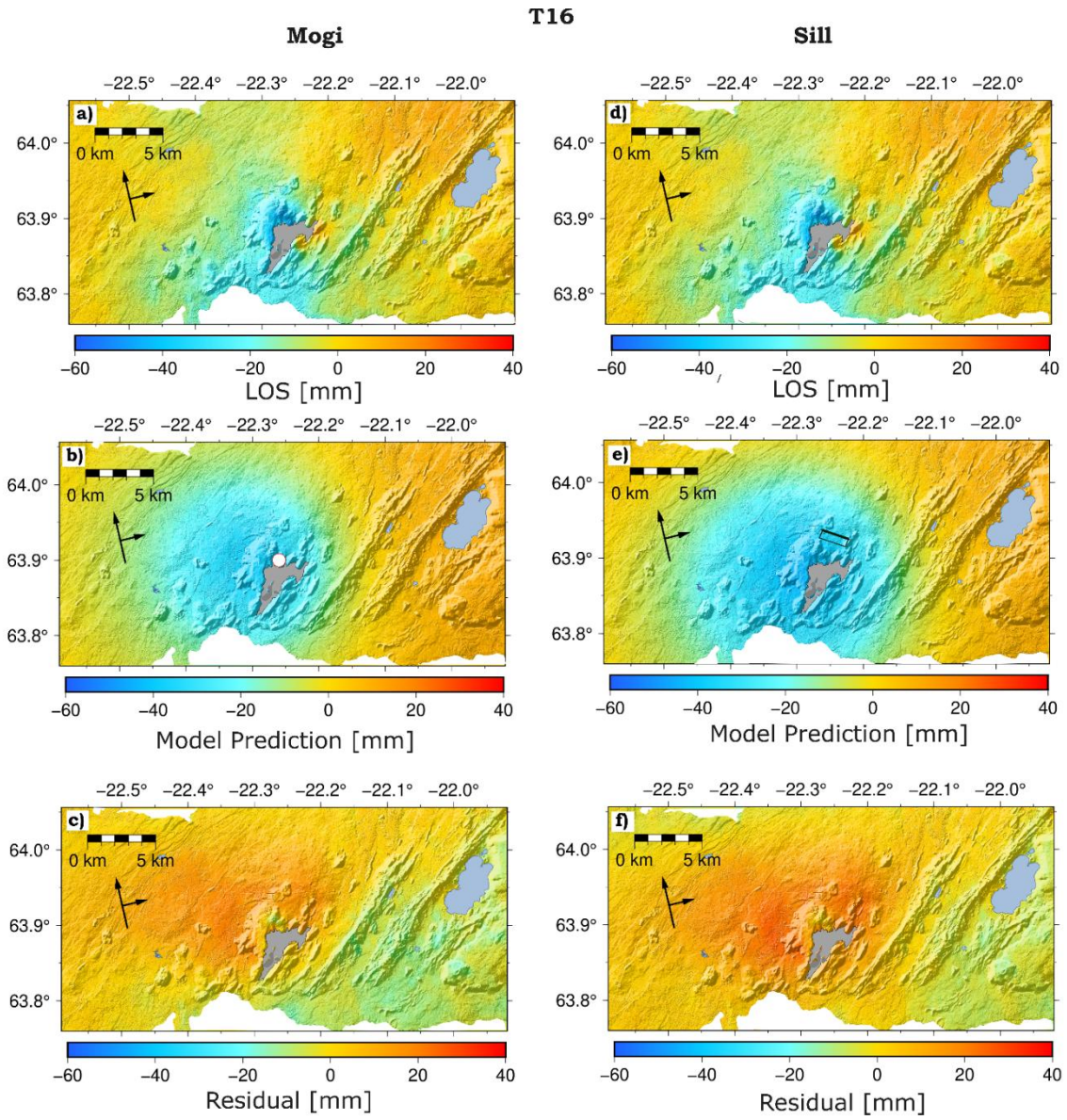

Figure 6. Modelling results for uncorrected six-months LOS change of the T16 InSAR track. (a) and (b) data, (c) and (d) model prediction, and (e) and (f) residuals for a Mogi and a sill source, respectively (left and right columns). The white circle in (b) indicates the best-fit Mogi source at 8.8 km depth (95% confidence interval: 8.3–9.2 km). Black outline in (b) shows the projection at surface of the modelled deflating sill, with the thicker line indicating the bottom of the sill best-fit solution at 12.6 km depth (95% confidence interval: 11.9–13.1 km). Black arrows show the heading and look direction of the satellite. In light grey, the Fagradalsfjall lava field at the end of the eruption and in light blue the lake Kleifarvatn to the east and in white the ocean.

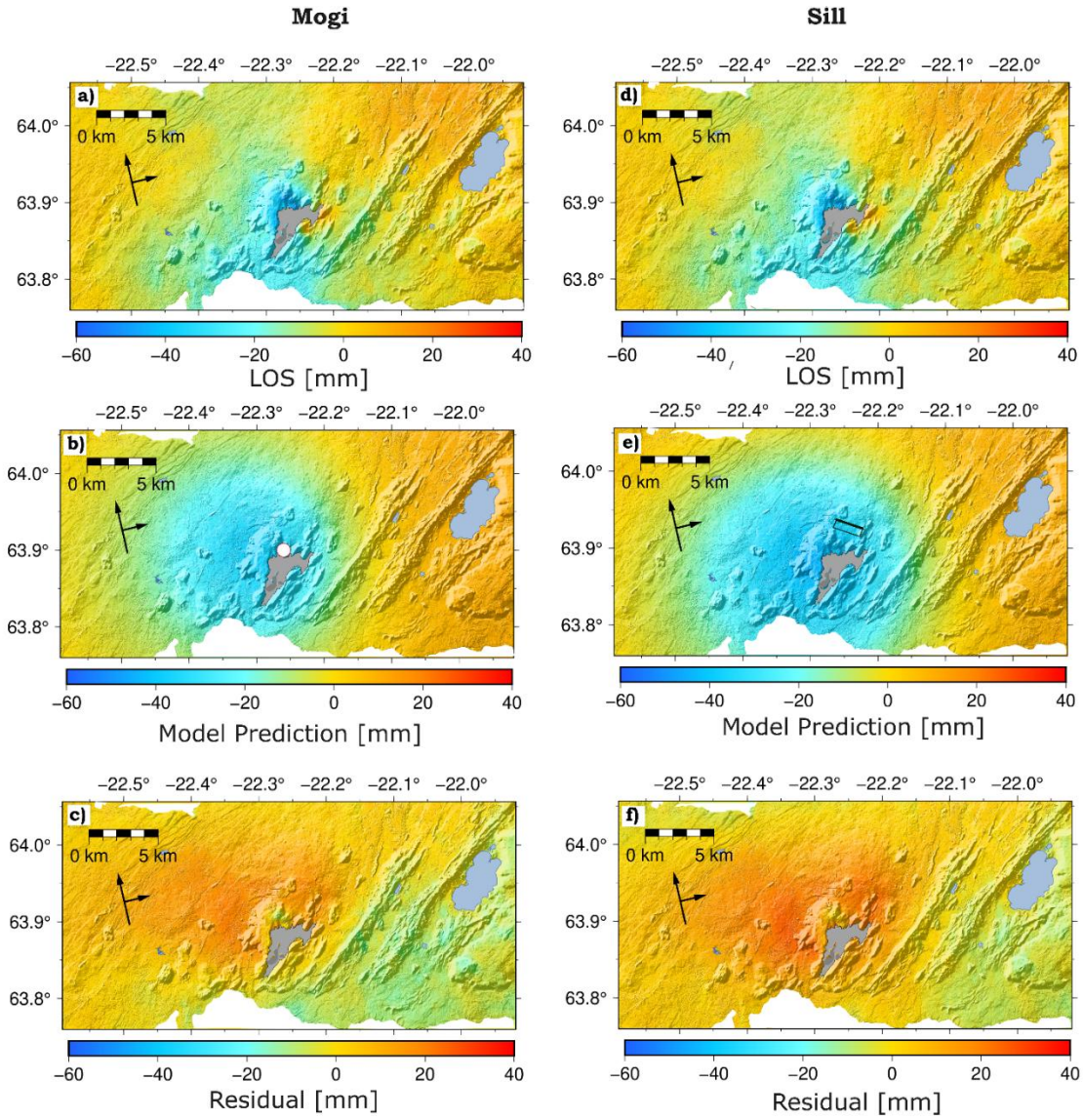

Figure 7. Modelling results for the loading corrected six-months LOS change of the T16 InSAR track for E = 30 GPa is used. (a) and (b) data, (c) and (d) model prediction, (e) and (f) residual for a Mogi and a sill geometry, respectively (left and right columns). The white circle in (b) indicates the best-fit solution of the Mogi source at 9 km (95% confidence interval: 8.6□9.5) km depth. Black outlines show the projection at surface of the modelled deflating sill top (thicker line) at a depth of 12.8 km (95% confidence interval 12.5–13.3 km). Black arrows show the heading and look direction of the satellite. In light grey, the Fagradalsfjall lava field at the end of the eruption and in light blue the lake Kleifarvatn to the east and in white the ocean.

TABLE 1. Results from GBIS inversion for the Mogi and sill cases based on the six-month uncorrected and corrected (E = 30 GPa) LOS data for the full eruptive period. Columns show model parameters, the latitude and longitude best-fit value of the source, and the 2.5 and 97.5 percentiles of posterior probability density functions for the geometry source parameters. The range for each parameter is the inferred 95% confidence interval.

	Six-month eruptive period			
	Mogi (uncorrected)	Sill (uncorrected)	Mogi-B (E=30 GPa)	sill-B (E=30 GPa)
Longitude	-22.265 – -22.256*	-22.247 – -22.235**	-22.265 –-22.255*	-22.247–-22.234***
Latitude	63.899 – 63.903*	63.901 – 63.893**	63.881 – 63.885*	63.901– 63.894***
Depth (km)	8.3 – 9.2	11.9 – 13.1	8.6 – 9.5	12.3 – 13.5
Deflating volume change (Mm^3)	(16 – 19)	(19 – 27)	(17 – 20)	(21 – 27)
Dip (°)		-(21 – 27)		(20 – 26)
Strike (°)		-(65 – 77)		-(63 – 76)
With (km)		0.5 – 1.5		0.5 – 1.4
Length (km)		1.7 – 5.2		2.1 – 5.5
Opening (m)		-(4 – 18)		-(5 – 18)
WRSS	0.31	0.30	0.34	0.30

*center of the source

**(best-fit solution of vertices of the top of the source)

***(best-fit solution of vertices of the bottom of the source)

The WRSS evaluation and residual plots favour the LOS corrected data using E = 30 GPa rather than E = 15 GPa, as the latter show a clear positive residual (Supplementary Figs. S12-S13). Thus, we focus our investigation on the Mogi-B and sill-B solutions (Fig. 7, Supplementary Fig. S14; Table 1; pdf in Supplementary Figs. S15-S18). The best-fit Mogi-B model locates a 8.5–9.5 km-deep source at the northern boundary of the lava field with a deflating ΔV of 18–20 Mm^3; while the sill-B is at d = 12.3–13.5 km (top) and deflating ΔV of 21–27 Mm^3, located around ~1 km north of the lava field, similar to the uncorrected data results. The horizontal and vertical GNSS model predictions fit overall the observed deflation pattern (Fig. 8). Local poorly fit is evident at several GNSS sites located in the western-southwestern parts of the peninsula, ~10 km away from the lava field. The overall fit favors the sill-B model over the Mogi-B model. The most striking difference between the uncorrected data and the sill-B solution is the improved fit around the lava field in the loading corrected data (Figs. 6-7).

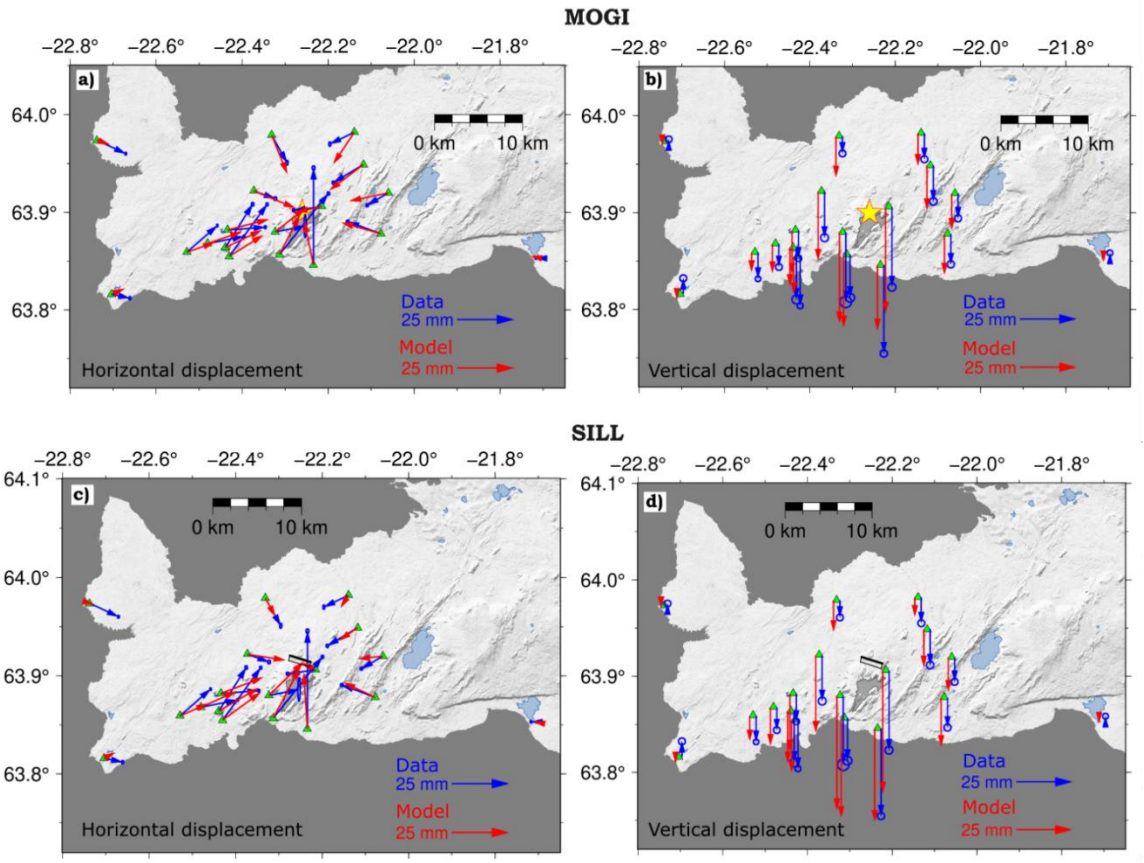

Figure 8. Modelling results for the six-months eruption period. Panels (a) and (b) show the horizontal and vertical observed GNSS and modelled displacements for Mogi B case, respectively. The yellow start indicates the best-fit Mogi location located at (8.5–9.5) km depth. Panels (c) and (d) show the horizontal and vertical data and modelled displacement for sill B case. Black outlines show the projection at surface of the modelled deflating sill at a depth of (12.5–13.3) km, with the thicker line indicating the top of the sill. In light grey, the Fagradalsfjall lava field at the end of the eruption and in light blue the lake Kleifarvatn to the east. Dark grey indicates the ocean.

4.3 Deformation source during the T2 phase (11 May – 31 July)

The modelling result for the T2 phase infers a Mogi source at 5.6–6.3 km depth (Fig. 9; Supplementary Figs. S19-S20; pdf in Supplementary Figs. S21-S22), shallower than the source depth estimation for CP. The deflating ΔV is 6–10 Mm^3. The sill source depth and volume estimate are more comparable with the favoured model (sill-B case) for the six-month eruptive period, with inferred depth of 11.1–12.4 km with deflating ΔV

of 11–17 Mm^3. Similarly to the CP, residual deformation signals are present in the north and west of the lava and the WRSS evaluation favours the sill, (WRSS=0.23), over the Mogi solution (WRSS=0.37); thus, we consider the sill as our preferred model.

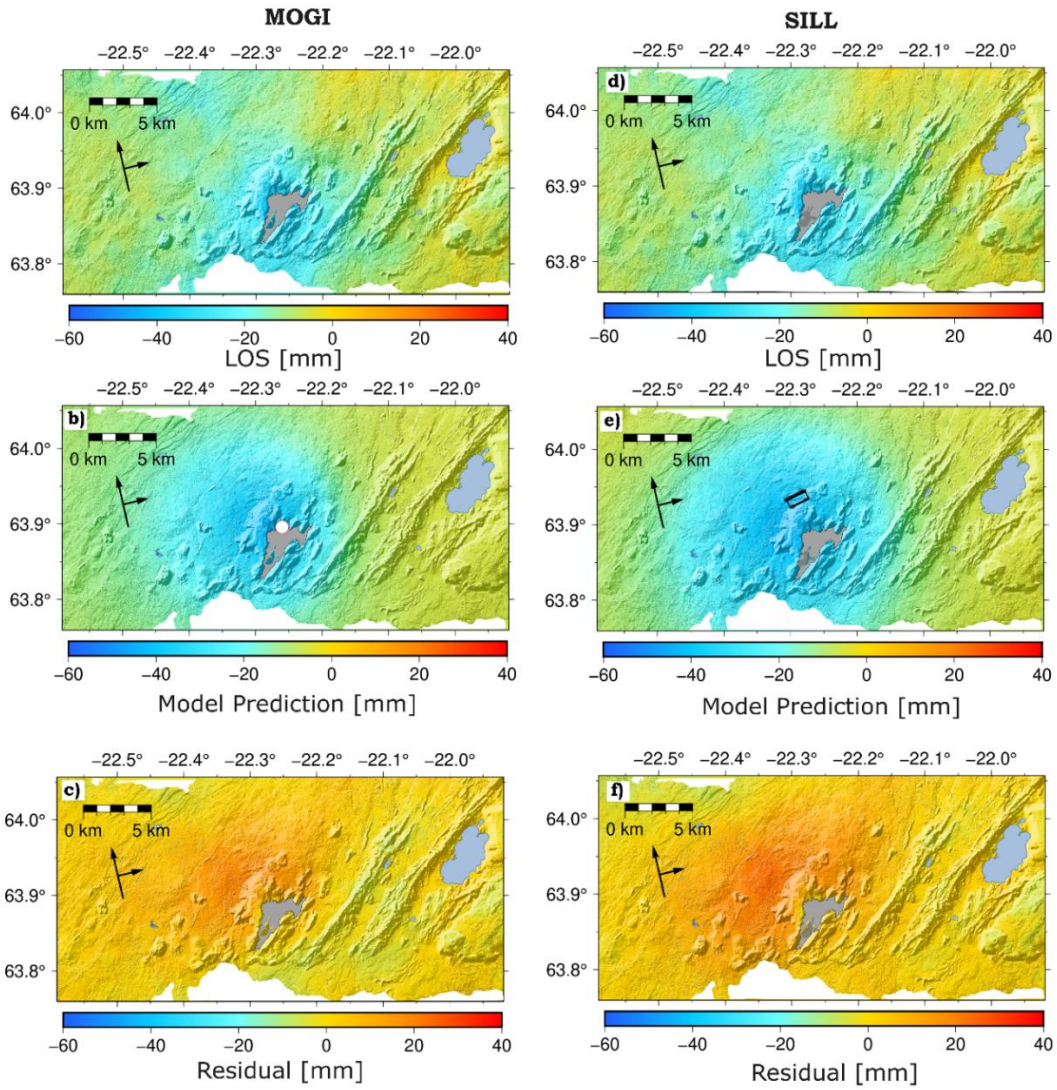

Figure 9. Modelling results for the T2 geodetic phase LOS change of the T16 InSAR. (a) and (b) data, (c) and (d) model prediction, (e) and (f) residual for a Mogi and a sill geometry, respectively (left and right columns). The white circle in (b) indicates the best-fit solution of the Mogi source at 6.0 km (95% confidence interval: 5.6–6.3 km) depth. Black outlines in (e) show the projection at surface of the modelled best-fit deflating sill at 11.7 km (95% confidence interval: 11.1–12.4 km), with the thicker line indicating the top of the sill. Black arrows show the heading and look direction of the satellite. In light grey, the Fagradalsfjall lava field at the end of the eruption and in light blue the lake Kleifarvatn to the east and in white the ocean. Model parameters of the Mogi and sill sources are presented in Supplementary Figs. S21 and S22, respectively.

4.4 Post-eruptive deformation (19 September - 20 December)

The inflation signal modelled with the T16 InSAR track and the GNSS data infers a 7.3–9.4 km-deep Mogi source beneath the surface with positive ΔV of 8–10 Mm^3; or alternatively, a sill at 11.5–13.7 km depth with an inflating ΔV of 8–25 Mm^3 (Fig. 10; pdf in Supplementary Figs. S24-S25). Both source depth locations are quite comparable to the co-eruptive deflating source estimation, but a few kilometers to the south of it (Fig. 10). The WRSS is 0.22 and 0.20 for the Mogi and sill solutions, respectively, favoring the latter. The horizontal GNSS model predictions (Supplementary Fig. S23) do not properly fit the GNSS data in both source geometries tested, especially in the sites located in the west part of the RP. The vertical GNSS model predictions provide a slightly better fit for the sites near the eruptive center and in the east part of the RP compared to the west part of the RP.

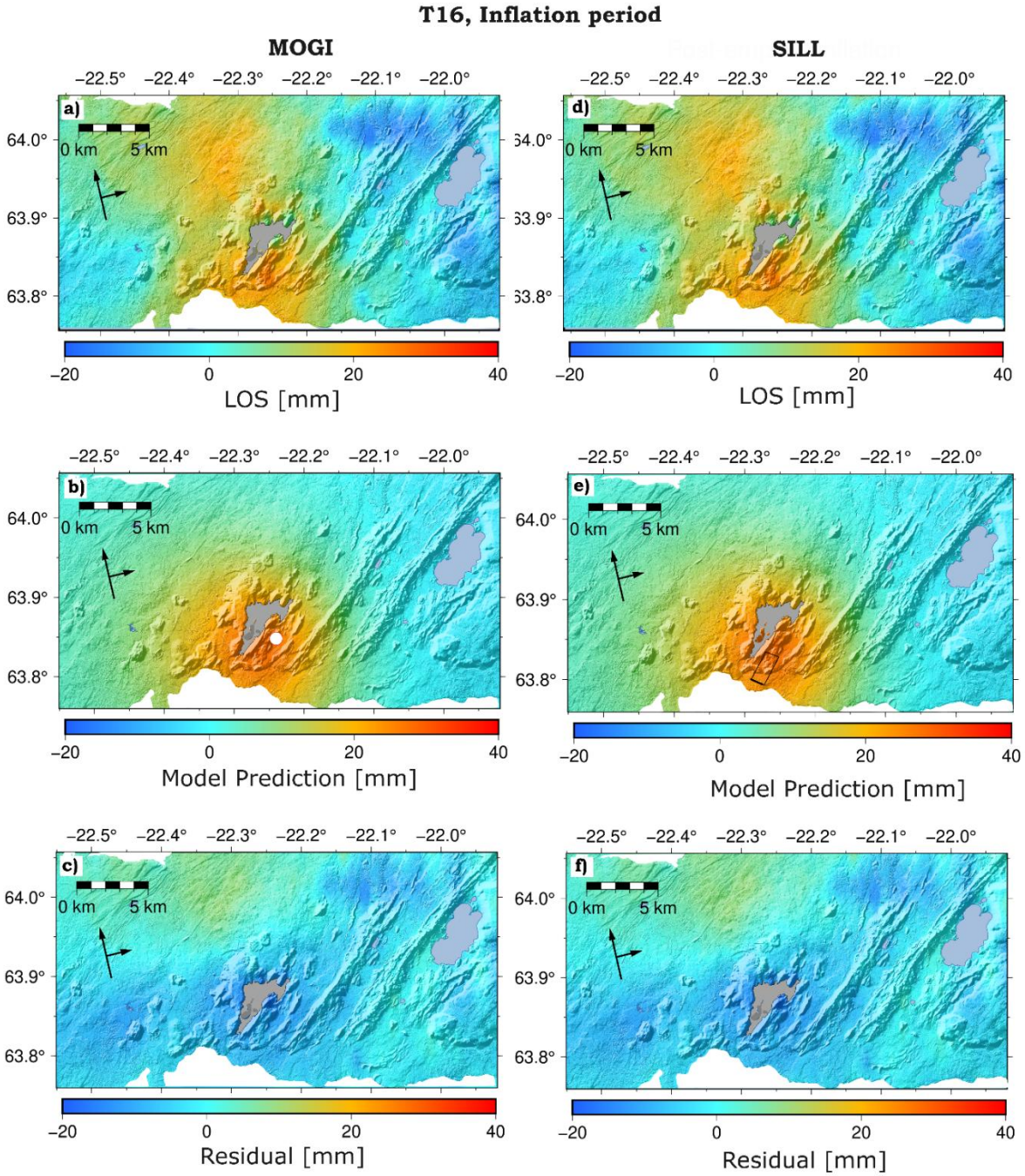

Figure 10. Modelling results for the post-eruptive inflation for the T16 track. a) data, b) model, c) residual for a Mogi solution, d) data, e) model, f) residual for a sill solution. The white circle in (b) points the best-fit location for the Mogi source at 8.00 km depth (95% confidence interval: 7.3-9.4 km). The black lines in (d) indicate the sill best-fit location at 12.3 km depth (95% confidence interval: 11.5–13.7 km). Light grey indicates the Fagradalsfjall lava field and in white the ocean. Model parameters of the Mogi and sill sources are presented in Supplementary Figs. S24 and S25, respectively.

5 Discussion

5.1 Eruption dynamics: Deep processes and surface observations

A fundamental research topic at volcanoes is the temporal and spatial evolution of a volcanic plumbing system. The cGNSS time series analysis allows us to study the temporal evolution in detail and to identify three distinct deformation stages during the 2021 Fagradalsfjall eruption. On the other hand, the spatial sampling of the deformation field was greatly improved by the Sentinel-1 data.

The maximum co-eruptive subsidence is ~35 mm (GNSS observations) and LOS lengthening ~50-60 mm at the edge of the northern part of the lava field (Fig. 4). The lava loading corrected data inversion results provide a better fit around the lava field compared to the uncorrected data, but modelling results for both datasets (uncorrected and corrected) favor a 12–14 km-deep sill and a deflating ΔV of 21–27 Mm^3 (Table 1). The bulk volume of the erupted material has been estimated ~150±3 Mm^3 (Pedersen et al. 2022), and an approximate Dense Rock Equivalent (DRE) of 110 Mm^3 has been estimated by Bindeman et al. (2024). The ratio between the DRE value and the best-fit ΔV inferred by our preferred model, sill-B, yields a value of ~4.5 and a ratio approximately of ~5.9 for the T2 phase. Pre-eruptive magma storage conditions on such historical basaltic lava are petrologically estimated at about 7–10 km depth for the Reykjanes and Svartsengi volcanic systems, and deeper crustal reservoirs, at ~14–21 km depth for Brennisteinsfjöll volcanic system (Caracciolo et al. 2023). Our depth estimate for the Fagradalsfjall sill model lies in between these values.

Is not uncommon that analytical geodetic modelled subsurface volume changes infer smaller values than the eruptive volume (e.g., Kilbride et al. 2016). This difference is often attributed to the influences of compressibility of magma stored at depth, after a partial draining of the magma body, as it expands and accommodates part of the volume change (Rivalta and Segall, 2008), or by oversimplification of the modelled homogeneous crustal volume (Foroozan et al. 2010). Yet, changing dynamics in the magmatic plumbing system, such as inflow into the magma storage feeding the eruption, may also play a key role in explaining such a difference. On 27 April, the activity concentrated at one vent and the extrusion rate almost doubled from an average value of 6.3±0.4 m^3/s to 11.4±0.5 m^3/s (Fig. 11) (Pedersen et al. 2022). This timing coincides with the transition from T1 to

T2 geodetic phase, and the beginning of pulsating behavior of the eruption. The duration of the pulsating activity alternated with repose times varied with time, with long fountain episodes (5-6 minutes) and short repose times (2-5 minutes) in early May and short episodes (2-3 minutes) and long repose time (3-12 minutes) in mid-June (Eibl et al. 2023). The greater effusion rate, the onset of pulsating events and ground deformation change likely followed deep recharge event feeding the eruption (Halldórsson et al. 2022; Marshall et al. 2024). Thus, we propose that the volume biases may be explained largely by inflow from a deeper source, with little accumulation time at mid-crustal depths, where ground deformation related to magma withdrawal from a deep reservoir is superimposed on the deformation of the shallower sources. The deformation signal from this deeper source is likely masked by the shallower source. Additionally, post-rifting stress relaxation due to the February-to-March 2021 dike intrusion may contribute to explaining the geodetic modelling residual. It has been investigated that ground deformation can persist several years in response to a dike intrusion (Cattin et al. 2005; Hamling et al. 2014; Hamlyn et al. 2018).

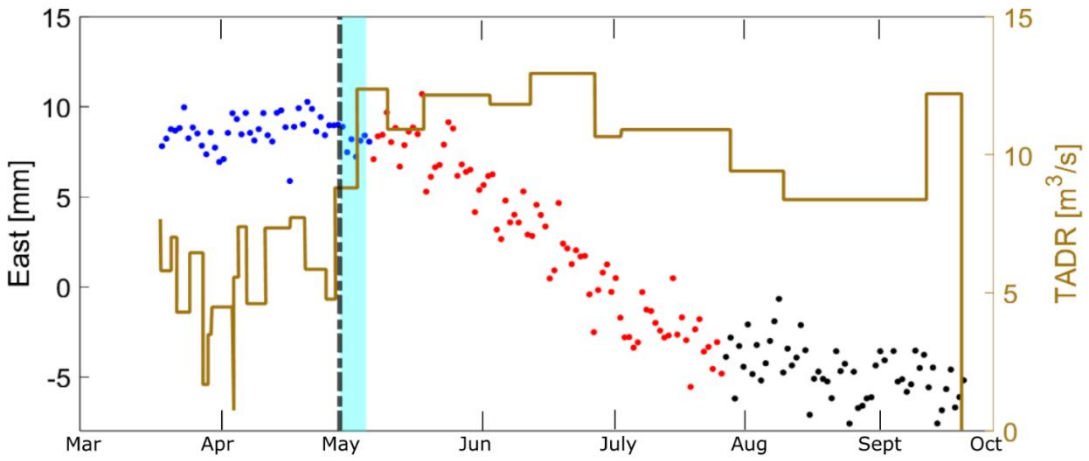

Figure 11. KRIV GNSS east displacement in relation to changes in the effusion rate and eruptive style. T1 geodetic phase, 19 March – 10 May 2021(blue dots), T2 geodetic phase, 11 May – 31 July 2021 (red dots), T3 geodetic phase, 1 August – 18 September 2021 (black dots). The brown line shows the evolution of the time average discharge rate, TADR, during the eruption (Pedersen et al. 2022). The vertical dashed black line indicates the beginning of lava fountain episodes according to seismic tremor observations on 2 May (Eibl et al. 2023), while the cyan shadow marks the acoustic energy increase period observed 2-8 May 2021 (Lamb et al. 2022).

An interesting feature of the seismicity are deep earthquakes at 10–12 km depth beneath Fagradalsfjall observed since June 2020 (Fig. 12), but not visible during the dike intrusion started on 24 February 2021, when the magma most likely broke through a rheological barrier and moved through the crust (Greenfield et al. 2022). Deep seismicity resumed in May 2021, located approximately ~0.5 km shallower and ~1 km southwest of the previous cluster (Greenfield et al. 2022). Interestingly, the timing of the resumed deep seismicity correlates quite well with the beginning of the T2 geodetic phase, the shift in radiogenic isotope composition of the erupted material, and TADR increase (Fig. 11). Furthermore, the T2 geodetic preferred sill model provides a slightly shallower depth estimation, 11.1–12.4 km, compared to CP, ~1 km west of the six-month source location (Figs. 7, 9, and 12). Collectively, these changes are most readily interpreted as evidence for two nearby mid-crustal sources under Fagradalsfjall. In El Hierro (Canary Islands), temporal evolution of deep seismicity coupled with deformation modelling constrained sill-like bodies at 14-16 km depth (Moho) between 2011-2012, most likely related to pulses of magma coming from mantle (Benito-Saz et al. 2017).

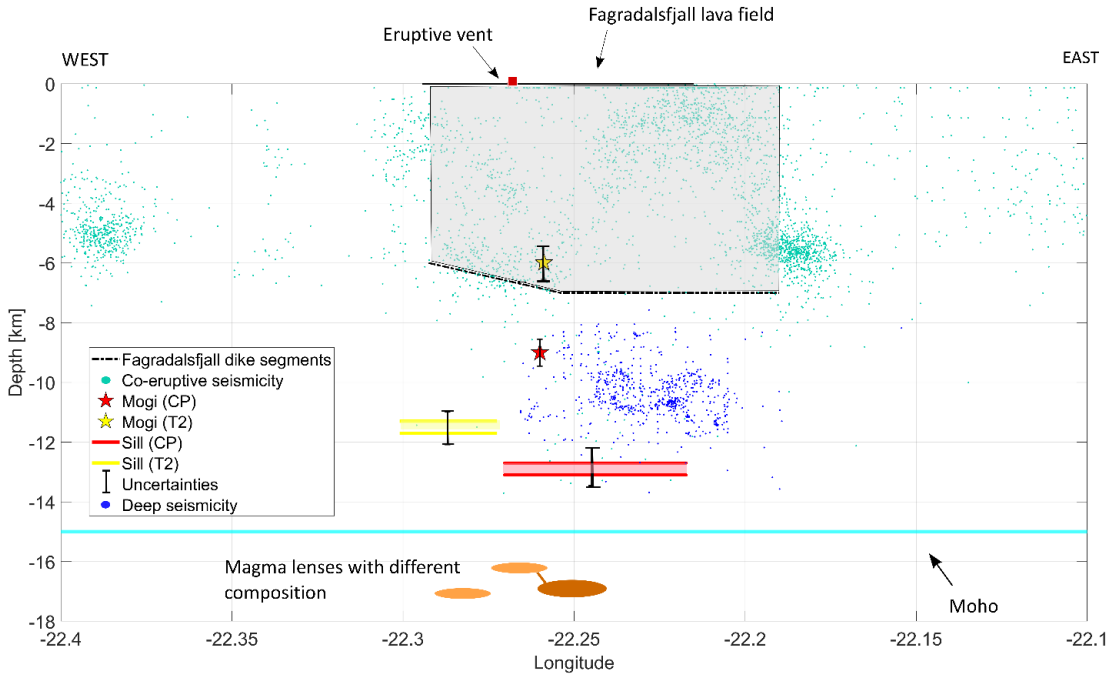

Figure 12. Schematic section showing the geodetic sources (see legend) inferred by this study for the CW and T2 periods with the seismicity (light green circles) from 19 March to 18 September 2021 beneath Fagradalsfjall. The earthquakes are from the seismic catalog by the Icelandic Meteorological Office available at https://skjalftalisa.vedur.is/. The deep seismicity by Greenfield et al. (2022) is in blue circles. The red square indicates the location of the eruptive vent at surface with the lateral horizontal extension of the 2021 Fagradalsfjall lava field shown as a black line (Pedersen et al. 2022). The grey background shadow indicates the area of the Fagradasfjall dike indicated with dashed black lines at 6 km depth (southern segment) and 7.5 km depth (northern segment) (Sigmundsson et al. 2022). The Moho (cyan line) at 15 km depth is based on Weir et al. (2001). The supply of magma from multiple petrologically and geochemically distinct separate sills is representative of the result of Marshall et al. (2024); their presentation do not account for lateral extension, which is highly uncertain. The thicker lines on the sill indicate the optimal top and optimal bottom of the sill inferred by the geodetic model. The uncertainties on the depth interval of the geodetic source are with respect to the center of the sill. Uncertainty values on the source geometry (length, width depth, etc...) can be found in Table 1 and Supplementary Figs. S21-22.

As the eruption progressed, around the end of July, the T2 high-deformation period evolved clearly into a low-deforming phase (T3) (Fig. 3 and Supplementary Figs. S1-S5). The fountain episodes that started in May transitioned from a minute-long episodic tremor to hour-long episodes, which dominate from 20 July (Eibl et al. 2024). Such a behavior was suggested to reflect the transition from an open vent system, where

the lava remains in the crater during repose time, to a semi-close vent system, where the crater is left empty and more time is required to initiate the new effusion event. Such a pattern relates to CO_2 cyclic degassing within a shallow (~100 m-deep) magma-filled cavity (Scott et al. 2023). We suggest that the lower discharge of magma at this stage of the eruption, evident from geodetic and TADR data, affects the net flow into the shallow cavity, as well as the lower flow rate may affect the relative portion of CO_2 transported with the magma.

We show that surface loading of the 2021 Fagradalsfjall lava contributes significantly to the co-eruptive subsidence signal within 1-2 km of the lava. Such an effect was observed e.g., at Montserrat volcano, where the deformation response (tens of cm in 14 years) is suggested to be largely elastic and controlled by the spatial and temporal distribution of erupted mass (Odbert et al. 2015). An inaccurate interpretation and conclusions of the geodetic modelling results may be reached if the deformation data are not properly corrected for loading effect (Odbert et al. 2015). In our case, the use of uncorrected and corrected lava load data as input in the modelling approach does not significantly differ in terms of the inferred parameters (Table 1) but uncorrected loading data provide poorer fit of near-field displacements.

5.2 Post-eruptive inflation (19 September - 20 December)

Post-eruptive inflation is commonly observed at volcanoes, e.g., Okmok Volcano, Alaska (Qu et al. 2015), Cordón Caulle, Southern Andes, Chile (Delgado et al. 2016), at several Icelandic volcanoes (Sturkell et al. 2006) and usually related to magma recharge, or if there is a viscoelastic aureole around a liquid magma than this can happen without a recharge, if the magma is sufficiently incompressible as the magmatic system equilibrates (Segall, 2016). Combination of both processes may also occur (Li et al. 2022). Additionally, cooling, crystallization and gas exsolution of a volatile-saturated source can produce inflation (Caricchi et al. 2014). The geodetic modelling results indicate that the best-fit source responsible for post-eruptive inflation is located at similar depth as the co-eruptive source, but ~2 km to the south of it (Supplementary Figure S25). Neither our time series analysis nor results of analytical modeling can distinguish between

the different re-inflation processes. More insight into the evolution of the plumbing system may come from incorporating cooling history of the previously injected magma and petrological information relating to the temperature and the crystallization and/or exsolution of residual melt in a similar manner as done by Caricchi et al. (2014).

Following the 2021 eruption and post-eruptive inflation, several deformation events have taken place at Fagradalsjall: a diking event 21–27 December 2021; 30 July–3 August 2022 (dike) and eruption 3–21 August (Parks et al. 2023); and end-June to August 2023 (dike and eruption). Inflation occurred in April-to-May 2022 at Svartsengi in a similar location as previous intrusions in 2020. There, from 27 October 2023 to January 2025, almost continuous inflation was observed, interrupted by deflation centered at Svartsengi and concurrent to a total of eight diking events and seven eruptions. The first and largest (~15 km-long) dike occurred on 10 November 2023, involving a geodetically inferred volume of 130-139 Mm^3 and deflating volume of the Svartsengi reservoir of 76-82 Mm^3 (Sigmundsson et al. 2024; Parks et al. 2025). Differently from the Fagradalsjall eruptions, the magma at Svartsengi accumulates at mid-crustal level prior to diking and eruption (Matthews et al. 2024; Parks et al. 2025).

6 Conclusions

We analyzed the co- and post-eruptive GNSS and LOS ground displacements of the 2021 Fagradalsfjall eruption. The analysis identifies three co-eruptive deformation phases which couple closely in time with changes in the eruptive flux, the eruption style (from continuous effusion of lava to episodic events), gradual enriched near-Moho magma of the material erupted, and temporal changes in deep seismicity as the eruption progressed. Emplaced lava on the surface contributed to the largest ground deformation observed north of the Fagradalsfjall lava field, as reproduced by a lava loading FEM model, with constraint of the elastic moduli of the surrounding crust. The modeling of the lava loading corrected co-eruptive geodetic data favors a sill at 12–14 km depth and volume change of 21–27 Mm^3. Involvement of the same lower-crust source is suggested for the post-eruptive period. This study shows the importance of combining results from

different field observations but also discriminating against different processes contributing to the observed ground deformation to investigate the evolution of magmatic systems.

Acknowledgements

This study received funding from the MaDRe Project (RANNIS grant number 228933-051) and support from the University of Iceland Research Fund. We would like to thank the work of the Natural Hazards Specialists on duty in the IMO monitoring room. Support from the Icelandic Volcanoes Supersite project (http://geo-gsnl.org/supersites/permanent-supersites/iceland-volcanoes-supersite/) through the Committee on Earth and Observing Satellites (CEOS) is acknowledged. We thank Magnús Tumi Guðmundsson and Benedikt G. Ófeigsson for their discussion on the gravity surveys around the Fagradalsfjall area and on the GNSS network, respectively; Tom Winder for his help in retrieval of the deep seismicity data and Sonja Greiner for helpful discussions throughout various stages of this work. We thank the European Space Agency for their open access for Sentinel data available on the Copernicus Data Space Ecosystem. The maps and plots are produced with Matlab (2023) and GMT software (Wessel et al., 2013).

References

Altamimi Z, Métivier L, Rebischung P, et al (2017) ITRF2014 plate motion model. Geophysical Journal International 209:1906–1912. https://doi.org/10.1093/gji/ggx136

Árnadóttir T, Geirsson H, Einarsson P (2004) Coseismic stress changes and crustal deformation on the Reykjanes Peninsula due to triggered earthquakes on 17 June 2000. J Geophys Res 109:2004JB003130. https://doi.org/10.1029/2004JB003130

Árnadóttir T, Jónsson S, Pollitz FF, et al (2005) Postseismic deformation following the June 2000 earthquake sequence in the south Iceland seismic zone. J Geophys Res 110:2005JB003701. https://doi.org/10.1029/2005JB003701

Árnadóttir T, Lund B, Jiang W, et al (2009) Glacial rebound and plate spreading: results from the first countrywide GPS observations in Iceland. Geophysical Journal International 177:691–716. https://doi.org/10.1111/j.1365-246X.2008.04059.x

Bagnardi M, Hooper A (2018) Inversion of Surface Deformation Data for Rapid Estimates of Source Parameters and Uncertainties: A Bayesian Approach. Geochem Geophys Geosyst 19:2194–2211. https://doi.org/10.1029/2018GC007585

Bali E, Caracciolo A, Gudfinnsson G, Marshall E, Bar Rasmussen M, Matthews S, Ranta E, Mibei G, Halldorsson S (2021) Melt Transport Directly from the Mantle During the Fagradalsfjall Eruption, Iceland. AGU Fall Meeting Abstracts, December 2021

Barsotti S, Parks MM, Pfeffer MA, et al (2023) The eruption in Fagradalsfjall (2021, Iceland): how the operational monitoring and the volcanic hazard assessment contributed to its safe access. Nat Hazards 116:3063–3092. https://doi.org/10.1007/s11069-022-05798-7

Benito-Saz MA, Parks MM, Sigmundsson F, et al (2017) Repeated magmatic intrusions at El Hierro Island following the 2011–2012 submarine eruption. Journal of Volcanology and Geothermal Research 344:79–91. https://doi.org/10.1016/j.jvolgeores.2017.01.020

Berardino P, Fornaro G, Lanari R, Sansosti E (2002) A new algorithm for surface deformation monitoring based on small baseline differential SAR interferograms. IEEE Trans Geosci Remote Sensing 40:2375–2383. https://doi.org/10.1109/TGRS.2002.803792

Bindeman IN, Deegan FM, Troll VR, et al (2022) Diverse mantle components with invariant oxygen isotopes in the 2021 Fagradalsfjall eruption, Iceland. Nat Commun 13:3737. https://doi.org/10.1038/s41467-022-31348-7

Bjarnason AD (2024) Bulk density of the 2021 lava in Natthagi, Reykjanes Peninsula, estimated with gravimetry. BS degree in Geophysics, University of Iceland, May 2024.

Björnsson S, Einarsson P, Tulinius H, Hjartardóttir ÁR (2020) Seismicity of the Reykjanes Peninsula 1971–1976. Journal of Volcanology and Geothermal Research 391:106369. https://doi.org/10.1016/j.jvolgeores.2018.04.026

Briole P, Massonnet D, Delacourt C (1997) Post-eruptive deformation associated with the 1986–87 and 1989 lava flows of Etna detected by radar interferometry. Geophysical Research Letters 24:37–40. https://doi.org/10.1029/96GL03705

Caracciolo A, Bali E, Halldórsson SA, et al (2023) Magma plumbing architectures and timescales of magmatic processes during historical magmatism on the Reykjanes Peninsula, Iceland. Earth and Planetary Science Letters 621:118378. https://doi.org/10.1016/j.epsl.2023.118378

Caricchi L, Biggs J, Annen C, Ebmeier S (2014) The influence of cooling, crystallisation and re-melting on the interpretation of geodetic signals in volcanic systems. Earth and Planetary Science Letters 388:166–174. https://doi.org/10.1016/j.epsl.2013.12.002

Cattin R, Doubre C, De Chabalier J-B, et al (2005) Numerical modelling of quaternary deformation and post-rifting displacement in the Asal–Ghoubbet rift (Djibouti, Africa). Earth and Planetary Science Letters 239:352–367. https://doi.org/10.1016/j.epsl.2005.07.028

Clifton AE, Kattenhorn SA (2006) Structural architecture of a highly oblique divergent plate boundary segment. Tectonophysics 419:27–40. https://doi.org/10.1016/j.tecto.2006.03.016

Cubuk-Sabuncu Y, Jónsdóttir K, Caudron C, et al (2021) Temporal Seismic Velocity Changes During the 2020 Rapid Inflation at Mt. Þorbjörn-Svartsengi, Iceland, Using Seismic Ambient Noise. Geophysical Research Letters 48:e2020GL092265. https://doi.org/10.1029/2020GL092265

Delgado F, Pritchard ME, Basualto D, et al (2016) Rapid reinflation following the 2011–2012 rhyodacite eruption at Cordón Caulle volcano (Southern Andes) imaged by InSAR: Evidence for magma reservoir refill. Geophysical Research Letters 43:9552–9562. https://doi.org/10.1002/2016GL070066

DeMets C, Gordon RG, Argus DF (2010) Geologically current plate motions. Geophysical Journal International 181:1–80. https://doi.org/10.1111/j.1365-246X.2009.04491.x

Di Traglia F, Nolesini T, Intrieri E, et al (2014) Review of ten years of volcano deformations recorded by the ground-based InSAR monitoring system at Stromboli volcano: a tool to mitigate volcano flank dynamics and intense volcanic activity. Earth-Science Reviews 139:317–335. https://doi.org/10.1016/j.earscirev.2014.09.011

Drouin V, Sigmundsson F (2019) Countrywide Observations of Plate Spreading and Glacial Isostatic Adjustment in Iceland Inferred by Sentinel-1 Radar Interferometry, 2015–2018. Geophysical Research Letters 46:8046–8055. https://doi.org/10.1029/2019GL082629

Drouin V, Parks M, Tolpekin V, Sigmundsson F, Leeb D, Strong S (2021). Conduits feeding new eruptive vents mapped by high-resolution ICEYE SAR satellite in a daily repeat orbit. In *AGU Fall Meeting Abstracts* (Vol. 2021, pp. G43A-01).

Ducrocq C, Geirsson H, Árnadóttir T, et al (2021) Inflation-Deflation Episodes in the Hengill and Hrómundartindur Volcanic Complexes, SW Iceland. Front Earth Sci 9:725109. https://doi.org/10.3389/feart.2021.725109

Ducrocq C, Árnadóttir T, Einarsson P, et al (2024) Widespread fracture movements during a volcano-tectonic unrest: the Reykjanes Peninsula, Iceland, from 2019–2021

TerraSAR-X interferometry. Bull Volcanol 86:14. https://doi.org/10.1007/s00445-023-01699-0

Dzurisin D (2006) Volcano Deformation. Springer Berlin Heidelberg, Berlin, Heidelberg

Ebmeier SK, Biggs J, Mather TA, et al (2012) Measuring large topographic change with InSAR: Lava thicknesses, extrusion rate and subsidence rate at Santiaguito volcano, Guatemala. Earth and Planetary Science Letters 335–336:216–225. https://doi.org/10.1016/j.epsl.2012.04.027

Eibl EPS, Moreland WM, Thordarson T, et al (2024) Overview of the shallow magma reservoir, conduit properties and effusion style throughout the 2021 eruption near Fagradalsfjall, Iceland. https://meetingorganizer.copernicus.org/EGU24/EGU24-11019.html. Accessed 3 Oct 2024

Eibl EPS, Thordarson T, Höskuldsson Á, et al (2023) Evolving shallow conduit revealed by tremor and vent activity observations during episodic lava fountaining of the 2021 Geldingadalir eruption, Iceland. Bull Volcanol 85:10. https://doi.org/10.1007/s00445-022-01622-z

Einarsson P (1991) Earthquakes and present-day tectonism in Iceland. Tectonophysics 189:261–279. https://doi.org/10.1016/0040-1951(91)90501-I

Einarsson P (2008) Plate boundaries, rifts and transforms in Iceland. Jök 58:35–58. https://doi.org/10.33799/jokull2008.58.035

Eysteinsson H. (2000). Elevation and gravity changes at geothermal fields on the Reykjanes Peninsula, SW Iceland. In Proceedings World Geothermal Congress (pp. 559-564).

Flóvenz ÓG, Wang R, Hersir GP, et al (2022) Cyclical geothermal unrest as a precursor to Iceland's 2021 Fagradalsfjall eruption. Nat Geosci 15:397–404. https://doi.org/10.1038/s41561-022-00930-5

Foroozan R, Elsworth D, Voight B, Mattioli GS (2010) Dual reservoir structure at Soufrière Hills Volcano inferred from continuous GPS observations and heterogeneous elastic modeling. Geophysical Research Letters 37:2010GL042511. https://doi.org/10.1029/2010GL042511

Geirsson H, Parks M, Vogfjörd K, et al (2021) The 2020 volcano-tectonic unrest at Reykjanes Peninsula, Iceland: stress triggering and reactivation of several volcanic systems. https://meetingorganizer.copernicus.org/EGU21/EGU21-7534.html

Greenfield T, Winder T, Rawlinson N, et al (2022) Deep long period seismicity preceding and during the 2021 Fagradalsfjall eruption, Iceland. Bull Volcanol 84:101. https://doi.org/10.1007/s00445-022-01603-2

Gudjónsdóttir SR, Ilyinskaya E, Hreinsdóttir S, et al (2020) Gas emissions and crustal deformation from the Krýsuvík high temperature geothermal system, Iceland. Journal of Volcanology and Geothermal Research 391:106350. https://doi.org/10.1016/j.jvolgeores.2018.04.007

Gudmundsson MT, Larsen G, Höskuldsson Á, Gylfason ÁG (2008) Volcanic hazards in Iceland. Jök 58:251–268. https://doi.org/10.33799/jokull2008.58.251

Halldórsson SA, Marshall EW, Caracciolo A, et al (2022) Rapid shifting of a deep magmatic source at Fagradalsfjall volcano, Iceland. Nature 609:529–534. https://doi.org/10.1038/s41586-022-04981-x

Hamling IJ (2021) InSAR observations over the Taupō Volcanic Zone's cone volcanoes: insights and challenges from the New Zealand volcano supersite. New Zealand Journal of Geology and Geophysics 64:347–357. https://doi.org/10.1080/00288306.2020.1721545

Hamlyn J, Wright T, Walters R, et al (2018) What causes subsidence following the 2011 eruption at Nabro (Eritrea)? Prog Earth Planet Sci 5:31. https://doi.org/10.1186/s40645-018-0186-5

Heap MJ, Villeneuve M, Albino F, et al (2020) Towards more realistic values of elastic moduli for volcano modelling. Journal of Volcanology and Geothermal Research 390:106684. https://doi.org/10.1016/j.jvolgeores.2019.106684

Herring TA(2003) MATLAB Tools for viewing GPS velocities and time series. GPS Solutions 7:194–199. https://doi.org/10.1007/s10291-003-0068-0

Herring TA, King RW, Floyd MA, McClusky SC (2018) GAMIT (GPS at MIT). In: Reference Manual Version 10.7. Department of Earth, Atmospheric, and Planetary Sciences Massachusetts Institute of Technology, Cambridge, MA, USA,

Hjartardóttir ÁR, Dürig T, Parks M, et al (2023) Pre-existing fractures and eruptive vent openings during the 2021 Fagradalsfjall eruption, Iceland. Bull Volcanol 85:56. https://doi.org/10.1007/s00445-023-01670-z

Hreinsdóttir S, Einarsson P, Sigmundsson F (2001) Crustal deformation at the oblique spreading Reykjanes Peninsula, SW Iceland: GPS measurements from 1993 to 1998. J Geophys Res 106:13803–13816. https://doi.org/10.1029/2001JB000428

Hreinsdóttir S, Árnadóttir T, Decriem J, et al (2009) A complex earthquake sequence captured by the continuous GPS network in SW Iceland. Geophysical Research Letters 36:2009GL038391. https://doi.org/10.1029/2009GL038391

Hrubcová P, Vavryčuk V (2023) Tectonic stress changes related to plate spreading prior to the 2021 Fagradalsfjall eruption in SW Iceland. Tectonophysics 851:229761. https://doi.org/10.1016/j.tecto.2023.229761

Juncu D, Árnadóttir Th, Geirsson H, et al (2020) Injection-induced surface deformation and seismicity at the Hellisheidi geothermal field, Iceland. Journal of Volcanology and Geothermal Research 391:106337. https://doi.org/10.1016/j.jvolgeores.2018.03.019

Juncu D, Árnadóttir Th, Hooper A, Gunnarsson G (2017) Anthropogenic and natural ground deformation in the Hengill geothermal area, Iceland. JGR Solid Earth 122:692–709. https://doi.org/10.1002/2016JB013626

Kahl M, Mutch EJF, Maclennan J, et al (2023) Deep magma mobilization years before the 2021 CE Fagradalsfjall eruption, Iceland. Geology 51:184–188. https://doi.org/10.1130/G50340.1

Keiding M, Árnadóttir T, Sturkell E, et al (2008) Strain accumulation along an oblique plate boundary: the Reykjanes Peninsula, southwest Iceland. Geophysical Journal International 172:861–872. https://doi.org/10.1111/j.1365-246X.2007.03655.x

Keiding M, Lund B, Árnadóttir T (2009) Earthquakes, stress, and strain along an obliquely divergent plate boundary: Reykjanes Peninsula, southwest Iceland. J Geophys Res 114:2008JB006253. https://doi.org/10.1029/2008JB006253

Kilbride BM, Edmonds M, Biggs J (2016) Observing eruptions of gas-rich compressible magmas from space. Nat Commun 7:13744. https://doi.org/10.1038/ncomms13744

Klein FW, Einarsson P, Wyss M (1977) The Reykjanes Peninsula, Iceland, earthquake swarm of September 1972 and its tectonic significance. J Geophys Res 82:865–888. https://doi.org/10.1029/JB082i005p00865

Lamb OD, Gestrich JE, Barnie TD, et al (2022) Acoustic observations of lava fountain activity during the 2021 Fagradalsfjall eruption, Iceland. Bull Volcanol 84:96. https://doi.org/10.1007/s00445-022-01602-3

Lanari R, Lundgren P, Sansosti E (1998) Dynamic deformation of Etna Volcano observed by satellite radar interferometry. Geophysical Research Letters 25:1541–1544. https://doi.org/10.1029/98GL00642

Li S, Sigmundsson F, Drouin V, et al (2021) Ground Deformation After a Caldera Collapse: Contributions of Magma Inflow and Viscoelastic Response to the 2015–2018 Deformation Field Around Bárðarbunga, Iceland. JGR Solid Earth 126:e2020JB020157. https://doi.org/10.1029/2020JB020157

Liu Z, Dai L, Li S, et al (2021) When plateau meets subduction zone: A review of numerical models. Earth-Science Reviews 215:103556. https://doi.org/10.1016/j.earscirev.2021.103556

LMI, (2021). Landmælingar Íslands. Available at: LMI (2021). Landmælingar Íslands. Available at: https://www.lmi.is/is/um-lmi/frettayfirlit/ny-uppfaersla-a-haedarlikani-af-islandi.

Lu Z, Dzurisin D, Wicks C, et al (2007) Diverse deformation patterns of Aleutian Volcanoes from satellite Interferometric Synthetic Aperture Radar (InSAR). In: Eichelberger J, Gordeev E, Izbekov P, et al. (eds) Geophysical Monograph Series. American Geophysical Union, Washington, D. C., pp 249–261.

Lucas LC, Albright JA, Gregg PM, Zhan Y (2022) The Impact of Ice Caps on the Mechanical Stability of Magmatic Systems: Implications for Forecasting on Human Timescales. Front Earth Sci 10:868569. https://doi.org/10.3389/feart.2022.868569

Lyard F, Lefevre F, Letellier T, Francis O (2006) Modelling the global ocean tides: modern insights from FES2004. Ocean Dynamics 56:394–415. https://doi.org/10.1007/s10236-006-0086-x

Makabayi B, Musinguzi M, Otukei JR (2021) Estimation of Ground Deformation in Landslide Prone Areas Using GPS: A Case Study of Bududa, Uganda. IJG 12:213–232. https://doi.org/10.4236/ijg.2021.123013

Mann D, Freymueller J, Lu Z (2002) Deformation associated with the 1997 eruption of Okmok volcano, Alaska. J Geophys Res 107: https://doi.org/10.1029/2001JB000163

Marshall EW, Caracciolo A, Bali E, et al (2024) The Petrology and Geochemistry of the 2021 Fagradalsfjall Eruption, Iceland: An Eruption Sourced From Multiple, Compositionally Diverse, Near-Moho Sills. AGU Advances 5:e2024AV001310. https://doi.org/10.1029/2024AV001310

Matthews SW, Caracciolo A, Bali E, et al (2024) A dynamic mid-crustal magma domain revealed by the 2023 to 2024 Sundhnúksgígar eruptions in Iceland. Science 386:309–314. https://doi.org/10.1126/science.adp8778

Mogi, K. Relation between the eruption of various volcanoes and the deformation of the ground surface around them. Bulletin of Earthquake Research Institute 36:99–134

Odbert H, Taisne B, Gottsmann J (2015) Deposit loading and its effect on co-eruptive volcano deformation. Earth and Planetary Science Letters 413:186–196. https://doi.org/10.1016/j.epsl.2015.01.005

Okada Y (1985) Surface deformation due to shear and tensile faults in a half-space. Bulletin of the Seismological Society of America 75:1135–1154. https://doi.org/10.1785/BSSA0750041135

Pagli C, Pedersen R, Sigmundsson F, Feigl KL (2003) Triggered fault slip on June 17, 2000 on the Reykjanes Peninsula, SW-Iceland captured by radar interferometry. Geophysical Research Letters 30:2002GL015310. https://doi.org/10.1029/2002GL015310

Parks M, Sigmundsson F, Drouin V, et al (2023) Deformation, seismicity, and monitoring response preceding and during the 2022 Fagradalsfjall eruption, Iceland. Bull Volcanol 85:60. https://doi.org/10.1007/s00445-023-01671-y

Parks M, Sigmundsson F, Sigurðsson Ó, et al (2020) Deformation due to geothermal exploitation at Reykjanes, Iceland. Journal of Volcanology and Geothermal Research 391:106438. https://doi.org/10.1016/j.jvolgeores.2018.08.016

Parks MM, Sigmundsson F, Drouin V, et al (2024) 2021–2023 Unrest and Geodetic Observations at Askja Volcano, Iceland. Geophysical Research Letters 51:e2023GL106730. https://doi.org/10.1029/2023GL106730

Parks M, Drouin V, Sigmundsson F, et al (2025) 2023–2024 inflation-deflation cycles at Svartsengi and repeated dike injections and eruptions at the Sundhnúkur crater row, Reykjanes Peninsula, Iceland. Earth and Planetary Science Letters 658:119324. https://doi.org/10.1016/j.epsl.2025.119324

Pedersen GBM, Belart JMC, Óskarsson BV, et al (2022) Volume, Effusion Rate, and Lava Transport During the 2021 Fagradalsfjall Eruption: Results From Near Real-Time Photogrammetric Monitoring. Geophysical Research Letters 49:e2021GL097125. https://doi.org/10.1029/2021GL097125

Poland MP, Zebker HA (2022) Volcano geodesy using InSAR in 2020: the past and next decades. Bull Volcanol 84:27. https://doi.org/10.1007/s00445-022-01531-1

Qu F, Lu Z, Poland M, et al (2015) Post-Eruptive Inflation of Okmok Volcano, Alaska, from InSAR, 2008–2014. Remote Sensing 7:16778–16794. https://doi.org/10.3390/rs71215839

Rahimi-Dalkhani A, Ágústsdóttir T, Gudnason EÁ, et al (2023) Transdimensional ambient-noise surface wave tomography of the Reykjanes Peninsula, SW Iceland. Geophysical Journal International 236:621–643. https://doi.org/10.1093/gji/ggad435

Rivalta E, Segall P (2008) Magma compressibility and the missing source for some dike intrusions. Geophysical Research Letters 35:2007GL032521. https://doi.org/10.1029/2007GL032521

Rosen PA, Gurrola E, Sacco GF, Zebker H (2012). The InSAR scientific computing environment. In EUSAR 2012; 9th European.

Sæmundsson K, Sigurgeirsson MÁ, Friðleifsson GÓ (2020) Geology and structure of the Reykjanes volcanic system, Iceland. Journal of Volcanology and Geothermal Research 391:106501. https://doi.org/10.1016/j.jvolgeores.2018.11.022

Sæmundsson K, Sigurgeirsson MA, Hjartarson Á, Kaldal I, Kristinsson SG (2016). Geological map of southwest Iceland, 1: 100 000, 2nd ed. Iceland GeoSurvey, Reykjavik

Segall P (2016) Repressurization following eruption from a magma chamber with a viscoelastic aureole. JGR Solid Earth 121:8501–8522. https://doi.org/10.1002/2016JB013597

Sigbjörnsson R, Snæbjörnsson JTh, Higgins SM, et al (2009) A note on the M w 6.3 earthquake in Iceland on 29 May 2008 at 15:45 UTC. Bull Earthquake Eng 7:113–126. https://doi.org/10.1007/s10518-008-9087-0

Sigmundsson F, Parks M, Geirsson H, et al (2024) Fracturing and tectonic stress drive ultrarapid magma flow into dikes. Science 383:1228–1235. https://doi.org/10.1126/science.adn2838

Sigmundsson F, Parks M, Hooper A, et al (2022) Deformation and seismicity decline before the 2021 Fagradalsfjall eruption. Nature 609:523–528. https://doi.org/10.1038/s41586-022-05083-4

Sturkell E, Einarsson P, Sigmundsson F, et al (2006) Volcano geodesy and magma dynamics in Iceland. Journal of Volcanology and Geothermal Research 150:14–34. https://doi.org/10.1016/j.jvolgeores.2005.07.010

Sturkell E, Sigmundsson F, Einarsson P, Bilham R (1994) Strain accumulation 1986–1992 across the Reykjanes Peninsula Plate Boundary, Iceland, determined from GPS measurements. Geophysical Research Letters 21:125–128. https://doi.org/10.1029/93GL03421

Tryggvason E (1973). Seismicity, earthquake swarms, and plate boundaries in the Iceland region. Bulletin of the Seismological Society of America, *63*(4), 1327-1348.

Vadon H, Sigmundsson F (1997) Crustal Deformation from 1992 to 1995 at the Mid-Atlantic Ridge, Southwest Iceland, Mapped by Satellite Radar Interferometry. Science 275:194–197. https://doi.org/10.1126/science.275.5297.194

Vardić K, Clarke PJ, Whitehouse PL (2022) A GNSS velocity field for crustal deformation studies: The influence of glacial isostatic adjustment on plate motion models. Geophysical Journal International 231:426–458. https://doi.org/10.1093/gji/ggac047

Weir NRW, White RS, Brandsdóttir B, et al (2001) Crustal structure of the northern Reykjanes Ridge and Reykjanes Peninsula, southwest Iceland. J Geophys Res 106:6347–6368. https://doi.org/10.1029/2000JB900358

Zumberge JF, Heflin MB, Jefferson DC, et al (1997) Precise point positioning for the efficient and robust analysis of GPS data from large networks. J Geophys Res 102:5005–5017. https://doi.org/10.1029/96JB03860

Supplementary material for

Transient ground deformation observed by GNSS and InSAR during and following the 2021 Fagradalsfjall eruption, Iceland

Chiara Lanzi (1, 2), Halldór Geirsson (1), Michelle Maree Parks (2), Vincent Drouin (2), Freysteinn Sigmundsson (1)

(1) Nordic Volcanological Center, Institute of Earth Sciences, University of Iceland, Reykjavik, Iceland

(2) Icelandic Meteorological Office, Reykjavik, Iceland

Table of content:

Figure S8-S11. Modelling results for the uncorrected six-months eruption and inferred probability density functions.

Figure S12-S18. Modelling results for the lava loading corrected six-months eruption and inferred probability density functions.

Figure S19-S22. Modelling results for T2 geodetic phase and inferred probability density functions.

Figure S23-25. Modelling results for post-eruptive phase and inferred probability density functions

Table S1. GNSS sites network.

S1 – Young's modulus evaluation in crustal layering at volcanic area

In reality, crustal rocks are heterogeneous, with rock properties changing laterally and with depth, and the parameter choice is highly relevant as it strongly affects the calculated deformation (Heap et al., 2020; Geyer and Gottsmann, 2010; O'Hara, 2023). For example, Hautmann et al. (2013), evaluate static Young's modulus (E) values between 6 and 42 GPa for the upper crust at Soufrière Hills Volcano when modelling the effects of an extrusion event in 2009, with mean value of E = 25 GPa at depth 5–6 km. The average Young's modulus value for the Icelandic crust has been estimated to be $E \sim$ 30 GPa (Drouin et al., 2016). Tor a two-layer model Auriac et al. (2013) found best-fitting values of E = 12.9–15.3 GPa in the upper layer (15–40 km-thick) and E = 67.3–81.9 GPa in a lower layer. We test two different values of E: 15 and 30 GPa to span the range of most likely values in the volcanic context in Iceland.

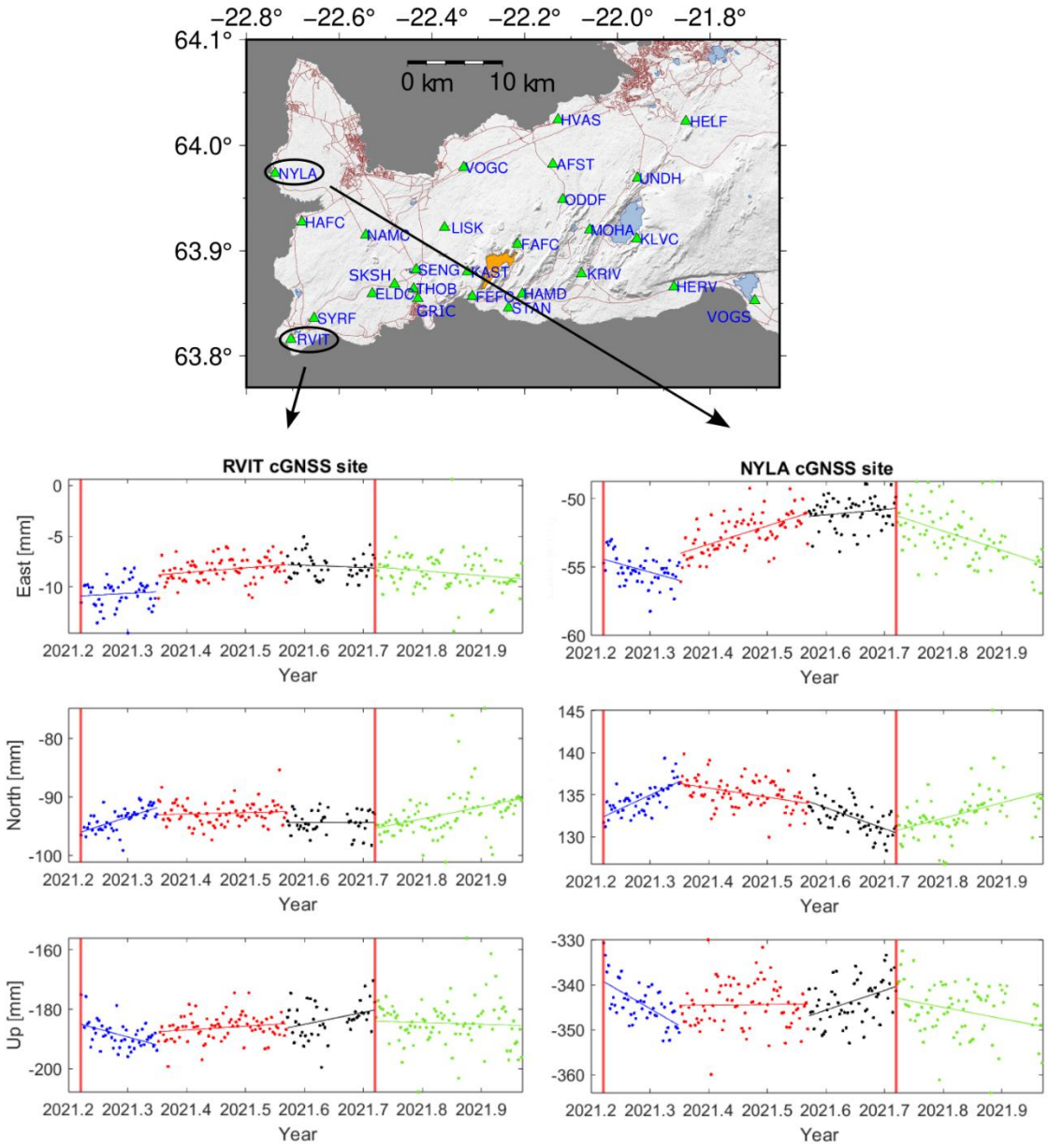

Figure S1. Deformation 19 March to 20 December 2021. The top panel shows the GNSS network (in green triangles) around the Reykjanes Peninsula with the Fagradalsfjall lava field at the end of the eruption (in orange). The lower panels display detrended RVIT (on the left) and NYLA (on the right) cGNSS times series (both located west from the eruption side) with the three co-eruptive deformation periods: T1, 19 March – 10 May (blue dots), T2 11 May - 31 July (red dots), T3, 1 August – 18 September /black dots), and post-eruptive deformation, 19 September – 20 December (green dots). The vertical red line indicates the beginning and end of the eruption. The time series are in the ITRF2014 reference frame, and linear, annual and semi-annual trends have been removed.

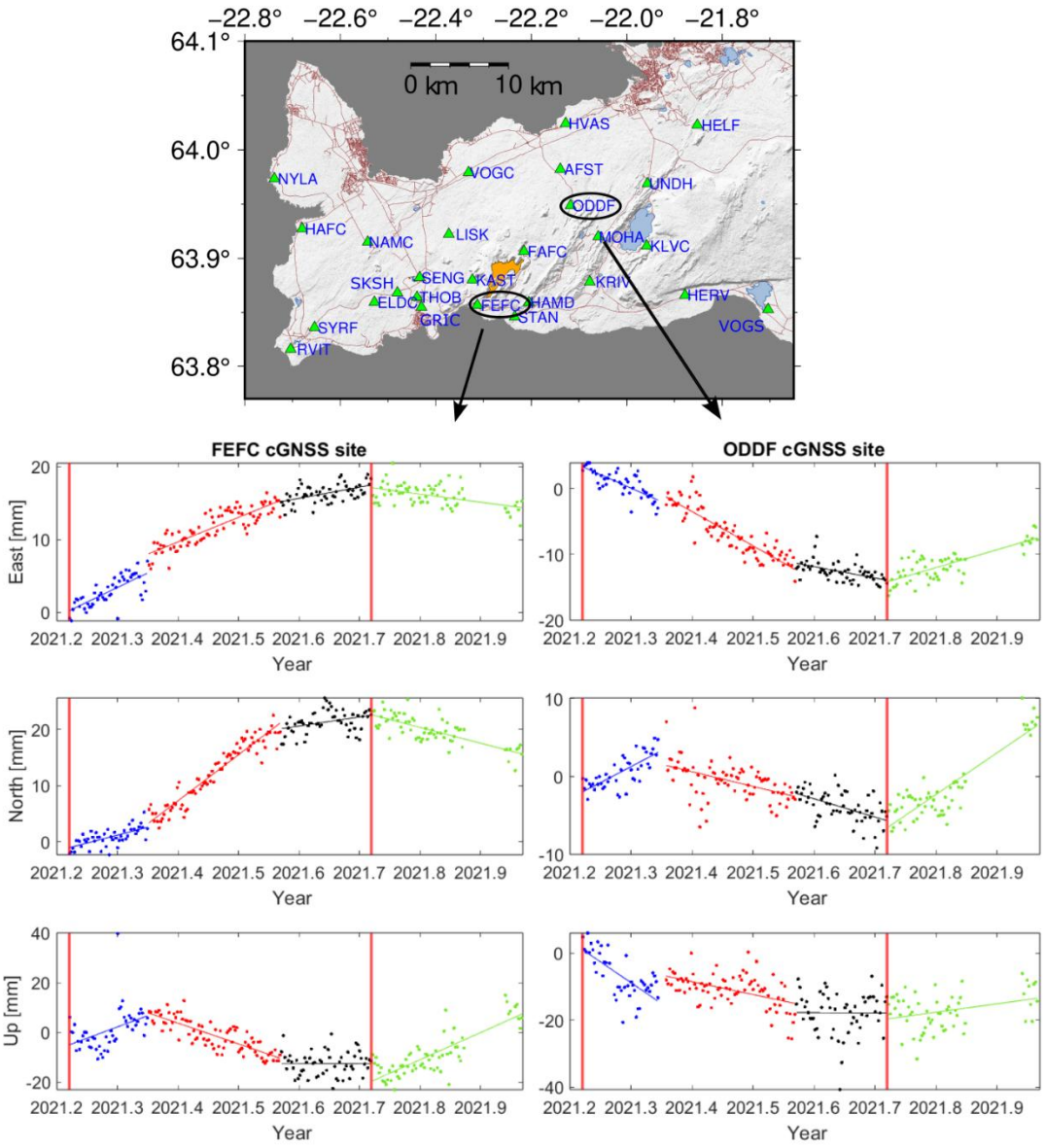

Figure S2. Deformation 19 March to 20 December 2021. The upper panel shows the GNSS network (in green triangles) around the Reykjanes Peninsula with the Fagradalsfjall lave field at the end of the eruption (in orange). The lower panels display FEFC (on the left) and ODDF (on the right) cGNSS times series (both located west from the eruption side) with the three co-eruptive deformation periods: T1: 19 March – 10 May (blue dots), T2: 11 May - 31 July (red dots), T3: 1 August – 18 September (black dots), and post-eruptive deformation, 19 September – 20 December (green dots). The vertical red line indicates the beginning and end of the eruption. The blue, red, black and green lines show the least-square fit for the different geodetic phases. The time series are in the ITRF2014 reference frame.

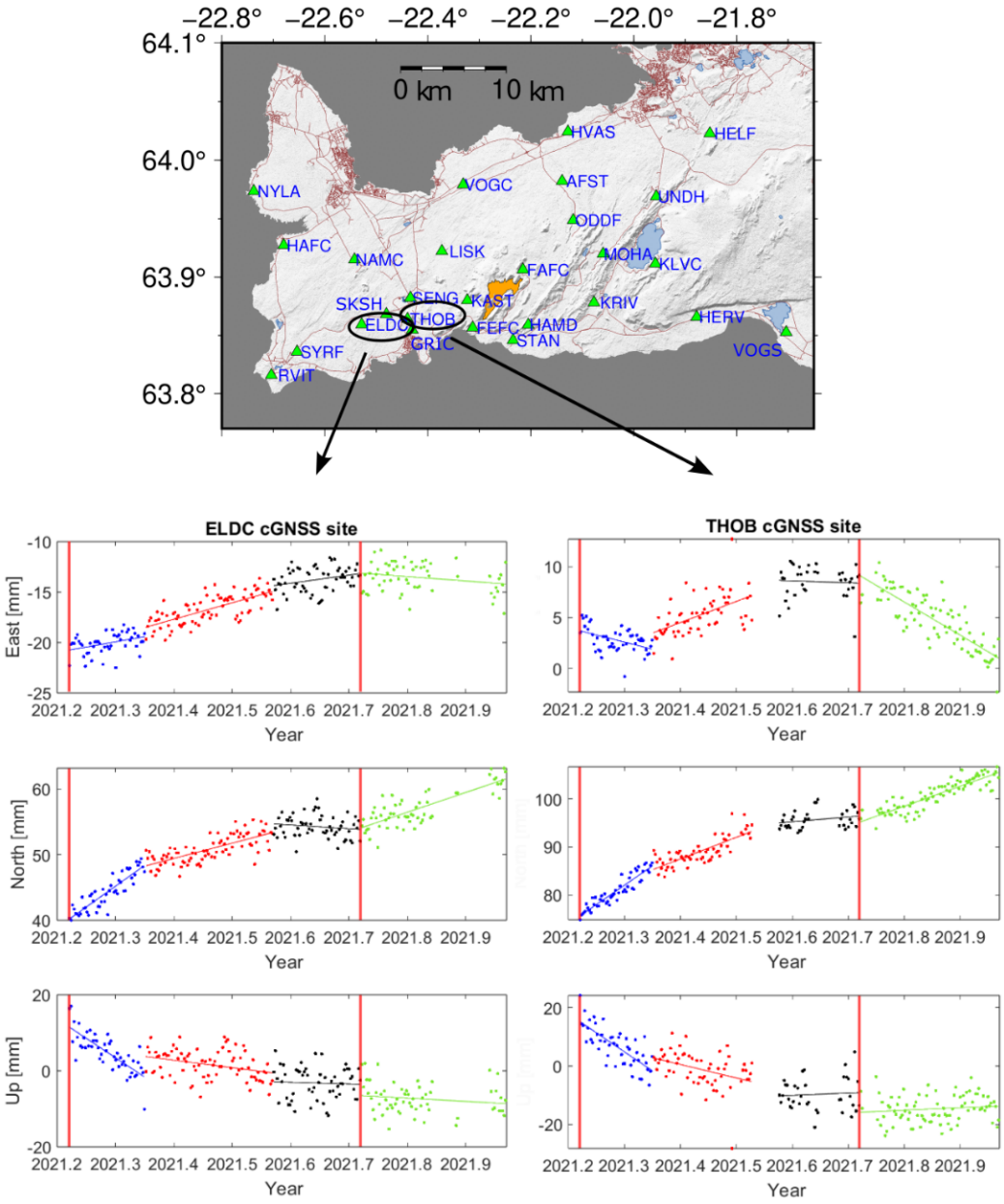

Figure S3. Deformation 19 March to 20 December 2021. The upper panel shows the GNSS network (in green triangles) around the Reykjanes Peninsula with the Fagradalsfjall lave field at the end of the eruption (in orange). The lower panels display ELDC (on the left) and THOB (on the right) cGNSS times series (both located west from the eruption side) with the three co-eruptive deformation periods: T1: 19 March – 10 May (blue dots), T2: 11 May - 31 July (red dots), T3: 1 August – 18 September (black dots), and post-eruptive deformation, 19 September – 20 December (green dots). The vertical red line indicates the beginning and end of the eruption. The blue, red, black and green lines show the least-square fit for the different geodetic phases. The time series are in the ITRF2014 reference frame.

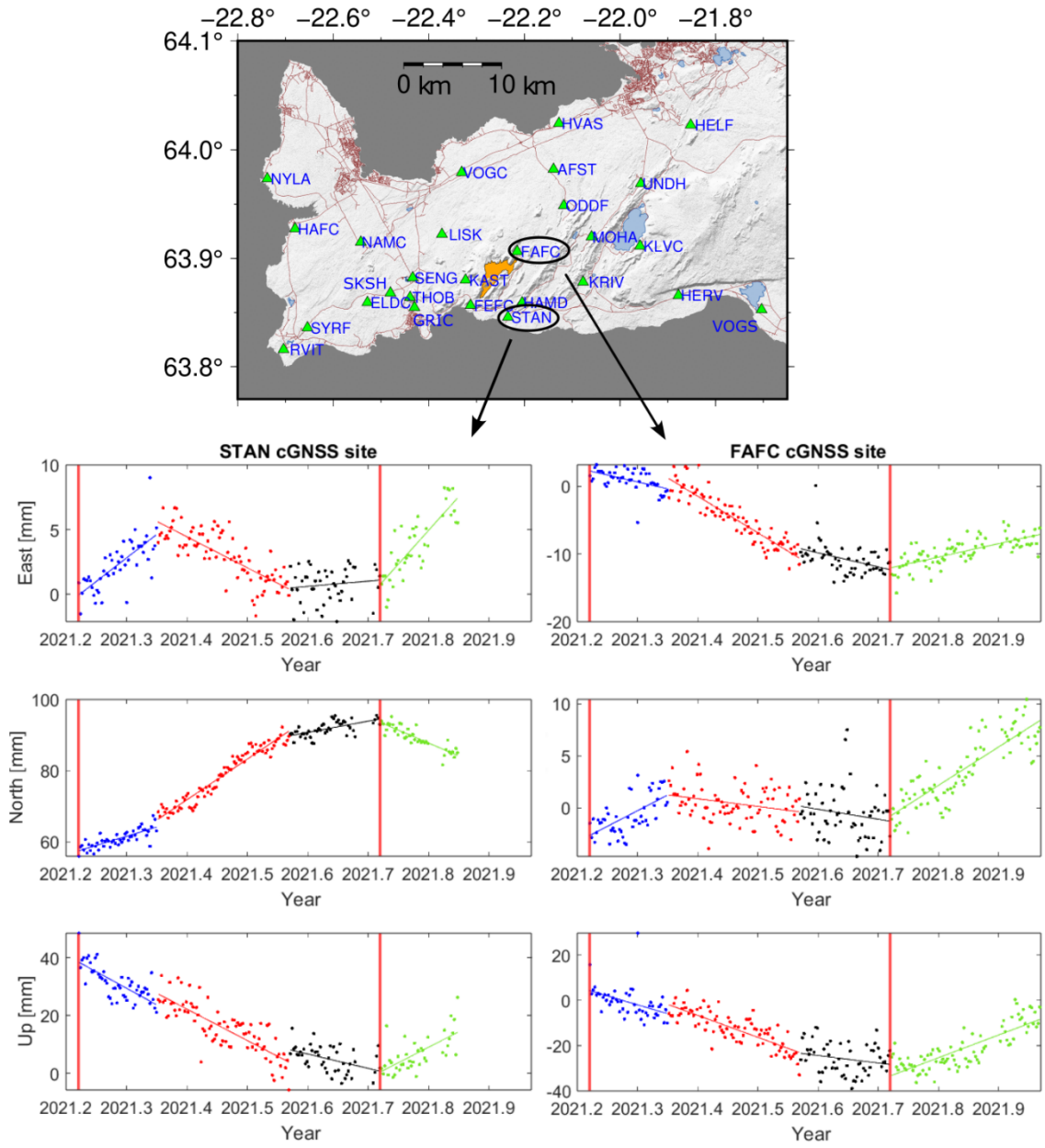

Figure S4. Deformation 19 March to 20 December 2021. The upper panel shows the GNSS network (in green triangles) around the Reykjanes Peninsula with the Fagradalsfjall lave field at the end of the eruption (in orange). The lower panels display STAN (on the left) and FAFC (on the right) cGNSS times series (both located west from the eruption side) with the three co-eruptive deformation periods: T1: 19 March – 10 May (blue dots), T2: 11 May - 31 July (red dots), T3: 1 August – 18 September (black dots), and post-eruptive deformation, 19 September – 20 December (green dots). The vertical red line indicates the beginning and end of the eruption. The blue, red, black and green lines show the least-square fit for the different geodetic phases. The time series are in the ITRF2014 reference frame.

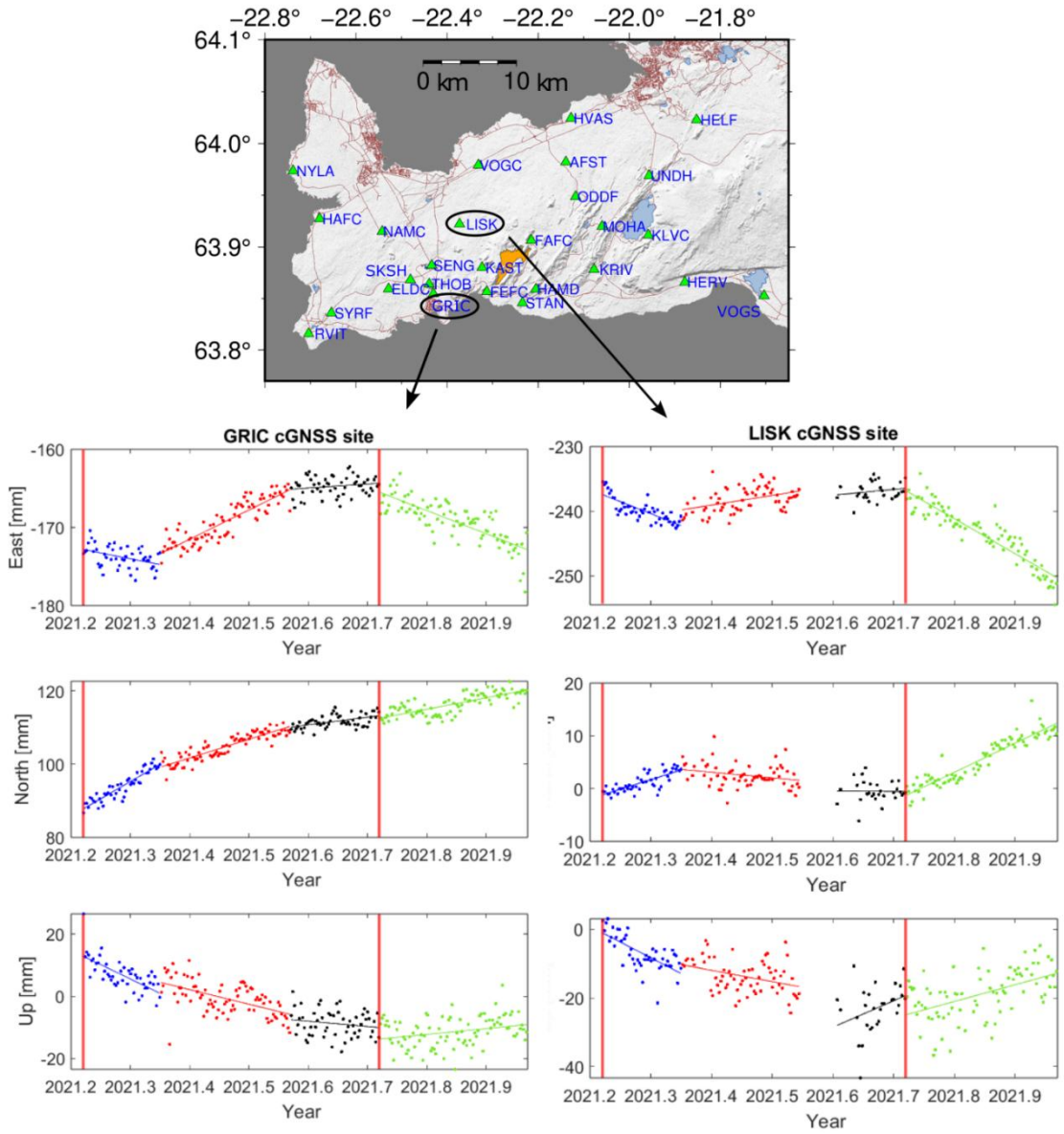

Figure S5. Deformation 19 March to 20 December 2021. The upper panel shows the GNSS network (in green triangles) around the Reykjanes Peninsula with the Fagradalsfjall lave field at the end of the eruption (in orange). The lower panels display SKSH (on the left) and GRIC (on the right) cGNSS times series (both located west from the eruption side) with the three co-eruptive deformation periods: T1: 19 March – 10 May (blue dots), T2: 11 May - 31 July (red dots), T3: 1 August – 18 September (black dots), and post-eruptive deformation, 19 September – 20 December (green dots). The vertical red line indicates the beginning and end of the eruption. The blue, red, black and green lines show the least-square fit for the different geodetic phases. The time series are in the ITRF2014 reference frame.

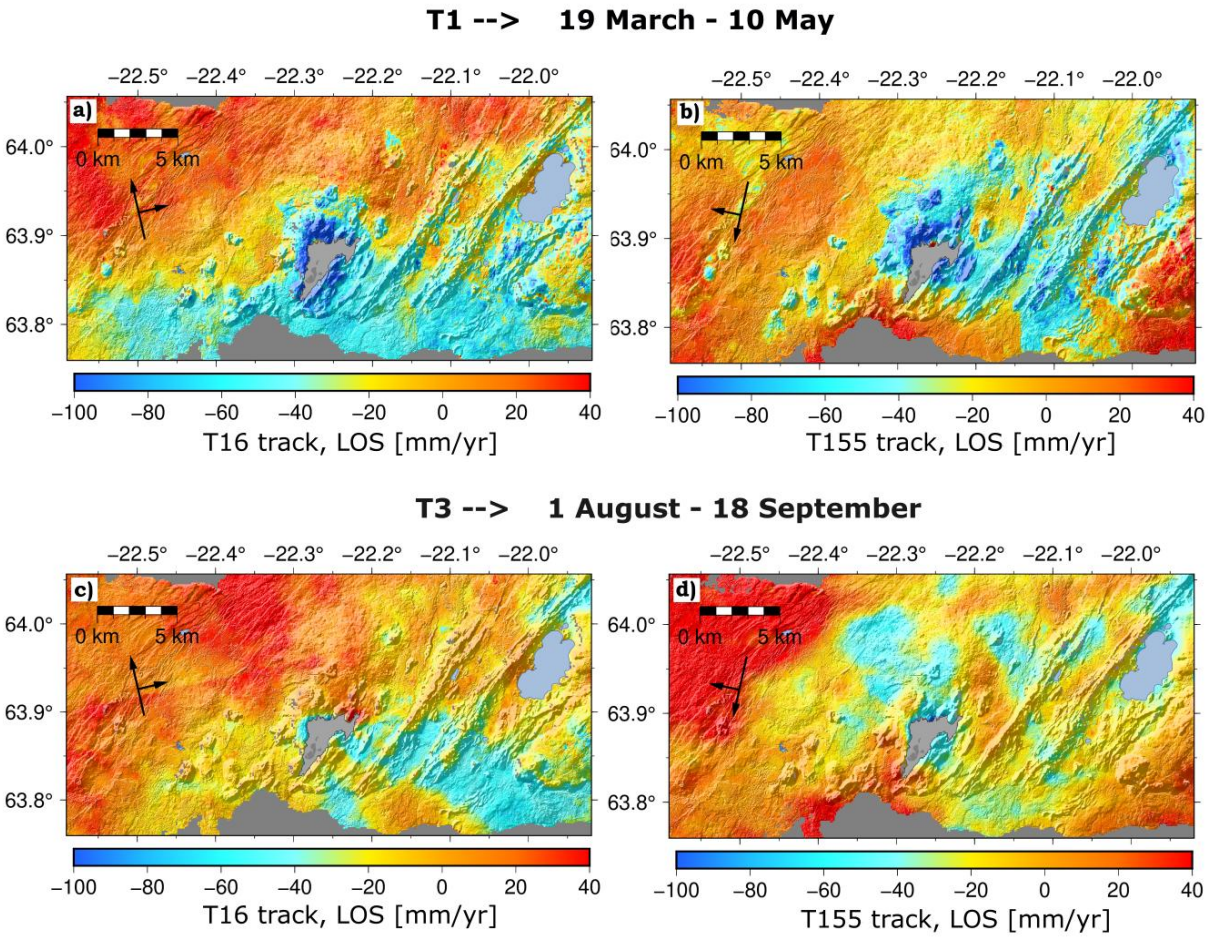

Figure S6. Line-of-Sight for two Sentinel-1 tracks, T16 (on the left) and T155 (on the right); T1 geodetic phase in a) and b), and T3 geodetic phase in c) and d). Black arrows show the heading and look direction of the satellite. In light grey, the Fagradalsfjall lava field at the end of the eruption and in light blue the lake Kleifarvatn to the east. Dark grey indicates the ocean.

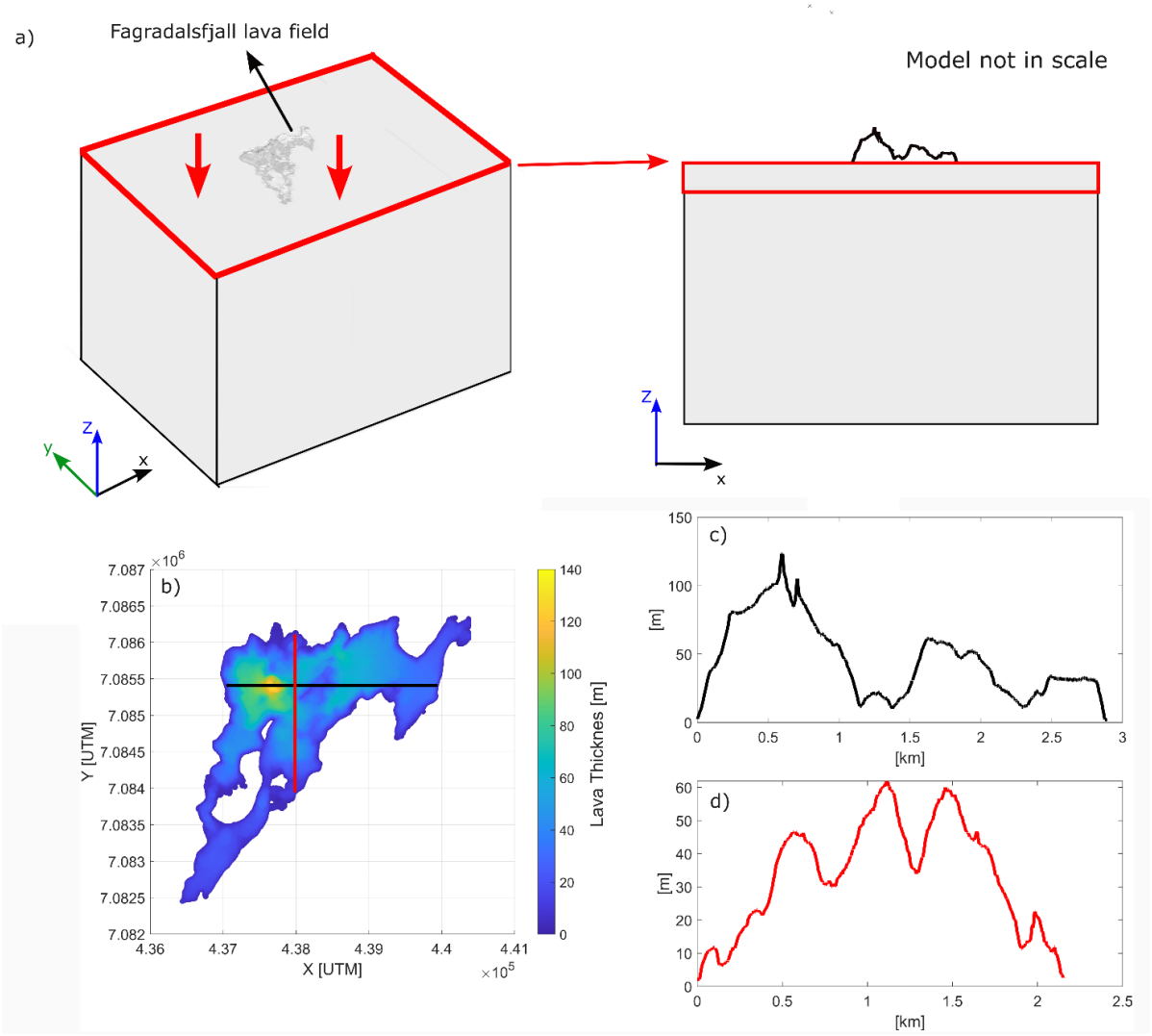

Figure S7. a) The finite element model setups. Model geometry for the lava loading model in a uniform elastic half-space. The boundary conditions are set as follows (panel on the left): a load (vertical red arrows) is applied at the surface in the form of: *-rho*g*z*, where *rho* is the density of the material, 2600 kg/m^3, *g* is the gravitational acceleration, 9.81 m^3/s, and *z* relates to the thickness of the lava field. Roller condition at the lateral sides of the block (yz and zx faces); that is, the displacement is zero in the direction perpendicular (normal) to the boundary, but the boundary is free to move in the tangential direction. The bottom of the model is fixed. The panel on the left is showing an exaggerated schematic xy view of the "loaded" horizontal layer applied to combine the lava DEM and the underlying half space. The W-E profile of the lava field is displayed in map view in black solid line in b) and profile in real scale in panel c), while panel d) shows the E-W (red) profile to show the irregular ending (≠ 0 thickness) of the lava DEM.

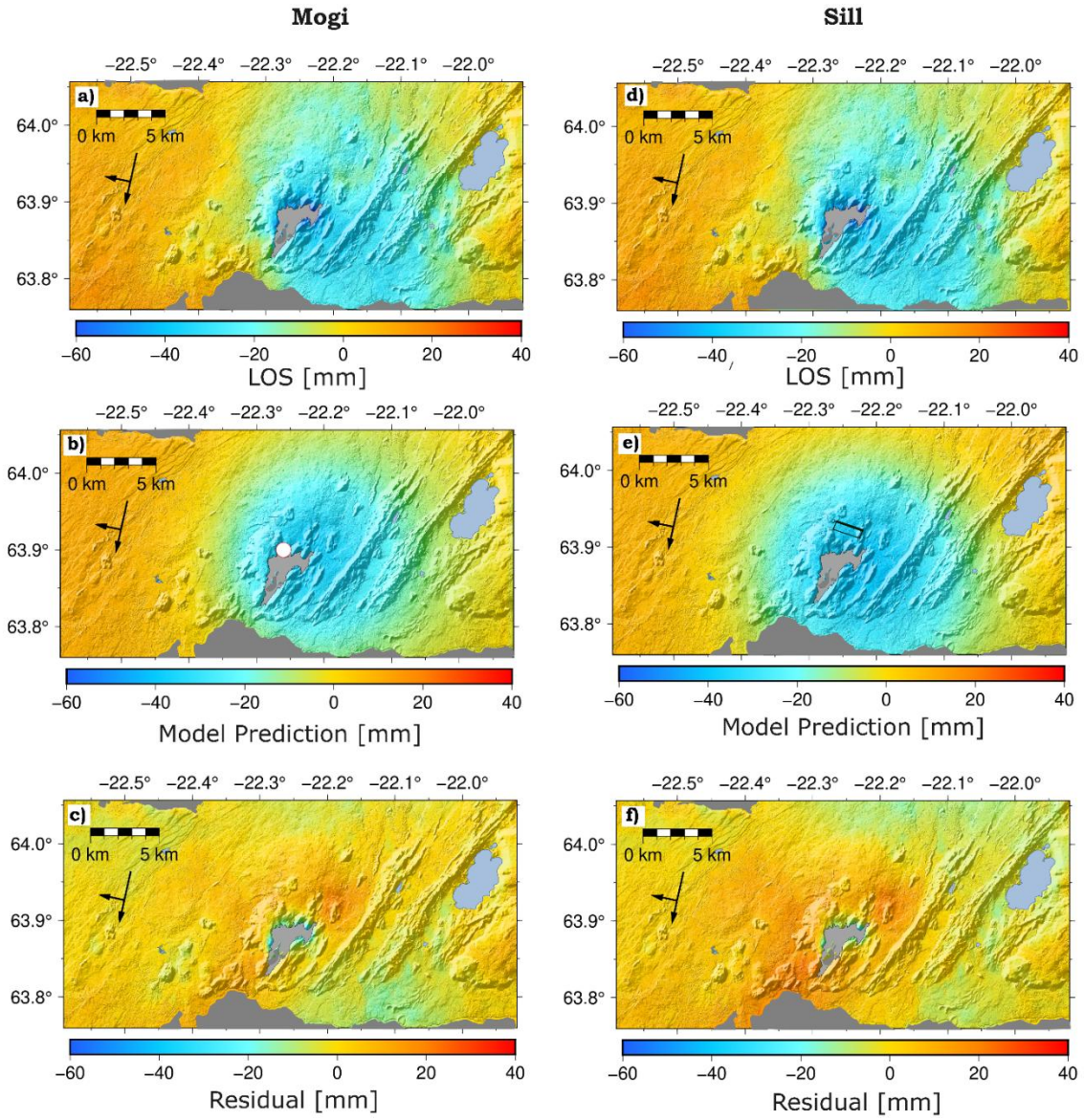

Figure S8. Modelling results for the uncorrected six-months data of the T155 InSAR track. (a) and (b) data, (c) and (d) model prediction, and (e) and (f) residuals for a Mogi and a sill source, respectively (left and right columns). Black outline in (b) shows the projection at surface of the modelled deflating sill, with the thicker line indicating the bottom of the sill best-fit solution at 12.6 km depth (95% confidence interval: 11.9–13.1 km). The white circle in (b) indicates the best-fit Mogi source at 8.8 km depth (95% confidence interval: 8.3–9.2 km). Black arrows show the heading and look direction of the satellite. In light grey, the Fagradalsfjall lava field at the end of the eruption and in light blue the lake Kleifarvatn to the east. Dark grey indicates the ocean.

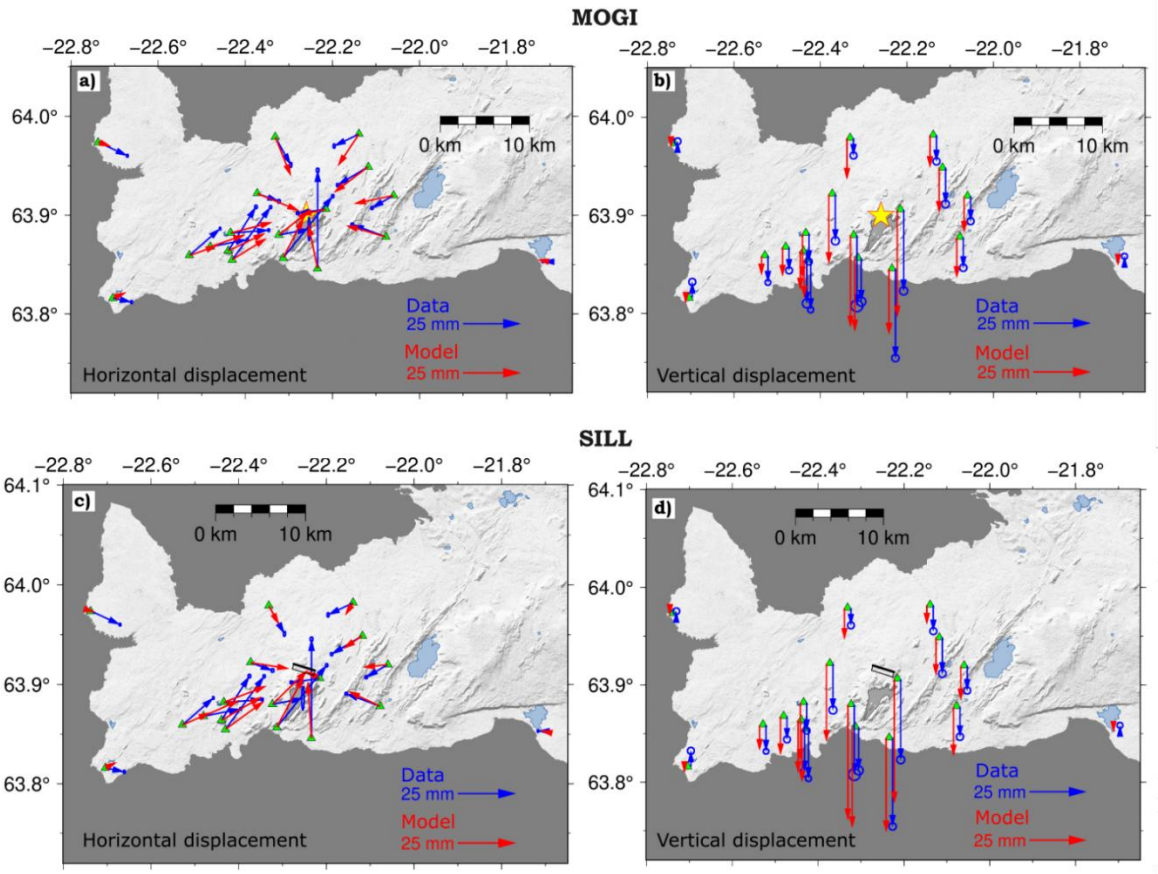

Figure S9. Modelling results for the uncorrected six-months eruption data. a) and b) show the horizontal and vertical data and modelled displacements. The yellow star indicates the best-fit solution of the Mogi source at 8.8 km depth (95% confidence interval: 8.3–9.2 km). c) and d) panels show the horizontal and vertical data and modelled displacement for sill B case. Black outline in (c) and (d) shows the projection at surface of the modelled deflating sill, with the thicker line indicating the bottom of the sill best-fit solution at 12.6 km depth (95% confidence interval: 11.9–13.1 km). In light grey, the Fagradalsfjall lava field at the end of the eruption and in light blue are indicated lakes in the area. Dark grey indicates the ocean.

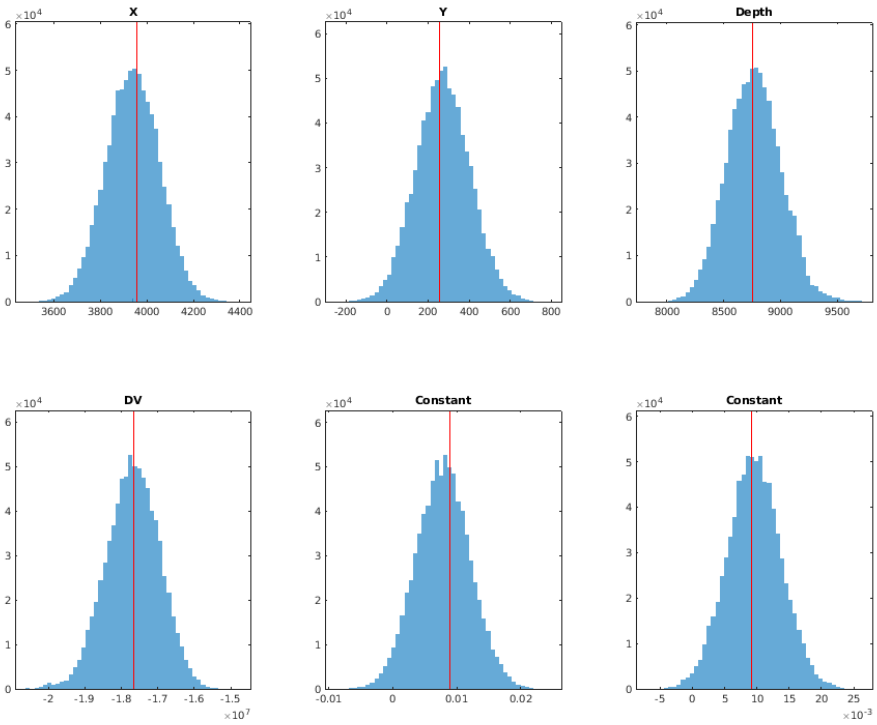

Figure S10. Inferred probability density functions for Mogi best fit model parameters (GBIS) for the uncorrected case. Source location (X and Y local coordinates in meters), depth in meters and volume change (ΔV) in m^3. Also inferred by the inversion are two offset parameters (InSAR Const.) for each of the InSAR satellite tracks used, as the input displacement fields may have an arbitrary offset. The InSAR Const. is a shift estimated in the LOS direction since all INSAR measurements are relative to an arbitrary reference point and it is in meter, the first panel is for the T16 and the second for the T155 track. The red lines indicate the optimal value of the parameter.

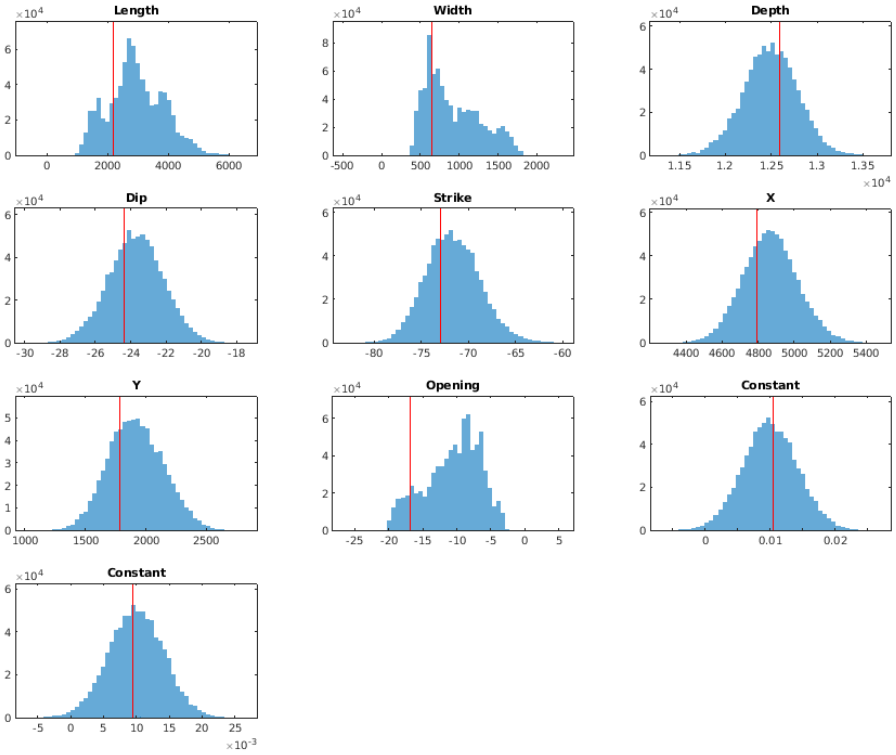

Figure S11. Inferred probability density functions for sill (uncorrected data) case best-fit model parameters (GBIS). Source location (X and Y local coordinates in meters), source depth, length, width and opening of the sill in meters; strike and dip are in degrees. Also inferred by the inversion are two offset parameters (InSAR Const.) for each of the InSAR satellite tracks used, as the displacement fields may have an arbitrary offset. The InSAR Const. is a shift applied to the entire dataset and it is in meter, the first panel is for the T16 and the second for the T155 track.The red line indicates the optimal value of the parameter.

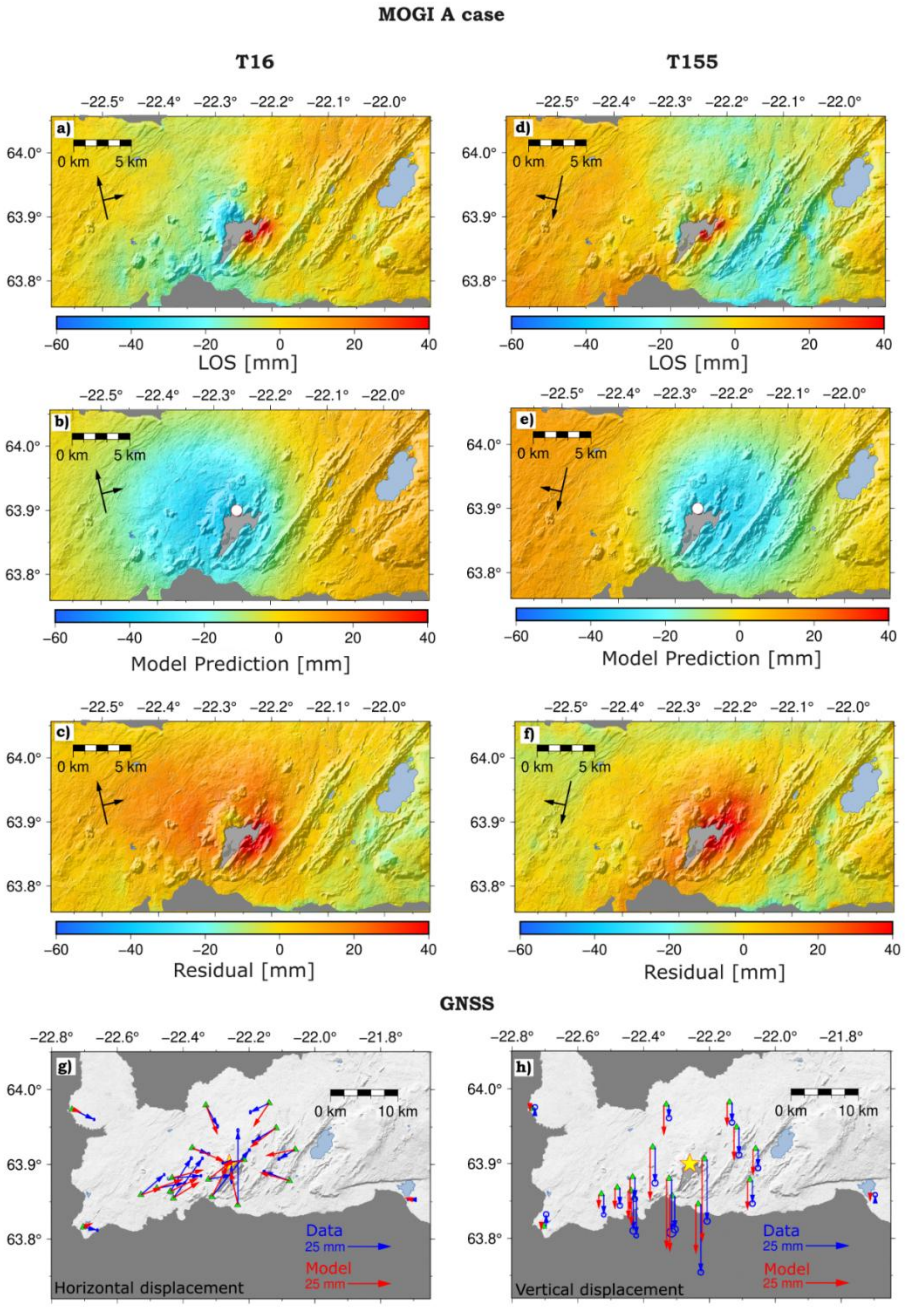

Figure S12. Modelling results for the loading corrected Mogi A case for the six-months eruptive period. a) data, b) model prediction; c) residual for track T16, d) data, e) model prediction and f) residual for track T155. The white circle indicates the best-fit solution of the Mogi source at 9.5km depth (95% confidence interval: 8.7–9.3 km). Black arrows show the heading and look direction of the satellite. g) and h) show the horizontal and vertical data and modelled displacement. The yellow start indicates the best-fit Mogi location. The WRSS estimated is 0.99 mm and 0.94 mm for the Mogi and sill geometry. In light grey, the Fagradalsfjall lava field at the end of the eruption and in light blue are indicated lakes in the area. Dark grey indicates the ocean.

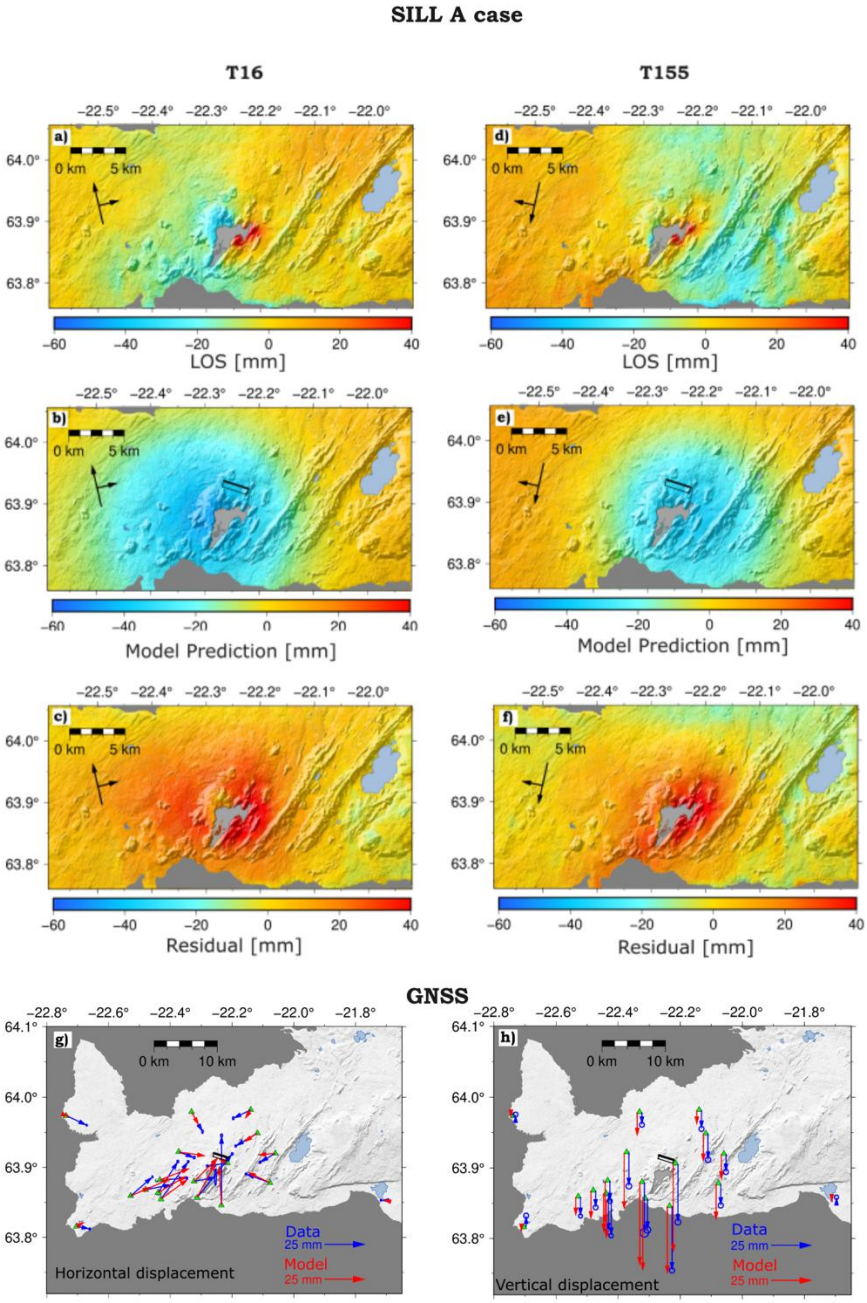

Figure S13. Modelling results for the loading corrected sill A case for the six-months eruptive period. a) data, b) model prediction; c) residual for track T16, d) data, e) model prediction and f) residual for track T155. Black lines indicate the best-fit solution of the sill source at 13.1 km depth (95% confidence interval: 12.7–13.5) km depth. Black arrows show the heading and look direction of the satellite. g) and h) show the horizontal and vertical data and modelled displacement. In light grey, the Fagradalsfjall lava field at the end of the eruption and in light blue are indicated lakes in the area. Dark grey indicates the ocean.

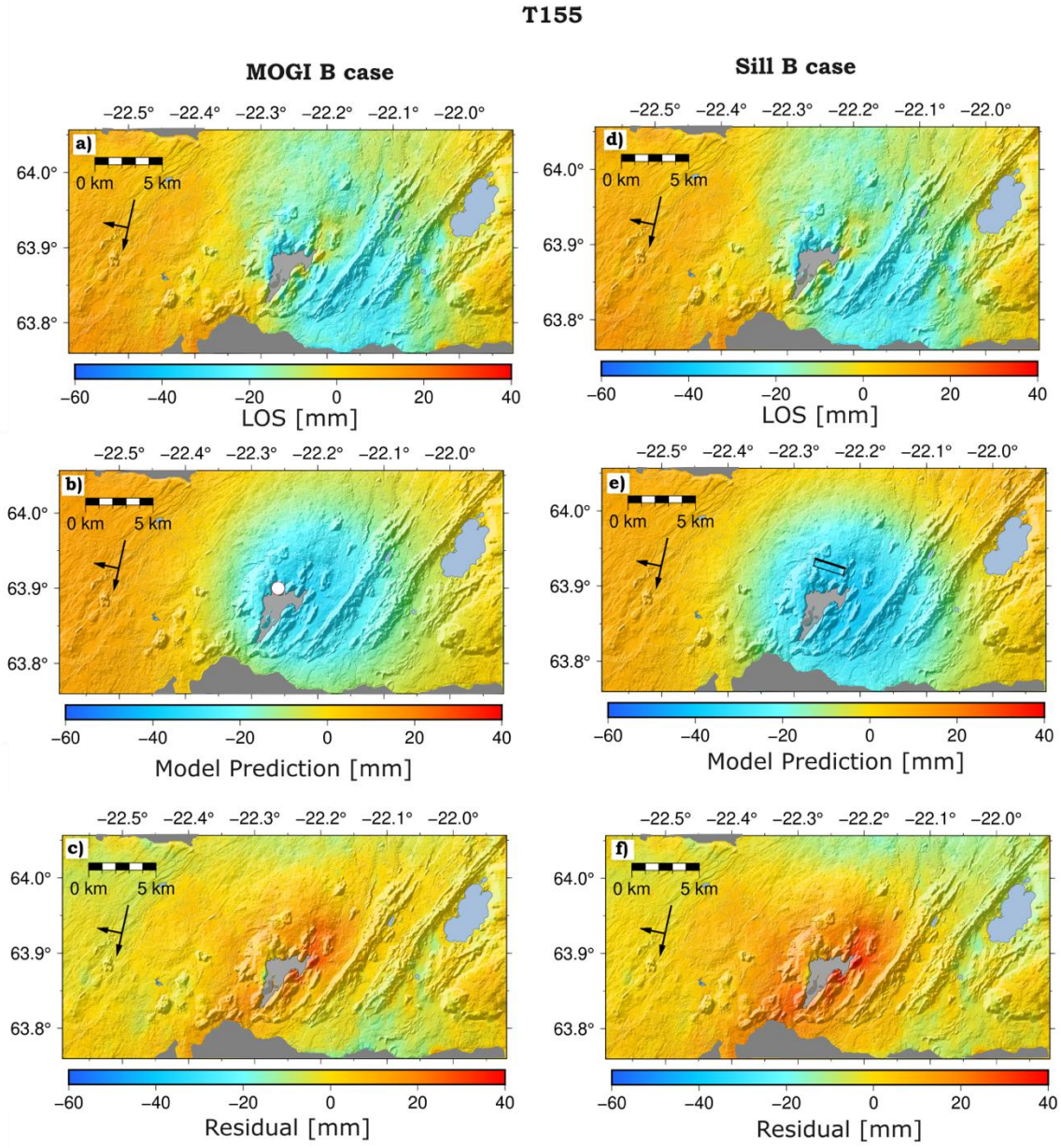

Figure S14. Modelling results for the loading corrected six-months eruption of T155 InSAR track when a crustal Young's modulus equal to 30 GPa is used. (a) and (b) data, (c) and (d) model prediction, (e) and (f) residual for a Mogi and a sill geometry, respectively (left and right columns). Black outlines show the projection at surface of the modelled deflating sill top (thicker line) at a depth of 12.8 km (95% confidence interval 12.5-13.3 km). The white circle indicates the best-fit solution of the Mogi source at 9 km (95% confidence interval: 8.6–9.5) km depth. Black arrows show the heading and look direction of the satellite. In light grey, the Fagradalsfjall lava field at the end of the eruption and in light blue the lake Kleifarvatn to the east. Dark grey indicates the ocean.

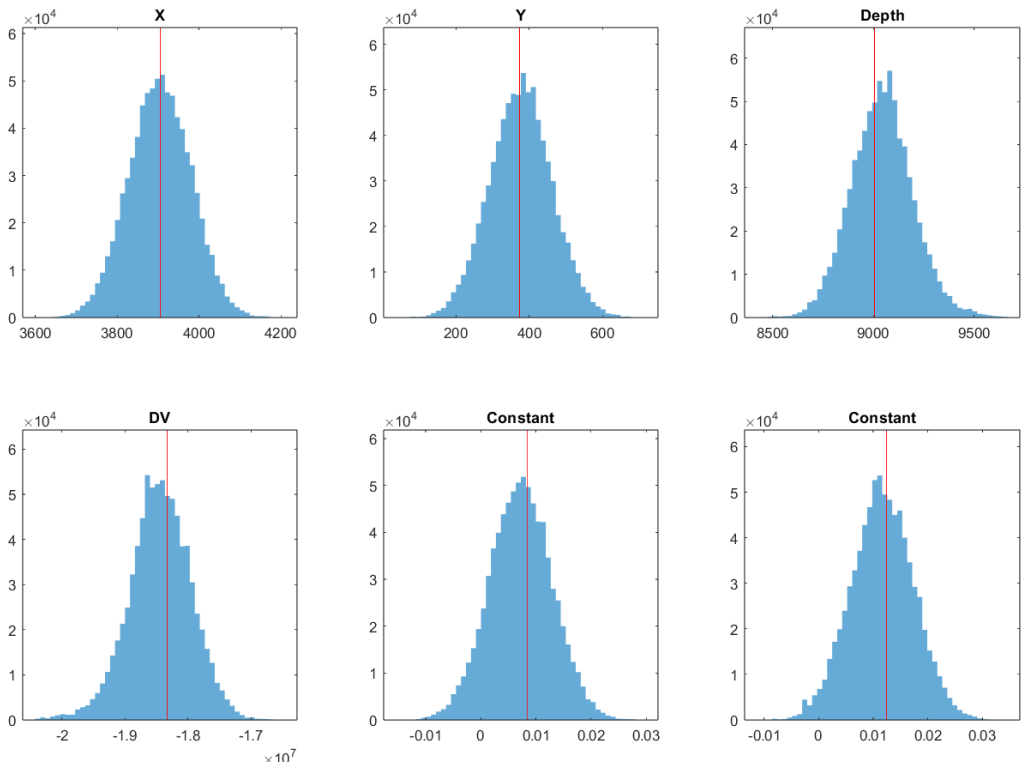

Figure S15. Inferred probability density functions for Mogi best fit model parameters (GBIS) for Mogi A case. Source location (X and Y local coordinates in meters), depth in meters and volume change (ΔV) in m^3. Also inferred by the inversion are two offset parameters (InSAR Const.) for each of the InSAR satellite tracks used, as the input displacement fields may have an arbitrary offset. The InSAR Const. is a shift applied to the entire dataset and it is in meter, the first panel is for the T16 and the second for the T155 track. The red lines indicate the optimal value of the parameter.

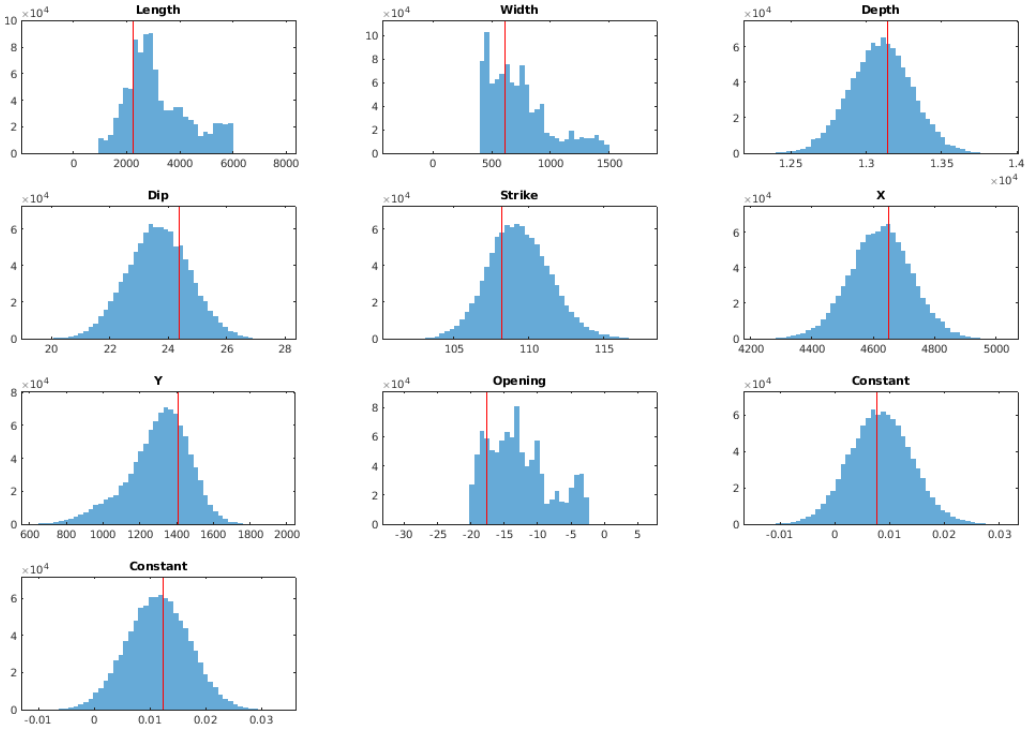

Figure S16. Inferred probability density functions for sill A case best-fit model parameters (GBIS). Source location (X and Y local coordinates in meters), source depth, length, width and opening of the sill in meters; strike and dip are in degrees. Also inferred by the inversion are two offset parameters (InSAR Const.) for each of the InSAR satellite tracks used, as the displacement fields may have an arbitrary offset The InSAR Const. is a shift applied to the entire dataset and it is in meter, the first panel is for the T16 and the second for the T155 track. The red lines indicate the optimal value of the parameter.

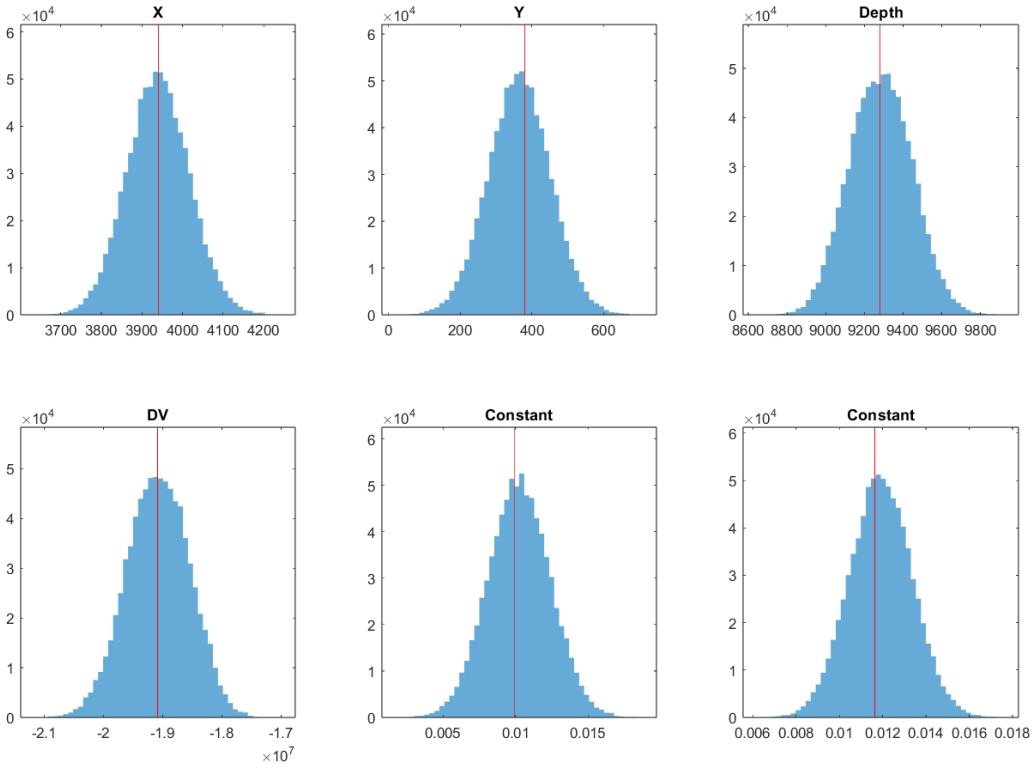

Figure S17. Inferred probability density functions for Mogi best fit model parameters (GBIS) for Mogi B case. Source location (X and Y local coordinates in meters), depth in meters and volume change (ΔV) in m^3. Also inferred by the inversion are two offset parameters (InSAR Const.) for each of the InSAR satellite tracks used, as the input displacement fields may have an arbitrary offset. The InSAR Const. is a shift applied to the entire dataset and it is in meter, the first panel is for the T16 and the second for the T155 track. The red line indicates the optimal value of the parameter.

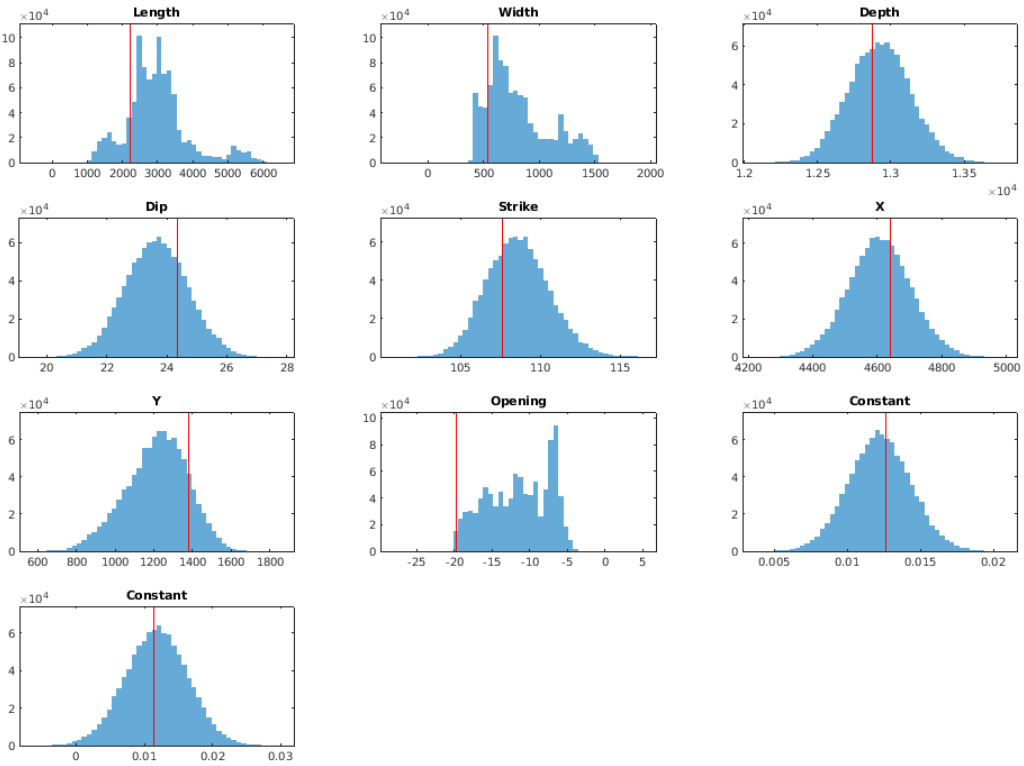

Figure S18. Inferred probability density functions for sill B case best-fit model parameters (GBIS). Source location (X and Y local coordinates in meters), source depth, length, width and opening of the sill in meters; strike and dip are in degrees. Also inferred by the inversion are two offset parameters (InSAR Const.) for each of the InSAR satellite tracks used, as the displacement fields may have an arbitrary offset. The InSAR Const. is a shift applied to the entire dataset and it is in meter, the first panel is for the T16 and the second for the T155 track. The red line indicates the optimal value of the parameter.

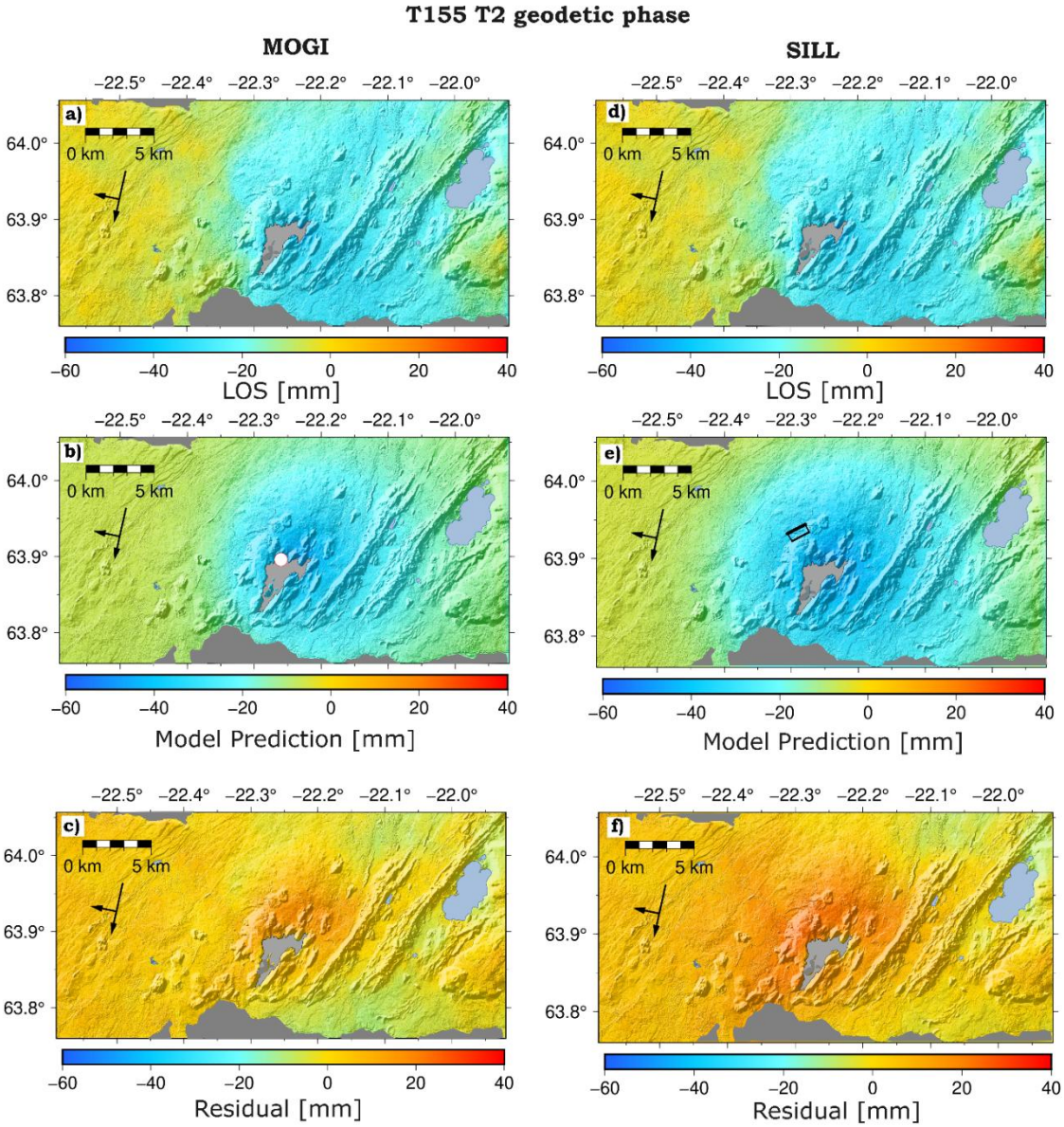

Figure S19. Modelling results for T2 geodetic phase of T155 InSAR track. a) and b) data, c) and d) model prediction, e) and f) residual for a point-source and a sill geometry, respectively. Black outlines show the projection at surface of the modelled best-fit deflating sill at 11.7 km (95% confidence interval: 11.1–12.4 km), with the thicker line indicating the top of the sill. The white circle indicates the best-fit solution of the Mogi source at 6 km (95% confidence interval: 5.6–6.3 km) depth. Black arrows show the heading and look direction of the satellite. Model parameter results for the Mogi are displayed in Supplementary Figure S21; while for the sill, they are in Supplementary Figure S22. In light grey, the Fagradalsfjall lava field at the end of the eruption and in light blue the lake Kleifarvatn to the east. Dark grey indicates the ocean.

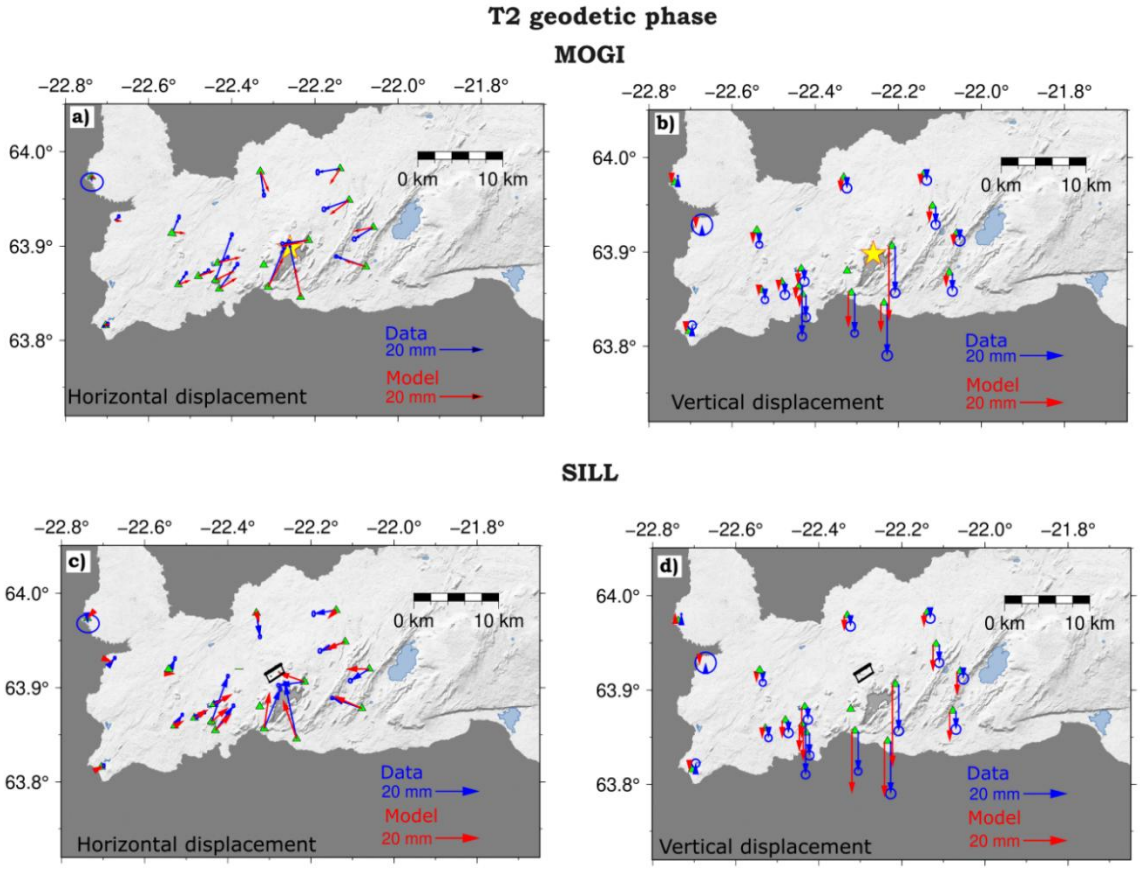

Figure S20. Modelling results for T2 geodetic phase for Mogi and sill sources. Horizontal a) and b) vertical GNSS data and model predictions for the Mogi source (yellow star) at 6.0 km depth ((95% confidence interval: 5.6–6.3) km depth located at -22.26°, 63.898°. Horizontal c) and Vertical d) data and model prediction for a sill source at a depth of 11.7 km (95% confidence interval: 11.1–12.4 km), (coordinate for the vertices: -22.285°, 63.923°, -22.302°, 63.918°, -22.296°, 63.912°, -22.277°, 63.917°). Model parameter results for the Mogi are displayed in Supplementary Figure S21; while for the sill, they are in Supplementary Figure S22. Black outlines show the projection at surface of the modelled deflating sill with the thicker line indicating the top of the sill. In light grey, the Fagradalsfjall lava field at the end of the eruption and in light blue are indicated lakes in the area. Dark grey indicates the ocean.

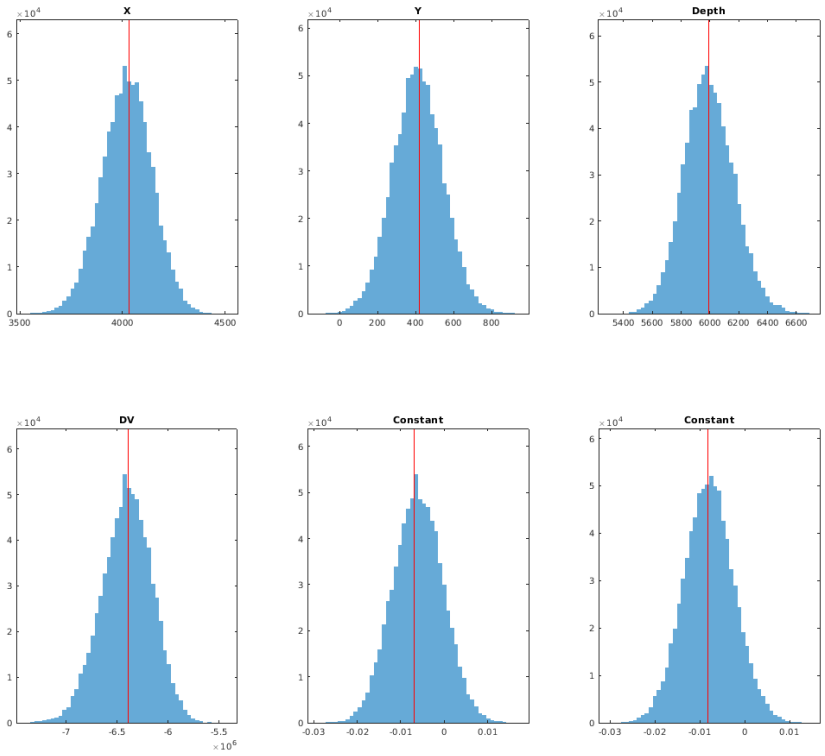

MODEL PARAMETER	Optimal	2.5 %	97.5%
Depth (km)	5.99	5.67	6.35
Deflating volume change (Mm^3)	6.39	6.91	5.95
Longitude	-22.258	-22.263	-22.253
Latitude	63.883	-63.881	63.886

Figure S21. Inferred probability density functions (pdf) for Mogi model parameters (GBIS) for the T2 geodetic phase with the parameter values in the table in terms of optimal, 2.5% and 97.5% results. Source location parameters X and Y are in local coordinates in meters in the pdf but presented in longitude and latitude in the table. Also inferred by the inversion are two offset parameters (InSAR Const.) for each of the InSAR satellite tracks used, as the input displacement fields may have an arbitrary offset. The InSAR Const. is a shift applied to the entire dataset and it is in meter, the first panel is for the T16 and the second for the T155 track. The red line indicates the optimal value of the parameter.

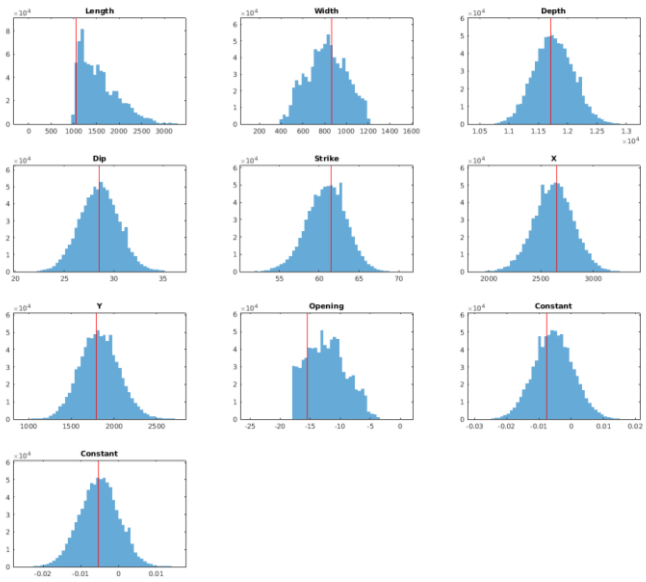

MODEL PARAMETER	Optimal	2.5 %	97.5%
Depth (km)	11.7	11.1	11.6
Length (km)	1.06	1.03	2.59
Width (km)	0.86	0.49	1.16
Strike (°)	61	56	66
Dip (°)	29	25	32
Longitude*	-22.286	-22.294	-22.279
Latitude*	63.896	63.893	63.901

Figure S22. Inferred probability density functions for sill geometry during the T2 geodetic phase for the optimal, 2.5% and 97.5% values. Source location X and Y are in local coordinates in meters in the pdf; but converted in latitude and decimal degrees in the table; the values referred to the bottom edges of the dislocation. Also inferred by the inversion are two offset parameters (InSAR Const.) for each of the InSAR satellite tracks used, as the displacement fields may have an arbitrary offset. The InSAR Const. is a shift applied to the entire dataset and it is in meter, the first panel is for the T16 and the second for the T155 track. The red line indicates the optimal value of the parameter.

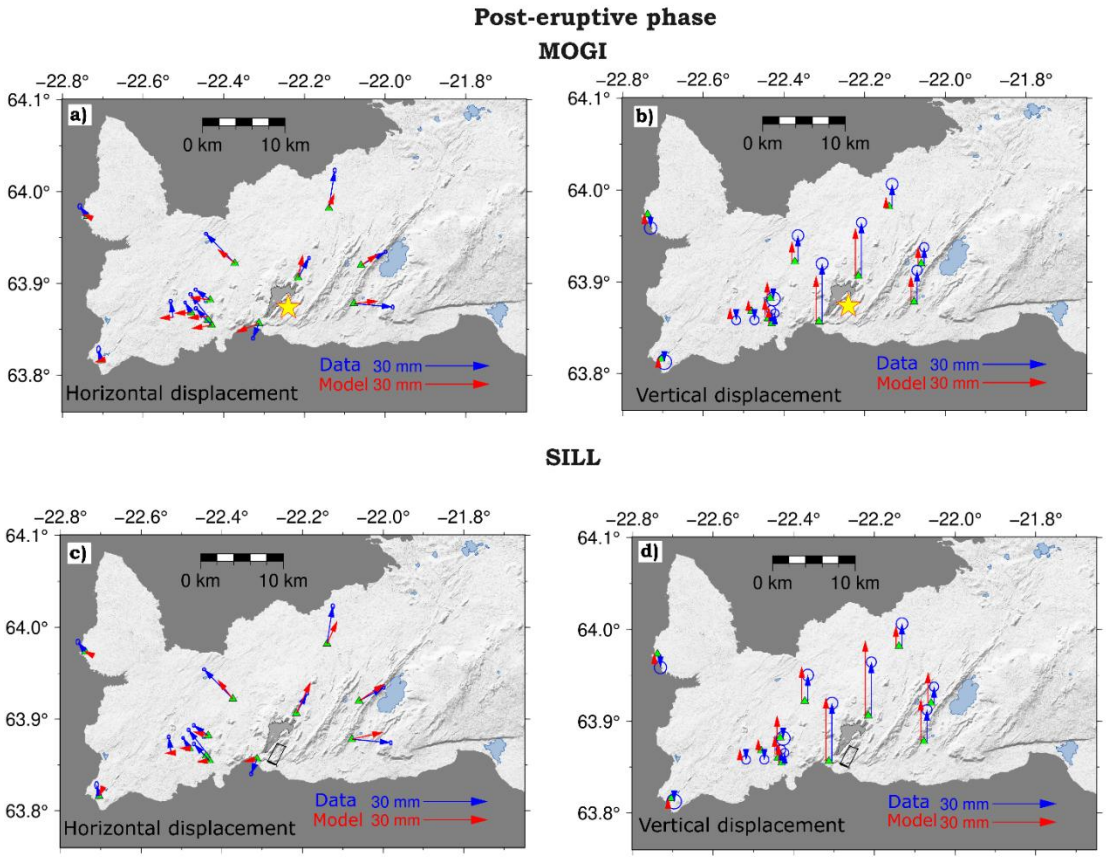

Figure S23. Modelling results for post-eruptive phase for Mogi and sill sources. Horizontal a) and b) vertical GNSS data and model predictions for the Mogi source (yellow star) at 8.00 km depth (95% confidence interval: 7.3-9.4 km). located at -22.26°, 63.89° (optimal values). Horizontal c) and Vertical d) data and model prediction for a sill source at a depth of 12.3 km depth (95% confidence interval: 11.5–13.7 km). Model parameter results for the Mogi are displayed in Supplementary Figure S24; while for the sill, they are in Supplementary Figure S25. Black outlines show the projection at surface of the modelled deflating sill with the thicker line indicating the top of the sill. In light grey, the Fagradalsfjall lava field at the end of the eruption and in light blue are indicated lakes in the area. Dark grey indicates the ocean.

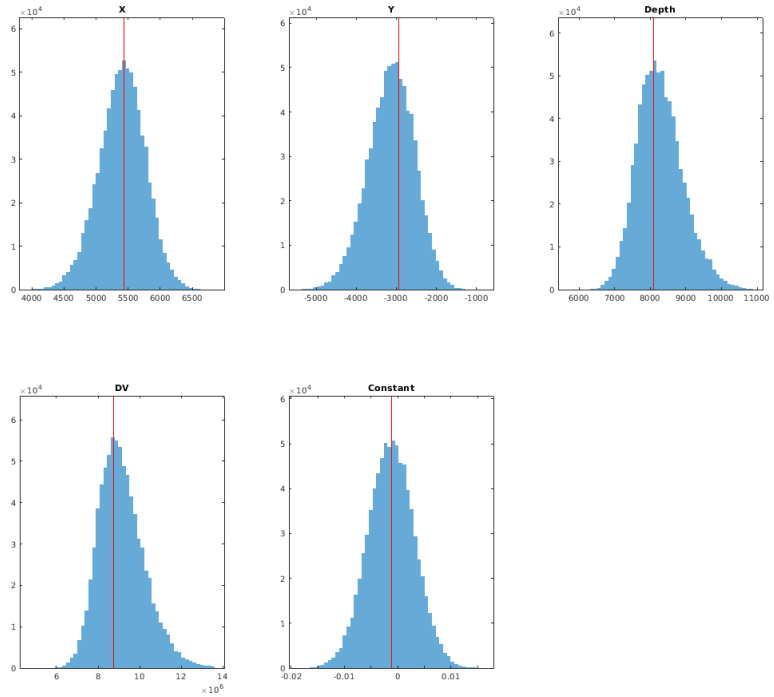

MODEL PARAMETER	Optimal	2.5 %	97.5%
Depth (km)	8.09	7.14	9.71
Deflating volume change (Mm^3)	8.76	7.28	11.7
Longitude	-22.229	-22.245	-22.216
Latitude	63.854	63.935	63.862

Figure S24. Inferred probability density functions for Mogi best fit model parameters (GBIS) for the post-eruptive phase modelling with the parameter values listed in the table below in terms of best-fit, 2.5% and 97.5% results. Source location parameters X and Y are in local coordinates in meters in the pdf but presented in longitude and latitude in the table. Also inferred by the inversion are two offset parameters (InSAR Const.) for each of the InSAR satellite tracks used, as the input displacement fields may have an arbitrary offset. The InSAR Const. is a shift applied to the entire dataset for track T16 and it is in meter. The red line indicates the optimal value of the parameter.

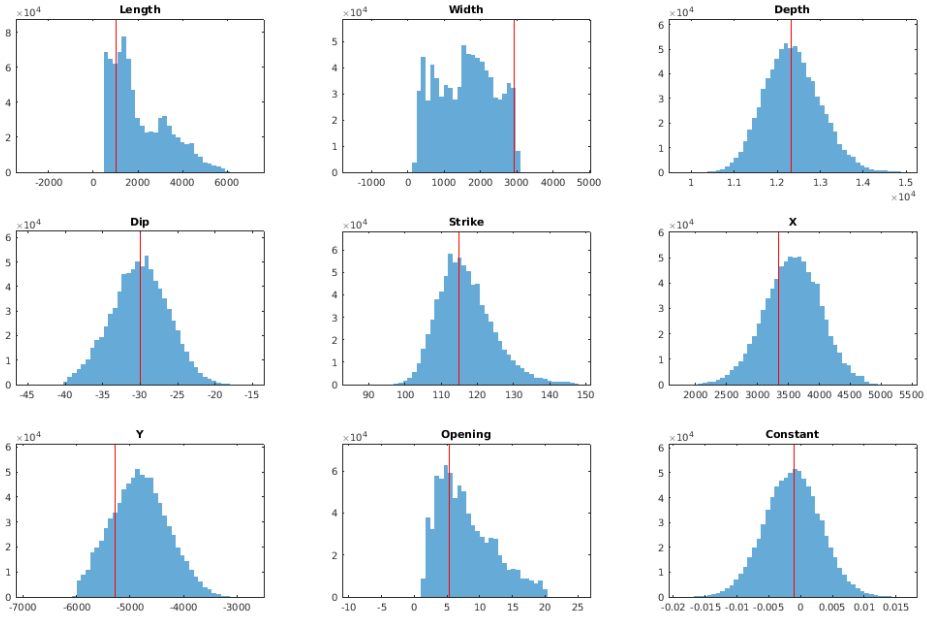

MODEL PARAMETER	Optimal	2.5%	97.5%
Depth (km)	12.3	11.2	13.7
Length (km)	1.04	0.551	4.93
Width (km)	2.92	0.315	2.92
Strike (°)	115	104	135
Dip (°)	-30	-37	-23
Longitude*	-22.284	-22.296	-22.249
Latitude*	63.838	63.828	63.828

Figure S25. Inferred probability density functions for sill geometry for the post-eruptive phase for the optimal, 2.5% and 97.5% values. Source location X and Y are in local coordinates in meters in the pdf, but converted in latitude and decimal degrees in the table; the values referred to the bottom edges of the dislocation. Also inferred by the inversion are two offset parameters (InSAR Const.) for each of the InSAR satellite tracks used, as the displacement fields may have an arbitrary offset. The InSAR Const. is a shift applied to the entire dataset and it is in meter, the first panel is for the T16 and the second for the T155 track. The red line indicates the optimal value of the parameter

TABLE S1. GNSS sites network.

GNSS Site Name	Longitude	Latitude	Linear velocity		Plate spreading signal removed according to the plate spreading model by Drouin & Sigmundsson (2019)	
			East (mm/yr)	North (mm/yr)	East (mm/yr)	North (mm/yr)
Short time series						
HAFC	-22.68	63.93	0.84	-20.03	-13.64	4.82
ELDC	-22.53	63.86	-7.64	-41.77	-9.96	3.14
LISK	-22.37	63.92	0.65	-35.15	-11.88	3.63
THOB	-22.44	63.86	-3.72	-35.37	-9.08	3.22
GRIC	-22.43	63.85	-6.18	-38.58	-8.41	3.41
FAFC	-22.21	63.90	20.09	-9.74	-9.36	3.15
FEFC	-22.31	63.86	-24.27	-44.25	- 6.91	3.88
ODDF	-22.12	63.94	28.12	5.33	-11.05	3.22
AFST	-22.14	63.98	20.59	-13.15	-12.67	3.99
NAMC	-22.54	63.92	-6.22	-27.70	- 12.76	4.17
VOGC	-22.33	63.98	3.11	4.42	-13.42	4.59
HERV	-21.88	63.87	8.39	-24.39	-3.49	2.85

STAN	-22.23	63.85	1.04	-54.37	-5.18	3.89

References

Drouin V, Heki K, Sigmundsson F, et al (2016) Constraints on seasonal load variations and regional rigidity from continuous GPS measurements in Iceland, 1997–2014. Geophys J Int 205:1843–1858. https://doi.org/10.1093/gji/ggw122

Geyer A, Gottsmann J (2010) The influence of mechanical stiffness on caldera deformation and implications for the 1971–1984 Rabaul uplift (Papua New Guinea). Tectonophysics 483:399–412. https://doi.org/10.1016/j.tecto.2009.10.029

Hautmann S, Camacho AG, Gottsmann J, et al (2013) The shallow structure beneath Montserrat (West Indies) from new Bouguer gravity data. Geophysical Research Letters 40:5113–5118. https://doi.org/10.1002/grl.51003

Heap MJ, Villeneuve M, Albino F, et al (2020) Towards more realistic values of elastic moduli for volcano modelling. Journal of Volcanology and Geothermal Research 390:106684. https://doi.org/10.1016/j.jvolgeores.2019.106684

O'Hara C (2023) Estimating deformation source parameters using a 3D elastic finite element model including topography and crustal heterogeneity at Askja, Iceland. Ms Thesis, University of Iceland. https://hdl.handle.net/1946/45701